Solar Wind Sodium and Potassium Abundance Analysis in Genesis Diamond-on-Silicon and Silicon Bulk Solar Wind Collectors, and How Hydration Affects the Microtexture of Olivine Phase Transformation at 18 GPa

by

Karen Dianne Rieck

A Dissertation Presented in Partial Fulfillment
of the Requirements for the Degree
Doctor of Philosophy

Approved October 2015 by the
Graduate Supervisory Committee:

Richard Lokke Hervig, Chair
Amy Jo Goldmintz Jurewicz
Thomas Sharp
Meenakshi Wadhwa
Peter Williams
Patrick Young

ARIZONA STATE UNIVERSITY

December 2015

ABSTRACT

The present work covers two distinct microanalytical studies that address issues in planetary materials: (1) Genesis Na and K solar wind (SW) measurements, and (2) the effect of water on high-pressure olivine phase transformations.

NASA's Genesis mission collected SW samples for terrestrial analysis to create a baseline of solar chemical abundances based on direct measurement of solar material. Traditionally, solar abundances are estimated using spectroscopic or meteoritic data. This study measured bulk SW Na and K in two different Genesis SW collector materials (diamond-like carbon (DlC) and silicon) for comparison with these other solar references. Novel techniques were developed for Genesis DlC analysis. Solar wind Na fluence measurements derived from backside depth profiling are generally lower in DlC than Si, despite the use of internal standards. Nevertheless, relative to Mg, the average SW Na and K abundances measured in Genesis wafers are in agreement with solar photospheric and CI chondrite abundances, and with other SW elements with low first ionization potential (within error). The average Genesis SW Na and K fluences are 1.01e11 (+9e09, -2e10) atoms/cm^2 and 5.1e09 (+8e08, -8e08) atoms/cm^2, respectively. The errors reflect average systematic errors. Results have implications for (1) SW formation models, (2) cosmochemistry based on solar material rather than photospheric measurements or meteorites, and (3) the accurate measurement of solar wind ion abundances in Genesis collectors, particularly DlC and Si.

Deep focus earthquakes have been attributed to rapid transformation of metastable olivine within the mantle transition zone (MTZ). However, the presence of H_2O acts to overcome metastability, promoting phase transformation in olivine, so olivine must be

relatively anhydrous (<75 ppmw) to remain metastable to depth. A microtextural analysis of olivine phase transformation products was conducted to test the feasibility for subducting olivine to persist metastably to the MTZ. Transformation (as intracrystalline or rim nucleation) shifts from ringwoodite to ringwoodite-wadsleyite nucleation with decreasing H_2O content within olivine grains. To provide accurate predictions for olivine metastability at depth, olivine transformation models must reflect how changing H_2O distributions lead to complex changes in strain and reaction rates within different parts of a transforming olivine grain.

TABLE OF CONTENTS

Page

CHAPTER Page

CHAPTER Page

CHAPTER Page

LIST OF TABLES

LIST OF FIGURES

Figure Page

Figure Page

Figure Page

Figure Page

1. CHAPTER 1 – PREFACE

SOLAR WIND SODIUM AND POTASSIUM ABUNDANCES MEASURED IN GENESIS DIAMOND-ON-SILICON AND SILICON BULK SOLAR WIND COLLECTORS BY SIMS

The Genesis mission collected samples of solar wind for terrestrial analysis to create a new baseline for the composition of the solar nebula. Using solar material to estimate solar nebula composition is an alternative to using either (1) solar photospheric data, which relies on theoretical models that are difficult to constrain, or (2) meteoritic material, specifically from CI chondrites, which are challenging to interpret because they have undergone hydrous alteration and volatile loss. This chapter discusses the measurement of bulk solar wind Na and K, the results, and the implications for (1) the solar physics of how solar wind is ionized and accelerated away from the Sun, and (2) the cosmochemistry based on solar material rather than CI chondrites.

1.1. Science Overview

1.1.1. Introduction

Determining the chemical composition of the early solar nebula is a key step toward understanding the origin and evolution of the solar system. There are a number of different approaches to achieving this goal. Firstly, one can analyze the outer portion of the Sun, the solar photosphere, to establish this cosmochemical baseline. The solar photosphere is thought to be decoupled from nucleosynthetic processes, leaving it essentially unchanged in composition from that of the early solar nebula. However, spectroscopic interpretation of this data is strongly dependent on the theoretical models employed, and elemental abundances modeled from spectroscopic measurements can have uncertainties estimated at 2-100% (Palme *et al.*, 2014). These methods need to be grounded with other observations.

An alternative approach is to measure the bulk elemental abundances of CI chondrite meteorites, considered to be representative of bulk solar system composition (except for volatile elements). Most non-volatile elemental abundances for CI chondrites agree with photospheric abundances within error (Figs. 1.1-1.3; Palme *et al.*, 2014). The primary benefit of CI chondrite data is that the abundances are more precise than photospheric analyses, but using abundances from CI chondrites for solar abundance estimates are only validated by comparison with photospheric measurements. CI chondrites have been aqueously altered from their original mineralogies (e.g., McSween, 1993; Scott and Krot, 2007), they have not preserved representative abundances of highly volatile elements (Palme *et al.*, 2014), and they are chemically inhomogeneous (Morlok *et al.*, 2006), particularly on scales <1 gram (Barrat *et al.*, 2012). These meteorites are

also extremely friable (Barrat *et al.*, 2012) and very rare (Krot *et al.*, 2014), so less material is available for analysis. Of the 10 CI chondrites, only 5 are falls, and most chemical data used for defining the composition of CI chondrite meteorites come from Orgueil, the most massive member of this group (Palme *et al.*, 2014). Consequently, the CI chondrite chemical baseline for estimating solar abundances is very dependent on small sample sizes from relatively few sources. This baseline will only remain stable if the chemistry of new CI chondrites remains consistent with previous measurements. The baseline might also be altered if Orgueil (total known weight: ~14kg) is chemically inhomogeneous on scales >>1g.

Measuring solar material directly is an alternative means to check these other approaches, and establish a stable baseline. As collecting material directly from the Sun is not feasible, solar wind is collected instead. Solar wind (SW) is a sampling of solar photospheric material, and as such it has a better provenance than CI chondrites for representing solar abundances.

Solar wind can be accelerated out from the Sun by different mechanisms, producing three solar wind regimes: 1) high-speed streams of solar wind that issue from coronal holes (e.g., Krieger *et al.*, 1973); 2) low-speed "interstream" solar wind (Fisk *et alet al.*, 1998); and, 3) transient wind associated with coronal mass ejections (CMEs) (Webb, 2000). Large-flux "solar energetic particles" (LSEPs) can originate from either CMEs or flares. The combination of these regimes constitutes the "bulk" solar wind.

One challenge inherent in using bulk SW to establish a cosmochemical baseline is that the processes underlying SW formation can cause elemental fractionation relative to the solar photosphere (Fig. 1.4). As solar wind is extracted from the solar photosphere the

elements that ionize less easily tend to remain behind. Consequently the solar wind is depleted in elements with high first ionization potential (FIP). Elemental abundances in solar wind differ from that of the photosphere not only according to FIP (e.g., Reisenfeld *et al.*, 2007; Schmeltz *et al.*, 2012; and Figs. 1.5-1.6), but also according to the type (or regime) of solar wind (e.g., Slow: Giammanco *et al.*, 2008; Slow & Coronal Holes: Bochsler, 2007; SEPs: Reames 1994; 1995; 1998; Breneman and Stone, 1985). Details concerning solar wind fractionation processes are beyond the scope of this project; for more information please refer to Laming *et al.*, 2015 and Schmeltz *et al.*, 2012.

The amount of fractionation must be well-quantified to provide a reliable correction that accurately translates solar wind data into solar photospheric values. Unfortunately, *in-situ* measurements of SW minor element abundances have yielded uncertainties of up to a few tens of percent (e.g., Ulysses: von Steiger *et al.*, 2000; SOHO: Ipavich *et al.*, 1999). To obtain more precise measurements, solar wind sample return was performed. On Earth, this material can be analyzed with a wider variety of tools and techniques than is currently available on spacecraft. Solar wind was first collected as part of the Apollo lunar missions 11, 12, 14, 15, and 16, but the range in elements that could be measured was greatly limited by the purity and abundance of the collector material, and the amount of solar wind collected. In 2004, the Genesis mission returned the longest-exposure bulk SW sample to date (852.83 days over a span of 27 months; Reisenfeld *et al.*, 2007). The spacecraft's diverse assemblage of SW collector materials, selected for their purity with respect to specific elements, permits analysis of a broad range of SW components. Prolonged collection time combined with modern

analytical techniques allow for more solar wind elements and isotopes to be analyzed than ever before.

1.1.2. Objective 1

Data from *in-situ* spacecraft suggest that when SW and photospheric element abundances are normalized to corresponding Mg abundances, SW elements with low first ionization potential (FIP; <10eV) are not fractionated relative to their photospheric counterparts (within error) (Reisenfeld *et al.*, 2007). Solar wind fractionation from photospheric abundances (X*) is defined as

$$X^* = X_{SW} / X_{Photosphere}$$

where X_{SW} and $X_{Photosphere}$ refer to the abundance of a given element normalized to a reference element. Here, elemental abundances are normalized to Mg, the lowest FIP element in the ACE/SWICS data set (Pilleri *et al*., 2015). That is, SW fractionation from photospheric abundances appears to plateau at 1 (within error) for low-FIP elements (Reisenfeld *et al.*, 2007; Figs. 1.5-1.6). However, Genesis data and advanced analytical techniques should decrease the measurement errors and thereby validate or refine the observed fractionation trend. This is the first objective of this work. Accurate and precise measurement of low FIP SW elements (e.g., Na and K) in returned SW samples may help to better constrain these fractionation processes, clarify whether small corrections for solar physics models must be applied, or verify whether the derived solar photospheric elemental abundances are correct. Prior to this study, there were only preliminary measurements of Genesis SW Na (Jurewicz *et al.*, 2007 and Heber *et al.* 2014b).

1.1.3. Objective 2

Assuming that the SW results are a better representation of solar chemistry (and hence, solar system chemistry), the second objective of this work is to compare Genesis solar wind measurements to the elemental abundances of CI chondrites to look for deviations suggestive of alteration or processing during their formation, which would have implications for the use of CI chondrites as a proxy for solar abundances.

1.2. Approach

1.2.1. Test of Success

Successful measurement of solar wind elemental abundances is determined by reproducibility. Ideally, there should be agreement 1) between analyses conducted within the same sample, 2) between samples having the same basic matrix composition, 3) between samples having different matrix compositions, 4) between analysis sessions, and 5) between analytical instruments. Measurement errors must be within those of spacecraft data (e.g., less than a few tens of percent (e.g., Ulysses: von Steiger *et al.*, 2000; 2010; von Steiger and Zurbuchen, 2011; and SOHO: Ipavich *et al.*, 1998 (as cited in Giammanco *et al.*, 2008); 1999 (as cited in Bochsler, 2007)); "substantial," Bochsler, 2001) and preferably within error of solar photospheric measurement (e.g., ~7-23% for Na and K; Lodders *et al.*, 2009; Scott *et al.*, 2015; Palme *et al.*, 2014). If errors are greater than these, the causes must be identified.

1.2.1.1. Comparison With In-Situ Measurements of Na and K Fluences

The composition of the SW has been measured *in-situ* by many spacecraft (e.g., ACE, SOHO, WIND, Ulysses, ISEE satellites, Voyager space probes, IMP spacecraft,

AMPTE Mission satellites, and others), yet there are few *in-situ* solar wind Na and K measurements reported in literature, and most (if not all) of these are specific to individual solar wind regimes rather than to bulk solar wind (e.g., interstream and coronal hole (Ipavich *et al.*, 1999; Bochsler, 2007), SEP (Reames, 1994; 1995; 1998; Breneman and Stone, 1985; Cook *et al.*, 1984), and slow solar wind (Giammanco *et al.*, 2008)). The mass resolution used for these measurements was only ~100 MRP at best (Ipavich *et al.*, 2001; MRP = Mass Resolving Power). Recent work by Pilleri *et al*. (2015) suggests some small fractionation of low FIP elements by *in-situ* spacecraft, but Na and K were not included in this study. Thus, measuring any bulk SW Na and K abundances in Genesis samples with >>100MRP may be considered success.

1.2.2. Materials

1.2.2.1. Solar Wind Collectors

This study focused on the analysis of the Genesis spacecraft's bulk solar wind collector arrays. Four diamond-like carbon (DlC) on silicon (DoS) wafers and two silicon (Si) wafers were selected for analysis. The advantage of using DlC is that it retains volatile elements more effectively than other Genesis collector-array materials when heated (Aisenberg and Chabot, 1971; Vainonen *et al.*, 1997; Heber *et al.*, 2009). Additionally, DlC is highly resistant to scratching, and chemically resistant to a number of reagents used for removing terrestrial surface contaminants, thereby facilitating some aspects of sample cleaning and analysis (Appendix A). The primary drawback to using DlC is that high internal stresses cause it to be very fragile. A rigid backing (e.g., Si) is necessary to keep DlC stable. This fragility places limits on what sample preparation work is feasible (Chapter 2; Appendix B). Sample images are presented in Appendix B.

Silicon (Si) collectors (primarily Czochralski-grown (CZ) crystals) were selected for comparison with DlC because Si is a very well-characterized substrate with high purity (Jurewicz *et al.*, 2003). Drawbacks to using CZ Si are that this substrate is less retentive of volatile elements than DlC (e.g., Heber *et al.*, 2009), less resistant to scratching than DlC, and not resistant to Micro-90® Cleaning Solution, which is used for removing terrestrial contaminants, particularly alkali elements. Sample images are presented in Appendix B. Additional information about all the Genesis collector materials may be found in Jurewicz *et al.* (2003).

1.2.2.2. Reference Materials

1.2.2.2.1. Ion Implants

The arrangement of samples for ion implantation is presented in Appendix C. The various stages of ion implantation are depicted in Appendix D. In order to ensure accurate calibration of SW measurements, reference ion species were implanted into matrices similar to (or identical to) the collector wafers of interest. This is particularly important for analysis by secondary ion mass spectrometry (SIMS; discussed later). If matrices are different, "matrix effects" can occur; in particular, ion sensitivity may change between standard and sample, reducing the accuracy of SW measurements.

Initially, external standards were used for calibrating SW measurements in this study. To create these standards, reference ions were implanted into the frontsides of non-flight Si and DoS wafers. When measurement discrepancies were observed between analyses (Chapter 2), standards were implanted directly into Genesis collectors to further reduce the risk of matrix effects. Reference ions implanted directly into Genesis SW collectors are referred to as "internal standards" here. Internal standardization ensured

that similar analytical conditions were maintained between measurement of the standard and the SW in both DlC and Si SW collectors. Furthermore, analyses that could measure both the standard and SW in the same depth profile were the most efficient.

Ion implantation of reference species (^{23}Na, ^{39}K, and/or ^{41}K) was performed professionally by Leonard Kroko, Inc. In preparation for ion implantation, samples were cleaned, mounted on rigid substrates and thinned as needed (thinning discussed later). Details of each implant are provided in Tables 1.1 and 1.2.

Reference ions can be implanted from either the front- or backside of a Genesis wafer to create an internal standard. To best distinguish solar wind ions from implanted reference ions, internal standardization was performed from the "backsides" of thinned wafers, away from the solar wind regions located in the "frontsides." The front surface of these Genesis wafers is also referred to as the "solar wind collection surface." Ion implantation from the backside was facilitated by the fact that Genesis Si and DoS SW collector wafers were already being oriented face-down and thinned for SIMS backside depth profiling analysis (Si: Heber *et al.*, 2014a, b, c; DlC: discussed later, Appendices B and C). Nevertheless, the proper balance of implant energy and ion fluence were needed to both 1) avoid interference with the SW on the frontside, and 2) reduce interference with backside surface contaminants. In general, implanting 2e12 atoms/cm^2 with 100 keV was sufficient.

Persistent measurement discrepancies (Chapter 2) suggested that there was a calibration problem, (e.g., the calibration was changing between the analysis of the reference standard and the analysis of the solar wind). Calibration can change if the matrix containing the reference standard is different from the matrix containing the

sample. In order to ensure that the matrix of the standard was as similar to that of the SW as possible, front-side ion implantation was performed on two samples of Genesis DoS, only one of which has been successfully analyzed to date. The reference ions were implanted directly into the front surfaces of the Genesis wafers to partly overlap the solar wind implanted region. If the peaks of the reference implants perfectly coincided with the shallow implant peaks of the solar wind elements of interest, it would be much more difficult to 1) distinguish SW ions from reference ions, and 2) distinguish reference ions from surface contaminants. The logic behind using this method was to test whether the presence of the bulk SW in the front surface of the Genesis collectors may change the matrix composition sufficiently to induce SIMS matrix effects. If the matrix changes between the front- and backsides of the Genesis collectors it would prohibit the use of backside ion implants for SW measurement calibration. Frontside internal standardization has already been shown to be successful in bringing Mg measurements in DlC and Si into agreement with each other (Fig. 1.7; Written Communication: A. J. G. Jurewicz; 44th LPSC Genesis Team Meeting (2013)). Thus, it was important to test for this effect for Na and K.

Again, only frontside-standardization of Genesis DoS has been attempted; frontside-standardization of Genesis Si has not yet been attempted, because it is more challenging, particularly for Na analysis. Firstly, cleaning Si surfaces is a challenge. The Micro-90® used for removing terrestrial Na and K from DlC surfaces can not be used on Si because it is too reactive, etching Si surfaces and removing implanted ions. Secondly, the implant profiles in Si are broader than they are in DlC owing to the lower density of Si, making it more challenging to distinguish SW signal from that of frontside-implanted

reference species. Fortunately, this overlap is less problematic for K than it is for Na. The minor species ^{41}K can be implanted as reference, with insignificant interference from SW ^{41}K. However, the ^{41}K reference implants often include a small amount of ^{39}K. The fluence of this ^{39}K can be measured in blank materials implanted concurrently with the Genesis sample. The "accidental" ^{39}K implant fluence measured in the blank is then subtracted from the Genesis ^{39}K measurement to derive the true solar wind ^{39}K fluence. In the future, if Genesis Si collectors can be cleaned sufficiently, it would be worth testing whether calibration of SW K measurements is affected by the position of the reference implant (frontside vs. backside).

1.2.2.2.2. Calibration

The nominal fluences of the ion implant standards were not sufficiently precise for calibrating SW measurements. Rutherford Backscattering Spectrometry (RBS) and RUMP data processing software were used to calibrate high dose (~1e16 atoms/cm^2) ^{23}Na and ^{39}K implants.

RBS work requires high fluence standards. Analyses focused on DoS because unlike the silicon in the Si SW collectors, the carbon in the DoS collectors does not interfere with RBS measurement of Na and K. The RBS analyses were conducted with a 2MeV He^{++} beam, oriented at an 8° theta angle. RBS measurements were calibrated by a bismuth standard in silicon (30keV; 4.75 (± 0.1) × 10^{15} atoms/cm^2; RM D4). Nonuniformity of the bismuth implant is less than 1%. Raw RBS profiles are provided in Appendix E. RBS data are provided in Table 1.3. Test analyses on a blank DoS wafer yielded Na and K backgrounds indistinguishable from signal noise.

Low- (2e12 atoms/cm^2) and medium-dose (~1e14 atoms/cm^2 and ~3e13atoms/cm^2) standards were made to facilitate calibration of solar wind measurements by SIMS. SIMS intercalibration works best for samples with fluences that differ by less than ~2-3 orders of magnitude. Greater differences generally necessitate a significant change in instrument parameters 1) to avoid incurring significant dead time effects for high fluence samples, or 2) to ensure sufficient signal for low fluence samples. However, changing parameters to increase/decrease yield within an analysis session inherently changes the calibration (Wilson *et al.*, 1989). In order to avoid this problem, low- and medium-dose standards (some made especially for this study, and others acquired from other Genesis researchers) were used to bridge the intercalibration gap between high fluence standards calibrated by RBS and SW, for which the predicted 2-year Na and K fluences were ~1.1e11 atoms/cm^2 and ~7.1e09 atoms/cm^2, respectively; (Burnett *et al.*, 2003). To permit comparison between the Na fluences measured in this study and the work of Heber *et al.* (2014b), the Na in Si standard used by Heber *et al.* (2014b; c) was procured and calibrated against the standards made for this study. The results of standard intercalibration are presented in Tables 1.1 and 1.2; and Fig. 1.8.

Simultaneous ion implantation into multiple substrates facilitated inter-calibration, as every sample in an implantation session should have received identical doses of ions, regardless of matrix. (For a discussion of implantation theory as it relates to Genesis sample analysis, see Burnett *et al.* (2015); for images of how the samples in the present study were arranged for ion implantation, please refer to Appendix C).

Co-implantation of Na and K reference ions improved measurement efficiency by allowing both elements to be measured in the same location. A drawback of having

multiple implants in a sample is that multiple overlapping high fluence implants can cause significant matrix effects. These matrix effects manifest as localized decreases in matrix ion yield during SIMS depth profiling analyses, and correlate with the depths of the highest concentrations of implanted reference ions. This effect was observed for both Si and DlC implanted with 1e16 atoms/cm^2 ^{23}Na and ^{39}K (Appendix F). Corrections for this effect were made by extrapolating the matrix ion signal measured in a more stable part of the depth profile over the "dip." The corrected matrix ion intensities were used to normalize Na^+ and K^+ ion intensities.

1.2.2.3. Sample and Reference Material Preparation

1.2.2.3.1. Cleaning

In order to remove terrestrial residue from Genesis SW collector wafer surfaces, most Si and DoS wafers were cleaned using a megasonic spray of Ultra-High Purity (UHP) water by the curatorial staff at Johnson Space Center, a procedure that removes particulates. All wafers (both collectors and reference materials) underwent additional cleaning at ASU, the details for which are provided in Appendix A. This study adapted the procedure from the full RCA cleaning method, and modifications presented by Sinha (2002). This general cleaning procedure was applied prior to 1) sample mounting for SIMS backside depth profiling (BDP) analysis, 2) frontside ion-implantation of reference ion species, and 3) frontside (traditional) SIMS depth profiling analysis. Samples thinned for BDP were too fragile to undergo any additional repetitions of the general cleaning procedure.

1.2.2.3.2. Sample Mounting and Thinning

Samples selected for BDP would be mounted face-down on conductive substrates with epoxy, in preparation for thinning. Genesis Si was mounted (onto Si) and mechanically polished by Evans Analytical Group (EAG) (Appendix D). One sample was polished to ~1.2 μm. Another sample was polished to a thickness of only ~2.5 μm to accommodate both an internal (backside) implant and the solar wind, both of which penetrate the Si more deeply than they do the DlC.

DoS samples require very gentle thinning methods to reduce the risk of damaging the fragile DlC film. The gentlest approach tested in this study used a chemical etchant. Grinding and polishing proved to be too harsh (Chapter 2). Consequently, the substrate and epoxy used for mounting the Genesis DoS had to be chemically resistant. Most Genesis DoS samples were mounted in-house on graphite planchets using a low viscosity adhesive: M-Bond® 610. A specially-designed press clamped the sample to the substrate during curing, while maintaining proper alignment. Mounted DoS samples were treated with XeF_2 at Argonne National Lab to etch away the Si that provided the backing for the DlC film ($2XeF_2$ (*vapor*) + Si (*s*) → 2Xe (*g*) + SiF_4 (*g*) ; Chang *et al.*, 1995; Brazzle *et al.*, 2004; Veryovkin *et al.*, 2014). After thorough etching, only the mounted DlC film remains, its back surface entirely exposed.

Early investigations by I. Veryovkin suggested that GaAs might be a better substrate for DlC film, because one could monitor Ga or As during BDP to determine where the DlC ended and the substrate began (I. Veryovkin, personal communication). The present study also explored the potential for GaAs wafers to serve as DlC substrates. Unfortunately, GaAs wafers proved too fragile for the methods used in this study. The

GaAs wafer used to support Genesis DlC (60407) broke once during cleaning and again during sample mounting. The GaAs (with the SW collector firmly epoxied to it) had to be mounted on a graphite planchet to save the sample. Images of sample 60407 are provided in Appendix B. I. V. Veryovkin also came to the same conclusion that, despite its other favorable attributes, GaAs was much too fragile to be used as a supporting substrate for DlC film (I. V. Veryovkin, personal communication).

The chemical reaction involved in XeF_2 etching likely imparted some heat to the samples (Chang *et al.*, 1995), but, compared with other methods, XeF_2 etching greatly minimized stress-related damage and distortion. A drawback of this approach is that there were always non-volatile compounds not removed by the etching process deposited on the backsides of the DlC film (Appendix B). This may be the whitish film referred to by Chang *et al.* (1995). In some cases, this material could be blown away with compressed air, but it was very difficult to impossible to remove all of it.

1.2.3. Data Collection

1.2.3.1. SIMS Overview

Secondary ion mass spectrometers are designed for depth-sensitive relative abundance ion measurements, and are often used to measure contaminants in semi-conductor wafers. This makes them ideal tools for measuring the abundances of solar wind elements in Genesis collectors. Mass spectrometers at Arizona State University (6f SIMS) and Caltech (7f SIMS) were used to conduct depth profiles into Genesis Si and DoS collectors.

1.2.3.1.1. Frontside Depth Profiling

Frontside depth profiling is primarily used for the analysis of external standards with relatively deep ion implants. The general sample cleaning procedure is performed prior to analysis to remove as much surface contamination as possible. Clean, defect-free areas away from sample edges are targeted for analysis.

The start of any SIMS depth profile is characterized by a brief instability of ion signal. This is called transient sputtering. It represents the period it takes for the ion yield to stabilize after profiling through a surface oxide layer. In general, the first several cycles of data are collected while the ion yield is stabilizing, and so these data can be misrepresentative of the actual abundances. Transient sputtering and surface contamination can both interfere with accurate measurement of near-surface implants. To date, only one frontside SW analysis of Na and K (performed in Genesis DoS 61090) was sufficiently clean and reliable to be reported here. This analysis was calibrated with a frontside-implanted internal ion standard. All other analyses reported here used either external standards, or backside-implanted internal ion standards. The primary benefits from using front side depth profiling are that 1) it is easier to see and avoid surface contaminants, 2) the surface is free from topography, and 3) the SW profiles are very time efficient, particularly when they utilize frontside-implanted internal standards.

1.2.3.1.2. Backside Depth Profiling

Traditionally, SIMS involves depth profiling from the front/top/polished surface of a sample. However, this approach is not ideal for most Genesis samples, where analytical transient artifacts and surface contamination resulting from the spacecraft's crash landing generally interfere with the measurement of the SW (Burnett *et al.*, 2007;

Heber *et al.*, 2010). The primary advantage of backside depth profiling is that it reduces signal contamination caused by ion beam mixing of surface contaminants into the upper layers of the sample, and therefore allows for better depth resolution and dynamic range. Backside depth profiling also allows for more time to reach the end of the transient sputtering region before sampling solar wind, or deep implants.

Prior to analysis, DlC film had to be delicately cleaned of as much post-etching debris as possible using compressed air, acetone, etc. Neither thinned Si nor DlC film was strong enough to undergo regular cleaning procedures. Consequently, finding clean areas to analyze was often very challenging.

Another challenge is charge dissipation during SIMS analysis of thinned samples. The small, delicate, thinned samples are generally not in direct contact with the sample holders. Accordingly, conductive paths must be made between samples and holders. Generally, this entails using the conductive substrates on which these samples are mounted. There are two primary ways to achieve this, either 1) the thinned sample and its substrate are gold-coated, which may inadvertently impart a layer of surface contaminants to the sample, or 2) a conductive path is drawn in, usually with graphite paint, over any exposed non-conducting epoxy. Note that any carbon paint on the sample itself restricts the space available for analysis.

For all BDP analyses, low-Na and low-K steady-state conditions (i.e., "background") were reached before sampling SW (e.g., Fig. 1.9). Within the background of the DlC were sharp periodic peaks in Na and K signal. These peaks correspond to non-uniform layers of contamination incorporated into the DlC at the time of manufacture. Each spike in signal from these contaminants marks an annealing step between

neighboring layers of DlC. These peaks were subtracted as part of the background signal (Figs. 1.10-1.11).

One downside to BDP is that the *exact* position of the original collection surface may be hard to identify, complicating extrapolation of signal to the surface. In these situations, ion implant models were employed to estimate the missing signal. Solar wind implant models were provided by C. Olinger (Los Alamos National Lab).

1.2.4. Fluence Calculation

Na^+ and K^+ count rates obtained by SIMS are normalized to the count rate of a matrix species ($^{12}C^+$ for DlC, $^{28}Si^+$ or $^{30}Si^+$ for Si) to correct for small drifts in primary current. Signal from background and contaminants is subtracted prior to integration. For each element of interest in each analysis session, a relative sensitivity factor (RSF; atoms/cm^3) was calculated from the fluence of an absolutely calibrated implant standard and the integrated signal from that standard:

$$RSF = F_{implant} / \int(I_{implant}/N_{matrix})_{std}\, dx \qquad (1)$$

where $F_{implant}$ represents the absolutely calibrated fluence of the ion implant,

$I_{implant}$ represents the count rate intensity of the implanted reference species of interest

N_{matrix} represents the count rate of a matrix species

and dx is the change in depth.

The RSF was applied to the integrated solar wind signal to calculate the fluence (atoms/cm^2) of the solar wind elements of interest:

$$F_{SW} = RSF \times \int(I_{sw}/N_{matrix})\, dx \qquad (2)$$

where F_{SW} represents the fluence of the SW species of interest

and I_{SW} represents the count rate of the SW species of interest.

The accuracy of dx can be affected by 1) primary ion current changes during analysis, which cause localized sputter rate changes that alter the depth profile shape relative to the TRIM model, and 2) error in crater depth measurements resulting from uneven crater floors, sample tilting, and error in profilometer/interferometer calibration.

1.3. Methods

1.3.1. SIMS Details and Parameters for Data Collection

A brief description of samples and methods are provided here and in the Tables 1.4-1.7. Details concerning techniques and technique development are provided in Chapter 2.

The analytical methods of Heber *et al.* (2012) were adapted to measure solar wind ^{23}Na and ^{39}K in Genesis Si and DoS collectors. An O_2^+ primary ion beam was used for these analyses because 1) it produces higher positive ion yield than a Cs^+ beam (Wilson *et al.*, 1989), and 2) it yields better depth resolution than an O^- primary beam (e.g., Schmitt and Zack, 2012). The primary ion beam was accelerated to +12.5-13kV. The sample was held at ~5 to 9 kV, depending on the analysis, which resulted in an impact energy of ~9 to 5kV, respectively. Sample voltages were adjusted to try to optimize depth resolution. Slits and energy windows were adjusted to reduce or eliminate mass interferences. Field apertures, contrast apertures, transfer optics settings, electronic gating (7f SIMS only), and raster sizes were adjusted to minimize contaminant signal originating from outside the selected target area. Raster sizes were kept as small as possible to be space efficient, and to mitigate the effects of breaking through the film at an angle, which can occur when the analysis crater floor is not perfectly parallel with the

collector's solar wind collection surface. Beam current was paired with slit and aperture settings to keep implant peak count rates ~1e5 counts/s or less to minimize the effects of instrumental deadtime on measurements. Beam current was further adjusted to ensure sputtering rates were low enough to provide enough cyclical measurements across a solar wind profile to adequately model the shape of the curve. Generally, the sputtering rate was ~1-3 Å/s. Oxygen flooding was not used for any of the SW depth profiles.

1.3.2. SIMS Profiling Techniques for DlC and Si and Rationale

Some analyses were divided into 2-3 parts in an effort to obtain sharper profiles and better calibrations. Often BDPs were paused just following measurement of the backside-implanted reference ions (if present), or just prior to encountering the SW. This allowed for the removal of the matrix ion species (and any non-critical reference species) from the analysis routine. Limiting the analysis routine to the measurement of only solar wind species increases the amount of time spent gathering solar wind signal. This translates into more solar wind ions collected, which facilitates SW profile modelling and improves the error on the signal integration. The matrix species count rate for the early portion of the BDP is extrapolated linearly over the SW region. SW species are normalized to the extrapolated matrix signal, prior to integration, as described in Equation 2, above. The drawback of this approach is that it is difficult to correct for primary beam current or sputtering rate instabilities that coincide with solar wind profiles. Also, without a baseline count rate, it becomes difficult to identify or interpret signal anomalies. On rare occasions, a matrix species would be left in the analysis routine during SW measurement to check for such factors.

The backside-implanted sample of Genesis Si (61189) required a special 3-step approach to analysis, because of its thickness: 1) presputter with a Cs^+ primary beam, 2) measure SW in presputtered crater, and 3) measure backside-implanted ion reference standard outside of Cs^+ crater. If an O_2^+ primary ion beam were used to profile through all 2.5μm of Si, it would cause significant crater floor roughening, which negatively affects depth resolution and changes ion yield. The Cs^+ pre-sputter raster thins the sample evenly in a localized area (~500 μm × 500 μm) so that less Si must be removed by the O_2^+ primary ion beam before sampling SW. This approach, used and recommended by professional agencies, e.g., Evans Analytical Group, reduces crater floor roughening and its associated effects (e.g., Wilson *et al.*, 1989). The O_2^+ primary ion beam was rastered over a much smaller area (~100 μm × ~100 μm) within the main Cs^+ raster to measure SW. This allowed multiple measurements to be conducted within the pre-sputtered region. Separate analyses using the O_2^+ primary ion beam (again, ~100 μm × ~100 μm raster) was conducted outside the Cs^+ crater to measure the backside-implanted standard to calibrate the SW measurements.

1.3.3. Methods for Extrapolating and Integrating SIMS Depth Profiles

1.3.3.1. Solar Wind Quantification

Implant profiles must be well-separated from the signal from internal and external contaminants. However, in most cases there is at least some contribution from contaminants (usually surficial) that must be excluded from SW signal integration. Only the cleanest SW profiles were used for integration in the present study. Generally, integration is performed between saddle points occurring on either side of the main implant curve, although implant signal extrapolation to the surface may be employed in

situations where the contamination is such that the preceding method underestimates SW signal (e.g., Figs. 1.12-1.13). A discussion of extrapolation models and approaches are provided in the following sections.

1.3.3.2. Models

Numerical ion implantation models were used for extrapolating SIMS depth profiles, approximating where the collector surface should be, and estimating what percentage of the near-surface implant signal is missing. These models are made using a program called TRIM (TRansport of Ions in Matter). TRIM is the core routine of a group of computer programs called SRIM (Stopping and Range of Ions in Matter) originally developed by J. F. Ziegler and J. P. Biersack and made available free of charge for public use. Details are available online at the URL: www.srim.org.

Some of the primary factors that affect the shape of the TRIM models are the mass and energy of the implanted ions, the angle of implantation, and the chemical composition and density of the target matrix. TRIM models describing lab-based ion implantation differ from TRIM models describing solar wind ion implantation. Lab-based ion implantation assumes all atoms of a particular element leave the source with the same charge state, and impact the target with the same energy. Thus, TRIM models of lab-based ion implants have relatively symmetric profiles. However, solar wind atoms of the same element leave the sun with a range of charge states (e.g., Bochsler, 2000; 2007), and travel at different speeds depending on the regime from which they originated (e.g., Reisenfeld *et al.*, 2013). Thus, solar wind ions impact the target with a range of energies, and thus, models of solar wind ion implantation have asymmetric profiles, with tails extending deeper into the target. TRIM models of solar wind profiles were provided by

C. Olinger (Los Alamos National Laboratory). TRIM models of lab-based ion implantation were made both by A. J. G. Jurewicz, and as part of the present study.

1.3.3.3. Graphic Approach

This approach can be applied to profiles whether or not the SW peak can be distinguished from surface contamination, although it works best for the most complete profiles. This method assumes that at least part of the profile is sufficiently free from surface contamination to be matched to a solar wind implant model. This is the method used for much of the data presented here. It is the most conservative approach, and consequently the errors calculated using this approach are up to tens of percent.

TRIM model curves for SW Na and K produced by C. Olinger (LANL) were used to extrapolate SW profiles to the front surfaces to fill in sections that were obscured by surface contaminant signal and/or signal from underlying adhesive (Fig. 1.12). This approach involves scaling the model profile to match the measured profile as closely as possible. The SIMS data is integrated up to the point that the two curves diverge. The percentage of the profile that is missing is calculated using the model profile and is added back into the integration.

Matching the model profile shape to the SIMS profile shape was complicated by SIMS ion beam mixing effects, which broadened profiles, drawing them out to deeper depths. Ion channeling in Si during solar wind collection (Heber *et al.*, 2014c) may have also extended Na and K profiles. Another limitation of the TRIM models is that they are strongly dependent on current solar physics models. Consequently, as the field of solar physics advances, it is likely the models will undergo revision and refinement (C. Olinger, oral communication).

1.3.3.4. Analytic Approach

This approach entails monitoring another SW element, like Mg, to estimate the depth of the front surface of the Genesis SW collector during backside depth profiling. Mg is less abundant in terrestrial contamination than elements like Na or K, so the SW profiles are cleaner, and modelling can be applied more easily to estimate distance from the front surface. This approach can be applied wherever the peaks of the SW implants are easily distinguished. It has been recommended by D. Woolum, and is used by A. Jurewicz. Although this method can yield smaller errors and greater reproducibility, it requires cleaner profiles than the graphic approach.

The following are the steps in this approach: Step 1 - Find the peaks of C. Olinger's TRIM model curves for Mg, Na, and K analytically by fitting 6^{th} order polynomial trendlines to the models, and taking the derivatives. Step 2 - Use the model Mg peak, Mg data collected alongside the Na and/or K profiles, and depth-determined sputtering rate to precisely find the surface of the collector in the depth profile. Step 3 - Knowing the depth in the profile where the collector surface was (effectively) located, shift the Mg SW profile along the depth scale so that the collector surface is at "0 Å" and re-plot SW Na and K data accordingly. Then, scale the intensity of C. Olinger's models to fit SW Na and SW K. Integrate each SIMS SW profile up to the peak, and integrate the scaled model data for the near-surface portion of the profile. Finally, combine the two measurements.

1.3.3.5. Two-Function Approach

This approach assumes there is at least 50% data coverage at the front side. Heber *et al.* (2014c) used a pair of functions to describe the measured SW data. The first of

these is an asymmetric power function, which fits the entire profile, but its extrapolation is asymptotic. A quadratic polynomial was used to model the profile from the peak to the frontside of the collector, permitting extrapolation to the real target surface. This approach could not be used in the present study because there was insufficient data coverage on the front sides of the Na and K profiles.

1.4. Results

1.4.1. Implant Calibration and the Intercalibration of DoS and Si

The results of the absolute calibration of high dose DlC standards with RBS and subsequent standard intercalibration by SIMS are presented in Tables 1.1-1.3. Calibration of the standard used by Heber *et al.* (2014b) raised their SW fluence measurement from 1.00e11 to 1.28e11 (± 4e09) atoms/cm^2.

1.4.2. Measured Sodium and Potassium Fluences

1.4.2.1. Sodium

Minimally-processed solar wind Na depth profiles are available in Appendix G. Backside depth profile measurements of Na in DlC are in agreement with each other, and the measurements are corroborated by both 6f and 7f SIMS instruments (Fig. 1.14; Table 1.8). However, there is a factor of 2-3 disparity between these Na data from backside depth profiling measurements in DlC and most other Na measurements, including a single frontside depth profile into Genesis DoS (61090) (Fig. 1.14; Tables 1.8-1.9).

This frontside depth profile into Genesis DoS (61090) is the only Na measurement in DlC that is in good agreement with Na measurements in Si. The Na fluence derived from the frontside measurement was initially calibrated with an external

standard, and then later by an internal, frontside-implanted standard (as shown in Fig. 1.14). Both frontside internal standardization and external standardization produced the same fluence within error.

Following calibration of the standard used by Heber *et al.* (2014b) (this study), the bulk SW Na fluence (Si) of Heber *et al.* (2014b; 1.28e11 (±4e09) atoms/cm^2) is in agreement with the average bulk SW Na fluence (Si) of this study (1.30e11 (+1e10, -3e10) atoms/cm^2: Table 1.9). It is not in agreement with the average bulk SW Na fluence (DlC) of this study (Fig. 1.14; 7.2e10 (+7e09, -1e10) atoms/cm^2; Table 1.8), which is primarily based on Na measurements from the backside depth profiles into DlC.

1.4.2.2. Potassium

Minimally-processed solar wind K depth profiles are available in Appendix G. SW K fluences are low, and parts of the SW K profile overlap signal from K-containing components on the collector surface. During profile analysis there was variable success distinguishing the SW K signal from that of the K-containing surface components. Consequently, K fluences measured in Genesis DlC and Si were scattered. On average, the K fluence measured in DlC (3.6e09 (+5e08, -4e08) atoms/cm^2; Table 1.8) was lower than the K fluence measured in Si (6e09 (+1e09, -1e09) atoms/cm^2; Table 1.9) by a factor of ~1.7 (Tables 1.8 and 1.9), but the scatter, large errors, and relatively few measurements on Si make it difficult to discern whether there is a real discrepancy between these matrices. Nevertheless, the dissimilarity (DlC: Low, Si: High) is like that observed for Na. The SW K fluence measured in Genesis DoS 61090 by frontside depth-profiling and calibrated by frontside standardization was in agreement with two other high K measurements in DlC and the three lowest K measurements in Si.

1.4.2.3. Average Fluence Calculation

The broad distribution of Na and K data, and the peculiar factor of ~2-3 discrepancies observed between matrices makes determination of the solar wind Na and K fluences particularly challenging. Although there are some possible explanations for the observed spread (Discussion) the exact cause(s) could not be determined, and so there was no reason to reject any of these measurements. To reduce sampling bias, the data have been carefully averaged. First, average Na and K fluences are calculated for each Genesis sample (Tables 1.8 and 1.9). Then, the averages corresponding to the same matrix are averaged. This produces average Na and K fluences for each matrix: DlC and Si (Tables 1.8 and 1.9). Finally, DlC and Si averages are averaged together to derive a single final average fluence for each element. ^{39}K is only ~93.3% of all solar K, so ^{39}K fluences measured in this study were normalized by its relative solar abundance to derive the total SW K fluence. Na only has one stable isotope (^{23}Na), so it does not require normalization to derive the total SW Na fluence. The final average fluences of total SW Na (1.01e11 (+9e09, -2e10) atoms/cm^2) and K (5.1e09 (+8e08, -8e08) atoms/cm^2) are presented in Table 1.10.

1.5. Discussion

This section discusses the following topics:

1) The fluence discrepancy between backside depth profiles in DlC and Si

2) Comparable *in-situ* solar wind Na and K measurements

3) Genesis solar wind elemental fractionation from solar abundances as represented by photospheric measurements versus FIP

4) Genesis solar wind elemental fractionation from solar abundances as represented by chondritic chemistry versus FIP

5) Cosmochemical implications of the new SW Na and K fluences measured in the present study

1.5.1. Fluence Discrepancy Between Backside Depth Profiles in DlC and Si

There are a number of scenarios that could potentially create a fluence discrepancy like that observed between DlC and Si: 1) matrix differences between external and internal standards, 2) intrinsic vertical inhomogeneity in the collector wafers, 3) Na and K diffusion out of DoS or into Si, 4) charge driven Na and K diffusion during analysis, 5) solar wind-induced matrix effects, 6) insufficient mass resolution for SIMS analyses, and 7) data correction challenges contributing to measurement error (e.g., interference from surface contamination, background, and sample inhomogeneity, and uncertainty in the models and modeling). Chapter 2 (Discussion) provides details and assessment of all possible explanations. This section will focus on a discussion of only the most likely scenarios: 6 and 7.

The most abundant element in the solar wind is hydrogen. This SW H is concentrated in the near-surface of the collector wafers (Fig. 1.15). Two H-containing molecular ions potentially causing the greatest mass interference with ^{23}Na measurement in Si are $^{29}Si^{16}O^{1}H^{2+}$ (MRP: 151,586) and $^{28}Si^{16}O^{1}H_2^{2+}$ (MRP: 5,781). Whether these molecular ions (or others) are sufficiently abundant to cause significant mass interfences remains to be tested. $^{29}Si^{16}O^{1}H^{2+}$ is unresolvable from ^{23}Na with current methods.

Low fluence Na and K measurement is particularly challenging because these elements are ubiquitous in the terrestrial environment and ionize easily under a SIMS

primary ion beam. Samples must be exceptionally clean prior to analysis, and integration must exclude all terrestrial and background interferences, without eliminating signal from the SW or reference ions of interest. Deconvolving the SW or the implanted reference ions from surface contaminants generally requires a model or a set of carefully considered assumptions regarding how the implants and contamination combine near the sample surface. In general, this is one of the largest known sources of error in the present study. SW TRIM models have been undergoing revision as solar physics models are updated. Testing whether a model is accurate for near-surface implants is difficult if the near-surface depth profiles are always obstructed by surface contaminants.

Implant modeling and proper calibration of SIMS ion signal are both highly dependent on matrix. Variations in matrix density would alter profiles, leading to over- or underestimation of the implant signal. Both backside and frontside implanted standards reproduced the results of external standards for Na and K measurement in DlC, suggesting these matrices are sufficiently similar. Internal standardization may have had a small effect on measurements in Si, but additional analyses would be necessary to confirm whether this change truly reflects a matrix difference, rather than, e.g., error in surface contaminant correction. Chapter 2 provides an extended discussion of other, albeit less likely, factors affecting Na and K measurement in Si and DlC.

1.5.2. *In-Situ* Measurements of Solar Wind Na/Mg and K/Mg

To date there have been no *in-situ* measurements of bulk Na/Mg or bulk K/Mg reported in the literature (D. B. Reisenfeld, personal communication on June 15, 2015). In theory, regime abundances can be combined in proper proportions to provide a synthetic bulk solar wind composition. Reisenfeld *et al.* (2013) estimates Genesis spent

39.7% of its collection time gathering slow SW, 37.3% gathering coronal hole SW, and 23.0% collecting CME SW. *In-situ* Na measurement has been performed on slow and fast regimes, gradual SEP events, the solar upper atmosphere, the corona, and flares (e.g., Cook *et al.*, 1984; Breneman and Stone, 1985; Reames, 1994; 1995; 1998; Ipavich *et al.*, 1998; 1999; Feldman and Laming, 2000; Bochsler, 2007; and Giammanco *et al.*, 2008), but not on CME. Similarly, *in-situ* K measurement has been performed on slow SW, gradual SEP events, the corona, and flares (e.g., Breneman and Stone, 1985; Reames 1994; 1995; 1998; Feldman & Laming, 2000; Giammanco *et al.*, 2008), but not on either fast SW or CME.

This lack of spacecraft data on bulk SW Na and K makes the results from Genesis crucial for better understanding the bulk solar wind abundances for these minor elements.

1.5.3. Genesis Solar Wind Elemental Fractionation from Solar Abundances as Represented by Photospheric Measurements vs. FIP

As stated in the introduction of this chapter, the processes that generate solar wind can result in elemental fractionation relative to the solar photosphere. This fractionation correlates well with first ionization potential for elements with high FIP, but the overall (non-linear) trend becomes less distinct for elements with low FIP. Photospheric abundances are measured from neutral or singly ionized atoms (e.g., Na: Baumüller *et al.*, 1998; K: Caffau *et al.*, 2001), whereas the atoms in the solar wind are in much higher ionization states (e.g., Bochsler, 2007). To investigate how the results of the present study compare with photospheric abundances, Genesis solar wind elemental fluences were normalized to the Genesis solar wind Mg fluence, and plotted against corresponding photospheric X/Mg (Figs. 1.16-1.18). Photospheric data are from Palme *et al.* (2014).

Scott *et al.*, 2015 provides an alternative source for photospheric elemental abundances, but, generally the values from these two sources are closely comparable. Additional Genesis data are from Heber *et al.* (2009; 2014b; c; and in preparation). The Na datum (Figs. 1.16-1.20) refers to the total average SW Na measured in the present study (Results). The K datum (Figs. 1.16-1.20) represents the total average SW K measured in the present study. (Note: This value is based on the normalization of ^{39}K by its relative solar abundance (~93.3%) to determine total K). The Na (V.H.) datum represents the measurement from Heber *et al.* (2014b) after absolute calibration of their Si standard (calibration conducted in this study). This datum was a backside depth profile into Si that was calibrated with an external standard.

The SW Na/Mg abundance measured in this study plots within error of the 1:1 $(X/Mg)_{solar\ wind}$: $(X/Mg)_{photosphere}$ correlation line (Figs. 1.16-1.17). This indicates that with respect to Mg, bulk solar wind Na is not fractionated in the solar wind relative to the solar photosphere. This point is not consistent with the data from Heber *et al.*, 2014b (after calibration), which plots above the correlation line, implying Na enrichment in the solar wind relative to the photosphere. The measured K/Mg abundance measured in this study also plots on the 1:1 correlation line (Figs. 1.16 and 1.18) within error. This indicates that with respect to Mg, bulk solar wind K is not fractionated in the solar wind relative to the solar photosphere.

Fractionation factors (defined as $F(X)_{Mg} = (X/Mg)_{Bulk\ Solar\ Wind} / (X/Mg)_{Photosphere}$) were calculated and plotted against FIP to investigate how photosphere-based SW fractionation relates to FIP at low FIPs (Figs. 1.19-1.20). Photospheric data are from

Palme *et al.*, 2014, and additional Genesis bulk solar wind data is from Heber *et al.*, (2009; 2014b; c; and in preparation).

The data presented in Figures 1.19-1.20 indicate that with respect to Mg, Na and K are neither enriched nor depleted in the solar wind relative to the solar photosphere. This is in agreement with the idea that FIP <10 eV is too small to cause significant fractionation during solar wind generation (Reisenfeld *et al*., 2007). However, the errors are still too great to discern whether or not there is a very small continuous increase in fractionation with decreasing FIP for the low FIP elements up through Na, or if fractionation is unchanging. The fact that the K/Mg datum is lower than the Na/Mg datum, despite having a lower FIP, supports the hypothesis that FIP does not significantly affect its fractionation.

1.5.4. Genesis Solar Wind Elemental Fractionation from Solar Abundances as Represented by Chondritic Chemistry vs. FIP

As mentioned in the introduction to this chapter, most element abundances in CI chondrites reflect element abundances in the solar photosphere within error (Figs. 1.1-1.3; Palme *et al.*, 2014). Most of the chemical data representing CI chondrites comes from a single meteorite, Orgueil, which is volatile-depleted, aqueously altered, and inhomogeneous on scales less than 1 g (McSween, 1993; Scott and Krot, 2007; Barrat *et al.*, 2012). The fact that most of the bulk elemental abundances in CI chondrites match the elemental abundances in the solar photosphere suggests aqueous alteration occurred in a closed system (Morlok *et al.*, 2006). Nevertheless, aqueous alteration redistributed elements in CI chondrites (Barrat *et al.*, 2012). Na and K, both highly mobile in aqueous solutions (e.g., Burger and Brearley, 2005), were the two most inhomogeneous elements

measured by Barrat *et al.* (2012) in six 0.6-1g samples of Orgueil (relative standard deviations for Na and K were 22% and 20%, respectively). There is a factor of 2 difference between the highest and lowest Na concentrations measured by Barrat *et al.*, (2012).

To investigate how the solar wind chemistry compares with that of CI chondrites, Genesis solar wind elemental fluences were normalized to the Genesis SW Mg fluence, and plotted against corresponding CI chondrite X/Mg (Figs. 1.21-1.23). Like the photospheric data, CI chondrite data are from Palme *et al.* (2014). These chondrite data are exclusively predicated on analyses of Orgueil. Additional Genesis data are from Heber *et al.* (2009; 2014b; c; and in preparation). The notation used in Figs. 1.21-1.25, is the same as for similar comparisons with the solar photosphere in the preceding section: i.e., the Na datum refers to the total average Na measured in the present study. The K datum represents the total average K measured in the present study. (Note: This value is based on the normalization of ^{39}K by its relative solar abundance (~93.3%) to determine total K). The Na (V.H.) datum represents the measurement from Heber *et al.* (2014b) after absolute calibration of their Si standard. (Note: Na (V.H.) was an average of their backside depth profiles into Si, calibrated with an external standard).

The measured SW Na/Mg and K/Mg abundances measured in this study plot within error of the 1:1 $(X/Mg)_{\text{solar wind}}$: $(X/Mg)_{\text{CI chondrite}}$ correlation line (Figs. 1.21-1.23). This is consistent with the view that CI chondrites retained most of their original (non-volatile) components (e.g., Palme *et al.*, 2014). It is also consistent with the interpretation that aqueous alteration occurred within a closed system (Morlok *et al.*, 2006).

Like photosphere element abundances, CI chondrite element abundances can be used to represent solar element abundances to calculate fractionation factors for solar wind elements. To investigate how (chondrite-based) fractionation factors relate to FIP at low FIPs, bulk solar wind (X/Mg) abundances were normalized to their CI chondrite (X/Mg) equivalents and plotted against FIP (Figs. 1.24-1.25). CI chondrite data is from Palme *et al.*, 2014, and Genesis bulk solar wind data is from Heber *et al.* (2009; 2014b; c; and in preparation).

Like comparisons with photospheric data, the data presented in Figs. 1.24-1.25 suggest that relative to Mg, there has been neither enrichment nor depletion of either SW Na or K. Within error there may be a shallow, continuous increasing fractionation with decreasing FIP for the low FIP elements, but the fact that the K/Mg fractionation does not rise significantly, despite having the lowest FIP of all elements analyzed by Genesis, supports the hypothesis that for FIP <<10eV, FIP no longer plays a major role in controlling species enrichment or depletion in the solar wind.

Although successfully measuring additional low FIP elements could be helpful in further investigating low FIP fractionation trends, only Rb, Cs, and Fr have lower FIPs than K, and their bulk SW fluences are well below what is currently possible to measure precisely.

1.5.5. Implications of New Solar Wind Na and K Fluences for Cosmochemistry

The fluence measurements presented here suggest that relative to Mg the three proxies for solar abundances (the solar wind, the solar photosphere and CI chondrites) agree on Na and K abundances. If any Na/Mg or K/Mg enrichment (or depletion) exists, it is smaller than the measurement precision of the present study.

The degree to which nominal fractionation factors compare with actual fractionation factors is strongly dependent on the precision of both the results of this study and on the precision of the photospheric and CI chondrite measurements. Future analysis of SW K and Na using updated technologies and refined methodologies may yield better reproducibility and better errors. The same may be true for photospheric measurements. Over time, additional CI chondrites may be found, analyzed, and incorporated into chondrite elemental abundance averages to which we compare solar wind and photospheric data, strengthening this data set.

1.6. Summary and Conclusions

Accurate and precise measurement of SW Na and K in Genesis collectors is challenging, requiring clean, well-prepared samples, optimized instrument parameters, robust integration models, reproducible integration methods, and well-calibrated, matrix-matched standards. Comparing multiple samples, and experimenting with different analytical approaches and calibration methods can reveal how sensitive the measurements are to different procedures, and may reveal previously unrecognized sources of error.

The average fluence of SW Na measured in Genesis solar wind Si and DlC collectors is 1.01e11 (+9e09, -2e10) atoms/cm^2. The average SW K fluence measured in Genesis solar wind Si and DlC collectors is 5.1e09 (+8e08, -8e08). With respect to Mg, the Na and K abundances derived from the solar wind, solar photosphere, and CI chondrites are in agreement (within error), suggesting solar wind is neither enriched nor depleted in Na or K, and that any one of the three solar proxies is representative of bulk solar Na and K. Quantifying SW-photosphere fractionation is an important problem for

both solar physics and cosmochemistry. The ultimate purpose for the Genesis Mission, and therefore the SW data derived from Genesis collectors, is to provide a cosmochemical baseline. Better solar wind data will constrain fractionation theories, and better fractionation theories will help with the interpretation of Genesis data. Similarly better cosmochemical data helps to constrain alteration processes on planetary bodies.

Table 1.1. ^{23}Na Fluences in Standards: Nominal Versus Implanted.

Table 1.1. ^{23}Na Fluences in Standards: Nominal Versus Implanted.

Standard*	^{23}Na implant Energy (keV)	Nominal ^{23}Na Fluence	Measured ^{23}Na Fluence	% Nominal ^{23}Na Fluence
1e14 (Si) Stevie	100	1E+14	9.1E+13	91
1e16 (Si & DoS) R&J**	100	1E+16	1.1E+16	114
1e14 (Si) R&J	100	1E+14	1.1E+14	115
1e14+1e16 (Si & DoS) R&J	100	1.01E+16	1.2E+16	118
2e12 (1) (Si & DoS) R&J	100	2E+12	1.9E+12	97
2e12 (2) (Si & DoS) R&J	100	2E+12	1.9E+12	97
3e13 (DoS) Kroko	66	3E+13	2.7E+13	90
5e13 (Si) CEA 3140	100	5E+13	5.8E+13	117
1e13 (Si) Heber	100	1E+13	1.3E+13	127

* R&J (Rieck and Jurewicz) denotes standards synthesized as part of the present study.
** Directly calibrated with RBS.

Table 1.2. K Fluences in Standards: Nominal Versus Implanted.

Table 1.2. K Fluences in Standards: Nominal Versus Implanted.

Standard*	K Isotope Species	K implant Energy (keV)	Nominal K Fluence	Measured K Fluence	% Nominal K Fluence
1e14 (Si) Stevie	39	100	1E+14	9.9E+13	99
1e16 (Si & DoS) R&J**	39	100	1E+16	1.1E+16	109
1e14 (Si) R&J	41	100	1E+14	1.1E+14	108
1e14+1e16 (Si & DoS) R&J	41, 39	100	1.01E+16	1.1E+16	112
2e12 (1) (Si & DoS) R&J	41	100	2E+12	1.7E+12	86
2e12 (2) (Si & DoS) R&J	41	100	2E+12	1.7E+12	87
3e13 (DoS) Kroko	41	129	3E+13	2.2E+13	75

* R&J (Rieck and Jurewicz) denotes standards synthesized as part of the present study.
** Directly calibrated with RBS.

Table 1.3. RBS Results.

Table 1.3. RBS Results.			
DoS #1 (ad041000.a Control)	100keV ^{23}Na	100keV ^{39}K	
Run 1	1.10E+16	1.09E+16	
Run 2	1.12E+16	1.09E+16	
Run 3	1.11E+16	1.08E+16	
Run 4	1.16E+16	1.10E+16	
Run 5	1.19E+16	1.10E+16	
Average	1.14E+16	1.09E+16	
Standard Error of the Mean	1.69E+14	3.74E+13	
% Standard Error of the Mean	1%	0%	
DoS #2 (ad032100.a #2)	100keV ^{23}Na	100keV ^{39}K	
Run 1	1.10E+16	1.07E+16	
Run 2	1.16E+16	1.10E+16	
Run 3	1.14E+16	1.07E+16	
Run 4	1.15E+16	1.06E+16	
Run 5	1.13E+16	1.10E+16	
Average	1.14E+16	1.08E+16	
Standard Error of the Mean	1.03E+14	8.37E+13	
% Standard Error of the Mean	1%	1%	
Average fluence of both samples	**1.14E+16**	**1.09E+16**	**atoms/cm^2**
	1.14	**1.09**	**atoms/Å^2**

Table 1.4. SIMS Analytical Approaches for DlC From Genesis DoS Solar Wind Collectors.

NASA code	SIMS	FS/BS DP*	Standard**	^{23}Na	^{39}K	Source Voltage (kV)	Sample HV (kV)	Impact Energy (kV)	Analysis	Session
60630	6f	BS	External	✓		12.5	5	7.5	1	2012_09_12
	"	"	"	✓		12.5	5	7.5	2	"
	7f	BS	External	✓		13	5	8	1	2012_11_14-16
	"	"	"	✓		13	5	8	2	"
	"	"	"	✓		13	5	8	3	"
	"	"	"	✓		13	5	8	4	"
	"	"	"	✓	✓	13	5	8	5	"
	"	"	"		✓	13	5	8	6	"
	"	"	"		✓	13	5	8	7	"
	"	"	"		✓	13	5	8	8	"
60407	7f	BS	BS	✓	✓	13	7	6	1+2	2013_11_18-21
	"	"	"	✓		13	7	6	3+4+5	"
60867	7f	BS	BS	✓		13	7	6	4+5	2013_11_18-21
	"	"	"	✓		13	7	6	6+7	"
	"	"	"		✓	13	7	6	12+13	"
61090	7f	FS	FS	✓	✓	13	7	6	1	2015_01_12-16

*FS/BS DP = Frontside/Backside Depth Profile (details in text and Appendix D).

**Internal standards are either frontside (FS) or backside (BS) ion implants (details in text and Appendix D).

Table 1.5. SIMS Analytical Approaches for Genesis Si Solar Wind Collectors.

Table 1.5. SIMS Analytical Approaches for Genesis Si Solar Wind Collectors.

NASA code	SIMS	FS/BS DP*	Standard**	^{23}Na	^{39}K	Source Voltage (kV)	Sample HV (kV)	Impact Energy (kV)	Analysis	Session
60824	7f	BS	External	✓		13	9	4	1	2012_11_14-16
	"	"	"		✓	13	9	4	2	"
	"	"	"	✓		13	9	4	3	"
61189	7f	BS	BS	✓	✓	13	7	6	3	2015_01_12-16
	"	"	"	✓	✓	13	7	6	4	"
	"	"	"	✓		13	7	6	6?	"
	"	"	"		✓	13	7	6	11	"

*BS DP = Backside Depth Profile (details in text and Fig. Appendix D).
**Internal standards are either frontside (FS) or backside (BS) ion implants (details in text and Appendix D).

Table 1.6. SIMS Analytical Parameters for DlC From Genesis DoS Solar Wind Collectors.

Table 1.6. SIMS Analytical Parameters for DlC From Genesis DoS Solar Wind Collectors.

NASA code	SIMS	L4	CA (µm)	FA (µm)	Energy Window (eV)	Raster Size (µm)	Max. Area (µm)	Analyzed Area (µm)	Egate (%)	MRP	Analysis	Session
60630	6f		400	750	125	150	75	30	none		1	2012_09_12
	"		400	750	125	150	75	30	none		2	"
	7f	400	400	400	125	100	101		80	521	1	2012_11_14-16
	"	400	400	400	125	100	101		80	521	2	"
	"	400	400	400	125	100	101		80	521	3	"
	"	400	400	400	125	100	101		80	521	4	"
	"	250	400	400	125	100	102		80	1200	5	"
	"	250	400	400	125	100	102		80	1200	6	"
	"	250	400	400	125	100	102		80	1200	7	"
	"	250	400	400	125	100	102		80	1200	8	"
60407	7f	400	400	400	58	100	76	30	80	1200	1+2	2013_11_18-21
	"	400	400	400	58	120	76	30	80	1200	3+4+5	"
60867	7f	400	400	400	58	120	77	30	30?	1200	4+5	2013_11_18-21
	"	400	400	400	58	120	76	30	30?	1200	6+7	"
	"	400	400	400	58	120	76	30	30?	701?	12+13	"
61090	7f	400	250	400	58	100	100	35-40	80	2500	1	2015_01_12-16

Table 1.7. SIMS Analytical Parameters for Genesis Si Solar Wind Collectors.

Table 1.7. SIMS Analytical Parameters for Genesis Si Solar Wind Collectors.

NASA code	SIMS	L4	CA (µm)	FA (µm)	Energy Window (eV)	Raster Size (µm)	Max. Area (µm)	Analyzed Area (µm)	Egate (%)	MRP	Analysis	Session
60824	7f	250	400	400	76	100	77		80	521	1	2012_11_14-16
	"	250	400	400	76	100	77		80	521	2	"
	"	250	400	400	76	100	77		80	1200	3	"
61189	7f	400	250	400	58	100	100	35-40	80	2800	3	2015_01_12-16
	"	400	250	400	58	100	100	35-40	80	2800	4	"
	"	400	250	400	58	100	100	35-40	80	2800	6?	"
	"	400	250	400	58	100	100		80	1200	11	"

Table 1.8. Solar Wind Na and K Fluences in Genesis DoS Solar Wind Collectors.

NASA code	^{23}Na	^{23}Na upper error	^{23}Na lower error	^{39}K	^{39}K upper error	^{39}K lower error	Profile	Analysis	Session
60630	4.6E+10	3E+09	1E+10				a	1	2012_09_12
	5.3E+10	4E+09	1E+10				b	2	"
	5.2E+10	6E+09	9E+09				c	1	2012_11_14-16
	4E+10	1E+10	2E+10				d	2	"
	4.8E+10	6E+09	8E+09				e	3	"
	5.7E+10	4E+09	1E+10				f	4	"
	4.6E+10	2E+09	8E+09	1.8E+09	3E+08	2E+08	g	5	"
				2.7E+09	5E+08	5E+08	h	6	"
				4.9E+09	4E+08	8E+08	i	7	"
				3.0E+09	3E+08	5E+08	j	8	"
Average:	**5.0E+10**	**5E+09**	**1E+10**	**3.1E+09**	**4E+08**	**5E+08**			
60407	6.0E+10	5E+09	2E+10	2.2E+09	1E+08	2E+08	k	1+2	2013_11_18-21
	6.8E+10	5E+09	2E+10				l	3+4+5	"
Average:	**6.4E+10**	**5E+09**	**2E+10**	**2.2E+09**	**1E+08**	**2E+08**			
60867	5.2E+10	3E+09	1E+10				m	4+5	2013_11_18-21
	5.7E+10	5E+09	1E+10				n	6+7	"
				4.5E+09	1E+09	6E+08	o	12+13	"
Average:	**5.4E+10**	**4E+09**	**1E+10**	**4.5E+09**	**1E+09**	**6E+08**			
61090	1.2E+11	1E+10	1E+10	4.5E+09	4E+08	4E+08	p	1	2015_01_12-16
Average:	**1.2E+11**	**1E+10**	**1E+10**	**4.5E+09**	**4E+08**	**4E+08**			
Ave. DoS:	**7.2E+10**	**7E+09**	**1E+10**	**3.6E+09**	**5E+08**	**4E+08**			
w/o 61090:	5.6E+10	5E+09	1E+10	3.3E+09	5E+08	4E+08			

Table 1.8. Solar Wind Na and K Fluences in Genesis DoS Solar Wind Collectors.

Table 1.9. Solar Wind Na and K Fluences in Genesis Si Solar Wind Collectors.

Table 1.9. Solar Wind Na and K Fluences in Genesis Si Solar Wind Collectors.

NASA code	^{23}Na	^{23}Na upper error	^{23}Na lower error	^{39}K	^{39}K upper error	^{39}K lower error	Profile	Analysis	Session
60824	1.69E+11	5E+09	5E+10				q	1	2012_11_14-16
				8E+09	1E+09	2E+09	r	2	"
	1.43E+11	3E+09	2E+10				s	3	"
Average:	**1.56E+11**	**4E+09**	**3E+10**	**8E+09**	**1E+09**	**2E+09**			
61189	9E+10	1E+10	3E+10	3.8E+09	9E+08	4E+08	t	3	2015_01_12-16
	1.2E+11	2E+10	4E+10	5.2E+09	2E+09	6E+08	u	4	"
				3.7E+09	5E+08	2E+08	v	11	"
Average:	**1.0E+11**	**2E+10**	**3E+10**	**4.2E+09**	**1E+09**	**4E+08**			
Ave. Si:	**1.3E+11**	**1E+10**	**3E+10**	**6E+09**	**1E+09**	**1E+09**			

Table 1.10. Solar Wind Na and K Fluences in Genesis Si Solar Wind Collectors.

Table 1.10. Solar Wind Na and K Fluences* in Genesis Solar Wind Collectors.

NASA code	Fluence	Upper error	Lower error
Na	1.01E+11	9E+09	2E+10
Na (V.H.) (non-calibrated)**	1.00E+11	4E+09	4E+09
Na (V.H.)	1.28E+11	4E+09	4E+09
K	5.1E+09	8E+08	8E+08

* Na and K fluences are based on averages of DoS and Si data from Tables 1.8 and 1.9. The K fluence represents total K, where ^{39}K is ~93.3% total K.
** Fluence measurement "calibrated" using the nominal fluence of a non-calibrated reference material (Heber *et al*., 2014b).

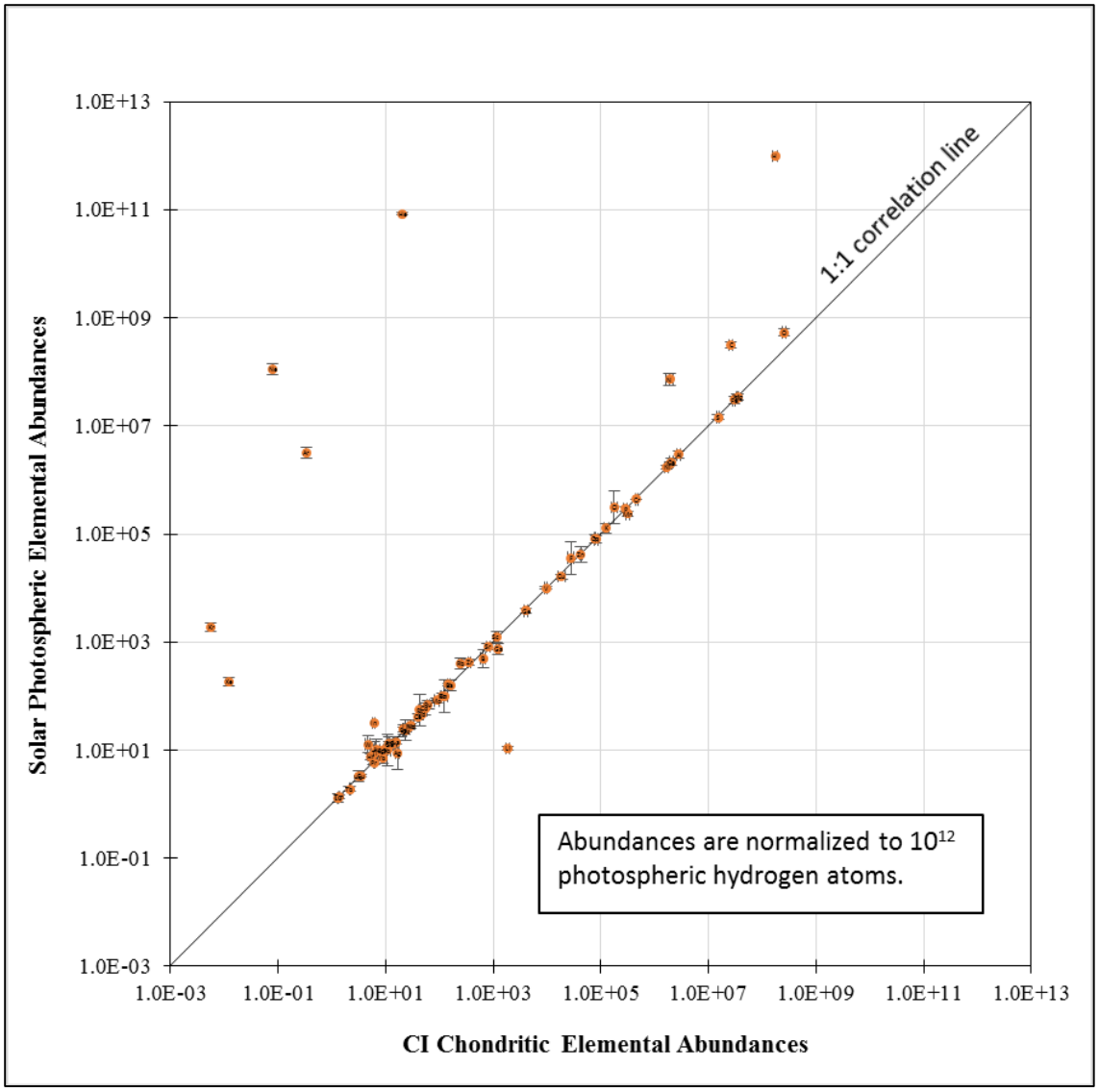

Fig. 1.1. Solar Photospheric Elemental Abundances Versus CI Chondritic Elemental Abundances.

Data are from Palme *et al.*, 2014. Abundances are normalized to 10^{12} photospheric hydrogen atoms. Error propagation was performed to illustrate the combined 1 s.d. errors reported for solar photosphere and CI chondrite measurements.

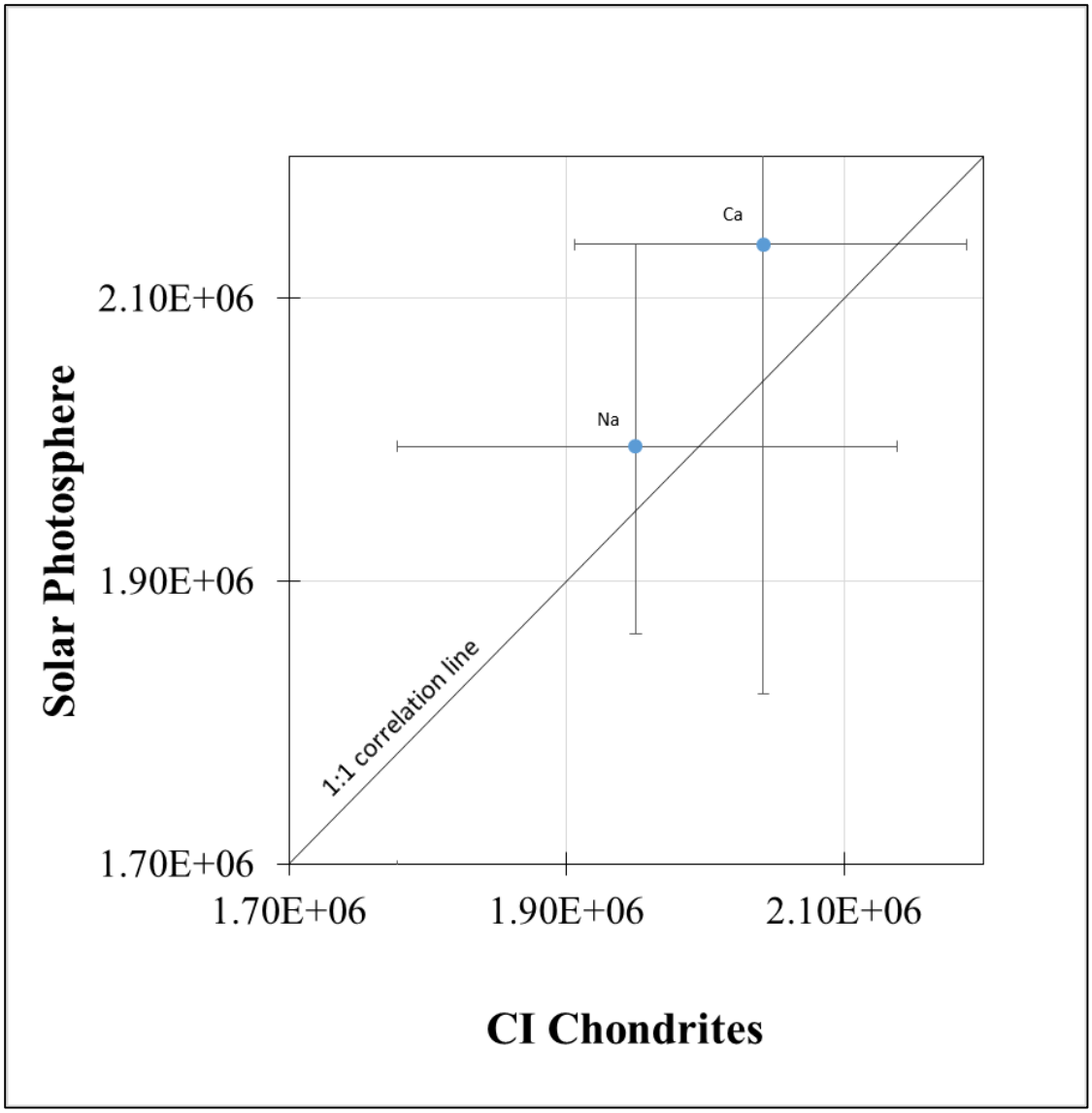

Fig. 1.2. A Subset of Fig.1.1. That Focuses on Solar Photospheric Sodium Abundance Versus CI Chondritic Sodium Abundance.

Data are from Palme *et al.*, 2014. Abundances are normalized to 10^{12} photospheric hydrogen atoms. Error propagation was performed to illustrate the combined 1 s.d. errors reported for solar photosphere and CI chondrite measurements.

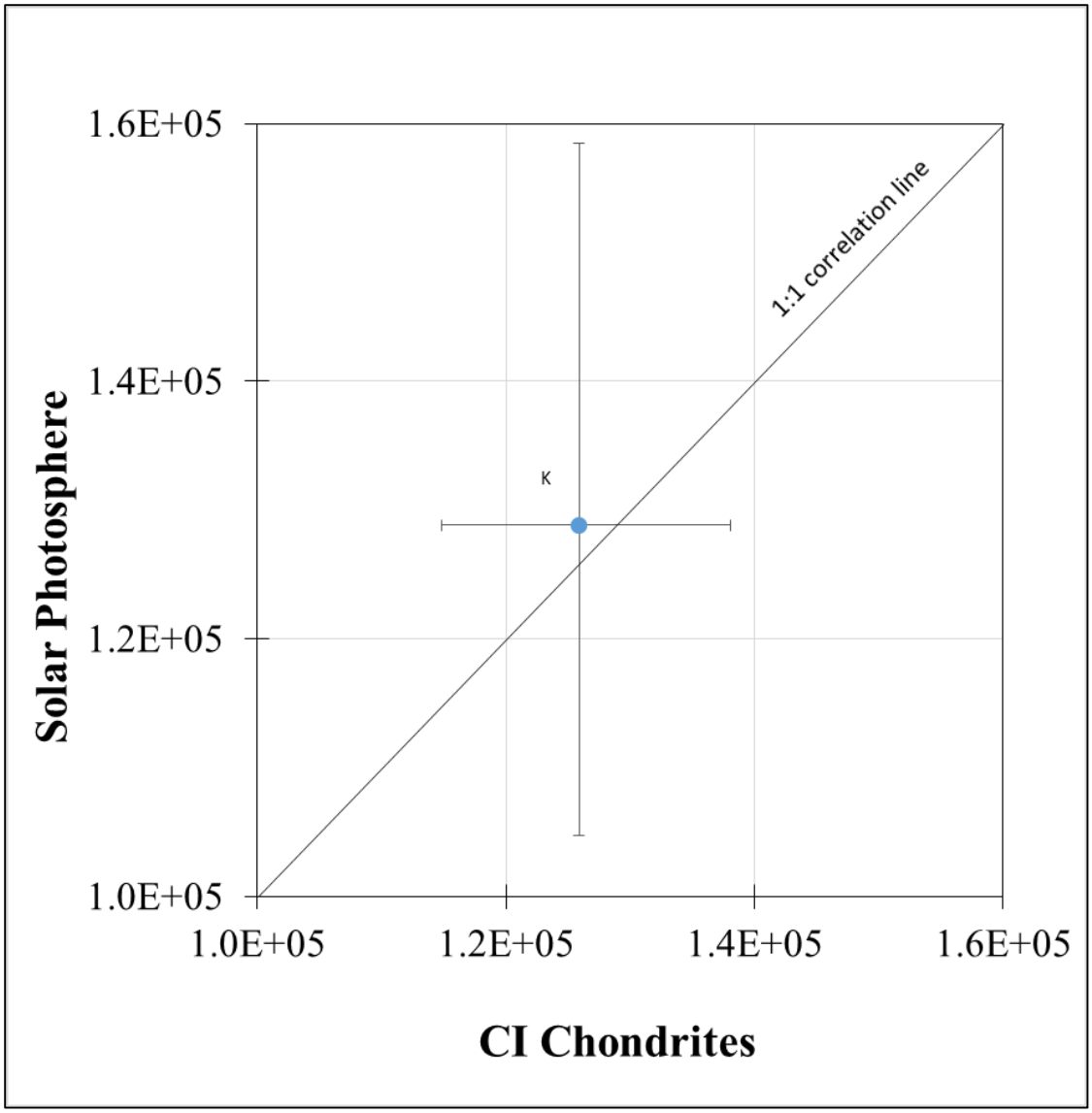

Fig.1.3. A Subset of Fig.1.1. That Focuses on Solar Photospheric Potassium Abundance Versus CI Chondritic Potassium Abundance.

Data are from Palme *et al.*, 2014. Abundances are normalized to 10^{12} photospheric hydrogen atoms. Error propagation was performed to illustrate the combined 1 s.d. errors reported for solar photosphere and CI chondrite measurements.

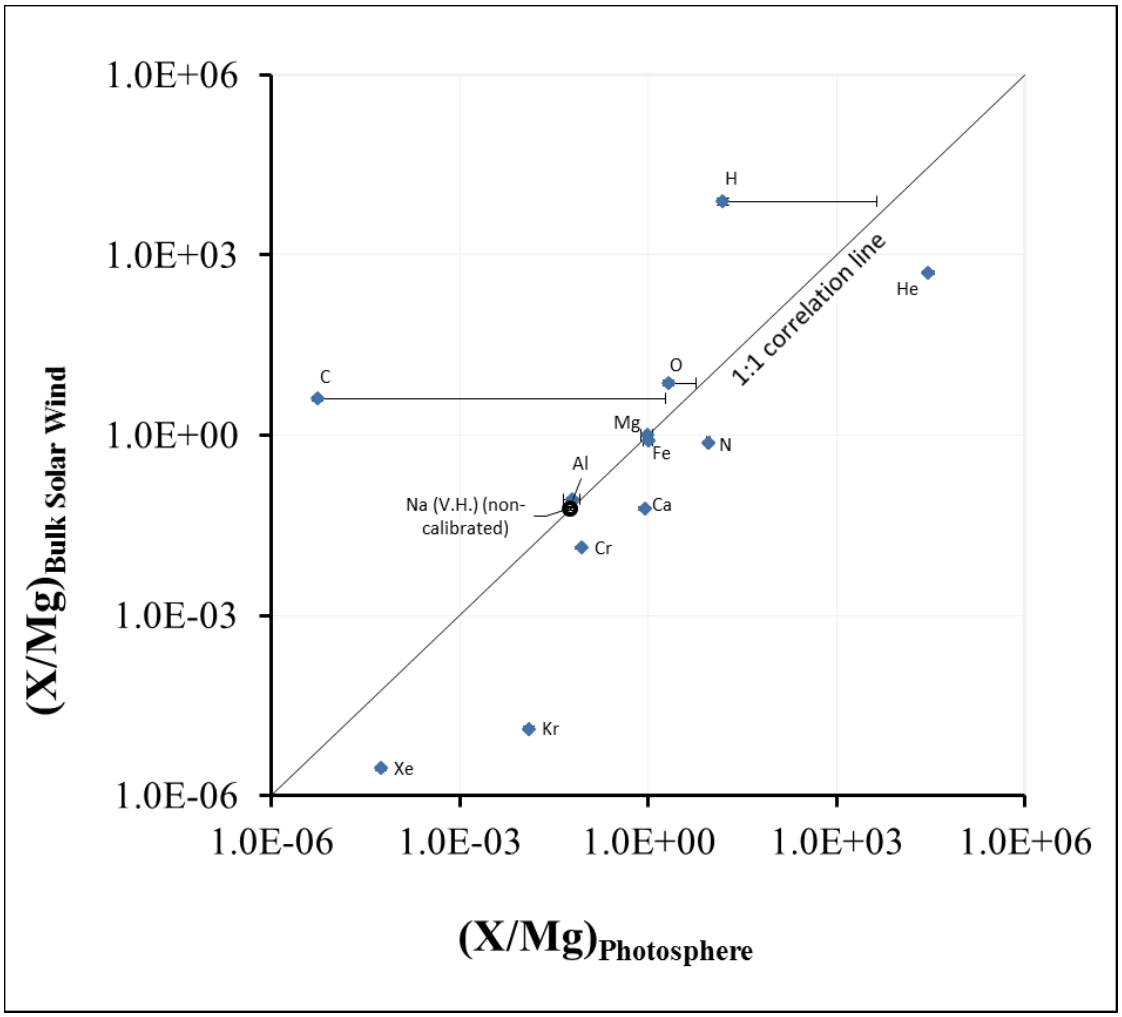

Fig. 1.4. Genesis Bulk Solar Wind Element Abundances Normalized to Genesis Bulk Solar Wind Magnesium Versus Photospheric Element Abundances Normalized to Photospheric Magnesium.

Data shown are prior to this study. Solar wind abundances are from Heber *et al.* (2009; 2014b; c; in prep.). SW Al, Ca, Cr, N, and Na data presented in this plot are based on nominal (not calibrated) fluences of reference ion implants. Photospheric abundances are from Palme *et al.* (2014). No Genesis SW K measurements were performed prior to the present study. Error propagation was performed to illustrate the combined 1 s.d. errors reported for solar wind and solar photospheric measurements.

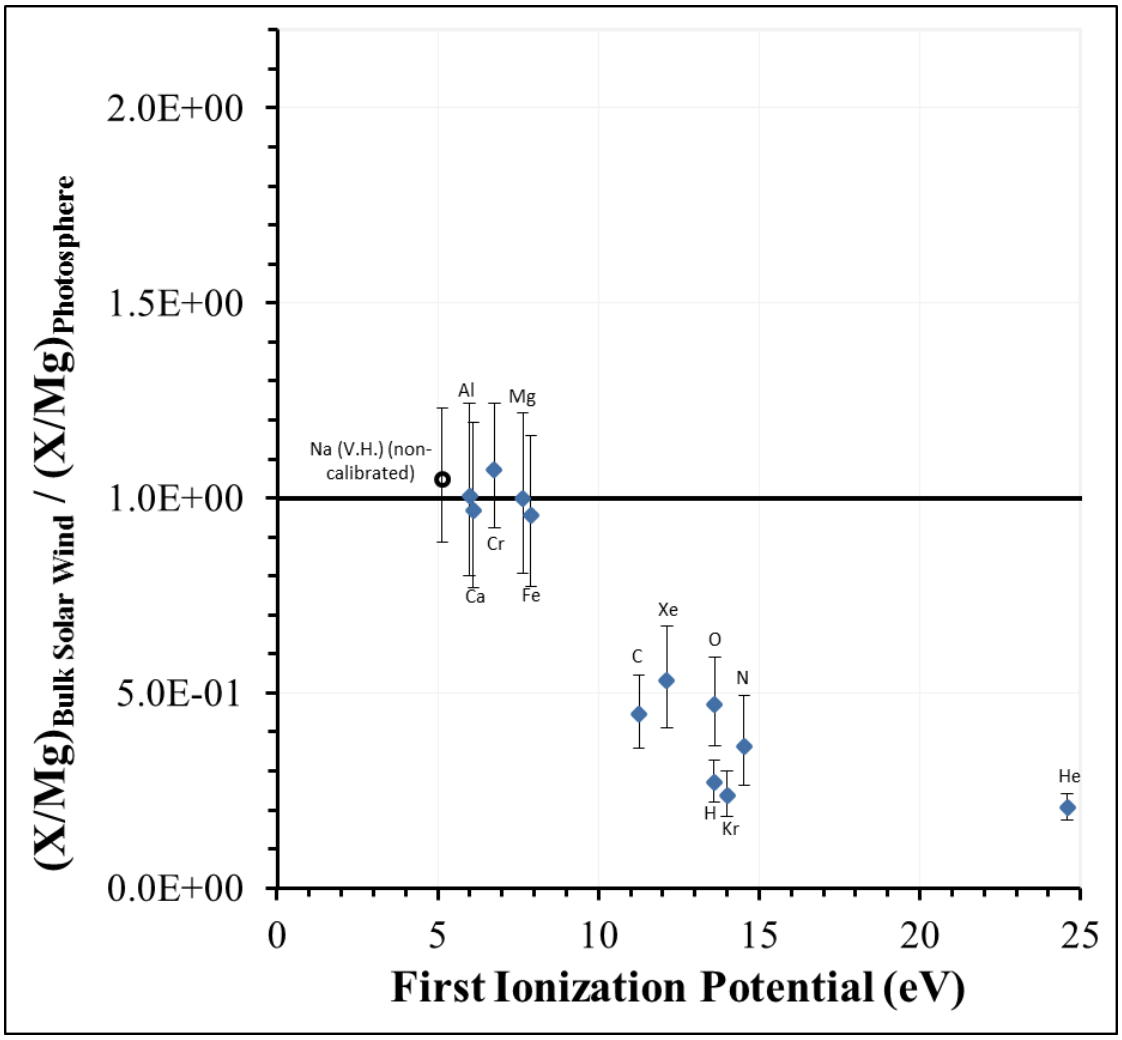

Fig. 1.5. Genesis Bulk Solar Wind Element/Magnesium Normalized to Photospheric Element/Magnesium Versus First Ionization Potential (i.e., FIP).

Data shown are prior to this study. Solar wind abundances are from Heber *et al.* (2009; 2014b; c; in prep.). SW Al, Ca, Cr, N and Na data presented in this plot are based on nominal (not calibrated) fluences of reference ion implants. Photospheric abundances are from Palme *et al.* (2014). No SW K measurements were performed prior to the present study. Error propagation was performed to illustrate the combined 1 s.d. errors reported for solar wind and solar photospheric measurements.

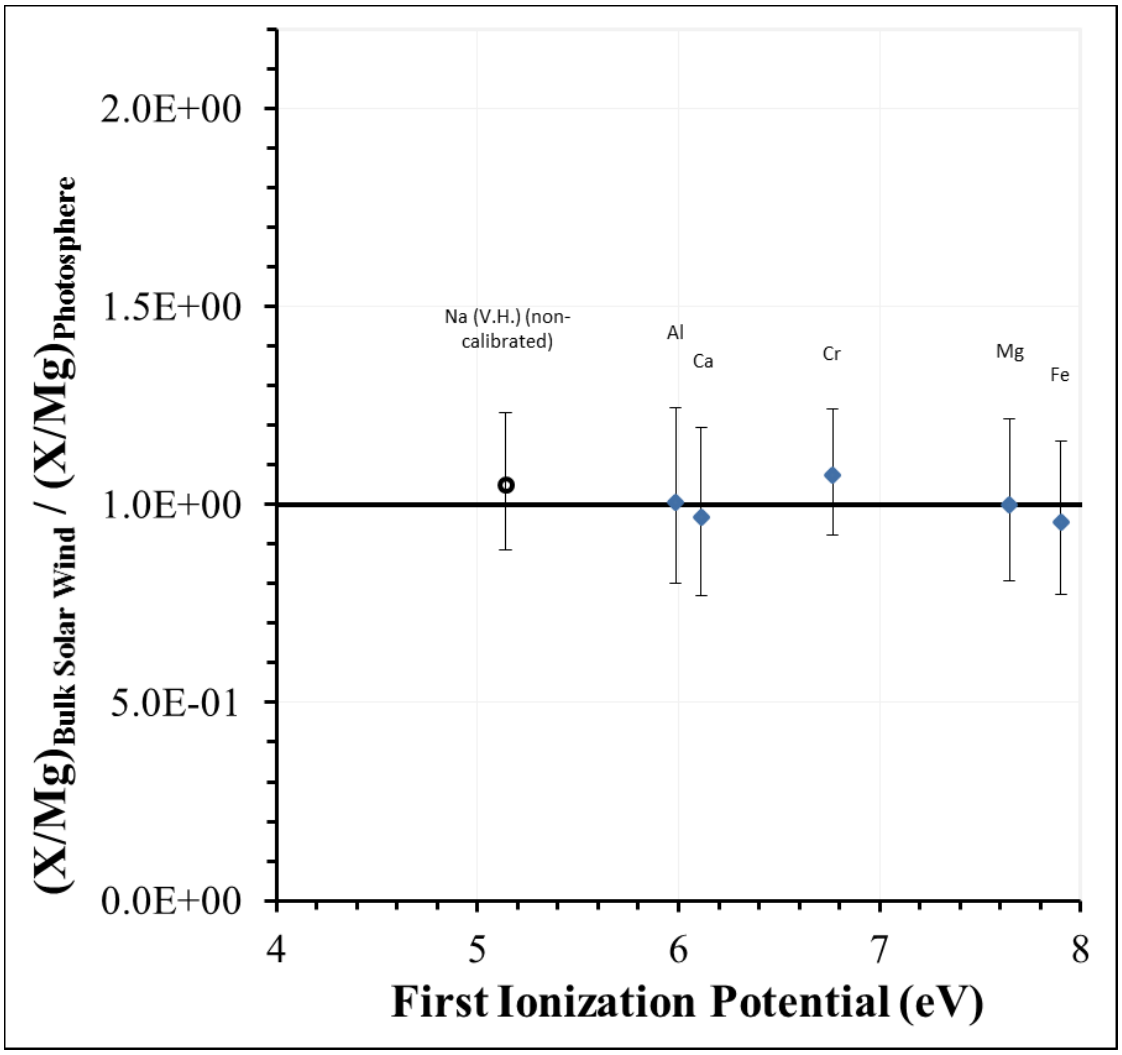

Fig. 1.6. A Subset of Fig.1.5. Featuring Genesis Bulk Solar Wind Element/Magnesium Normalized to Photospheric Element/Magnesium for Elements With Low First Ionization Potential (i.e., FIP).

Data shown are prior to this study. Solar wind abundances are from Heber *et al.* (2009; 2014b; c; in prep.). SW Al, Ca, Cr, and Na data presented in this plot are based on nominal (not calibrated) fluences of reference ion implants. Photospheric abundances are from Palme *et al.* (2014). No SW K measurements were performed prior to the present study. Error propagation was performed to illustrate the combined 1 s.d. errors reported for solar wind and solar photospheric measurements.

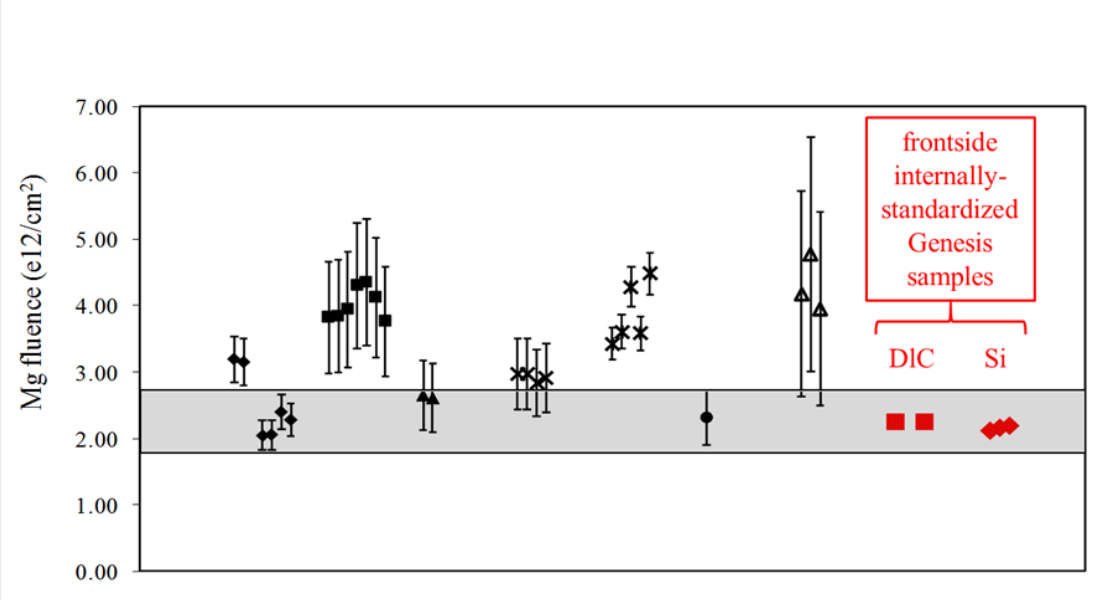

Fig. 1.7. Mg Measurements in DlC and Si Collectors.

Data are from D. S. Burnett. The plot is modified from written communication with A. J. G. Jurewicz. Measurements are ordered by run date. Externally standardized data for Mg in silicon and Sandia diamond-like carbon (DlC) are given by the grey bar and black data points, respectively. Externally-standardized data from Genesis DlC is substantially more variable than data from Genesis Si. To mitigate this, ^{25}Mg implanted directly into the front sides of Genesis flight samples was used as an internal standard, resulting in very consistent Mg data (red data points). Thus, internal standardization via front-side implantation of reference ion species eliminated Mg fluence measurement discrepancies between Si and DlC. Genesis flight samples contain additional solar wind components (e.g., hydrogen); internal standardization may have mitigated calibration variations from any associated structural/chemical inhomogeneities in the amorphous DlC caused by the implantation of these additional components.

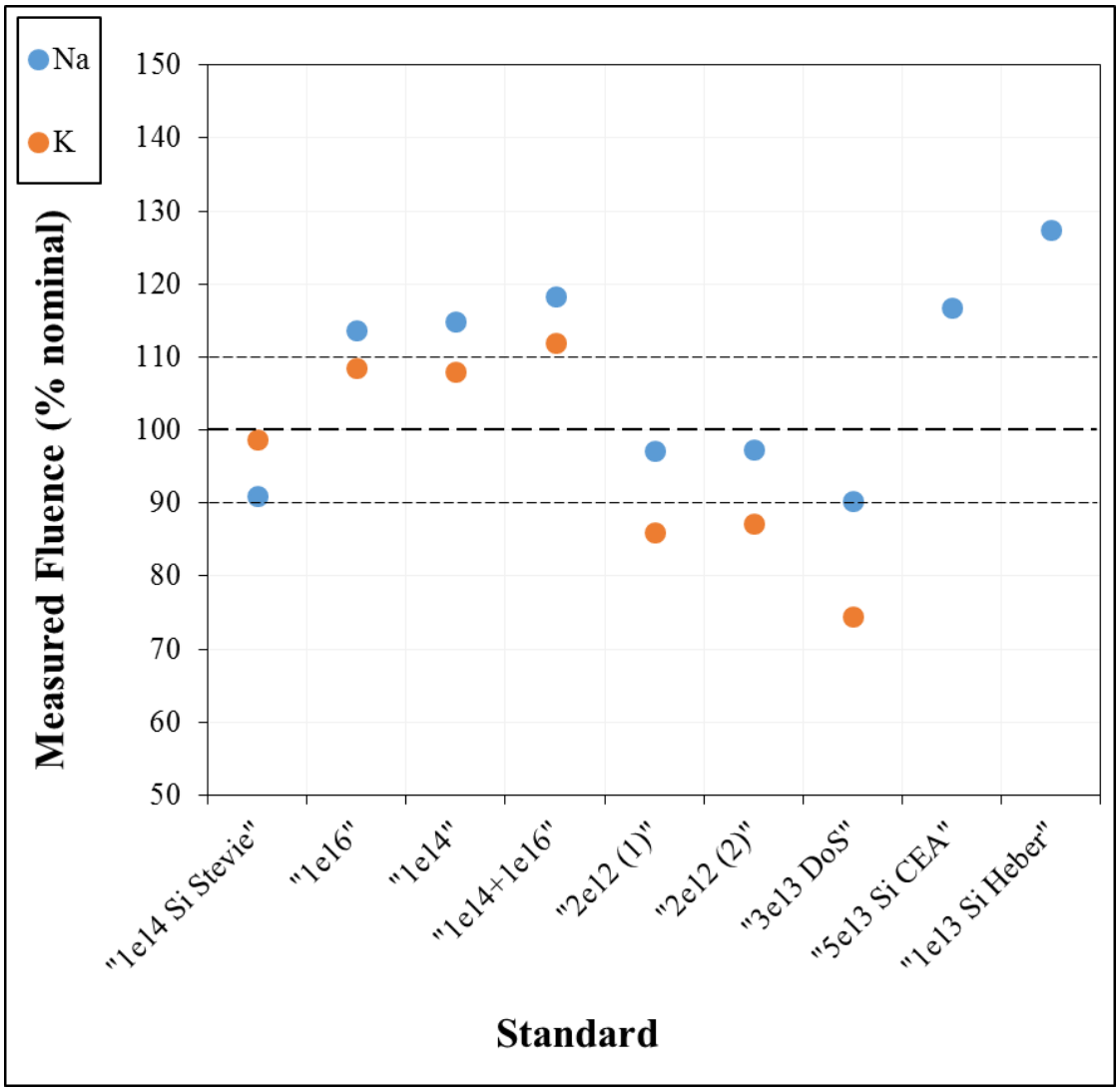

Fig. 1.8. Calibrated Fluences of the Na and K Implants in the Standards Used in the Present Study, Expressed as a Percentage of the Reported Nominal Fluences.

Long dashed line indicates the expected (or nominal) implant dosage. Short dashed lines indicate 10% deviation from the nominal value. When the actual fluence is compared with the nominal fluence, the actual fluence can be high or low by tens of percent. See also Tables 1.1 and 1.2.

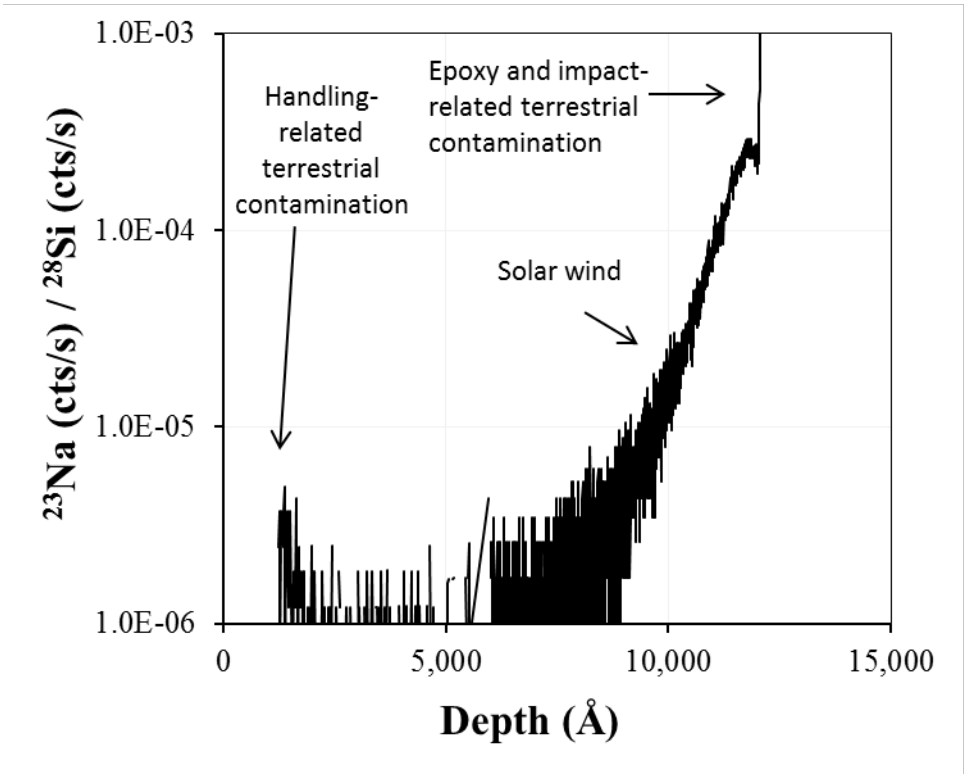

Fig. 1.9. An Example Na Depth Profile in Si, Where the Polished Back Surface of the Genesis Wafer (60824) is at 0 Å and the Frontside is at ~12,000 Å.

In this sample there is no internal standard. Thicker Genesis Si wafers (~2.5 μm) are used for internal standards implants to accommodate the extra ions. Na on the polished backside surface is primarily contamination from handling. Note how this backside contamination is lower than the mounting epoxy and impact-related terrestrial contamination on the frontside. Background levels of Na were reached prior to SW analysis. The solar wind likely continues beyond the depth at which it can be distinguished from front-side surface contamination, in particular because of ion mixing. Modelling has been used to extract the missing counts from the last part of the profile (e.g., Fig. 1.12).

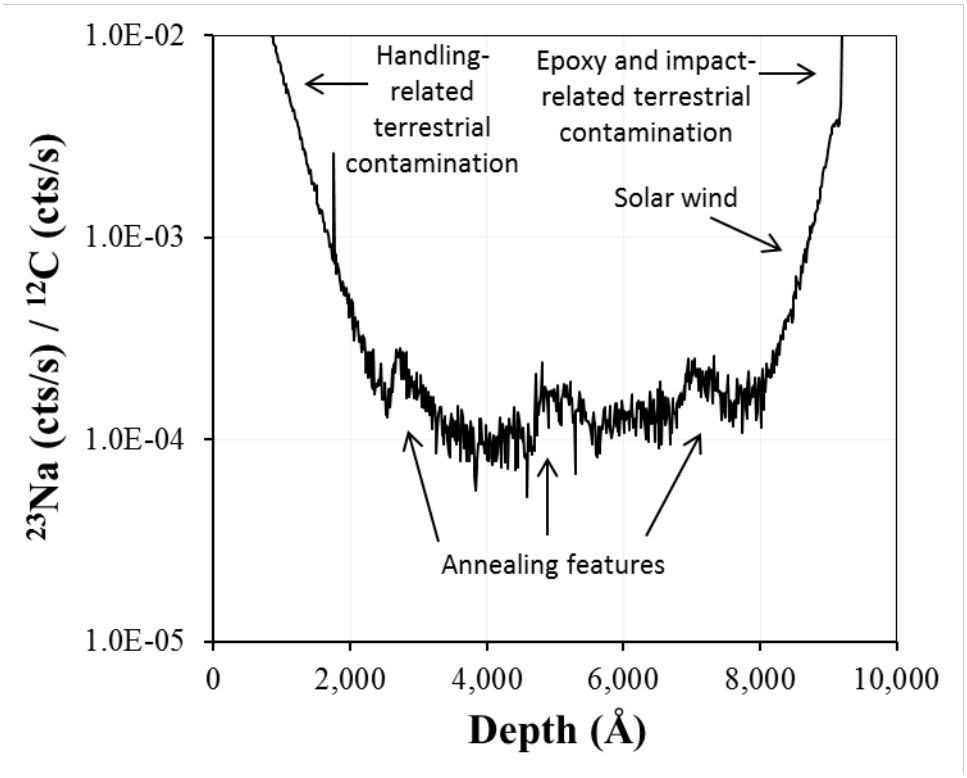

Fig. 1.10. Example Na Depth Profile in DlC.

The etched back surface of the Genesis wafer (60630) is at 0 Å and the frontside is at ~10,000 Å. In this sample there is no internal standard. Na on the XeF_2 etched backside surface is primarily terrestrial contamination from handling. Later handling techniques were able to reduce the abundance of surface Na. Background levels of Na were reached prior to SW analysis. Saw-tooth stepwise pattern is apparent once background-level count rates are reached. This pattern is variable in intensity wafer-to-wafer in the DoS, and is thought to be due to a series of annealing steps performed as part of the (custom-made) DoS fabrication process. The mounting epoxy and impact-related terrestrial contamination are sources of Na on the frontside of the wafer. The solar wind likely continues beyond the depth at which it can be distinguished from front-side surface contamination, in particular because of ion mixing. Modelling has been used to extract the missing counts from the last part of the profile (e.g., Fig. 1.12).

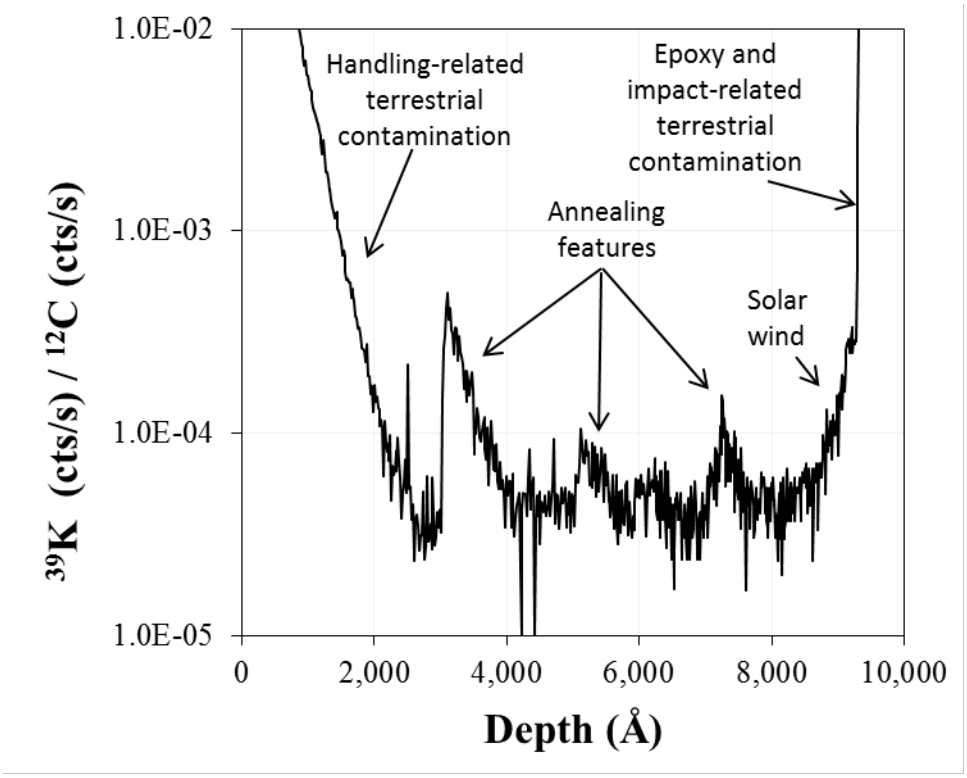

Fig. 1.11. Example ^{39}K Depth Profile in DlC.

The etched back surface of the Genesis wafer (60630) is at 0 Å and the frontside is at ~10,000 Å. In this sample there is no internal standard. ^{39}K on the XeF_2 etched backside surface is primarily terrestrial contamination from handling. Later handling techniques were able to reduce the abundance of surface ^{39}K. Background levels of ^{39}K were reached prior to SW analysis. Saw-tooth stepwise pattern is apparent once background-level count rates are reached. This pattern is variable in intensity wafer-to-wafer in the DoS, and is thought to be due to a series of annealing steps performed as part of the (custom-made) DoS fabrication process.The mounting epoxy and impact-related terrestrial contamination are sources of K on the frontside of the wafer. The solar wind likely continues beyond the depth at which it can be distinguished from front-side surface contamination, in particular because of ion mixing. Modelling has been used to extract the missing counts from the last part of the profile (e.g., Fig. 1.12).

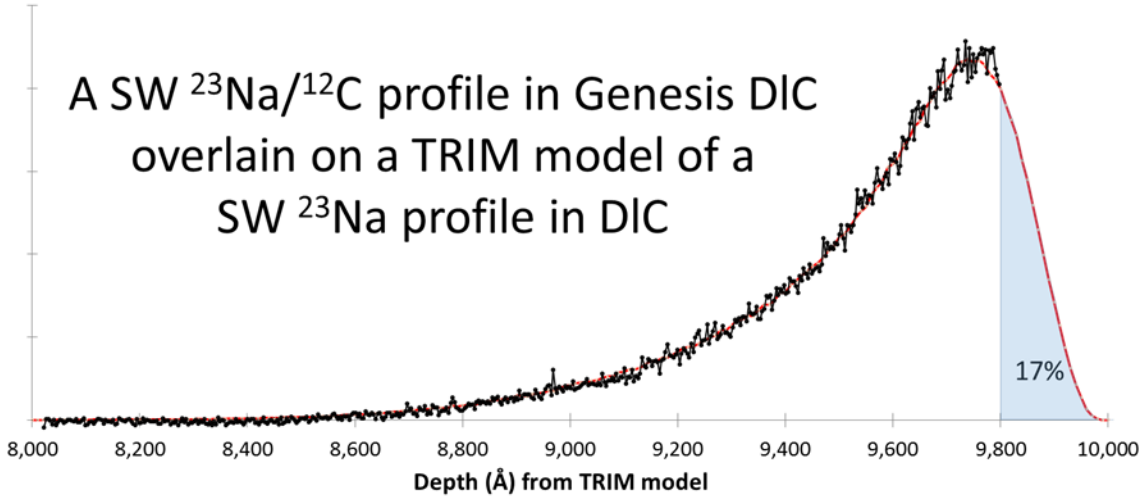

Fig. 1.12. An Example of Curve Fitting a Backside Depth Profile to a TRIM Model to Estimate Material Lost at the Wafer-Epoxy Boundary.

The amount of material lost near the surface depends on how inclined the crater floor is relative to the wafer surface. The degree of inclination is strongly controlled by sample tilt, primary beam focus, and how uniform the rastering mechanism on the SIMS is. The amount of material lost at the sample-epoxy interface was rarely more than 30%.

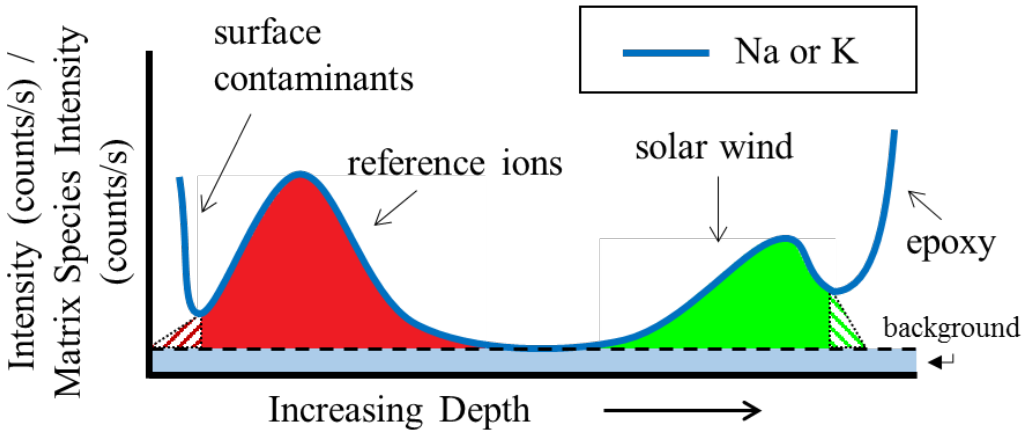

Fig. 1.13. Integration of Reference Ion and Solar Wind Ion Signals.

The dark blue line represents a backside depth profile into a backside-implanted Genesis collector wafer. There are two methods for integration depicted here, and each method has inherent assumptions. The first integration method involves integration of the solid red and green regions. The other method involves the integration of both solid and striped red and green regions. The blue field under the dashed line represents a uniform background signal, which is not included in the integration. For most cases this background was very low. Integrating only the solid red and green areas assumes that the amount of contaminant signal being included in the integration is equal to the implant signal being excluded from the integration. Integrating solid and striped red and green regions assumes that extrapolation of the curve to the surface, and integrating to the surface, includes more implant signal than contaminant signal. When used appropriately, these methods produce very little difference to the overall integration.

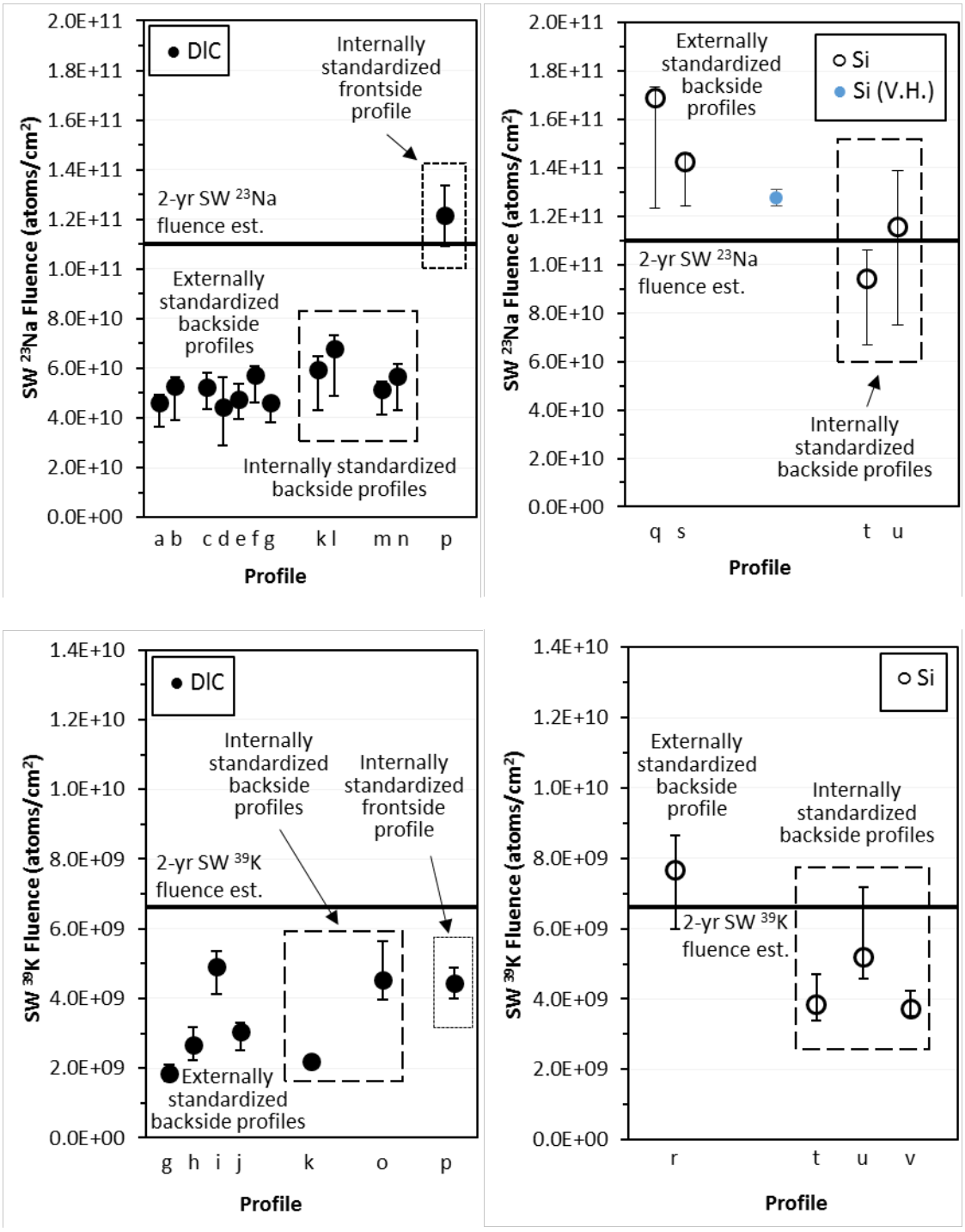

Fig. 1.14. Solar Wind Na and K Fluences Measured in Genesis Collectors.

Numerical values for these data are provided in Tables 1.8 and 1.9. The corresponding, minimally-processed SW depth profiles from which these data are based, are provided in Appendix G. Lowercase letters (below each data point) are provided to

facilitate data comparison between this figure, Tables 1.8 and 1.9, and the profiles in Appendix G. Thick black horizontal lines represent 2-year fluence estimates made prior to the return of Genesis (Burnett *et al.*, 2003). Note: Bulk Genesis fluences represent 852.83 days of collection time (Reisenfeld *et al.*, 2013). Solid circles represent measurements in diamond-like carbon. Rings represent measurements in silicon. Si (V.H.) represents the calibrated measurement by Heber *et al.* (2014b). Boxes around data indicate measurements that were internally standardized. Boxes with broad dashed lines indicate data calibrated with backside-implanted internal standards. Boxes with fine dotted lines indicate data calibrated with front-side internal standards. Only the data calibrated with frontside-implanted reference ions were acquired with frontside depth profiling, the remaining analyses were conducted using backside depth profiling into thinned wafer material. Error on Si (V.H.) is 1 σ standard deviation of 39 measurements, and includes calibration and sputter rate errors (both negligible) obtained from reference implants (V. Heber, LPSC 2014, poster). Error bars on data from the present study represent systematic errors. Systematic errors applied to frontside analyses (this study) are nominally 10%. All other systematic errors (this study) are uncertainties associated with curve-fitting profile models, and are generally much larger than the errors of counting statistics. Systematic errors are more representative of the true analysis uncertainty in the present study than errors associated with counting statistics. The statistical errors of the individual measurements are generally less than ~4%, and were they plotted here, would be smaller than the data points in this figure.

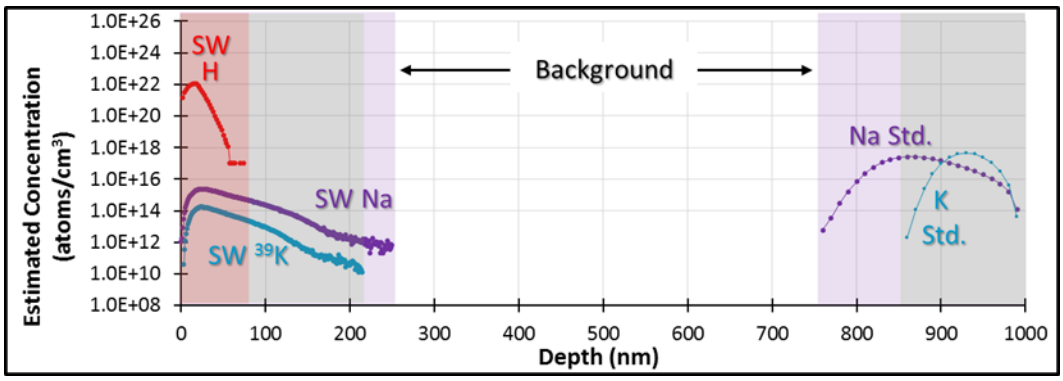

Fig. 1.15. Model Implant Profiles for a Backside-Standardized Diamond-like Carbon Film.

The solar wind hydrogen profile overlaps solar wind Na and K profiles, but not backside-implanted reference ion standards.

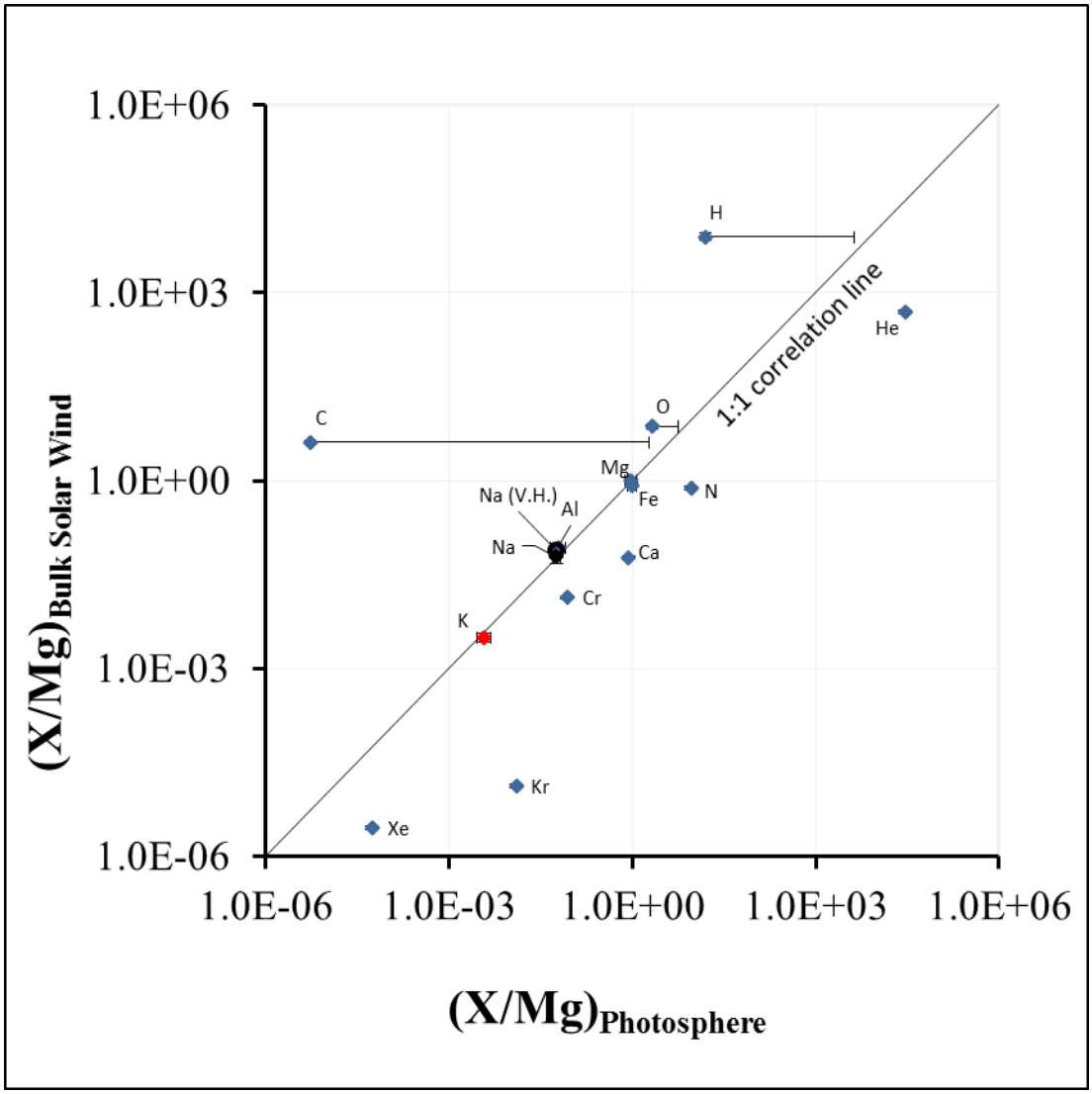

Fig. 1.16. Genesis Bulk Solar Wind Element Abundances Normalized to Genesis Bulk Solar Wind Magnesium Versus Photospheric Element Abundances Normalized to Photospheric Magnesium.

The Na data are represented by black points. The K datum is represented by a red point. The solar wind values for "Na" and "K" are averages of the (possibly discrepant) DlC and Si measurements from the present study. The solar wind datum for "Na (V.H.)" is the calibrated Na abundance measurement reported in Heber *et al.* (2014b). Other solar wind data are from Heber *et al.* (2009; 2014b; c; in prep.). SW Al, Ca, Cr, and N data presented in this plot are based on nominal (not calibrated) fluences of reference ion implants. Photospheric data are from Palme *et al.* (2014). Error propagation was performed to illustrate the combined 1 s.d. errors for solar wind and solar photospheric measurements.

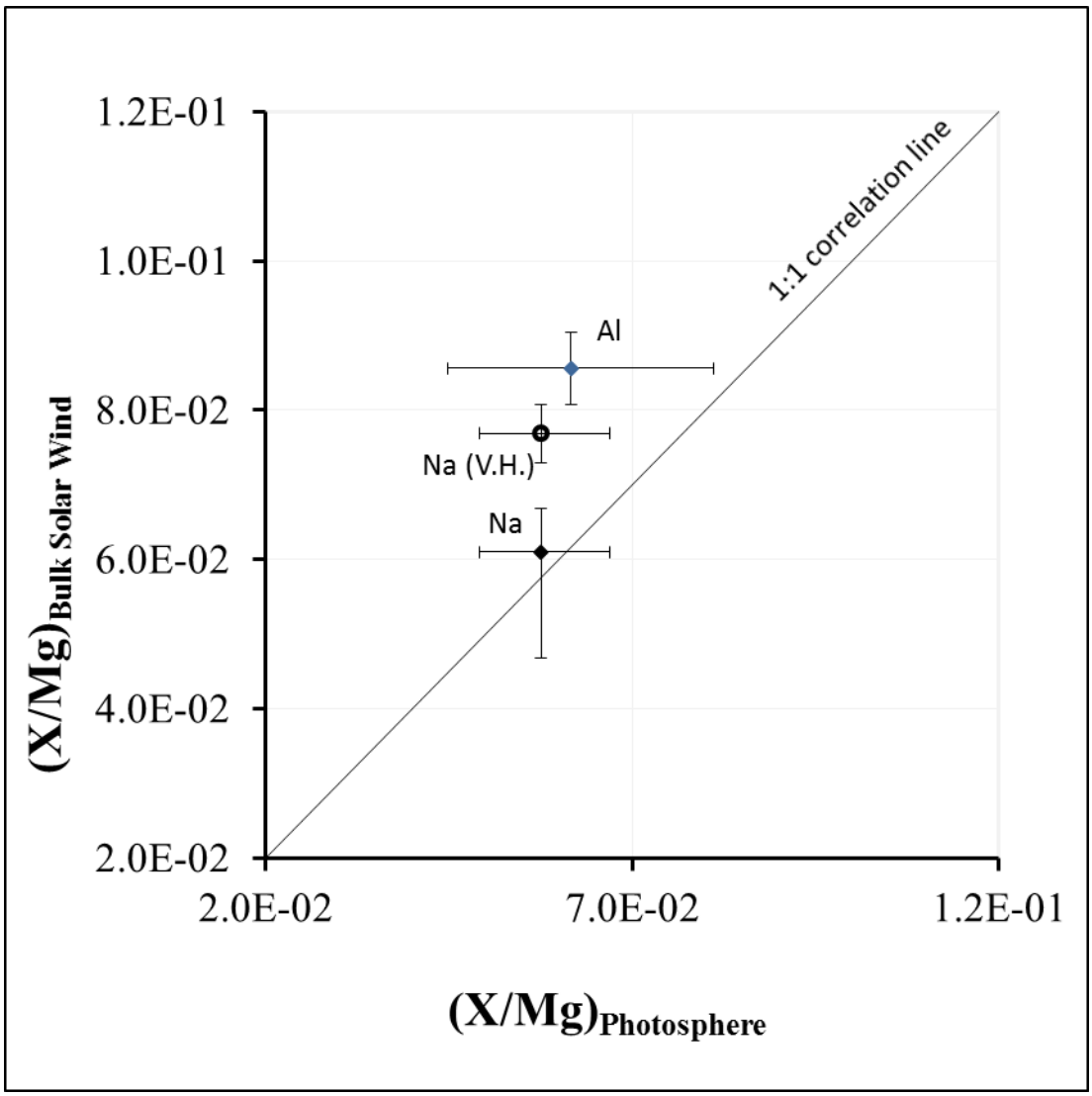

Fig. 1.17. Subset of Fig. 1.16, Featuring Sodium. Genesis Bulk Solar Wind Element Abundances Normalized to Genesis Bulk Solar Wind Magnesium Versus Photospheric Element Abundances Normalized to Photospheric Magnesium.

The solar wind value for "Na" is an average of the (possibly discrepant) DlC and Si measurements from the present study. The solar wind datum for "Na (V.H.)" is the calibrated Na abundance measurement reported in Heber *et al.* (2014b). SW Al datum is from Heber *et al.* (2009; 2014b, c; in prep.). SW Al datum is based on a nominal (not calibrated) fluence of a reference ion implant. Photospheric data are from Palme *et al.* (2014). Error propagation was performed to illustrate the combined 1 s.d. errors for solar wind and solar photospheric measurements.

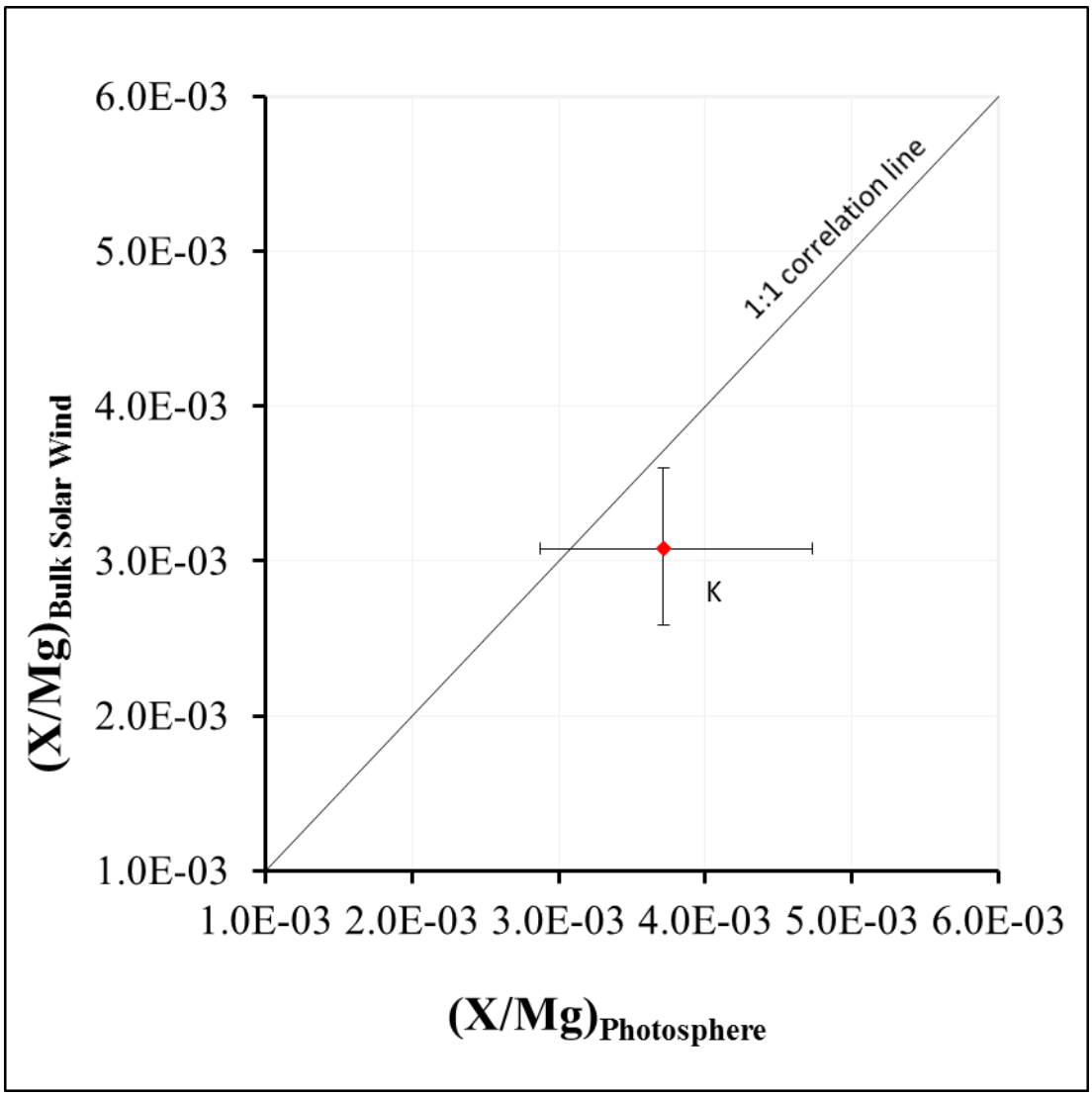

Fig. 1.18. Subset of Fig. 1.16, Featuring Potassium. Genesis Bulk Solar Wind Potassium Abundance Normalized to Genesis Bulk Solar Wind Magnesium Versus Photospheric Potassium Abundance Normalized to Photospheric Magnesium.

The solar wind value for "K" is an average of the (possibly discrepant) DlC and Si measurements from the present study. The photospheric datum for K is from Palme *et al.* (2014). Error propagation was performed to illustrate the combined 1 s.d. errors for solar wind and solar photospheric measurements.

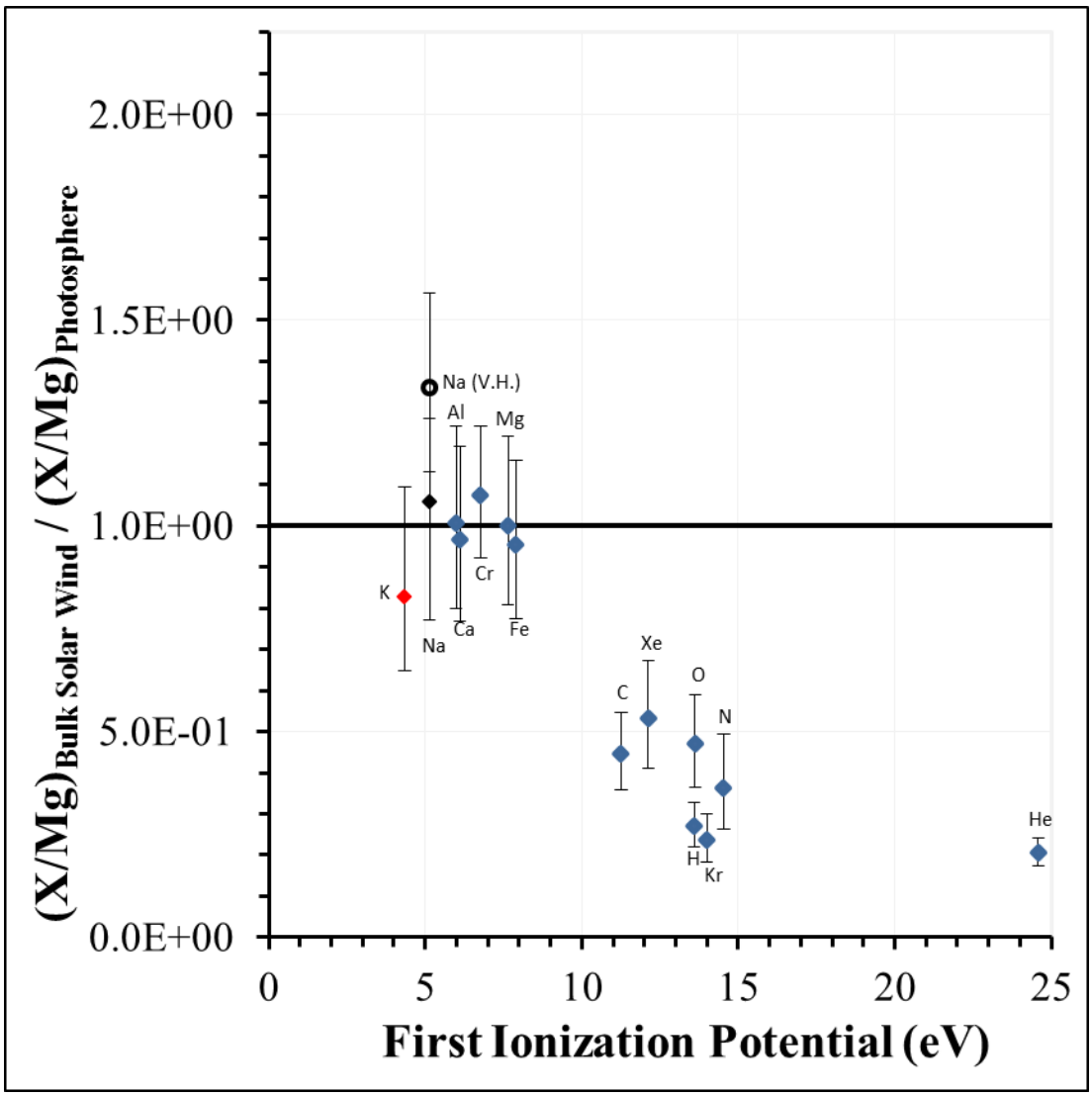

Fig. 1.19. Genesis Bulk Solar Wind Element/Magnesium Normalized to Photospheric Element/Magnesium Versus First Ionization Potential (i.e., FIP).

The Na data are represented by black points. The K datum is represented by a red point. The solar wind values for "Na" and "K" are averages of the (possibly discrepant) DlC and Si measurements from the present study. The solar wind datum for "Na (V.H.)" is the calibrated Na abundance measurement reported in Heber *et al.* (2014b). Other solar wind data are from Heber *et al.* (2009; 2014b; c; in prep.). SW Al, Ca, Cr, and N data presented in this plot are based on nominal (not calibrated) fluences of reference ion implants. Photospheric data are from Palme *et al.* (2014). Error propagation was performed to illustrate the combined 1 s.d. errors for solar wind and solar photospheric measurements.

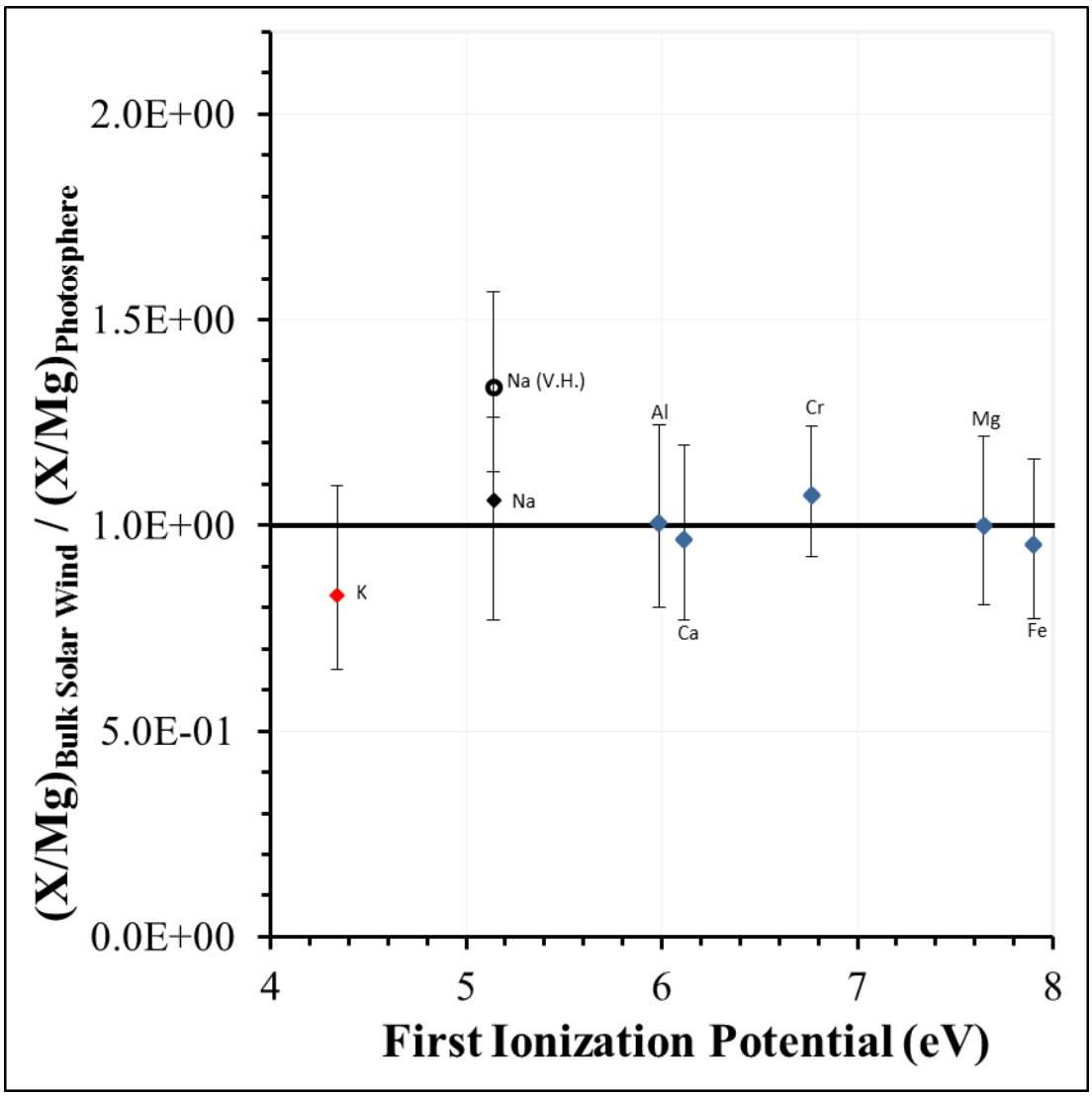

Fig. 1.20. Subset of Fig. 1.19, Featuring Elements With Low First Ionization Potential. Genesis Bulk Solar Wind Element/Magnesium Normalized to Photospheric Element/Magnesium Versus First Ionization Potential (i.e., FIP).

The Na data are represented by black points. The K datum is represented by a red point. The solar wind values for "Na" and "K" are averages of the (possibly discrepant) DlC and Si measurements from the present study. The solar wind datum for "Na (V.H.)" is the calibrated Na abundance measurement reported in Heber *et al.* (2014b). Other solar wind data are from Heber *et al.* (2009; 2014b; c; in prep.). SW Al, Ca, and Cr data presented in this plot are based on nominal (not calibrated) fluences of reference ion implants. Photospheric data are from Palme *et al.* (2014). Error propagation was performed to illustrate the combined 1 s.d. errors for solar wind and solar photospheric measurements.

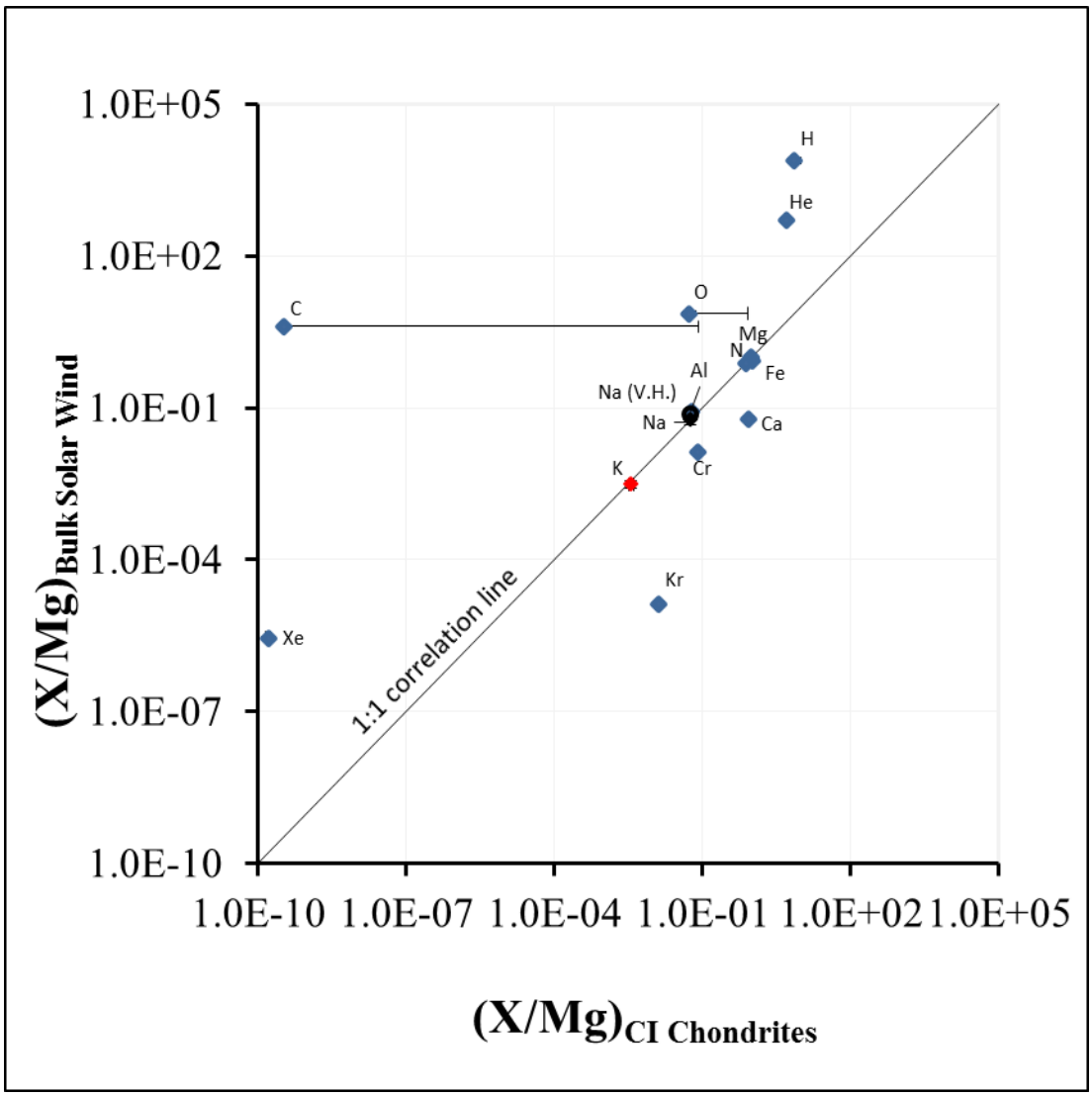

Fig. 1.21. Genesis Bulk Solar Wind Element Abundances Normalized to Genesis Bulk Solar Wind Magnesium Versus CI Chondritic Element Abundances Normalized to CI Chondritic Magnesium.

The Na data are represented by black points. The K datum is represented by a red point. The solar wind values for "Na" and "K" are averages of the (possibly discrepant) DlC and Si measurements from the present study. The solar wind datum for "Na (V.H.)" is the calibrated Na abundance measurement reported in Heber *et al.* (2014b). Other solar wind data are from Heber *et al.* (2009; 2014b; c; in prep.). SW Al, Ca, Cr, and N data presented in this plot are based on nominal (not calibrated) fluences of reference ion implants. CI chondritic data are from Palme *et al.* (2014). Error propagation was performed to illustrate the combined 1 s.d. errors for solar wind and CI chondritic measurements.

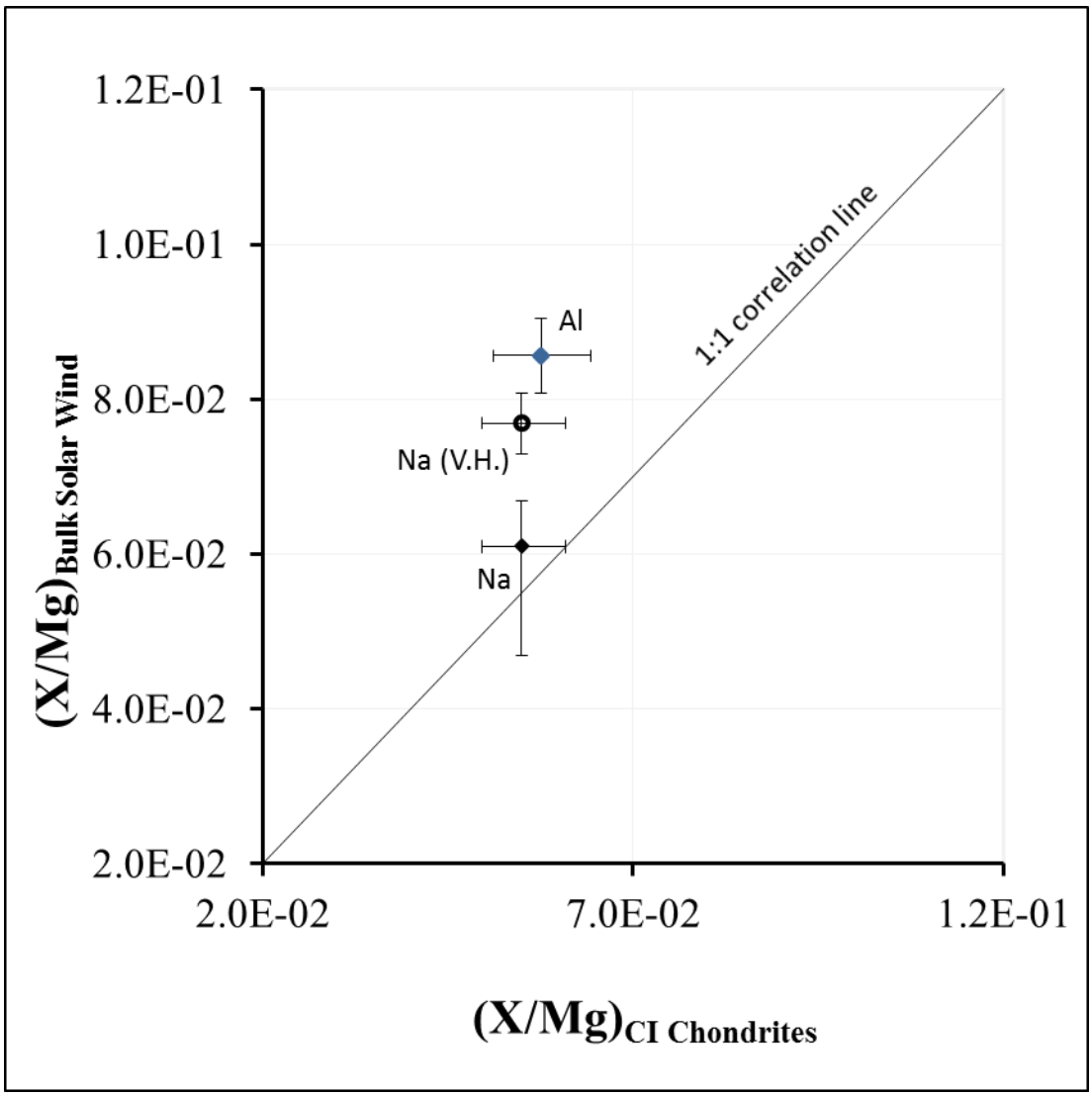

Fig. 1.22. Subset of Fig. 1.21, Featuring Sodium. Genesis Bulk Solar Wind Element Abundances Normalized to Genesis Bulk Solar Wind Magnesium Versus CI Chondritic Element Abundances Normalized to CI Chondritic Magnesium.

The solar wind value for "Na" is an average of the (possibly discrepant) DlC and Si measurements from the present study. The solar wind datum for "Na (V.H.)" is the calibrated Na abundance measurement reported in Heber *et al.* (2014b). Other solar wind data are from Heber *et al.* (2009; 2014b; c; in prep.). SW Al datum is based on a nominal (not calibrated) fluence of a reference ion implant. CI chondritic data are from Palme *et al.* (2014). Error propagation was performed to illustrate the combined 1 s.d. errors for solar wind and CI chondritic measurements.

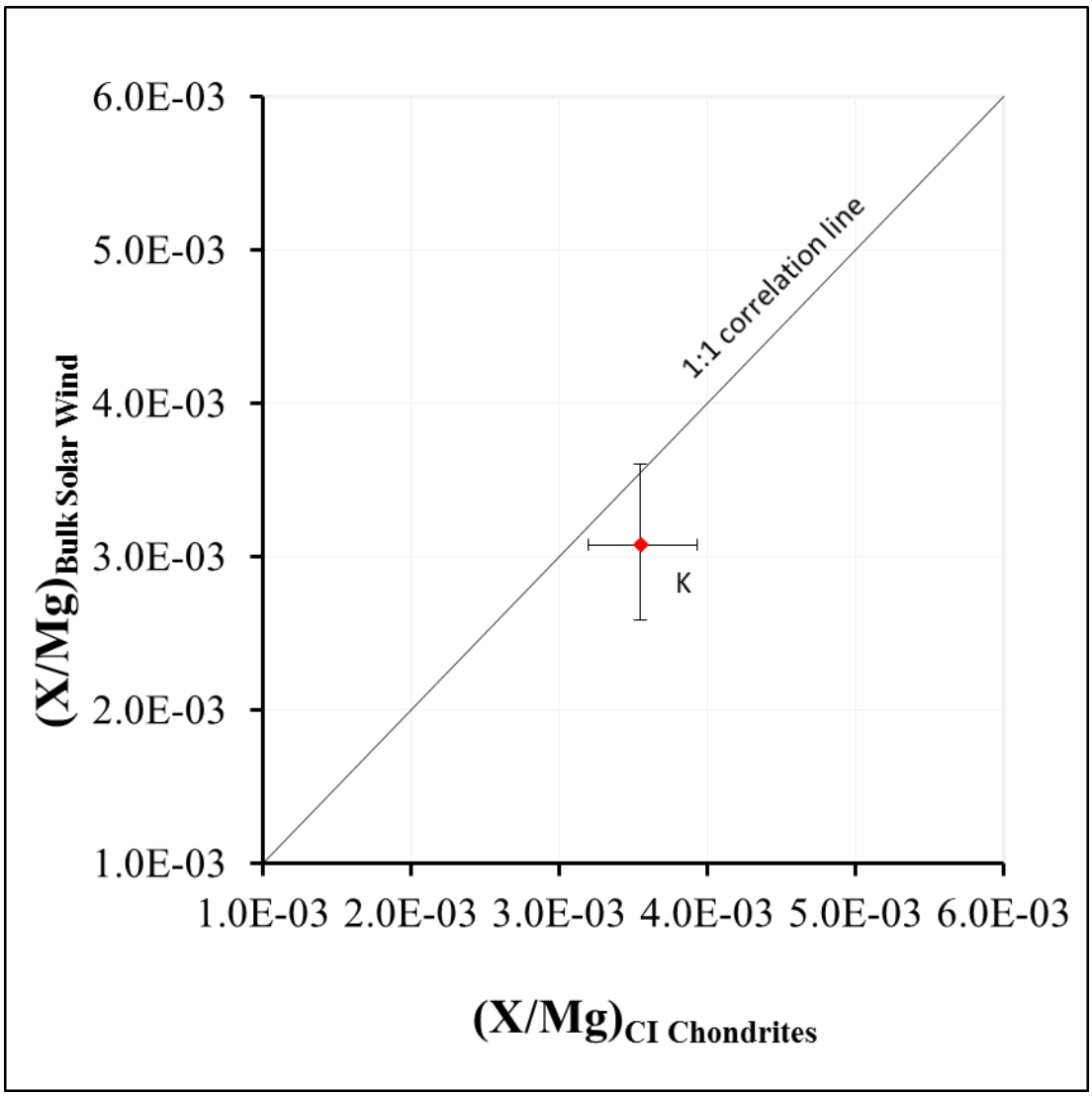

Fig. 1.23. Subset of Fig. 1.21, Featuring Potassium. Genesis Bulk Solar Wind Potassium Abundance Normalized to Genesis Bulk Solar Wind Magnesium Versus CI Chondritic Potassium Abundance Normalized to CI Chondritic Magnesium.

The solar wind value for "K" is an average of the (possibly discrepant) DlC and Si measurements from the present study. The CI chondritic datum for K is from Palme *et al.* (2014). Error propagation was performed to illustrate the combined 1 s.d. errors for solar wind and CI chondritic measurements.

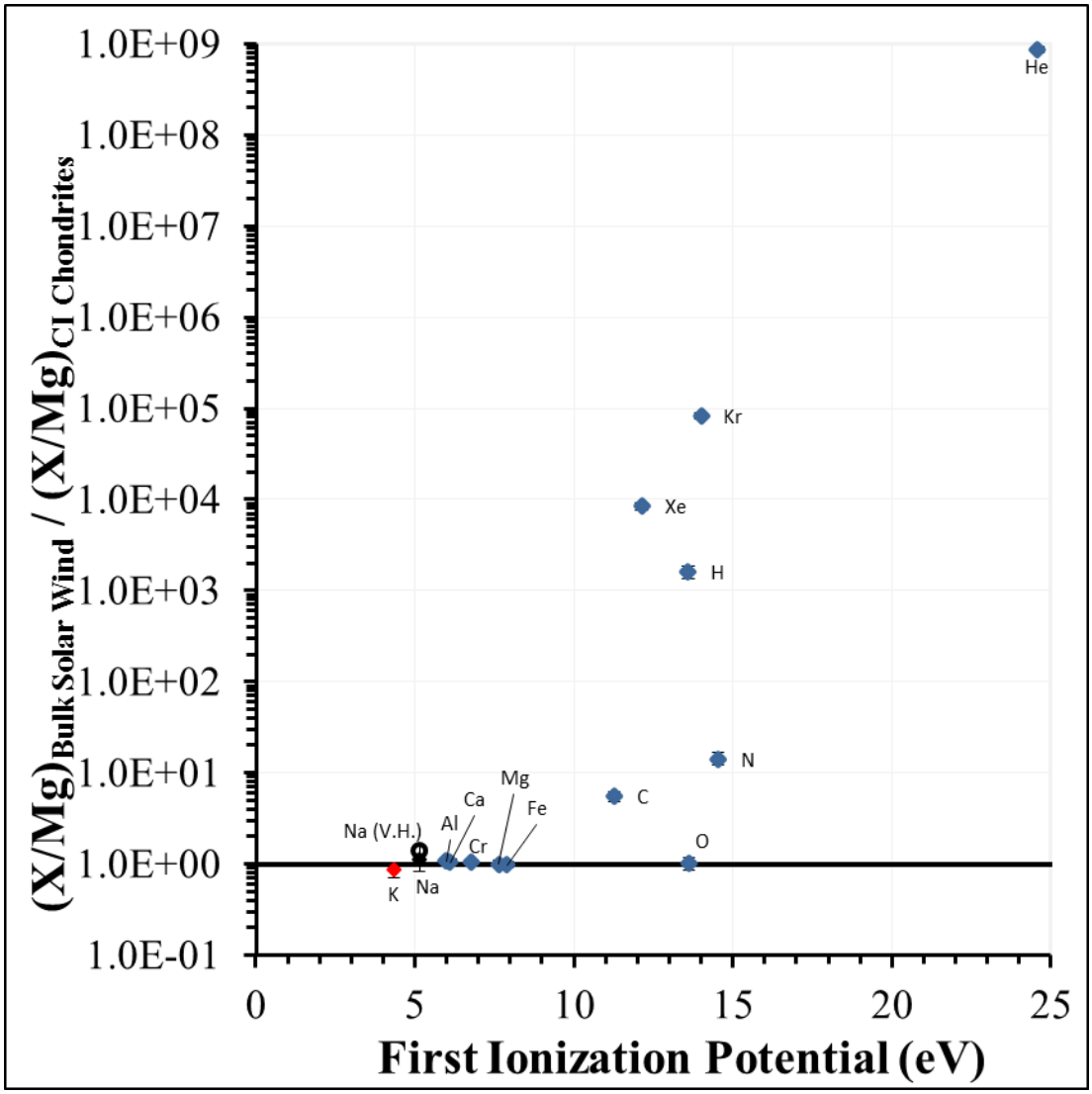

Fig. 1.24. Genesis Bulk Solar Wind Element/Magnesium Normalized to CI Chondritic Element/Magnesium Versus First Ionization Potential (i.e., FIP).

The Na data are represented by black points. The K datum is represented by a red point. The solar wind values for "Na" and "K" are averages the (possibly discrepant) DlC and Si measurements from the present study. The solar wind datum for "Na (V.H.)" is the calibrated Na abundance measurement reported in Heber *et al.* (2014b). Other solar wind data are from Heber *et al.* (2009; 2014b; c; in prep.). SW Al, Ca, Cr, and N data presented in this plot are based on nominal (not calibrated) fluences of reference ion implants. CI chondritic data are from Palme *et al.* (2014). Error propagation was performed to illustrate the combined 1 s.d. errors for solar wind and CI chondritic measurements.

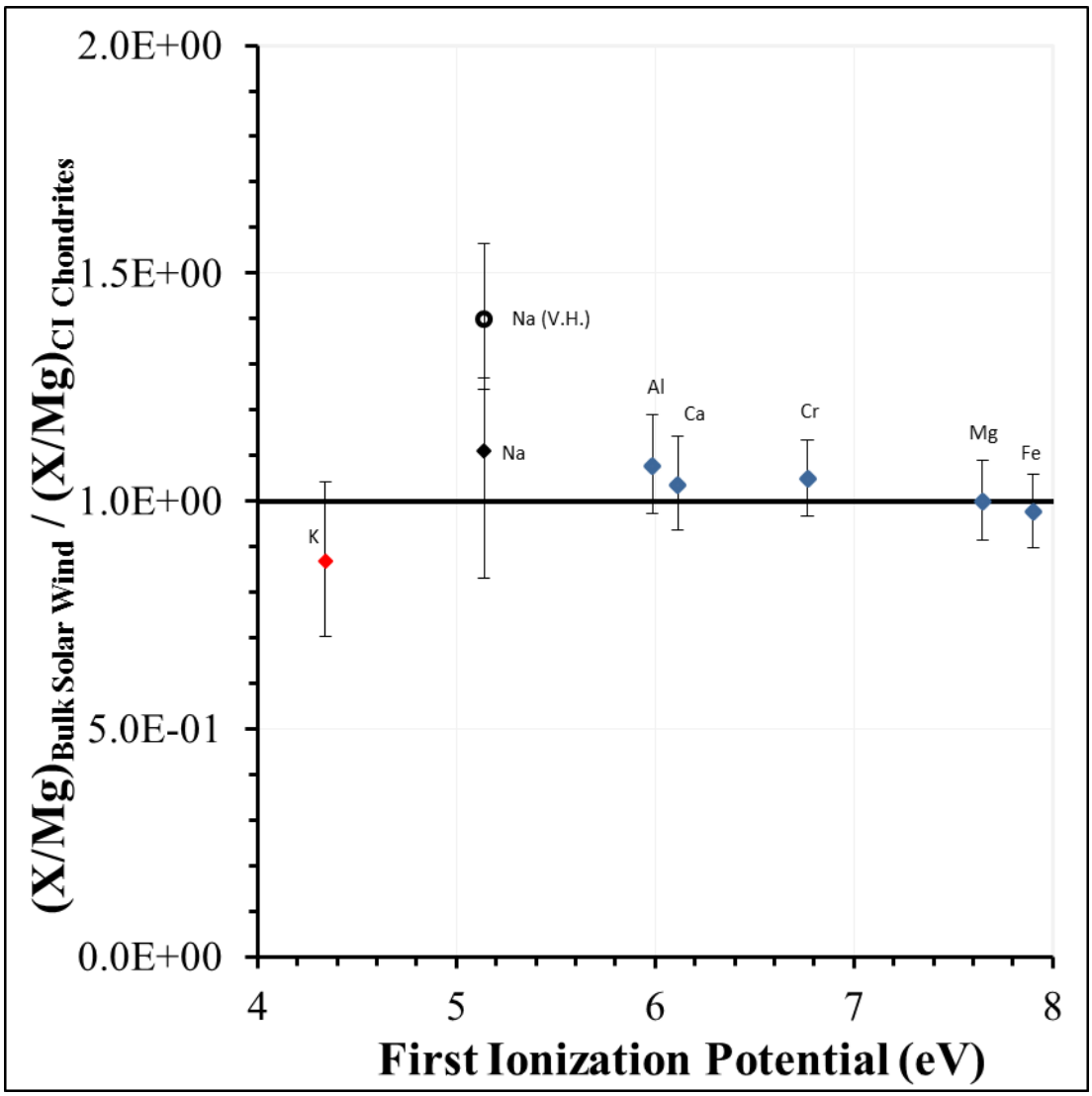

Fig. 1.25. Subset of Fig. 1.24, Featuring Elements With Low First Ionization Potential. Genesis Bulk Solar Wind Element/Magnesium Normalized to CI Chondritic Element/Magnesium Versus First Ionization Potential (i.e., FIP).

The Na data are represented by black points. The K datum is represented by a red point. The solar wind values for "Na" and "K" are averages the (possibly discrepant) DlC and Si measurements from the present study. The solar wind datum for "Na (V.H.)" is the calibrated Na abundance measurement reported in Heber *et al.* (2014b). Other solar wind data are from Heber *et al.* (2009; 2014b; c; in prep.). SW Al, Ca, and Cr data presented in this plot are based on nominal (not calibrated) fluences of reference ion implants. CI chondritic data are from Palme *et al.* (2014). Error propagation was performed to illustrate the combined 1 s.d. errors for solar wind and CI chondritic measurements.

1.7. Acknowledgements

This work has been supported in part by NASA grant #NNX09AC35G (D. S. Burnett and A. J. G. Jurewicz), and the NASA Earth and Space Science Fellowship 2012-13, 2013-14, and 2014-15 (R. L. Hervig and K. D. Rieck). Use of the Center for Nanoscale Materials at Argonne National Laboratory was supported by the U.S. Department of Energy, Office of Science, Office of Basic Energy Sciences, (Contract #DE-AC02-06CH11357). F. Stevie and V. Heber provided use of their standards. C. T. Olinger provided solar wind ion implant models. I. V. Veryovkin & C. Miller provided XeF_2 etching assistance. The Genesis curation team at Johnson Space Center provided the samples. Leonard Kroko Inc. performed the ion implantation. Evans Analytical Group performed the Si collector thinning.

Special thanks to advisors, staff, and colleagues in the Center for Meteorite Studies (ASU), the W. M. Keck Foundation Laboratory for Environmental Biogeochemistry (ASU), Secondary Ion and Mass Spectrometry Lab (ASU), the Caltech Microanalysis Center, the UCLA MegaSIMS Laboratory, the LeRoy Eyring Center for Solid State Science (ASU), and the NanoSIMS Facility (ASU).

1.8. References for Chapter 1

Aisenberg S. and Chabot R. 1971. Ion-Beam Deposition of Thin Films of Diamondlike Carbon. *Journal of Applied Physics* 42:2953-2958.

Asplund M., Grevesse N., Sauval A. J., and Scott P. 2009. The Chemical Composition of the Sun. *Annual Review of Astronomy and Astrophysics* 47:481-522.

Barrat J. A., Zanda B., Moynier F., Bollinger C., Liorzou C., and Bayon G. 2012. Geochemistry of CI chondrites: Major and trace elements, and Cu and Zn Isotopes. *Geochimica et Cosmochimica Acta* 83:79–92.

Baumüller D., Butler K., and Gehren T. 1998. Sodium in the Sun and in metal-poor stars. *Astronomy and Astrophysics* 338:637-650.

Bochsler P. 2000. Abundances and Charge States of Particles in the Solar Wind. *Reviews of Geophysics* 38:247–266.

Bochsler P., Wimmer-Schweingruber R. F., and Wurz P. 2001. Sun, solar wind, meteorites and interstellar medium: What are the compositional relations? In *Solar and Galactic Composition,* edited by Wimmer-Schweingruber R. F. *Proceedings of the Joint SOHO/ACE Workshop in Bern, Switzerland 6–9 March 2001.* American Institute of Physics *Conference Proceedings* **598**:381-387.

Bochsler P. 2007. Minor ions in the solar wind. *The Astronomy and Astrophysics Review.* 14:1-40.

Brazzle J. D., Doheci M. R., and Mastrangelo C. H. 2004. Modeling and Characterization of Sacrificial Polysilicon Etching Using Vapor-Phase Xenon Difluoride. *Institute of Electrical and Electronics Engineers Micro Electro Mechanical Systems (Maastricht, The Netherlands, 2004).* pp. 737-740.

Breneman H. H. and Stone E. C. 1985. Solar Coronal and Photospheric Abundances from Solar Energetic Particle Measurements. *The Astrophysical Journal* 299:L57-L61.

Burger P. V. and Brearley A. J. 2005. Localized Chemical Redistribution During Aqueous Alteration in CR2 Carbonaceous Chondrites EET 87770 AND EET 92105 (abstract #2288). 36th Lunar and Planetary Science Conference.

Burnett D. S., Barraclough B. L., Bennett R., Neugebauer M., Oldham L. P., Sasaki C. N., Sevilla D., Smith N., Stansbery E., Sweetnam D., and Wiens R. C. 2003. The Genesis discovery mission: Return of solar matter to Earth. *Space Science Reviews* 105:509–534.

Burnett D. S., Woolum D. S., Jurewicz A. J. G., McKeegan K. D., and Guan Y. 2007. Solar Wind Elemental Abundances from Genesis Collectors (abstract #1843). 38th Lunar and Planetary Science Conference.

Burnett D. S., Jurewicz A. J. G., Woolum D. S., Wang J., Paque J. M., Nittler L. R., McKeegan K. D., Humayun M., Hervig R., Heber V. H., and Guan Y. 2015. Ion Implants as Matrix-Appropriate Measurement Standards for Geochemical Ion Probe Analyses. *Geostandards and Geoanalytical Research* 39:265-276.

Caffau E., Ludwig H.-G., Steffen M., Freytag B., and Bonifacio P. 2011. Solar Chemical Abundances Determined with a CO5BOLD 3D Model Atmosphere. *Solar Physics* 268: 255–269.

Chang F. I., Yeh R., Lin G., Chu P. B., Hoffman E., Kruglick E. J. J., and Kristofer S.J. Pister Gas-phase silicon micromachining with xenon difluoride. 1995. *SPIE* 2641:117-128.

Cook W. R., Stone E. C., and Vogt R. E. 1984. Elemental Composition of Solar Energetic Particles. *The Astrophysical Journal*. 279:827-838.

Feldman U. and Laming J. M. 2000. Element Abundances in the Upper Atmospheres of the Sun and Stars: Update of Observational Results. *Physica Scripta* 61:222-252.

Friedmann T. A., Sullivan J. P., Knapp J. A., Tallant D. R., Follstaedt D. M., Medlin D. L., and Mirkarimi P. B. 1997. Thick stress-free amorphous-tetrahedral carbon films with hardness near that of diamond. *Applied Physics Letters* 71:3820-3822.

Fisk L. A., Schwadron N. A., and Zurbuchen T. H. 1998. On the Slow Solar Wind. *Space Science Reviews* 86:51-60.

Giammanco C., Wurz P., and Karrer R. 2008. Minor Ion Abundances in the Slow Solar Wind. *The Astrophysical Journal* 681:1703-1707.

Gloeckler G., Balsiger H., Bürgi A., Bochsler P., Fisk L. A., Galvin A. B., Geiss J., Gliem F., Hamilton D. C., Holzer T. E., Hovestadt D., Ipavich F. M., Kirsch E., Lundgren R. A., Ogilvie K. W., Sheldon R. B., and Wilken B. 1995. The solar WIND and suprathermal ion composition investigation on the WIND spacecraft. *Space Science Reviews* 71:79-124.

Heber V. S., Wieler R., Baur H., Olinger C. T., and Burnett D. S. 2009. Noble gas composition of the solar wind as collected by the Genesis mission. *Geochimica et Cosmochimica Acta* 73:7414–7432.

Heber V. S., Guan Y., Jurewicz A. J. G., Kallio A. P., Olinger C., Woolum D. S., McKeegan K. D., Burnett D. S. 2010. Solar Wind Elemental Fractionation: Genesis C and O Fluences by Backside SIMS Profiling – Preliminary Data. (abstract #2234). 41st Lunar and Planetary Science Conference.

Heber V. S., Jurewicz A. J. G., Janney P., Wadhwa M., McKeegan K. D., and Burnett D. S. 2012. Magnesium Isotopic Composition of Solar Wind as Test for Isotopically Fractionated Solar Wind: A Progress Report (abstract # 2921). 43rd Lunar and Planetary Science Conference.

Heber V. S., McKeegan K. D., Smith S., Jurewicz A. J. G., Olinger C., Burnett D. S., and Guan Y. 2014a. Accurate Analysis of Shallow Solar Wind Ion Implants by SIMS Backside Depth Profiling (abstract #1203). 45th Lunar and Planetary Science Conference.

Heber V. S., McKeegan K. D., Bochsler P., Duprat J., Burnett D. S. 2014b. The Elemental Composition of Solar Wind with Implications for Fractionation Processes During Solar Wind Formation (abstract #2117). 45th Lunar and Planetary Science Conference.

Heber V. S., McKeegan K. D., Burnett D. S., Duprat J., Guan Y., Jurewicz A. J. G., Olinger C. T., Smith S. P. 2014c. Accurate analysis of shallowly implanted solar wind ions by SIMS backside depth profiling. *Chemical Geology* 390:61–73.

Huss G. R., Ogliore R. C., Jurewicz A. J. G., Burnett D., S. and Nagashiima K. 2015. Estimate of Solar Wind Hydrogen Fluence from the Genesis Collectors (abstract #2577). 46th Lunar and Planetary Science Conference.

Ip W.-H. and Axford W. I. 1991. On the First Ionization Potential Effect of the Solar Corona. *Advances in Space Research* 11:(1)247-(1)250.

Ipavich F. M., *et al.* 1998. *Journal of Geophysical. Research* 103(A8):17215.

Ipavich F. M., Bochsler P., Lasley S. E., Paquette, J. A., and Wurz P. 1999. The Abundance of Sodium in the Solar Wind as Measured by SOHO/CELIAS/MTOF. *EOS* 80:256.

Ipavich F. M., Paquette J. A., Bochsler P., Lasley S. E., and Wurz P. 2001. Solar wind iron isotopic abundances: Results from SOHO/CELIAS/MTOF. In *American Institute of Physics Conference Proceedings.* Institute of Physics Publishing Ltd. 121-126.

Jones C. L., Brearley A. J. 2006. Experimental Aqueous Alteration of the Allende Meteorite under Oxidizing Conditions: Constraints on Asteroidal Alteration. *Geochimica et Cosmochimica Acta* 70:1040–1058.

Jurewicz A. J. G., Burnett D. S., Wiens R. C., Friedmann T. A., Hays C. C., Hohlfelder R. J., Nishiizumi K., Stone J. A., Woolum D. S., Becker R. H., Butterworth A. L., Campbell A., Ebihara M., Franchi I. A., Heber V. S., Hohenberg C. M., Humayun M., McKeegan K. D., McNamara K., Meshik A. P., Pepin R. O., Schlutter D. J., and Wieler R. 2003. The Genesis solar-wind collector materials. *Space Science Reviews* 105:535–560.

Jurewicz A. J. G., Burnett D. S., Woolum D. S., McKeegan K. D., Guan Y., and Hervig R. L. 2007. SIMS Results for Solar-Wind Elemental Abundances from Genesis Collectors (contribution # 5299). 70th Annual Meteoritical Society Meeting.

Jurewicz A. J. G., Burnett D. S., Woolum D. S., McKeegan K. D., Guan Y., and Hervig R. 2008. Solar Elemental Abundances from Genesis Collectors: Fe/Mg, Constraining Solar-Wind FIP Fractionation, and Comparisons with CI Chondrites (abstract # 2272). 39th Lunar and Planetary Science Conference.

Jurewicz A. J. G., Burnett D. S., Woolum D. S., McKeegan K. D., Heber V., Guan Y., Humayun M., and Hervig R. 2011. Solar-Wind Fe/Mg and a Comparison with CI Chondrites (abstract # 1917). 42nd Lunar and Planetary Science Conference.

Krieger A. S., Timothy A. F., and Roelof E. C. 1973. A Coronal Hole and its Identification as the Source of a High Velocity Solar Wind Stream. *Solar Physics* 29:505-525.

Krot A. N., Keil K., Scott E. R. D., Goodrich C. A., and Weisberg M. K. 2014. Classification of Meteorites and Their Genetic Relationships. In *Meteorites and Cosmochemical Processes,* edited by Davis A. M. Treatise on Geochemistry (Second Edition), vol. 1. Amsterdam: Elsevier. pp. 1-63.

Laming J. M. 2015. The FIP and Inverse FIP Effects in Solar and Stellar Coronae. *Living Reviews in Solar Physics.* arXiv:1504.08325v1 [astro-ph.SR].

Lodders K., Palme H., and Gail H. P. 2009. Abundances of the elements in the solar system. In *Landolt-Börnstein, New Series, Astronomy and Astrophysics, Vol. VI/4B, Chap. 4.4,* edited by Trümper J. E. Berlin, Heidelberg, New York:Springer-Verlag. pp. 560-630.

McSween H. Y. 1993. Cosmic or Cosmuck? *Meteoritics* 28:3-4.

Morlok A., Bischoff A., Stephan T., Floss C., Zinner E., and Jessberger E. K. 2006. Brecciation and Chemical Heterogeneities of CI chondrites. *Geochimica et Cosmochimica Acta* 70:5371–5394.

Palme H., Lodders K., and Jones A. 2014. Solar System Abundances of the Elements. In *Planets, Asteroids, Comets and the Solar System,* edited by Davis A. M. Treatise on Geochemistry (Second Edition), vol. 2. Amsterdam: Elsevier. pp.15-36.

Pilleri P., Reisenfeld D. B., Zurbuchen T. H., Lepri S. T., Shearer P., Gilbert J. A., von Steiger R., and Wiens R. C. 2015. Variations in Solar Wind Fractionation as Seen by ACE/SWICS and the Implications for Genesis Mission Results. *The Astrophysical Journal* 812:1-10.

Raymond J. C. 1999. Composition Variations in the Solar Corona and Solar Wind. *Space Science Reviews* 87:55–66

Reames D. V. 1994. Coronal Element Abundances Derived from Solar Energetic Particles. *Advances in Space Research* 14:(4)177-(4)180.

Reames D. V. 1995. Coronal Abundances Determined from Energetic Particles. *Advances in Space Research* 15:(7)41-(751).

Reames D. V. 1998. Solar Energetic Particles: Sampling Coronal Abundances. *Space Science Reviews* 85:327-340.

Reisenfeld D. B., Burnett D. S., Becker R. H., Grimberg A. G., Heber V. S., Hohenberg C. M., Jurewicz A. J. G., Meshik A., Pepin R. O., Raines J. M., Schlutter D. J., Wieler R., Wiens R. C., and Zurbuchen T. H. 2007. Elemental Abundances of the bulk solar wind: Analyses from Genesis and Ace. *Space Science Reviews* 130:79–86.

Reisenfeld D. B., Wiens R. C., Barraclough B. L., Steinberg J. T., Neugebauer M., Raines J., and Zurbuchen T. H. 2013. Solar Wind Conditions and Composition During the Genesis Mission as Measured by in situ Spacecraft. *Space Science Reviews* 175:125–164.

Schmeltz J. T., Reames D. V., von Steiger R., and Basu S. 2012. Composition of the Solar Corona, Solar Wind, and Solar Energetic Particles. *The Astrophysical Journal* 755:33 doi:10.1088/0004-637X/755/1/33.

Schmitt A. K. and Zack T. 2012. High-sensitivity U–Pb rutile dating by secondary ion mass spectrometry (SIMS) with an O_2^+ primary beam. *Chemical Geology 332-333: 65-73.*

Scott E. R. D. and Krot A. N. 2007. Chondrites and their components. In *Meteorites, Comets and Planets, Chapter 1.07,* edited by Davis. A. M. Treatise on Geochemistry Update 1, Elsevier, online at http://www.sciencedirect.com/science/referenceworks/9780080437514

Scott P., Grevesse N., Asplund M., Sauval A. J., Lind K., Takeda Y., Collet R., Trampedach R., and Hayek W. 2015. The elemental composition of the Sun.: I. The intermediate mass elements Na to Ca.* *Astronomy & Astrophysics* 573, A25:1-19.

Sinha D. 2002. Correlating Chemical and Water Purity to the Surface Metal on Silicon Wafer During Wet Cleaning Process. *Chemical Engineering Communications.* 189:974-984.

Vainonen E., Likonen J., Ahlgren T., Haussalo P., Keinonen J., and Wu C. H. 1997. Hydrogen migration in diamond-like carbon films. *Journal of Applied Physics* 82: 3791-3796.

Veryovkin I. V., Zinovev A. V., Tripa C. E., and Burnett D. S. 2014. Depth Profiling of Genesis Diamond-on-Silicon Collectors: Direct Comparison Between Frontside and Backside Approaches (abstract # 2795). 45th Lunar and Planetary Science Conference.

Vogel N., Heber V. S., Baur H., Burnett D. S., and Wieler R. 2011. Argon, krypton, and xenon in the bulk solar wind as collected by the Genesis mission. *Geochimica et Cosmochimica Acta* 75:3057-3071.

von Steiger R., Schwadron N. A., Fisk L. A., Geiss J., Gloeckler G., Hefti S., Wilken B., Wimmer-Schweingruber R. F., and Zurbuchen T. H. 2000. Composition of quasistationary solar wind flows from Ulysses/Solar Wind Ion Composition Spectrometer. *Journal of Geophysical Research* 105:27217–27238.

von Steiger R., Zurbuchen T. H., and McComas D. J. 2010. Oxygen flux in the solar wind: Ulysses observations. *Geophysical Research Letters*, vol. 37, L22101, doi:10.1029/2010GL045389.

von Steiger R. and Zurbuchen T. H. 2011. Polar coronal holes during the past solar cycle: Ulysses observations. *Journal of Geophysical Research*, vol. 116, A01105, doi:10.1029/2010JA015835.

Wang W. H., Bolse W., Illgner C., Lieb K. P., Keinonen J., and Ewert J. C. 1997. Recrystallization and diffusion in sodium-implanted silicon. *Thin Solid Films* 295:169-177.

Webb D. F. (2000) Coronal Mass Ejections: Origins, Evolution, and Role in Space Weather. *IEEE Transactions on Plasma Science* 28:1795-1806.

Williams P. 1979. The Sputtering Process and Sputtered Ion Emission. *Surface Science* 90:588-634.

Wilson R. G., Stevie F. A., and Magee C. W. 1989. Secondary ion mass spectrometry: A practical handbook for depth profiling and bulk impurity analysis. New York: John Wiley and Sons, Inc. 384 p.

2. CHAPTER 2 – PREFACE

DISCUSSION ON USING GENESIS DIAMOND-LIKE CARBON ON SILICON WAFERS FOR MEASUREMENTS BY SIMS

A diamond-like carbon film on silicon made in the laboratory of T.A. Friedmann (Sandia National Laboratories) was chosen by the Genesis mission to be one of several types of solar wind collectors. Factors in this choice included the carbon base (low backscatter), low H content, retention of volatiles under mission conditions, etc. It has successfully been used to measure solar wind noble gasses (Heber *et al.*, 2012), and looks extremely promising for elemental analysis by RIMS (Veryovkin *et al.*, 2014). Measurements of Na and K in Genesis DlC by SIMS have been difficult, and it has been extremely difficult to reconcile measurements in DlC with measurements in Si. This chapter will discuss the reasons why DoS was selected, the drawbacks of using Genesis diamond-like carbon for SIMS analysis of solar wind, and explain techniques explored to obtain both precise and accurate measurements.

2.1. Introduction

NASA's Genesis spacecraft carried a variety of materials to collect solar wind for terrestrial analysis (Jurewicz *et al.*, 2003). Among these was diamond-like carbon (DlC) on silicon (DoS) manufactured by Sandia National Laboratories. This section provides a general description of the physical and chemical properties of DlC, modifications made by Sandia National Laboratories, and modifications made for use on the Genesis spacecraft.

2.1.1. Properties of Diamond-like Carbon

Diamond-like carbon is an amorphous allotrope of carbon, in which the atoms are held together by a mixture of sp^3 (tetrahedral, diamond-like) and sp^2 (graphitic) bonds (Outka *et al.*, 1994; Robertson, 2002; Gottimukkala, 2005). Its physical and chemical properties have made it a commonly used material in the engineering of micro-electro-mechanical systems (MEMS). For example, DlC film is optically transparent, chemically inert, stiff, and nearly as hard as diamond, with high tensile (elastic or Young's) modulus values, high thermal conductivity, and low coefficients of thermal expansion, friction, and surface adhesion (Aisenberg and Chabot, 1971; Robertson, 2002; Cho *et al.*, 2005; Luo *et al.*, 2007). DlC is a wide band gap semiconductor (Luo *et al.*, 2007). DlC film can be made to be electrically insulating or conducting through fabrication techniques that control the bonding structure (Robertson, 2002), or by chemical doping (Luo *et al.*, 2007). Some DlC is highly insulating (Aisenberg and Chabot, 1971). Ion diffusion rates through DlC are low (Aisenberg and Chabot, 1971; Vainonen *et al.*, 1997; Heber *et al.*, 2009).

Some of these properties made DlC an attractive addition to the Genesis collectors. Chemically inert surfaces facilitate cleaning and terrestrial contaminant removal with assorted reagents (Appendix A). The fact that ions do not diffuse easily through this material is critically important for retaining captured solar wind ions, volatiles in particular (Aisenberg and Chabot, 1971; Vainonen *et al.*, 1997; Heber *et al.*, 2009). Conductivity is important for SIMS analysis. Scratch resistance facilitates cleaning, ion retention and analysis.

A drawback of DlC is that it has intrinsic compressive and tensional stresses, resulting from the disordered metastable mix of sp^3 and sp^2 bonds (Outka *et al.*, 1994; Robertson, 2002; Luo *et al.*, 2007). High internal stresses cause DlC to be very fragile. A rigid backing that is chemically compatible with the DlC (e.g., Si) is necessary to keep highly-stressed DlC stable (Outka *et al.*, 1994). Internal stresses also limit how thick these films can be made before they delaminate from their supportive substrates. These factors limit the practical applications of DlC (Outka *et al.*, 1994; Robertson, 2002).

2.1.2. DlC Improvements Made by Sandia National Laboratories

Sandia National Laboratories approached this problem by producing an anhydrous, sp^3-rich variety of DlC that can be easily annealed to balance internal stresses, without losing all its diamond-like characteristics (Friedmann *et al.*, 1996; 1997; Kelires, 2001; Alam *et al.*, 2002). This DlC is referred to as tetrahedral amorphous carbon (ta-C or a-tC; Fig. 2.1). Pulsed laser deposition is used to create a series of layers of ta-C, each ~0.1–0.2 μm thick. These layers are deposited at room temperature. After application of each layer, the intrinsic stress (~6–8 GPa) is relieved by a short ~2 min. anneal at 600 °C (Friedmann *et al.*, 1997). This process is repeated until the film has reached the desired

thickness (Fig. 2.2). The average density of DlC is 2.85 g/cm^3, but the density can vary according to the abundance of sp^2 and sp^3 bonds (A. J. G. Jurewicz; personal communication).

This method for producing DlC is particularly successful because, unlike some other methods, it avoids the use of hydrogen during the manufacturing process. If hydrogen were incorporated into the DlC during manufacturing, the sp^3 (diamond-like) bonds would break down during annealing, transforming the material into a more graphite-like sp^2-rich phase (Friedmann *et al.*, 1996).

2.1.3. Genesis Diamond-like Carbon

Annealing reduces the likelihood of DlC delamination from a supporting substrate, but each annealing step provides an opportunity for trace contaminants present in the Sandia sputtering system to build up at interlayer surfaces. For example, equilibration with the chamber atmosphere during these annealing steps produces an internal layered distribution of terrestrial contaminants every 1,000-1,500 Å throughout the DLC film (Jurewicz *et al.*, 2003; Figs. 1.10 and 1.11). These trace contaminants can interfere with the measurement of low-fluence implants. In order to avoid internal contamination in the zone destined to collect solar wind, the penultimate annealing step was skipped for the DoS quadrant of the solar wind concentrator target (Jurewicz *et al.*, 2003). Although some contaminants may have entered the very upper surface of the DlC in the final annealing step, the upper 2,000-3,000 Å did not have an internal layer of terrestrial contaminants (Jurewicz *et al.*, 2003). Skipping annealing steps may have made this Genesis DlC more fragile than fully-annealed material. In contrast to the concentrator DoS, all the annealing steps were performed between the layers of the DoS hexagons in

the solar wind collector arrays. Consequently, small amounts of terrestrial contaminants inherently interfere with solar wind measurements for the bulk solar wind DoS collectors (Jurewicz *et al.*, 2003).

In addition, all Genesis DlC contains a component incorporated after the manufacturing process that makes it distinct from all other DlC: solar wind. The solar wind ions implanted in the upper layers of the DlC consist of a fairly representative sampling of solar photospheric material (Burnett *et al.*, 2003). How solar wind implantation, and exposure to solar radiation in general, affects the physical and chemical properties of this material has not been thoroughly investigated.

2.2. SIMS Depth Profiling Through Genesis DlC: Solar Wind Sodium and Potassium Analysis

There are inherent advantages and disadvantages to choosing DlC for analysis, rather than other Genesis collector materials, like silicon. There are also advantages and disadvantages specific to the use of SIMS depth profiling for measuring solar wind in these collectors. These topics are discussed here.

2.2.1. Analyzing DoS by SIMS

As discussed in Chapter 1, secondary ion mass spectrometers are designed for depth-sensitive ion abundance measurements, in particular, the measurement of ion implant fluences in semi-conductor wafers. This makes these instruments ideal tools for measuring the abundances of solar wind elements in Genesis collectors. For this work, mass spectrometers at Arizona State University (6f SIMS) and Caltech (7f SIMS) were

used to conduct depth profiles into Genesis Si and DoS collectors to measure Na and K fluences (Chapter 1).

In the present study, Genesis's DoS solar wind collectors were targeted in particular for bulk solar wind Na and K measurement by SIMS. The DlC matrix properties offered a number of advantages over other Genesis materials both as a solar wind collector in general and, in theory, for analysis by SIMS. Unfortunately, there are also a number of drawbacks, some of which were discovered in the course of this study. The material properties that affect SIMS are summarized in Tables 2.1 and 2.2. Below is an overview of why DoS was used for the present study, and the ways in which DoS can be a challenging material to work with.

2.2.1.1. Why DoS Was Selected for Analysis

DoS array material has a combination of properties that made it an attractive target for Na and K analysis. First, this material has very low background levels of Na and K, which allows for the measurement of low fluence implants of solar wind Na and K. Second, Na and K were not predicted to diffuse in this material under Genesis collection conditions. DoS retains even the most volatile elements more effectively than other Genesis collector materials (Heber *et al.*, 2009). Third, because C is such a light element, this material produces little backscatter of impinging ions. Fourth, smooth, clean surfaces could be recovered from DoS array material, making possible the analysis of shallow implants of terrestrially ubiquitous moderately volatile elements. Its diamond-like hardness made the material highly scratch resistant, and its chemical resistance to cleaning reagents facilitates cleaning. (Details about cleaning procedure are available in Chapter 1 and in Appendix A.). Fifth, in spite of its mostly diamond-like bonding, DlC is

semiconductive, so in theory, it should still allow for charge dissipation during SIMS analysis without a gold- or carbon-coat. Sixth, the ion stopping power of DlC produces relatively sharp (less diffuse) implant profiles, and prevents deep mixing of surface contaminants into the profiles by the SIMS primary ion beam, making it much easier to obtain reproducible measurements.

Monitoring matrix species is necessary to help correct for small drifts in primary current. The largest potential interference with ^{12}C measurement is $^{24}Mg_2$, but solar wind Mg is many orders of magnitude less abundant than the matrix species ^{12}C, and only 1600 Mass Resolving Power (MRP) is needed to resolve ^{12}C and $^{24}Mg^{2+}$. The next most likely interference is $^{11}B^{1}H$, but solar wind B is even less abundant than solar wind Mg, and it is even easier to resolve ^{12}C and $^{11}B^{1}H$; only 700 MRP is required. The only potential carbide interference with ^{23}Na is $^{11}B^{12}C$, which is not significantly abundant in the solar wind region of the DlC matrix, and is easily resolvable (MRP ~1200). However, carbides complicate ^{39}K and ^{41}K measurement in DlC. An MRP of ~2200 is needed to resolve ^{39}K from $^{27}Al^{12}C$ in the solar wind region of the DlC collectors. Resolving $^{29}Si^{12}C$ and $^{28}Si^{13}C$ from ^{41}K requires ~2800 MRP and ~2200 MRP, respectively.

2.2.1.2. Issues with DoS

Unlike some of the other array materials (e.g., Si, Sapphire), Genesis DoS is not a commercially available material. Each wafer was hand-crafted, and the proprietary process was performed in a laboratory (Sandia National Laboratories), rather than in a large-scale semiconductor manufacturing facility. Accordingly, Genesis DoS has some variability, and some features that would not typically be found in a commercial product.

For example, there are trace terrestrial contaminants at annealing steps. These contaminants can complicate profile integration. Sharp peaks in Na and K signal occur at interlayers, periodically. Interference with the profile occurs where contaminant peaks align with profile peaks such that the relative contributions are indistinguishable. Generally, interlayer contaminants are much less abundant than solar wind, and do not contribute significantly to the Na and K profiles. In these cases, the solar wind profiles match the shapes predicted by ion implantation software (TRIM; see Chapter 1 for details). The fluences derived from such profiles do not show evidence of contamination, in fact most solar wind Na fluences derived from DlC are lower than predicted (Chapter 1), though subtle contributions from internal contaminants may explain minor scatter, particularly among K measurements. For situations in which the contribution from internal contaminants visibly distorted the solar wind profile, the data from the profile were not used.

Besides the inter-layer contaminants at annealing steps, there are larger, localized, particle-like contaminants embedded randomly throughout the DlC layers that can significantly interfere with solar wind measurement. If these particles intersect the surface they can be identified in the first few seconds of analysis using ion imaging and a rastered primary beam. These particles appear as temporary, localized spots of increased ion intensity. However, these particles are commonly embedded, so most are not discovered until the profile is underway, and anomalous ion intensities are detected, either in the measured count rate or in the ion image. These peaks in ion intensity can be larger than those caused by interlayer contaminants, and can have significant effects on profile shapes and integration. Generally, profiles noticeably affected by particulate

contaminants are not used. Depending on the sample, it may be common for multiple analyses to be performed before a clean profile can be obtained.

Another way in which DlC is spatially non-uniform is with respect to analytical "dead spots." Dead spots have been detected in DlC where either the matrix- or implant-ion signal is diminished by varying degrees (Jurewicz *et al.*, 2009 and Rieck *et al.*, 2010). Spatial variability in ion count rate (or ion yield) may occur despite homogeneous ion implantation (Figs. 2.3 and 2.4). The exact causes for these effects are unknown, but are thought to be matrix-related, e.g., caused by inhomogeneity. One possible explanation is that the relative abundances of sp^3 and sp^2 bonds vary locally, creating localized changes in sample conductivity. Alternative, instrument-related explanations include using a large primary beam size relative to the analysis area, and issues with the SIMS ion detectors.

These changes in ion detection (relative sensitivity) due to the aforementioned DLC quirks make DlC particularly ill-suited for isotopic measurements where per mille precision is needed (e.g., Rieck *et al.*, 2010). This is why Genesis DlC is no longer used for Mg isotope measurement despite its other excellent properties.

DlC has high internal stresses, making it very fragile. This fragility limits the sample preparation and handling that can be performed prior to SIMS analysis. The implications are detailed below.

2.2.2. Frontside and Backside Depth Profiling

Frontside depth profiling (FDP) was primarily used for the analysis of external standards (refer to Chapter 1 for details). FDP of Genesis samples was attempted on only two wafers in this study (both DoS), and only one analysis was successful. Success was primarily the result of finding an exceptionally clean, pristine space for analysis after

extensive cleaning attempts. Backside depth profiling (BDP) was primarily used for the analysis of backside-implanted internal standards and most solar wind measurements. The inherent advantages and disadvantages to both approaches are reviewed here.

2.2.2.1. Frontside Depth Profiling of DlC (From DoS Wafers)

In general, frontside depth profiling is not ideal for most Genesis samples, because most of the implants are relatively shallow, and all surfaces have high abundances of terrestrial contaminates due to the crash (Burnett *et al.*, 2007; Heber *et al.*, 2014). Terrestrial Na and K contamination is ubiquitous, and solar wind Na and K implants in DlC are not deep, making frontside analyses less likely to be successful. D. S. Burnett and A. J. G Jurewicz conducted feasibility studies prior to the present work (Burnett *et al.*, 2007), but the results were not satisfactory.

Specifically, frontside depth profiling with SIMS is non-ideal for measuring near surface implants. Implants must be sufficiently deep to allow time for the secondary ion yield to stabilize. The period of instability at the start of an analysis is commonly referred to as the "transient sputtering region." The frontside sample surface must also be sufficiently clean, such that the contaminant signal dissipates before significant portions of the implant profile are sampled. Otherwise, the contaminants interfere with measurement of the implant.

Frontside depth profiling is such that it requires much less sample preparation than backside depth profiling. Provided that the DlC is in good contact with the SIMS sample holder the conductivity should be sufficient for analysis (in theory). Frontside internal standards are possible with this method (Jurewicz *et al.*, 2008; 2011). However, internal standardization from the front surface of Genesis DlC is primarily reserved for

multi-isotopic elements. Frontside-implanted internal reference ions overlap their solar wind counterparts. Usually a minor isotope is implanted, and a major solar wind isotope is measured, this allows the relative contributions of each to be easily distinguished during SIMS analysis. The measurement process is more complicated and incurs significantly more error for monoisotopic elements, because the solar wind ions are isotopically indistinguishable from the implanted reference ions. In these cases the reference ions must be implanted deeper than the solar wind ions, and model profiles must be applied to distinguish the relative contributions of each. Monoisotopic elements are more efficiently internally standardized by implantation from the back (Appendix D). However, in order to conduct frontside analysis, the sample must be supported from the back. This inherently blocks access to the back surface of the sample, making it impossible to implant reference ions from the backside. Any internal references must be implanted from the frontside if frontside depth profiling is to be used.

2.2.2.2. Backside Depth Profiling of DlC (From DoS Wafers)

Backside analysis is preferred for the measurement of shallow SW profiles (e.g., Heber *et al.*, 2010; 2011; 2012; 2014a; c; Veryovkin *et al.*, 2014). BDP techniques had already been successfully applied to the measurement of minor SW ions in Genesis Si (e.g., Heber *et al.*, 2014c) and DlC collectors (Veryovkin *et al.*, 2014). Starting a solar wind analysis on the backside of the Genesis DlC provides enough time and depth for the sputtering rate to stabilize before sampling ions implanted near the front surface. It is also preferred for the analysis of samples with abundant surface contaminants. Backside contaminant signal dissipates well before solar wind ions are sampled. Figures 1.10 and 1.11 illustrate how BDP allows the signal from severe surface contamination on Genesis

DlC to come down to safe levels before SW Na is sampled. Backside depth profiling also produces clearer profiles because fewer frontside surface contaminants are ion mixed into the solar wind profile. Another advantage of BDP is that it allows for backside-implantation of internal standards. Details are provided in the Backside Implantation section (below).

The primary disadvantage of backside depth profiling is that it requires much additional sample preparation. Although BDP of DlC is similar (in principal) to the commercial technique previously applied to Genesis Si collectors (e.g., Heber *et al.*, 2012; 2014), it is very different in practice. Profiling through hundreds of microns of silicon to reach the backside of the DlC is inefficient, so samples must be thinned. After sample preparation has been performed, the sample is left in a very fragile, and often partly delaminated state.

In summary, SIMS depth profiling in DoS can be performed from the front/top/polished sample surface, as is the traditional approach, or from the backside (this study) if the sample has been thinned by removal of the Si backing (Chapter 1).

2.2.3. Backside Thinning Genesis DoS

To conduct a depth profile from the backside of a DoS wafer most of the backside of the wafer must be removed (e.g., Heber *et al.*, 2010; 2014c). Although this procedure is performed routinely and commercially for Si, it is neither routine nor easy for Genesis DoS. Backside depth profiling DlC requires ultra-thin sections of the collector fragments (<1μm thick), but high internal stresses cause extreme fragility that precludes commercial mechanical thinning procedures.

Thinning is one step among many required to prepare Genesis DoS for backside depth profiling analysis. Samples must be cleaned, mounted, and thinned, and then, if so desired, samples can be implanted with reference ions. The details of steps are reviewed in the following sections.

2.2.3.1. Cleaning

In preparation for thinning, Genesis DoS wafers are cleaned according to procedures provided in Appendix A. Even after cleaning some terrestrial particulates may remain adhered to the DlC surface. If the particulates are large they can potentially warp the DlC film once the Si backing is removed. Some samples require multiple cleanings. Only the cleanest samples may proceed through the following stages of sample preparation.

2.2.3.2. Sample Mounting

Cleaned Genesis DoS is mounted face-down on conductive, chemically resistant substrates. A conductive, chemically resistant, low viscosity, low volatile epoxy or adhesive should be used to adhere the sample to the substrate. Most Genesis DoS samples were mounted in-house on graphite planchets using: M-Bond® 610. A specially designed piston-cylinder-shaped press clamped the sample to the substrate during curing, maintaining proper alignment. After the epoxy had fully cured the samples were ready for thinning.

M-Bond® 610 adhesive was more volatile-rich than anticipated. The epoxy released volatiles that formed small bubbles under and around the samples during curing. The adhesive is also non-conductive, requiring either carbon paint or a gold coat to properly ground a mounted sample for SIMS analysis. Applying these coats puts the

sample at greater risk for acquiring unwanted surface contaminants. Evans Analytical Group commonly uses a low volatile epoxy for mounting Si which does not impede conductivity during BDP of Si. If this epoxy is at least as chemically resist to XeF_2 (used for sample thinning) as M-Bond 610®, it would be an improvement.

Carbon planchets were the most successful substrate investigated here. They were smooth, conductive, and M-Bond 610® epoxy adhered to them well. There was one structural failure, which occurred when a planchet broke in half along a crystallographic plane of weakness as it was being removed from a metal implant target plate, to which it was securely attached by carbon tape. GaAs wafers proved far more fragile. A Genesis DoS sample (60407) had been mounted on a GaAs wafer that broke during cleaning and broke again during sample mounting. The GaAs substrate had to be mounted on a graphite planchet to save the sample. Silicon wafers are commonly used substrates for mounting Genesis Si for thinning, but this material could not be used for supporting Genesis DlC, because it is not resistant to XeF_2 etching used for thinning the samples. Glass slides are non-conductive, making them non-ideal for charge dissipation during SIMS analysis, although gold coating a mounted sample can help overcome this obstacle. Glass substrates were not tested in the XeF_2 etch system, so its suitability as a substrate is uncertain.

2.2.3.3. Removing the Silicon from the DoS

The Si backing needed to be removed from the DoS wafer so that only the ~1 μm thick DlC was left for analysis. The most successful technique was found to be XeF_2 etching. However, all tests and results for different procedures of Si removal attempted are described below. Sample images are presented in Appendix B.

2.2.3.3.1. Chemical Etching Tests

Chemically etching Si with ammonia was among the first methods for thinning DoS tested in this study. DoS samples were placed in ammonia solutions and heated on a hotplate. Although the Si dissolved (slowly), the treatment weakened the epoxy bond between sample and substrate. When the bond was weakened, the sample peeled off. New, well-annealed DlC could be remounted about as easily as remounting plastic cling film, however flight spare DlC that skipped annealing steps would succumb to internal stresses and curl and/or rapidly fracture. Ammonia etching was abandoned.

2.2.3.3.2. Mechanical Thinning Tests

Mechanical thinning was tested, first on modern material and then on flight spare DoS. The modern DlC used for these tests was very well-annealed, so it tolerated mechanical polishing of its Si substrate relatively well with minimal damage. Some DlC was abraded away by shearing, but most survived. With practice, backside thinning of modern DoS by grinding was eventually successful.

In contrast to the well-annealed modern DoS, the flight spare material was less annealed, and consequently backside thinning attempts resulted in many spectacular failures. Physically polishing away the Si on a MiniMet® polisher imparted enough stress to the flight spare DlC film that once most of the Si had been removed, the sample would (with very little provocation) rapidly fracture into dust. A dimple-making tool was used to remove a small patch of Si backing from the DoS in the hope that the remaining Si would keep the sample well-braced. However, in the space where most of the Si was removed, the exposed DlC film bulged outward. The compressive stresses intrinsic to the

DlC had caused the material to delaminate from the substrate at that point. SIMS works best on level surfaces, so this sample preparation approach was also abandoned.

2.2.3.3.3. XeF_2 Etching

Many sample thinning tests were performed on both modern non-flight and flight-era materials before the XeF_2 etching was adopted. To date, the most gentle and efficient method for removing the Si substrate from Genesis DoS has been XeF_2 etching. This technique was developed at Argonne National Lab (ANL; Veryovkin *et al.*, 2014), which has an Xactix® X4 Series™ XeF_2 etch system. Mounted DoS samples were treated with XeF_2 at ANL to etch away the Si that provided the backing for the DlC film ($2XeF_2$ (*vapor*) + Si (*s*) → 2Xe (*g*) + SiF_4 (*g*); Chang *et al.*, 1995; Brazzle *et al.*, 2004; Veryovkin *et al.*, 2014). Sample images are presented in Appendix B.

Following thinning, samples are at risk of delamination from their new substrate. Thinned DlC films are generally less flat due to localized delamination resulting from lingering intrinsic internal stresses and were too fragile to undergo the general cleaning procedure. XeF_2 etching likely imparted some heat to the samples (Chang *et al.*, 1995), which can affect its stability, but compared with other methods for sample thinning this approach greatly minimized stress-related damage and distortion.

There were unidentified compounds that were not removed by the etching process. These were deposited on the backside of the DlC film (Appendix B). This may be the whitish film referred to by Chang *et al.* (1995). In some cases this material could be blown away with compressed air, but it was very difficult to impossible to remove all of it. Attempts to rinse this material off with water only served to adhere it more strongly to the surface. Acetone could dissolve it, but it could also redistribute the components and

redeposit them upon evaporation. The components would then re-bond with the sample surface. Care had to be taken to rinse a sample from the same direction to avoid recontamination of clean areas. Unfortunately, repeated exposure to evaporating acetone created a cooling effect that would induce thermal shocks to the sample/substrate, and/or weaken the epoxy. Repeated thermal shocks of this kind would cause the sample to succumb to internal stresses, break and/or bow outward in localized areas or as part of branching networks (Appendix B).

2.2.3.3.4. Other Experiments

To try to keep the DlC layer intact, and to create separation between the DlC and the Na- and K-rich adhesive underneath, the surfaces of some test DoS were coated with metal using chemical vapor deposition prior to thinning. Although the M-Bond 610 adhesive worked relatively effectively to keep the DoS bonded to a carbon planchet during XeF_2 etching, it could not keep metal-coated DoS affixed (Appendix B). No further attempts were made to coat the DlC surfaces with metal before etching.

2.2.4. Internal Standardization of Genesis DlC

In the present study, calibrated ion implants were used as measurement standards for depth profiling analyses, a practice commonly used by others in the field (e.g., Heber *et al.*, 2014c; Burnett *et al.*, 2015). Details concerning the use of ion implants for calibration of SIMS analyses are provided in Burnett *et al.* (2015). An overview of this method and details concerning how this method was adapted for the present study are provided below.

2.2.4.1. Overview of Internal Standardization of Na and K Measurements in DLC Using Ion Implants

The ideal SIMS reference standard has a matrix chemistry identical to that of the sample. Jurewicz *et al.* (2008; 2011) attributed a solar wind Mg measurement discrepancy between Genesis DoS and Si collectors to matrix effects in hand-made DlC, caused by subtle differences in the DlC between the standard and flight wafer materials. They used an ion implant as an internal standard to resolve this discrepancy. Accordingly, a discrepancy observed between Na measurements in DlC and Si prompted the use of internal standards in the present study. Internal standardization assumes that the matrix of the sample is homogeneous, such that the calibration does not change between measurement of the reference implant and measurement of the sample. In addition to decreasing the likelihood of matrix effects, internal standards can correct for minor sample tilt effects on ion yield. In general, both the sample and the internal standard can be measured simultaneously, or in sequence within the same depth profile, or in neighboring profiles on the same wafer. This makes analyses more efficient, and helps preserve similar analytical conditions between the standard and sample.

Reference ion implantation was performed professionally by Leonard Kroko, Inc. Ion implantation can be performed from either the frontside or backside of DlC. In preparation for ion implantation, samples were cleaned, mounted on a rigid substrates and thinned as needed, and finally mounted onto a conductive target plate using conductive materials (e.g., carbon paint, carbon tape, screws, etc.). Samples were carefully spaced within a 2-inch circle to ensure uniform ion implantation. A series of implants were performed to create standards with a range of fluences (from 1e16atoms/cm^2 to 2e12

atoms/cm^2). High dose implants in DlC were calibrated with Rutherford Backscattering Spectrometry (RBS), and SIMS was used to intercalibrate the high-dose standards with the lower-dose standards.

Frontside and backside ion implantation have inherent advantages and disadvantages, and may require different measurement approaches. These topics are discussed here.

2.2.4.2. Frontside Implantation (i.e., Implantation Through the Solar Wind Collection Surface)

Burnett and Jurewicz used frontside internal standardization for quantifying their solar wind Fe and Mg measurements (A. J. G. Jurewicz; verbal communication, 2013 LPSC). Their method uses a minor isotope reference implant to calibrate the measurement of a major isotope. The isotopic difference allows implant and solar wind profiles to be distinguished during SIMS depth profiling analysis even when they overlap in depth space. However, frontside implantation of internal standards is more challenging when the element of interest is monoisotopic (e.g., Na), as in the present study. If the monoisotopic ion implant and solar wind profiles overlap, then ion implant profile modelling is necessary to estimate the relative abundances of each. Reliance on modelling reduces the precision of front-side internally-standardized analyses of monoisotopic species. For this reason, only two frontside internal standards were made (both Genesis flight DoS).

2.2.4.3. Backside Implantation (I.e. Implantation Through the Side Opposite the Solar Wind Collection Surface)

Backside implantation of reference ions proved to be a useful approach for quantifying implants in homogeneous matrices. Implanting reference ions from the backside of a Genesis DlC sample provided sufficient separation between the reference implant and the solar wind, facilitating integration of Na, a monoisotopic element. Access to the back surface of the DlC film was made possible by the backside thinning procedure required for backside depth profiling. The backside reference ions used in this study were implanted with the proper balance of energy and fluence to 1) avoid interference with the SW, and 2) reduce interference with surface contaminants.

2.2.4.4. Quantification of Solar Wind and Reference Ion Profiles

A brief description of profile analysis methods are provided here; details are provided in Chapter 1. Profile integration was performed according to the methods of Chapter 1. High dose implants in DlC were calibrated with Rutherford Backscattering Spectrometry (RBS), and SIMS was used to intercalibrate the high-dose standards with the lower-dose standards.

Solar wind ion implant models created with the TRIM program within the SRIM software package were used to extrapolate solar wind ion implant profiles through obfuscating surface contamination to the boundary between the flight wafer and the underlying adhesive (see Chapter 1). Note: These solar wind implant models are subject to revision and refinement in accordance with new developments in the field of solar physics. A more basic ion-implant TRIM model, which assumes particles impact a target with equal energy, is best suited for modeling laboratory implants. Thus, a basic model

was used to separate frontside-implanted reference Na from solar wind Na. Only one frontside-standardized measurement was sufficiently clean for this procedure.

The accuracy of all TRIM models is dependent on having a well-characterized sample, and a properly tuned ion beam. Diamond-like carbon can have a range of properties and densities depending on whether it has more graphitic or more diamond-like bonds. If the density varies through a sample, or if it differs between samples the TRIM model may not fit the implant well, leading to integration errors. SIMS ion beam mixing, and changes in sputtering rate during analysis can also cause subtle changes to the measured profile shape, complicating the modelling process.

The Na^+ and K^+ count rates were integrated and normalized to matrix ion count rates to correct for small drifts in primary current. (This approach is inherently limited by the degree to which these ion count rates scale linearly with current.) Ion ratios were corrected for additional background interferences and terrestrial contaminants, as necessary. The background-corrected integrated signal from the reference ions was used to calculate the SIMS instrument's relative sensitivity to the ions of interest. These relative sensitivities were used to quantify the integrated signal from the solar wind to obtain bulk solar wind fluences. Details of this process are provided in Chapter 1.

2.2.5. Sources of Error and Accommodations

There are a variety of sources of error to be expected when analyzing or calibrating both the ion implants and the trace solar wind. In the present study, procedures and analytical techniques were modified to mitigate, minimize, and/or correct for all the anticipated sources of error. These sources of error are described below, and a

summary is provided in Table 2.3. Additional sources of error, discovered as part of the present study, are presented in Results, and discussed in Discussion.

Sample tilting can result in significant measurement error (e.g., Deng and Williams, 1989). Precautions were taken when mounting samples and choosing positions for analyses. Specially-made sample holders were used during SIMS depth profiling analysis to ensure samples and standards were kept in the same position during analysis, facilitating reproducibility. Analyses were performed as close to the center of the sample mount as possible to avoid voltage deflections caused by the sample holder, but care was taken to avoid regions that were damaged, contaminated, irregular, or pre-sputtered. Thus the proximity of a given analysis to the exact center of the holder was often limited by the availability of clean, level, raster-sized spaces free from prior episodes of ion beam sputtering. Variable topography was most common for backside-thinned samples, DlC in particular, which would locally delaminate from its carbon planchet substrate, and warp around surface contaminants, and bubbles in the underlying epoxy. These areas of distortion were avoided, as they tended to adversely affect secondary ion yield, changing the measurement calibration.

The intensity of the SIMS secondary ion signal was adjusted using primary ion beam current, and the size of the analysis area in order to provide adequate counting statistics for low fluence ion implants at high MRP, without incurring significant instrumental dead time. To accomplish this, peak count rates were kept at or below ~1e5 counts/s.

Maintaining proper geometry of SIMS craters is also important, as rough or inclined crater floors reduce depth resolution during SIMS analysis, interfere with

relative ion yield, and complicate crater depth measurements required for ion implant signal integration. Profiling through the sample, and deep into the mounting epoxy (or Si substrate) with an O_2^+ primary beam can create rough crater floors (Appendix H). Most depth profiling analyses in DlC were kept shallow (~1μm) and were conducted using a well-focused primary ion beam. After each analysis session, profilometry and/or interferometry were used to check the topography of crater floors for smoothness.

Where issues were unavoidable, corrections were made as accurately as possible. For example, ion beam mixing of surface contaminants into implant signal was always an issue to some extent. Model implant curves, which represent how ions are distributed after implantation, were used to separate out surface contaminants and estimate missing implant signal. It is important to reiterate, that SIMS profiles differ from these models because of ion beam mixing, and may also differ if there are changes in sputter rate, e.g., from changes in matrix density or other properties. An O_2^+ primary ion beam with low impact energy was used to minimize ion mixing, and limit the depth to which surface contaminants were incorporated into the sample during analysis. Whether the profiles were also subject to charge-driven diffusion, or segregation (Wilson *et al.*, 1989) is unknown.

When signal interference was observed (e.g., from high surface contamination or "rogue" particulates in matrix interiors), the analysis was repeated elsewhere. Signal from contaminants at the annealing layers within DlC samples were estimated and subtracted from ion profiles as part of the background signal. Alternatively, the SW signal would be extrapolated through the contamination to distinguish the relative contributions of each.

Matrix effects observed in high dose implants also required correction. There were localized decreases in matrix ion yield correlating with the depths of the high dose standards (Appendix F). To adjust for this, the matrix ion signal measured in a more stable part of the profile was extrapolated over the "dip." These corrected ion intensities were used for ion normalization.

2.3. Results

Backside depth profile measurements of solar wind Na in Genesis DlC calibrated with backside-implanted *internal* reference Na^+ are consistent with backside depth profile measurements in Genesis DlC calibrated with frontside-implanted *external* reference Na^+ (Fig. 1.14). Na fluence measurements measured by backside depth profiling and calibrated with either external standards or backside implanted standards, are consistently lower in Genesis DlC than in Genesis Si. In contrast, the single solar wind Na measurement (frontside depth profile) calibrated with a frontside-implanted internal reference standard was consistent with Na measurements in Si. When this frontside depth profile measurement was calibrated with an external standard instead of the frontside implanted internal standard, the result was the same within error. Na backside depth profile measurements in Si calibrated with backside-implanted internal standards are (on average) slightly lower than Na backside depth profile measurements in Si calibrated with external standards.

The switch from external to internal standardization did not significantly improve precision or reduce scatter in the Na measurements conducted in either DlC or Si. In

general, precision is better for backside depth profile measurements of Na in DlC than for backside depth profile measurements of Na in Si.

Unlike measurements in DlC, most of the Na fluences measured in Si are consistent with the results of Heber *et al.*, 2014b following calibration of their data. Unlike previous work in which internal standardization immediately mitigated fluence measurement differences between Genesis DoS and Si, or Silicon-on-Sapphire (SoS) collectors (Jurewicz *et al.*, 2008; 2011), the ion implants into Genesis DlC in this study did not resolve a similar measurement discrepancy (SW Na fluence) between DoS and Si. Details are provided in Chapter 1 (Results).

Depth profile measurements of solar wind K in Genesis DlC (both backside and frontside depth profiles) calibrated with either frontside-implanted or backside-implanted *internal* reference K are consistent with depth profile measurements in Genesis DlC calibrated with frontside-implanted *external* reference K (Fig. 1.14). The highest solar wind K fluences measured in DlC are consistent with the lowest solar wind K fluences measured in silicon. The average K fluence measured in DlC is lower than the average K fluence measured in Si (Chapter 1). As for Na, backside depth profile measurements of K in Si calibrated with internally-implanted reference species are (on average) slightly lower than a backside depth profile measurement of K in Si calibrated with an external standard.

There is more scatter among K measurements than among Na measurements due to greater analytical difficulties associated with measuring lower fluence elements. The switch from external to internal standardization did not significantly improve K

measurement precision or reduce scatter in the data. (There are no similar measurements of bulk solar wind Na and K obtained by *in-situ* spacecraft available for comparison.)

2.4. Discussion: Fluence Discrepancy Between Backside Depth Profiles in DlC and Si

Many possibilities were explored to identify the source of the discrepancy. A number of these possibilities are discussed below.

2.4.1. Are There Matrix Differences Between External and Internal Standards?

SW Na measurements in DlC did not depend on the location of the reference ion implants (frontside versus backside; internal versus external). To test whether there was a change in calibration between external standards and the samples, internal standardization via backside ion implantation was implemented. Backside depth profiling analyses conducted in DlC and calibrated with backside-implanted internal standards reproduced the results of backside depth profiling analyses in DlC calibrated with external standards (within error). Thus there is no inherent difference between external and internal standards for DlC.

In contrast, backside depth profiling analyses conducted in Si and calibrated with backside-implanted internal standards produced lower fluences, compared with externally-standardized backside depth profile measurements in Si. However, because of the small data set, additional testing would be necessary to confirm whether there is truly a matrix effect occurring in Si, rather than a surface contamination or modelling issue.

2.4.2. Is There Intrinsic Vertical Inhomogeneity in the DoS Collector Wafers?

Implanting *blank* DlC from the front (external standard) and implanting Genesis DlC from the *blank backside* (internal standard) yield comparable results. Thus, the blank front and backsides of DlC have sufficiently similar matrices.

2.4.3. Was the SIMS Mass Resolving Power Sufficient?

Mass interferences have the potential to artificially increase the measured signal. The likelihood that an interfering molecular ion forms increases as 1) the abundances of the isotopes composing the molecule increase, 2) the number of atoms in the molecule decreases, and 3) the charge on the molecule decreases. It is critical that interferences be eliminated wherever possible, or else reduced through the adjustment of SIMS instrument parameters such that the measured signal from these interfering species is not a significant contribution to the overall measurement. $^{30}Si^{16}O^{2+}$ was unresolvable from ^{23}Na, potentially leading to higher SW "^{23}Na" signal in Genesis Si matrices in the vicinity of the SW O implant. However, this is not likely to be a significant effect, because the primary O_2^+ beam saturates the Si with ^{16}O throughout the profile, so the formation of any significant $^{30}Si^{16}O^{2+}$ should be observed in the general background and be subtracted. Unless SW radiation damage increases the production of $^{30}Si^{16}O^{2+}$ in the vicinity of the SW radiation damaged zone only, this is not the cause of the discrepancy.

The most abundant element in the solar wind is hydrogen. This SW H is concentrated in the near-surface of the collector wafers (Fig. 1.15). Two H-containing molecular ions potentially causing the greatest mass interference with ^{23}Na measurement in Si are $^{29}Si^{16}O^{1}H^{2+}$ (MRP: 151,586) and $^{28}Si^{16}O^{1}H_2^{2+}$ (MRP: 5,781). Whether these

molecular ions (or others) are sufficiently abundant to cause significant mass interfences remains to be tested. $^{29}Si^{16}O^{1}H^{2+}$ is unresolvable from ^{23}Na with current methods.

2.4.4. Did the DlC Lose Na or K?

If Na and K diffused out of the DlC it would explain the discrepancy. However, DoS collectors were selected for analysis primarily because DlC retains volatile elements more effectively than other Genesis collector materials when heated (Aisenberg and Chabot, 1971; Vainonen *et al.*, 1997; Heber *et al.*, 2009). Experiments suggest that Na does not readily diffuse in either DlC (<127 °C), or Si <500 °C (Aisenberg and Chabot, 1971; Wang *et al.*, 1997; respectively). There is no evidence that more mobile elements (e.g., He) move in Genesis DlC (Heber *et al.*, 2009). The profile peak shapes measured in the present study are as sharp as expected from theoretical models (i.e., the profiles do not appear level or "stretched out"). The profiles of annealing features are also sharp. The shapes of the profiles suggest there was no diffusive redistribution of ions. Heber *et al.* (2014a) agrees that there is no evidence for diffusive loss of Na.

2.4.5. Is Charge-Driven Diffusion, Segregation, or Preferential Sputtering of Na and K Occurring?

Charge-driven diffusion, segregation, and preferential sputtering are three processes that can interfere with accurate depth profile measurements. Charge-driven diffusion may occur in materials that charge under an incident ion beam (Wilson *et al.*, 1989). Whether charge-driven diffusion can occur in DlC is speculative, but DlC can become less conductive as the number of diamond-like (sp^3) bonds increases, so charge-driven diffusion is theoretically possible, but would require additional testing to verify whether it may have affected the results of the present study.

Segregation occurs when a species in a multi-element solid increases in concentration at the surface, because it is a site of lower chemical potential than the bulk of the sample (Wilson *et al.*, 1989). This effect can result from ion beam mixing, or the adsorption of oxygen (Williams and Baker, 1981). Si atoms, for example, readily react with surface oxygen, and may segregate to the surface of a sample (Wilson *et al.*, 1989). Segregation of Na can be reduced by profiling with an oblique angle of incidence and a low primary ion beam energy (Wilson *et al.*, 1989). Sputter angle could not be directly adjusted in the present study, so this was not a viable option for the present study. With the use of an O_2^+ primary ion beam, segregation may become significant if the primary beam incidence angle is sufficiently low to promote surface oxide layer formation (Wilson *et al.*, 1989). It is unknown to what degree surface oxides formed in these samples or whether segregation significantly affected the results of the present study.

Enrichment of one species in the surface due to a low partial sputtering yield, i.e., preferential sputtering, is not likely to be affecting the results from the present study, because the use of matrix-matched standards should have calibrated for this effect (Wilson *et al.*, 1989).

2.4.6. Is the Solar Wind Inducing Matrix Effects?

External and internal standardization suggest that the front- and backsides of blank DlC are inherently identical. However, Genesis solar wind collectors are no longer "blank" on their frontsides. Initially, when a solar wind Na measurement calibrated with frontside-implanted reference ions reproduced the results from Si, it suggested that solar wind was causing matrix effects in the frontside region. However, a frontside implanted

external standard corroborated the measurements! Thus, SW-induced matrix effects were not affecting the calibration significantly.

Ideally, a similar test should be performed on the Genesis Si used for comparison. Frontside-standardization of Genesis Si for Na and K measurement has not yet been performed, primarily because surface contamination, broader implant peaks, and deep ion beam mixing make model curve fitting and accurate integration particularly challenging. If sufficiently clean surfaces can be achieved to permit reliable measurements, it would likely help assess whether matrix effects dominated the measurements in Si instead of the measurements in DlC.

2.4.7. Are the Data Corrections Accurate?

Given the prevalence of surface contamination, ion beam mixing and uneven breakthrough at the collector-epoxy interface, another possible factor is that frontside surface contamination correction methods are too lax for both Si and frontside depth profiles in DlC, or that they under-correct for missing profile in DlC. However, Na profiles in Si by Heber *et al.* (2014b), are very clean (Heber *et al.*, 2014a), and yet yield higher fluences than any of the backside depth profiles conducted in DlC in the present study. It is unlikely that contamination of Si profiles is the primary or sole cause the discrepancy.

Curve matching to model profiles is used for all analyses to restore the part of each profile that is lost at the sample-epoxy interface (Fig. 1.12). However, these models continue to undergo refinement, and modelling what happens near the surface may be difficult if there are few ultra-high resolution depth profiles against which to check the model for near-surface accuracy.

As previously mentioned, TRIM profiles do not adjust for changes in sputtering rate, ion beam mixing, segregation effects, or charge driven ion diffusion. If changes in sputter rate are not recognized, non-linear sputtering over the peak of the implant would skew the calculated solar wind fluence. After the initial transient sputtering region, any changes in ion yield produced by changing matrix chemistry could not be distinguished from primary beam effects, so it is unclear whether there were matrix-related sputter rate changes with depth in Genesis DlC. The fact that backside analyses in DlC were more reproducible than measurements in Si suggests that any lateral matrix inhomogeneity in DlC had a relatively limited effect on measurements in DlC.

The ability to properly model the profiles may be related to the direction from which the depth profile was conducted. Would a frontside-standardized SW Na measurement conducted with backside depth profiling yield a high fluence like the frontside depth profile in this study, or a low fluence, like the other backside depth profiles of Na in DlC? Answering this question may help pinpoint whether there is a systematic error affecting the DlC analyses.

2.5. Summary and Conclusions: Use of DoS for SIMS Analyses

There are a number of analytical advantages and disadvantages of Genesis DoS for solar wind Na and K measurement. The present study demonstrates that both frontside and backside analysis of Genesis DlC is possible, and that the location of the reference ions (external or internal, frontside-implanted or backside-implanted) does not affect Na or K measurements in DlC.

A disadvantage is that there is a persistent, unresolved measurement discrepancy between backside depth profiles in DlC and Si. The most likely explanation for disagreement between fluences measured in DlC and Si is that they are limited by the accuracy of the implant models used for integration and surface contamination subtraction. Other contributing factors may include mass interferences, charge-driven diffusion, and segregation. Additional investigations are necessary to determine the exact cause(s) of the observed discrepancy.

Table 2.1. Advantageous Material Properties of DoS Relevant to SIMS Analyses of Genesis Solar Wind.

Table 2.1. Advantageous Material Properties of DoS Relevant to SIMS Analyses of Genesis Solar Wind.

Property	Relevance
Low backscatter	Nearly all incident solar wind implants into the wafers; implants provide representative solar fluences
Low diffusivity (Heber *et al.*, 2009)	Highest retention of implanted solar wind of all collector array materials
Hard (scratch resistant)	Smooth collection surfaces available for SIMS analysis despite damage from crash
Chemically resistant to cleaning reagents and XeF_2	Easy to remove terrestrial contaminants, and thin samples for SIMS backside depth-profiling analysis without damaging the collection surface (details in Chapter 1 and Appendix A)
Relatively dense (2.7-3.2 g/cm^3)	Ion stopping power produces sharp implant profiles, and minimizes ion beam mixing of surface contaminants into implant profiles during SIMS analysis
Matrix C bonds with H	Reduces the production of secondary inorganic hydrides during SIMS analysis, thereby reducing some potential sources of mass interference
Matrix is relatively pure with respect to ^{24}Mg	Minimal mass interferences with the matrix species ^{12}C, so this isotope can be easily monitored during SIMS analysis. Solar wind $^{24}Mg^{2+}$ can be easily resolved from matrix ^{12}C with 1600 MRP
Semiconductive	Theoretically, allows for charge dissipation during SIMS analysis without the need for gold- or carbon-coating samples (debatable)

Table 2.2. Disadvantageous Material Properties of DoS Relevant to SIMS Analyses of Genesis Solar Wind.

Table 2.2. Disadvantageous Material Properties of DoS Relevant to SIMS Analyses of Genesis Solar Wind.

Property	Relevance
Matrix carbon may bond with implanted species	Some carbides formed during sputtering are mass interferences
Terrestrial contamination at annealing steps and embedded contaminant particles	Internal contamination complicates background subtraction and profile integration. Significant interferences require reanalysis in a new location.
Lateral inhomogeneity	Analytical dead spots, secondary ion yields diminished
High internal stress	Exceedingly fragile, limits sample preparation

Table 2.3. General Sources of SIMS Measurement Error.

Table 2.3. General Sources of SIMS Measurement Error.

Source	Method for Mitigation	Error
Counting statistics	Analyzed area must be large enough to compensate for low yield resulting from low fluences and high mass resolving power	<4%
Dead time	Count rate of highest-fluence implant kept ≤ ~1e5 counts/s to avoid significant count losses	< a few percent
Sample orientation (specific to external standardization)	Specially-made sample holders ensured samples and standards were kept in the same position during analysis, which helped ensure reproducibility	see Deng and Williams (1989)
Analysis position in SIMS sample holder (specific to external standardization)	In general, analyses were performed in the center of the mounted sample to avoid voltage deflections caused by the sample holder. Terrestrial surface contaminants, sample topography, and prior analyses limited how close to center the analyses could be performed.	NA
Sample topography	Only the most level regions were analyzed to avoid possible distortions of the energy field, and ion deflections	NA
Crater floor morphology	Samples were thinned to keep profiles shallow, reducing the likelihood of developing rough crater floors. The primary ion beam was tuned to be as sharp and uniform as possible.	see Wilson *et al.* (1989)
Ion beam mixing	The impact energy was kept low to reduce the depth of ion beam mixing of surface contaminants into implant signal. This, in turn, facilitated use of ion implant models to separate the signal from ion implants from that of surface contaminants.	Generally, <30%
Contaminant signal from surface, annealing interlayers, and other embedded particulates	For low levels of contamination, background was subtracted from the integration. For high levels of contamination, the analysis was aborted and another attempt was made elsewhere.	Variable
Matrix effects from high-dose implants	The matrix ion signal measured in a more stable part of the profile was extrapolated over the affected region. These corrected ion intensities were used for ion normalization.	Up to ~20%

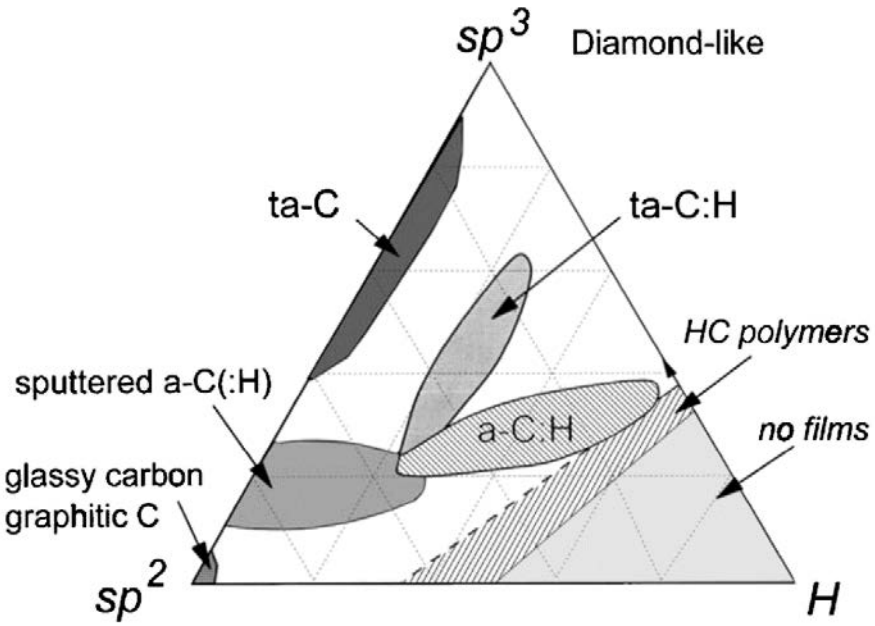

Fig. 2.1. Ternary Phase Diagram of Bonding in Amorphous Carbon-Hydrogen Alloys from Robertson (2002).

The Genesis Mission used ta-C (tetrahedral amorphous carbon) to make the DoS solar wind collectors.

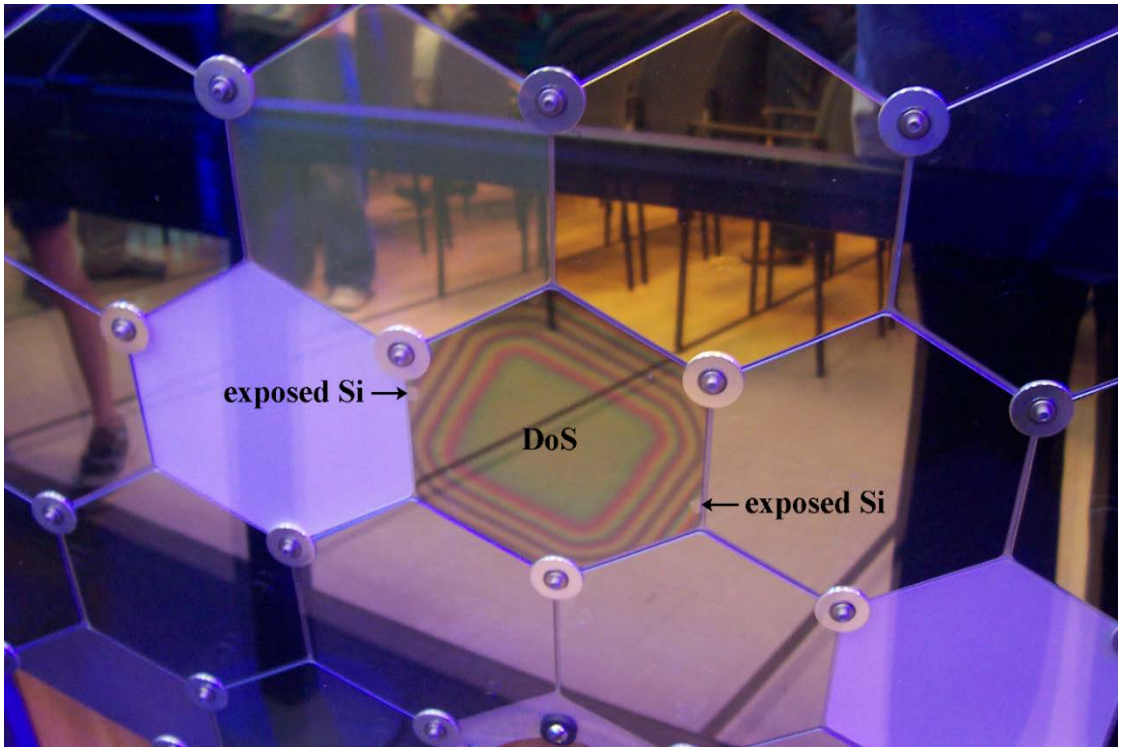

Fig. 2.2. A Non-Flight Genesis DoS Wafer Produced by Sandia National Laboratories.

The appearance of "Newton's Rings" in DlC can be used to identify regions of uniform thickness and provide evidence of strain resulting from localized internal stresses. Similar ring patterns appear in Genesis Si (e.g., 60824; Appendix B). Disruptions in the ring pattern along the outer edge of the DoS wafer featured here are places where the fragile DlC film has flaked off, exposing the Si backing. This DoS wafer is one of the flight spare wafers used for the Genesis spacecraft mock-up. Each hexagon is ~10 cm corner to corner. All the DoS flight wafers were shattered upon landing.

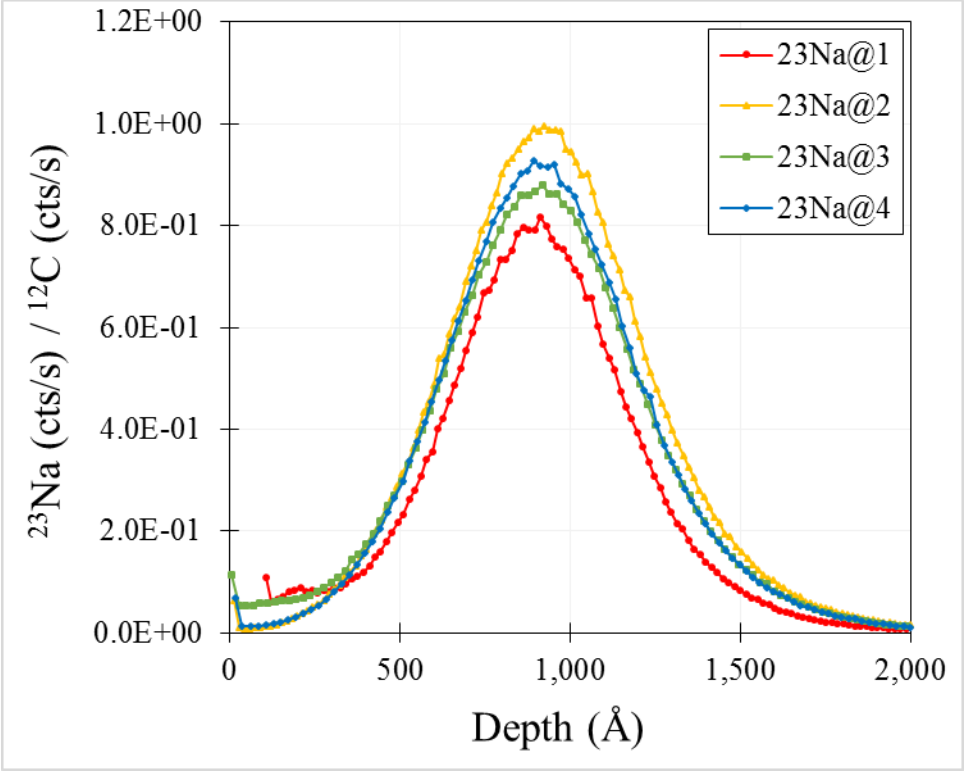

Fig. 2.3. The ^{23}Na/^{12}C Measured in a DlC Standard ("3e13 DoS").
The ratio varies by location. Compare with Fig. 2.4.

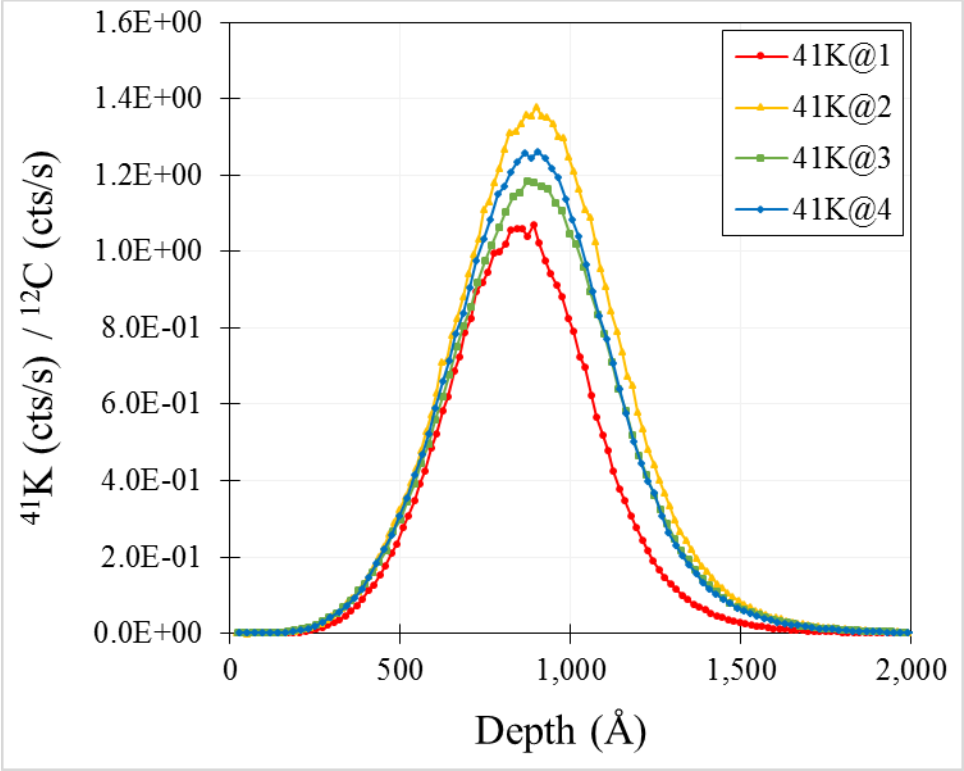

Fig. 2.4 The $^{41}K/^{12}C$ Measured in a DlC Standard ("3e13 DoS").
The ratio varies by location. Compare with Fig. 2.3.

2.6. Acknowledgements

This work has been supported in part by NASA grant #NNX09AC35G (D. S. Burnett and A. J. G. Jurewicz), and the NASA Earth and Space Science Fellowship 2012-13, 2013-14, and 2014-15 (R. L. Hervig and K. D. Rieck). Use of the Center for Nanoscale Materials at Argonne National Laboratory was supported by the U.S. Department of Energy, Office of Science, Office of Basic Energy Sciences, (Contract #DE-AC02-06CH11357). F. Stevie and V. Heber provided use of their standards. C. T. Olinger provided solar wind ion implant models. I. V. Veryovkin & C. Miller provided XeF_2 etching assistance. The Genesis curation team at Johnson Space Center provided the samples. Leonard Kroko Inc. performed the ion implantation. Evans Analytical Group performed the Si collector thinning.

Special thanks to advisors, staff, and colleagues in the Center for Meteorite Studies (ASU), the W. M. Keck Foundation Laboratory for Environmental Biogeochemistry (ASU), Secondary Ion and Mass Spectrometry Lab (ASU), the Caltech Microanalysis Center, the UCLA MegaSIMS Laboratory, the LeRoy Eyring Center for Solid State Science (ASU), and the NanoSIMS Facility (ASU).

2.7. References for Chapter 2

Aisenberg S. and Chabot R. 1971. Ion-Beam Deposition of Thin Films of Diamondlike Carbon. *Journal of Applied Physics* 42:2953-2958.

Alam T. M., Friedmann T. A., and Jurewicz A. J. G. 2002. Solid State ^{13}C MAS NMR Investigations of Amorphous Carbon Thin Films. In *Thin Films: Preparation, Characterization, Applications*, edited by Soriaga M. P., Stickney J., Bottomley L. A., and Kim Y.-G. New York: Springer, US. pp. 277-289.

Allton J. H., Kuhlman K. R., Allums K. K., Gonzalez C.P., Jurewicz A. J. G., Burnett D. S., and Woolum D. S. 2015. Genesis Solar Wind Sample 61422: Experiment in Variation of Sequence of Cleaning Solvent for Removing Carbon-Bearing Contamination (abstract 1896). 46th Lunar and Planetary Science Conference.

Allums K. K., Gonzalez C. P., Kuhlman K. R., and Allton J. H. 2015. Enhanced Cleaning of Genesis Solar Wind Sample 61348 for Film Residue Removal (abstract 2024). 46th Lunar and Planetary Science Conference.

Brazzle J. D., Dokmeci M. R., and Mastrangelo C. H. 2004. Modeling and Characterization of Sacrificial Polysilicon Etching Using Vapor-Phase Xenon Difluoride. *Institute of Electrical and Electronics Engineers Micro Electro Mechanical Systems (Maastricht, The Netherlands, 2004)*. pp. 737-740.

Burnett D. S., Barraclough B. L., Bennett R., Neugebauer M., Oldham L. P., Sasaki C. N., Sevilla D., Smith N., Stansbery E., Sweetnam D., and Wiens R. C. 2003. The Genesis discovery mission: Return of solar matter to Earth. *Space Science Reviews* 105:509–534.

Burnett D. S., Woolum D. S., Jurewicz A. J. G., McKeegan K. D., and Guan Y. 2007. Solar Wind Elemental Abundances from Genesis Collectors (abstract #1843). 38th Lunar and Planetary Science Conference.

Burnett D. S., Jurewicz A. J. G., Woolum D. S., Wang J., Paque J. M., Nittler L. R., McKeegan K. D., Humayun M., Hervig R., Heber V. H., and Guan Y. 2015. Ion Implants as Matrix-Appropriate Measurement Standards for Geochemical Ion Probe Analyses. *Geostandards and Geoanalytical Research* 39:265-276.

Chang F. I., Yeh R., Lin G., Chu P. B., Hoffman E., Kruglick E. J. J., and Kristofer S.J. Pister Gas-phase silicon micromachining with xenon difluoride. 1995. *SPIE* 2641:117-128.

Cho S., Chasiotis I., Friedmann T. A., and Sullivan J. P. 2005. Young's modulus, Poisson's ratio and failure properties of tetrahedral amorphous diamond-like carbon for MEMS devices. *Journal of Micromechanics and Microengineering* 15:728–735.

Chu P., Chen J., Chu P., Lin G., Huang J., Warneke, B, and Pister, K. 1997. "Controlled Pulse-Etching with Xenon Difluoride," Int. Conf. Solid State Sensors and Actuators, (Transducers 97), pp. 665-668.

Deng R.-C. and Williams P. 1989. Factors Affecting Precision and Accuracy in Quantitative Analysis by Secondary Ion Mass Spectrometry. *Analytical Chemistry* 67:1946-1948.

Friedmann T. A., McCarty K. F., Barbour J. C., Siegal M. P., and Dibble D. C. 1996. Thermal stability of amorphous carbon films grown by pulsed laser deposition. *Applied Physics Letters* 68:1643-1645.

Friedmann T. A., Sullivan J. P., Knapp J. A., Tallant D. R., Follstaedt D. M., Medlin D. L., and Mirkarimi P. B. 1997. Thick stress-free amorphous-tetrahedral carbon films with hardness near that of diamond. *Applied Physics Letters* 71:3820-3822.

Goreva Y. G., Allums K. K., Gonzalez C. P., Jurewicz A. J., Burnett D. S., Allton J. H., Kuhlman K.R., Woolum D. 2015. Genesis Solar Wind Collector Cleaning Assessment: Update on 60336 Sample Case Study (abstract #2333). 46th Lunar and Planetary Science Conference.

Gottimukkala R. 2005. Growth and characterization of diamond and diamond like carbon films with interlayer. *M.S. thesis, Graduate School Theses and Dissertations, University of South Florida, Tampa, Florida, United States.* Paper 2904. http://scholarcommons.usf.edu/etd/2904.

Heber V. S., Wieler R., Baur H., Olinger C. T., and Burnett D. S. 2009. Noble gas composition of the solar wind as collected by the Genesis mission. *Geochimica et Cosmochimica Acta* 73:7414–7432.

Heber V. S., Guan Y., Jurewicz A. J. G., Kallio A. P., Olinger C., Woolum D. S., McKeegan K. D., and Burnett D. S. 2010. Solar Wind Elemental Fractionation: Genesis C and O Fluences by Backside SIMS Profiling – Preliminary Data. (abstract #2234). 41st Lunar and Planetary Science Conference.

Heber V. S., Guan Y., Jurewicz A. J. G., Smith S., Olinger C., McKeegan K. D., and Burnett D. S. 2011. Abundances of Carbon, Nitrogen and Oxygen in the Solar Wind Measured by Backside SIMS Depth Profiling (abstract #2642). 42nd Lunar and Planetary Science Conference.

Heber V. S., Jurewicz A. J. G., Janney P., Wadhwa M., McKeegan K. D., and Burnett D. S. 2012. Magnesium Isotopic Composition of Solar Wind as Test for Isotopically Fractionated Solar Wind: A Progress Report (abstract # 2921). 43rd Lunar and Planetary Science Conference.

Heber V. S., McKeegan K. D., Smith S., Jurewicz A. J. G., Olinger C., Burnett D. S., and Guan Y. 2014a. Accurate Analysis of Shallow Solar Wind Ion Implants by SIMS Backside Depth Profiling (abstract #1203). 45th Lunar and Planetary Science Conference.

Heber V. S., McKeegan K. D., Bochsler P., Duprat J., and Burnett D. S. 2014b. The Elemental Composition of Solar Wind with Implications for Fractionation Processes during Solar Wind Formation (abstract #2117). 45th Lunar and Planetary Science Conference.

Heber V. S., McKeegan K. D., Burnett D. S., Duprat J., Guan Y., Jurewicz A. J. G., Olinger C. T., and Smith S. P. 2014c. Accurate analysis of shallowly implanted solar wind ions by SIMS backside depth profiling. *Chemical Geology* 390:61–73.

Jurewicz A. J. G., Burnett D. S., Wiens R. C., Friedmann T. A., Hays C. C., Hohlfelder R. J., Nishiizumi K., Stone J. A., Woolum D. S., Becker R., Butterworth A. L., Campbell A. J., Ebihara M., Franchi I. A., Heber V., Hohenberg C. M., Humayun M., McKeegan K. D., McNamara K., Meshik A., Pepin R. O., Schlutter D., and Wieler R. 2003. The Genesis Solar-Wind Collector Materials. *Space Science Reviews* 105:535-560.

Jurewicz A. J. G., Burnett D. S., Woolum D. S., McKeegan K. D., Guan Y., and Hervig R. 2008. Solar Elemental Abundances from Genesis Collectors: Fe/Mg, Constraining Solar-Wind FIP Fractionation, and Comparisons with CI Chondrites (abstract # 2272). 39th Lunar and Planetary Science Conference.

Jurewicz A. J. G., Hervig R., Burnett D. S., Wiens R., Wadhwa M., and Rieck K. 2009. Fractionation of Mg Isotopes between the Sun's Photosphere and the Solar Wind (contribution # 5422). 72nd Annual Meteoritical Society Meeting.

Jurewicz A. J. G., Burnett D. S., Woolum D. S., McKeegan K. D., Heber V., Guan Y., Humayun M., and Hervig R. 2011. Solar-Wind Fe/Mg and a Comparison with CI Chondrites (abstract # 1917). 42nd Lunar and Planetary Science Conference.

Luo J. K., Fu Y. Q., Le H. R., Williams J. A., Spearing S. M. and Milne W. I. 2007. Diamond and diamond-like carbon MEMS. *Journal of Micromechanics and Microengineering* 17:S147–S163.

Outka D. A., Hsu W. L., Boehme D. R., Yang N. Y. C., Ottesen D. K., Johnsen H. A., Headley T. J., and Clift W. M. 1994. Compilation of Diamond-Like Carbon Properties for Barriers and Hard Coatings. *Sandia Report*, SAND94-8219, UC-404.

Rieck K. D., Jurewicz A. J. G., Wadhwa M., Burnett D. S., Hervig R., and Wiens R. 2010. SIMS Measurements of Mg Isotopes in the Solar Wind (abstract #2391). 41st Lunar and Planetary Science Conference.

Robertson. J. 2002. Diamond-like amorphous carbon. *Materials Science and Engineering* R 37:129-281.

Sinha D. 2002. Correlating Chemical and Water Purity to the Surface Metal on Silicon Wafer during Wet Cleaning Process. *Chemical Engineering Communications* 189:974-984.

Vainonen E., Likonen J., Ahlgren T., Haussalo P., Keinonen J., and Wu C. H. 1997. Hydrogen migration in diamond-like carbon films. *Journal of Applied Physics* 82: 3791-3796.

Veryovkin I. V., Zinovev A. V., Tripa C. E., and Burnett D. S. 2014. Depth Profiling of Genesis Diamond-on-Silicon Collectors: Direct Comparison between Frontside and Backside Approaches (abstract #2795). 45th Lunar and Planetary Science Conference.

Waeselmann N., Humayun M., Goreva Y. S., Burnett D. S., and Jurewicz A. 2015. Impact of Acid-Cleaning on the Solar Wind Layer of Genesis Flight Wafers – Partial Dissolution and Recovery of the Lithium-6 Implant (abstract #1266). 46th Lunar and Planetary Science Conference.

Williams P. and Baker J. E. 1981. Implantation and Ion Beam Mixing in Thin Film Analysis. *Nuclear Instruments and Methods* 182-183:15-24.

Wilson R. G., Stevie F. A., and Magee C. W. 1989. Secondary ion mass spectrometry: A practical handbook for depth profiling and bulk impurity analysis. New York: John Wiley and Sons, Inc. 384 p.

3. CHAPTER 3 – PREFACE

PHASE TRANSFORMATION IN OLIVINE:

A MICROTEXTURAL ANALYSIS

Deep focus earthquakes have been attributed to rapid transformation of metastable olivine within the mantle transition zone (MTZ). However, the presence of water acts to overcome metastability, promoting phase transformation in olivine, and there is evidence to suggest the mantle contains abundant H_2O (Bell and Rossman, 1992; Bai and Kohlstedt, 1992; Kohlstedt *et al.*, 1996; Pearson *et al.*, 2014). A microtextural analysis of olivine phase transformation products was conducted to test the feasibility for subducting olivine to persist metastably to the MTZ. At 18 GPa, transformation of the metastable olivine phase occurs as intracrystalline or rim nucleation, and shifts from ringwoodite to ringwoodite-wadsleyite nucleation with decreasing water content within olivine grains. To provide accurate predictions for olivine metastability at depth, olivine transformation models must take into account how changing water distributions lead to complex changes in strain and phase stability within different parts of a transforming olivine grain.

3.1. Introduction

3.1.1. Subducting Oceanic Lithosphere and Deep Focus Earthquakes

Olivine ($(Mg,Fe)_2SiO_4$) is a primary component of the oceanic lithosphere. Olivine has two high pressure polymorphs: ringwoodite and wadsleyite (Fig. 3.1). In subduction zones, lithospheric olivine is transported to depths where high pressure-temperature (P-T) conditions transform it to these polymorphs. If the descending slab is moving sufficiently fast to maintain a cold interior to depth, the transformation kinetics may proceed so slowly that olivine can persist metastably to ~400-700 km (Liu and Yund, 1995; Sung and Burns, 1976a). If so, metastable olivine phase transformations in the mantle transition zone (MTZ) might help explain some deep focus earthquakes (Liu and Yund, 1995; Sung and Burns, 1976b; Kirby *et al.*, 1996; Green II *et al.*, 2010; Fig. 3.2.). However, hydrogen enhances olivine transformation kinetics (e.g., Hosoya *et al.*, 2005; Kubo *et al.*, 1998; Diedrich *et al.*, 2009; Du Frane *et al.*, 2013), such that only olivine with less than 75 ppmw H_2O would be likely to survive metastably to the depth of the MTZ in the core of a cold subducting slab (Du Frane *et al.*, 2013).

3.1.2. Olivine Transformation Mechanisms

Burnley and Green (1989) proposed that the transformation of olivine to a high-pressure phase can occur by two different mechanisms, depending on the level of nonhydrostatic stress in the system. The first of these mechanisms was originally proposed by Sung and Burns (1976a; 1976b), and later demonstrated by Vaughan *et al.* (1982). It entails nucleation by an incoherent, diffusion-dependent, intracrystalline mechanism under hydrostatic pressure or low stresses and sufficiently high temperatures. The second mechanism, predicted by Poirier (1981), entails a shear-induced,

intracrystalline mechanism under high stresses. This second mechanism is a pseudo-martensitic mechanism that involves shear of the olivine oxygen sublattice followed by a rearrangement of the cations, known as syncroshear (Poirier, 1981).

Green and Burnley (1989) proposed that lens-like nucleation of olivine polymorphs formed in a similar manner as "anti-cracks," a term coined by Fletcher and Pollard (1981) to describe the stresses and displacements associated with stylolites. Burnley *et al.* (1991) later used this concept to explain transformational processes occurring in descending slabs. Investigations of the kinetics of olivine polymorph phase transformations (e.g., Sung and Burns, 1976b; Rubie and Ross, 1994; Kirby *et al.*, 1996) suggest that it is possible for olivine to exist metastably to the transition zone, and that transformational faulting may be linked to the occurrence of deep focus earthquakes.

3.1.3. The Effect of H_2O on Transformation

Olivine transformation to high pressure phases occurs at grain boundaries (forming rims), and within grains (intracrystalline nucleation). These high pressure phases are denser than olivine, and so they occupy less volume. If the reaction rim cannot deform fast enough (e.g., if the rim is too thick or rigid) to accommodate the volume reduction of the reaction, misfit strain (or elastic strain) increases along the interface between the olivine core and the transformed rim, slowing the reaction over time (Kerschhofer *et al.*, 1998; Liu *et al.*, 1998). Small amounts of H_2O can decrease misfit (elastic) strain and the activation energy necessary for the growth of high pressure phases. Elastic strain is reduced when H preferentially partitions into the ringwoodite (e.g., Diedrich *et al.*, 2009) and wadsleyite (e.g., Young *et al.*, 1993), facilitating transformation either by 1) mechanically weakening the rim and allowing it to deform

(e.g., Kubo *et al.*, 1998; Diedrich *et al.*, 2009), or 2) aiding diffusion across the growth interface (Rubie, 1986). This strain reduction can substantially increase the rate of transformation and eliminate time-dependent growth rates. Consequently, rims develop more rapidly for hydrous samples than for anhydrous ones (Du Frane *et al.*, 2013).

3.1.4. Mineralogy of the Transformation Rims

Elastic strain not only regulates the growth rates of transformation rims, it also controls the mineralogy of the rims. Hydrous olivine in the ringwoodite stability field forms rims primarily of ringwoodite (Diedrich *et al.*, 2009). As the rim increases in thickness, its H_2O content decreases, elastic strain energy builds, and the rate of transformation decreases (e.g., Mosenfelder *et al.*, 2001; Diedrich *et al.*, 2009; Du Frane *et al.*, 2013). When the H_2O available for rim growth reaches critically low levels, anhydrous growth conditions set in at the core-rim boundary. Nominally anhydrous olivine transforming in the ringwoodite stability field (18-20 GPa) initially nucleates ringwoodite rims, but later nucleation of wadsleyite at the transformation boundary becomes more energetically favorable (Kerschhofer *et al.*, 1998; 2000). The wadsleyite is metastable relative to external reaction conditions, but is stabilized by the pressure drop at the core-rim boundary (Liu *et al.*, 1998).

3.1.5. Purpose of This Study

Both Diedrich *et al.* (2009) and the Du Frane *et al.* (2013) measured reaction rim thickness to determine how hydration affects growth rates, but neither conducted a detailed micromineralogical characterization of the run products to investigate how transformation mechanisms change with H_2O availability. The rim micromineralogy can reveal the conditions under which the reaction shifts from nucleating ringwoodite to

nucleating wadsleyite. The core micromineralogy can reveal how H_2O affects intracrystalline nucleation and how this relates to rim growth. This study characterizes the micromineralogy of the experimental samples of Diedrich *et al.* (2009) and Du Frane *et al.* (2013) for the purpose of better understanding the role of water in the evolution of the olivine-ringwoodite/wadsleyite transformation mechanisms over the course of the reaction.

3.2. Methodology

3.2.1. Samples

San Carlos olivine spheres (samples #BB3xx and #BB5xx-BB7xx) were prepared by Diedrich *et al.* (2009) and Du Frane *et al.* (2013), respectively. Spheroids were milled to 425-500 μm diameter in a Bond-type air mill similar to that of Nitkiewicz and Sterner (1988). Hydrous (~289±72 ppm D_2O and ~75±15 ppm H_2O) and "nominally anhydrous" spheres were investigated. Mantle olivine, and San Carlos olivine in particular, is intrinsically dry (e.g., mantle olivine H_2O: 1-50 ppmw, Bell and Rossman, 1992; San Carlos olivine H_2O: 4ppm, Li *et al.*, 2008; San Carlos olivine H_2O: 0.3(1) ppmw, Mosenfelder *et al.*, 2011; <30 ppmw, Chen *et al.*, 2011). Hydration of olivine spheres was performed by Diedrich *et al.* (2009) and Du Frane *et al.* (2013) using end-loaded and non-end-loaded (Quick-Press) piston cylinders, respectively. Olivine was hydrated at 950 °C and either 3.5 GPa (Diedrich *et al.* 2009) or 2 GPa (Du Frane *et al.*, 2013) for 48 hrs. Samples referred to as "nominally anhydrous" are those that did not undergo this hydration process. The D_2O and H_2O abundances for the hydrous samples were given by Diedrich *et al.* (2009) and Du Frane *et al.* (2013), respectively.

3.2.2. Transformation

Both hydrous and nominally anhydrous grains were transformed within a COMPRES 10/5 assembly (Diedrich *et al.*, 2009; Leinenweber *et al.*, 2012) using a 1,100-ton multianvil press at Arizona State University (Diedrich *et al.,* 2009; Du Frane *et al.*, 2013). The COMPRES 10/5 assembly consists of a ceramic H_2O-free MgO + $MgAl_2O_4$ octahedron (Leinenweber *et al.*, 2006) outfitted with a hole into which a $LaCrO_3$ insulating sleeve and rhenium foil furnace are inserted. Inside the furnace, is a silver capsule with an MgO sleeve. The silver capsule holds two olivine spheres, separated by silver shavings. The capsule seals under pressure, preventing water loss. A thermocouple (7 mil, type-C wire) in alumina tubing with an MgO sleeve is positioned coaxially with the rhenium furnace. The hot junction is separated from the silver capsule by an alumina disk. MgO and zirconia plug the opposite end of the hole. Details are available in Diedrich *et al.* (2009).

All the samples selected for this study had been transformed in the ringwoodite stability field at 18 GPa and either 900 °C or 1100 °C. Diedrich *et al.*, (2009) observed a 4 °C temperature gradient across the transformation capsule lengthwise, and only 1 °C along its width.

3.2.2.1. Hydrous Contamination

The initial transformation runs of Du Frane *et al.* (2013) were prone to small H_2O gains (~0-80 ppmw), associated with the source and preparation of the silver capsules used for transformation. This initial approach is hereafter referred to as “Method 1.” The only samples produced using Method 1 that were included in the present study are the

following: BB621 (nominally anhydrous), BB527A (nominally ~75 ppmw), and BB583 (nominally ~75 ppmw).

Du Frane *et al.* (2013) later modified their experimental procedure (hereafter referred to as "Method 2") to exactly match that of Diedrich *et al.* (2009). Modifications included: 1) eliminating the use of oil for machining the capsules, and 2) annealing the capsules prior to assembly (800 °C for 1 hr.) to remove surface contaminants. Capsule annealing had the added benefit of reversing the effects of work hardening, allowing the capsules to seal more efficiently. According to Du Frane *et al.* (2013), there was <10 ppmw H_2O gain during transformation using Method 2.

3.2.3. Characterization

Diedrich *et al.* (2009) and Du Frane *et al.* (2013) cut and polished the partly transformed samples for thin section analysis. To perform detailed investigations of microtextural variation in these grains, and to identify the olivine polymorphs composing these textures (i.e., the work presented here), some of the samples required additional polishing. In total, 27 samples were analyzed optically in plane polarized light (PPL), cross-polarized light (XPL), and reflected light (RFL) using an Olympus BX60. Of these, 13 were analyzed with a micro-Raman Spectrometer at Arizona State University (described below), and of these, 12 were investigated further with scanning electron microscopy (described below), also at Arizona State University. The results for these 12 samples are reported here. A comprehensive compilation of sample images and Raman data is provided in Appendix I.

3.2.3.1. Raman

The Raman data were collected using a custom built Raman system in a 180° geometry. The sample was excited using a 150 mW coherent non-polarized sapphire single frequency laser with a 532 nm wavelength. The laser power was controlled using a neutral density filters wheel and an initial laser power of 100 mW. The laser was focused onto the sample using a 50× super long working distance plan APO Mitutoyo objective with a numerical aperture of 0.42. The signal was discriminated from the laser excitation using a Kaiser laser band pass filter followed by an Ondax® SureBlock™ ultranarrow-band notch filter and a Semrock edge filter. The data were collected using an Acton 300i spectrograph and a back thinned Princeton Instruments liquid nitrogen cooled CCD detector. A 1200 BLZ grating (300 nm) was used to measure within the 90-2000 cm^{-1} range. In general, 10 data accumulations were collected at each targeted location. Acquisition time for each accumulation was 10 s. Powers of about 0.65-5 mW were generally sufficient to obtain reliable data without burning the sample.

3.2.3.2. Scanning Electron Microscopy

An FEI XL30 Environmental Field Emission scanning electron microscope was used to analyze the samples. A 20 kV accelerating voltage and ~617 pA beam current were used. The working distance was set to ~11 mm. The probe diameter at the selected spot size (number 4) is approximately 2.6 nm.

3.3. Results

3.3.1. General Description of Samples and Reactions.

3.3.1.1. Rims

Analytical conditions for the 12 primary samples are given in Table 3.1. Each of these 12 samples displays a reaction rim of ringwoodite, with or without wadsleyite, surrounding a (primarily or exclusively) olivine core (Figs. 3.3-3.11). Ringwoodite nucleates first on the olivine grain surface, making up the outer edges of the transformation rims. Wadsleyite occurs in some rims, but only as a fine intergrowth with ringwoodite. Transformation rims thicken with longer reaction times, but rim growth rates are not constant over time. Rim growth rates can be slowed by the build-up of elastic strain associated with the negative volume change (ΔV) during transformation (e.g., Kerschhofer *et al.*, 1998; Kubo *et al.*, 1998; Liu *et al.*, 1998; Mosenfelder *et al.*, 2000; and Du Frane *et al.*, 2013).

3.3.1.2. Intracrystalline Transformation

In addition to rim growth, intracrystalline transformation occurs within the olivine cores (e.g., Figs. 3.12-3.14). The ringwoodite and wadsleyite inclusions take the form of acicular, needle-like, lens-like, or lath-like structures. Some appear kinked or irregular in shape. Inclusions can form short branching structures and polyphase clusters.

Intracrystalline nucleation is most common in hydrous samples and inclusions of high-pressure phases occur in the olivine cores for all samples except two nominally anhydrous samples (BB395 and BB392). For at least two samples (754Top and 759Top; Figs. 3.13 and 3.14), intracrystalline phases occur in a linear band across the core, perhaps following a pre-existing planar defect.

Like the reaction rims, intracrystalline inclusions are commonly segmented suggesting differential expansion between the high pressure phases and the olivine matrix during pressure quench. In most cases, the observed intracrystalline phases were too fine to be identified with Raman, and the fact that they are segmented by multiple fractures made sample preparation for TEM analysis challenging. For each sample in which the mineralogy of intracrystalline phases could be identified by Raman spectroscopy, the phase(s) (ringwoodite and/or wadsleyite) matched at least one component of the corresponding transformation rim (e.g., Figs. 3.3-3.11). Alternatively, there were no cases in which a phase observed in the core was not also observed in the rim.

Detailed image analysis (either by electronic processing or by crystal counting) can provide quantitative areal density information for intracrystalline phases. Given the limited scope of the project, detailed image analysis was not performed. However, qualitative areal densities estimated from BSE images are provided for each category. Areal densities for intracrystalline phases are ranked as low, moderate, and high relative to the other samples in the present study.

3.3.2. Nominally Anhydrous Olivine (1100 °C)

3.3.2.1. Transformation Rim Thickness and Reaction Rates

Rims on nominally anhydrous are among the thinnest rims investigated in the present study. However, there is an inconsistency: Sample BB621 (1.13 hrs.; 32(13) μm rim; Du Frane *et al.*, 2013) reacted for only ~13% longer than BB395 (1 hr.; 14(2) μm rim; Diedrich *et al.*, 2009), yet its rim is more than twice as thick. Similarly, the reaction rim on sample BB621 is thicker than that of sample BB392 (24 hrs.; 27(4) μm rim; Diedrich *et al.*, 2009) despite reacting for a much shorter time: 1.13 hrs. versus 24 hrs.

3.3.2.2. Mineralogy and Texture of the Rim

The mineralogy of the transformation rims, on nominally anhydrous samples reacted at 1100 °C, vary from outer to inner edge. These changes are observed optically, by Raman spectroscopy, and by BSE. In plane polarized light microscopy, ringwoodite is distinguished from the other polymorphs by its optical isotropy. Sufficiently large crystals of wadsleyite and olivine, both anisotropic, are distinguished from each other by their interference colors. For a sample ~30 μm thick, wadsleyite displays interference colors up to first order grey, whereas olivine (Fo90) displays up to 2nd order colors. However, when trying to identify overlapping crystals, or fine-grained crystals in a polyphase assemblage, optical approaches are not feasible. For individual crystals wider than the Raman beam (>10 μm), or for similarly sized clusters of crystals of the same phase, Raman spectra for the three olivine polymorphs are diagnostic (e.g., Figs. 3.3, 3.7, 3.11). The two main peaks for olivine (~825 cm^{-1} and ~855 cm^{-1}), ringwoodite (~800 cm^{-1} and ~840 cm^{-1}), and wadsleyite (~725 cm^{-1} and ~920 cm^{-1}) are all easily distinguished from each other. In BSE, the three olivine polymorphs produce different contrast, because of their different densities and/or small differences in iron content. Consequently, polyphase assemblages appear as “mottled” regions in BSE (Fig. 3.11). Raman and optical analysis supports these mineralogical interpretations (Figs. 3.3, 3.7, and 3.11).

Both ringwoodite and wadsleyite occur in the reaction rims of all three nominally anhydrous samples investigated (BB395, BB621, and BB392), with ringwoodite being the most abundant phase along the outer edges of the transformation rims (e.g., Figs. 3.3, 3.7, and 3.11). In some places this ringwoodite rim is very thin, e.g., ~5 μm or less

(Appendix I.) Fine-grained polyphase assemblages make up the greater part of nominally anhydrous reaction rims. Lath-like, individual crystals can be highly irregular in shape and are intergrown.

3.3.2.3. Texture of the Olivine-Rim Interface

Polyphase assemblages of ringwoodite and wadsleyite in the transformation rims of nominally anhydrous samples form acicular or lath-like structures that extend from the rim up to ~60 μm into the core (e.g. BB392), creating jagged rim-core boundaries (e.g., Figs. 3.7 and 3.11). The rim-core interface is irregular for all nominally anhydrous samples transformed at 1100 °C (BB395, BB621, and BB392).

3.3.2.4. Intracrystalline Transformation

Of the three nominally anhydrous samples investigated in this study, intracrystalline transformation was only observed in sample BB621. This is the same sample that had the highest transformation rate among the three nominally anhydrous samples. Most of the inclusions in sample BB621 are not intact, symmetrical, individual lenses; i.e., most are kinked, fractured lenses or irregularly-shaped aggregates. Most crystals or clusters of crystals are small, with exposed surfaces generally < 20 μm in diameter. Laths are generally ≤~3 μm wide. Overall, these inclusions have low to moderate areal density, compared with other samples in this study.

3.3.3. 75 ppmw H_2O (900 °C)

3.3.3.1. Transformation Rim Thickness and Reaction Rates

The rim thicknesses and reaction rates for samples BB755A (7 hrs.; 31(23) μm) and BB754 (26.13 hrs.; 109(54)-115(57) μm) are consistent within this category.

3.3.3.2. Mineralogy and Texture of the Rim

Unlike the nominally anhydrous samples, wadsleyite was not detected in either of the two partly transformed 75 ppmw (900 °C) samples investigated here. Based on optical, Raman, and BSE analysis, the reaction rims for samples BB755A (7 hrs., rim thickness = 31(23) μm) and BB754Top (26.13 hrs., rim thickness = 109(54)-115(57)) μm) are composed exclusively of ringwoodite. The rims are primarily very fine-grained, with localized regions where the grain size is more coarse and blocky or polygonal (~3-12μm?). BB754Top was almost entirely transformed, however, it transformed very unevenly; the rim on one side was more than half the width of the sample.

3.3.3.3. Texture of the Olivine-Rim Interface

The rim-core interface is irregular for both samples BB755A (7 hrs.) and BB754Top (26.13 hrs.). Ringwoodite forms acicular or lath-like structures that extend from the rim into the core. In some cases, there is no distinct boundary between the rim texture and the intracrystalline texture.

3.3.3.4. Intracrystalline Transformation

The inclusions in sample BB755A are generally long (up to ~40 μm in length) and narrow (≤~2 μm) lenses/laths. Many of the lenses in BB755A are aligned along one of two orientations. The inclusions in sample BB754Top are generally less perfectly lens-like and more irregular, with the exception of one long (~160 μm) narrow (≤1 μm) inclusion that extends across the olivine core to connect opposite sides of the reaction rim. There are some small clumps of intracrystalline phases, but these were too small to be identified with Raman. The density of inclusions in BB755A is moderately high,

whereas the density of inclusions in BB754Top is very high compared with other samples in this study.

3.3.4. 75 ppmw H_2O (1100 °C)

3.3.4.1. Transformation Rim Thickness and Reaction Rates

The rim of sample BB759Top (0.67 hr.; 41(11)-53(19) μm) has the same thickness (within error) as the rims of samples BB583 (0.25 hr.; 56(7) μm rim) and BB527A (0.17 hr.; 52(8) μm rim).

3.3.4.2. Mineralogy and Texture of the Rim

No abrupt change in rim mineralogy was observed for 75 ppmw (1100 °C) samples. For all samples investigated here, ringwoodite is the primary phase composing the rims. Raman did detect traces of wadsleyite in the rims of two samples: BB527A (reaction time = 0.17 hr.; rim thickness = 52(8) μm) and 759Top (reaction time = 0.67 hr.; rim thickness = 41(11)-53(19) μm). The trace amounts of wadsleyite were detected most commonly near the rim-core boundary regions, and also (less commonly) in mid- and outer-rim regions. Surprisingly, Raman did not detect any wadsleyite in a sample transformed for an intermediate length of time = 0.25 hr. (BB583; rim thickness = 56(7) μm).

Parts of the reaction rims of samples BB527A (0.17 hr.; 52(8) μm) and BB583 (0.25 hr.; 56(7) μm) display an abrupt, physical change characterized by their fracture patterns. A change in fracture pattern occurs midway between the inner and outer edges (e.g., Fig. 3.15): polygonal fractures in the outer rim, and roughly linear, radial fractures in the inner rim. The polygons have various sizes. No similar features were found in any of the nominally anhydrous samples, nor in the 75 ppmw H_2O (900 °C) samples, nor in

sample BB759Top (1100 °C). It did not appear as though this change corresponded with any phase changes. The fracture patterns in samples BB527A and BB583 suggest a transition from coarse, blocky crystals (outer rim) to fine crystals (inner rim), but given the limited scope of the project, the absolute sizes of these grains were not determined. This "double rim" feature was not observed in sample BB759Top.

3.3.4.3. Texture of the Olivine-Rim Interface

Of the 75 ppmw H_2O samples transformed at 1100 °C, the sample with the longest reaction time (BB759Top; 0.67 hr.) has the most irregular rim-core boundary (Fig. 3.13). Sample BB527A (0.17 hr.) polished unevenly, but the better polished portions show some irregularity (Appendix I). Sample BB583 (0.25 hr.) shows the least irregularity (Appendix I).

3.3.4.4. Intracrystalline Transformation

Inclusions in the samples reacted for 0.17 hr. and 0.25 hr. (BB527A and BB583, respectively), are relatively fine, acicular or lens-like. There are few clusters. The crystals and crystal clusters were too small to be identified by Raman. Most intracrystalline phases are ≤38 μm long and <4 μm wide in BB527A, and <53 μm long and <7 μm wide in BB583. The inclusion density is moderately high for both these samples, but the sample transformed over 0.67 hr. (BB759Top) has a very high inclusion density, and these inclusions form many long networks of branching structures and clusters (Fig. 3.14). These inclusions are made of both wadsleyite and ringwoodite. The largest intracrystalline chain in BB759Top is ~280 μm long and ~20 μm wide. The long chains of ringwoodite/wadsleyite observed in the sample may have nucleated along microcracks in the sample.

3.3.5. 289 ppmw ^2H_2O (900 °C)

3.3.5.1. Transformation Rim Thickness and Reaction Rates

The rim thicknesses and reaction rates for samples BB344 (10 hrs.; 69(7) μm) and BB383 (25 hrs.; 130(27) μm) are consistent within this category.

3.3.5.2. Mineralogy and Texture of the Rim

Raman detected traces of wadsleyite in the rims of both ~289 ppm D_2O samples transformed at 900 °C (BB344: reaction time = 10 hrs.; rim thickness = 69(7) μm), and BB383: reaction time = 25 hrs.; rim thickness = 130 (27) μm). However, there was no abrupt change in mineralogy from the outer to the inner edges of these transformation rims. For all samples, ringwoodite is the primary rim phase. The trace amounts of wadsleyite were most commonly found near the rim-core boundary regions, but were also found in mid-rim regions, suggesting a very subtle transition from ringwoodite to wadsleyite nucleation and growth.

The transformation rims display an abrupt textural change midway between the inner and outer edges, characterized by a change in fracture patterns (Appendix I; e.g., Fig. 3.15) similar to that observed for the ~75 ppmw samples. Polygonal fractures are observed in the outer rim, and roughly linear, radial fractures are observed in the inner rim. This feature is only partly represented in BB344, but is well-displayed in BB383, where these two kinds of rims completely encircle the last remains of the olivine core. As before, the change from the outer rim to the inner rim does not correlate with changes in rim mineralogy. The outer rim polygons have various sizes, and grade inward to smaller sizes. As before, our data does not confirm that the blocks are single crystals. Although,

the pattern suggests a transition from coarse, blocky crystals (outer rim) to fine crystals (inner rim).

3.3.5.3. Texture of the Olivine-Rim Interface

The interface was relatively smooth for both of the 289 ppmw H_2O samples transformed at 900 °C (BB344, BB383). There are only a few localized areas along the inner rim of BB344 (10 hrs. reaction time) that show acicular extensions from the rim into the core.

3.3.5.4. Intracrystalline Transformation

The intracrystalline phases in both samples were too small to be identified with Raman. The inclusions in BB344 are generally acicular or lens-shaped, <~30 μm long, <~2 μm wide, and not clustered. The inclusions in BB383 are acicular or irregularly-shaped and are generally much less than 10 μm long and ~1 μm wide.

3.3.6. 289 ppmw D_2O (1100 °C)

3.3.6.1. Transformation Rim Thickness and Reaction Rates

BB396 has the thickest transformation rim investigated here (172(49) μm). Doubling the reaction time (0.17 hr. to 0.33 hr.) between BB350 and BB396 only created a ~51% increase in rim thickness (114(10) μm to 172(49) μm. These 100+ μm transformation rims, which formed in 0.17 to 0.33 hr., are comparable to the rims on 298 ppmw D_2O samples reacted for 25 hrs. at 900 °C (BB383) and comparable to the rims on ~75 ppmw H_2O samples reacted for 26.13 hrs. at 900 °C (BB754Top). This is evidence that high temperatures remain a strong controlling factors in reaction rate.

3.3.6.2. Mineralogy and Texture of the Rim

The rims of ~289 ppmw H_2O samples transformed at 1100 °C (BB350 and BB396) are primarily composed of pure ringwoodite. However, there is a distinct mineralogical change midway between the inner and outer edges of the rim. Polyphase assemblages appear as "mottled" regions in BSE (Fig. 3.11). Raman and optical analysis supports these mineralogical interpretations (Figs. 3.5, 3.6, 3.9, and 3.10). These polyphase assemblages are fine-grained, and they are restricted to only the very inner edges of the reaction rims. Wadsleyite was not detected in the middle to outer parts of the rims. The distance between the outer edge of the wadsleyite-containing zone and the outer edge of the rim is ~ 75+ μm for BB350 and ~75-250 μm for BB396. This estimation is complicated by the unusually-shaped rim-core boundary in sample BB396.

The transformation rims of the 1100 °C 289 ppmw H_2O samples display an abrupt physical change midway between the inner and outer edges, unrelated to mineralogy. This change is characterized by a change in fracture propagation (e.g., Fig. 3.15) similar to that observed for two of the ~75 ppmw H_2O samples (1100 °C), and the other 289 ppmw H_2O samples reacted at 900 °C. Polygonal fractures are observed in the outer rim, and roughly linear, radial fractures are observed in the inner rim. These features are well-displayed in both samples (BB350 and BB396), where these two kinds of rims encircle, or nearly encircle the olivine core. As before, individual crystal sizes in the outer rim were not determined. However, the fracture pattern suggests a transition from coarse to fine crystals, and microscopy suggests that the inner rim contains finely intergrown ringwoodite and wadsleyite crystals. It is difficult to discern where individual crystals begin and end, but most of the feathery or irregularly-shaped, finely intergrown crystals

in polyphase assemblages are probably less than ~25 μm in length in either BB350 or BB396.

3.3.6.3. Texture of the Olivine-Rim Interface

Varying degrees of irregularity were noted at the rim-core interface for the ~289 ppmw H_2O samples transformed at 1100 °C. In general, the interface is more jagged for sample BB350 than it is for BB396. This may be related to the abundance of inclusions in the olivine core, which become incorporated into the rim as the rims thicken. Many of the acicular and lens-like features are irregular in shape.

3.3.6.4. Intracrystalline Transformation

There is a moderate areal density of inclusions in BB350. Many of the inclusions observed in BB350 are interconnected and branching, making crystal size estimation difficult. Most individual crystals are ≤~23 μm long, and <6 μm wide. There is a lower areal abundance of inclusions in BB396, with most being roughly lens-shaped. The longest chain observed (~98 μm long, and less than 5 μm wide) connected two parts of the rim. Wadsleyite was the only phase identified among the inclusions in sample BB396.

3.4. Discussion

3.4.1. Review of Rim Growth Rates

This section provides a review of growth rate results from Diedrich *et al.* (2009) and Du Frane *et al.* (2013) for comparison with the results of the present study.

3.4.1.1. Non-linear Growth Rate for Nominally Anhydrous Olivine (1100 °C)

According to Diedrich *et al.* (2009), the transformation rim growth rate for nominally anhydrous olivine (1100 °C, 18GPa) is initially 4.0 (±0.8) × 10^{-9} m/s.

However, this rate applies only to the first hour of transformation. After the first hour, the growth rate rapidly decreases with run duration. For example, the thickness of the transformation rim for a 24-hr. reaction (BB392; rim thickness: 27(4) μm), appears to be less than twice that of the 1-hr. reaction (BB395; rim thickness: 14(2) μm). Du Frane *et al.* (2013) recalculated the initial growth rate from Diedrich *et al.* (2009) using a narrower time frame and obtained: 7.1×10^{-9} m/s at 1100 °C. To model the full curve requires the use of a non-linear model. The present study used the data of Diedrich *et al.* (2009), to calculate the following non-linear model for the transformation of nominally anhydrous olivine at 1100 °C and 18 GPa:

$$y = 4.71E\text{-}06\ln(x) - 2.63E\text{-}05$$

where y is the reaction rim thickness (in meters), and x is the reaction time (in seconds). This model and the data from which it is based (Diedrich *et al.*, 2009) are provided in Figure 3.16.

3.4.1.2. Rim Growth Rate for ~75 ppmw (900 °C) Samples

Unlike the nominally anhydrous samples (1100 °C), there is no significant reduction in rim-growth rate over time (up to at least 26 hours) for the 75 ppmw H_2O (900 °C) samples. The reaction rims of samples BB755A and BB754Top grow linearly with time (within the timescales of the experiments), permitting the use of the following linear rim-growth rate: $2.3\ (\pm 0.3) \times 10^{-9}$ m/s (Du Frane *et al.*, 2013). This rate is only ~58% the initial transformation rate for nominally anhydrous grains at 1100 °C (Diedrich *et al.*, 2009), but is sustained for the timescales of the experiments.

3.4.1.3. Rim Growth Rate for ~75 ppmw (1100 °C) Samples

Du Frane *et al.*, (2013) reported that at 1100 °C, reaction rims grew faster on the hydrous olivine (75 ppmw H_2O) than on nominally anhydrous olivine, but the transformation rate decreases with time. The initial growth rate, which applies only to the first ~10 min., is 7.3 (±1.8) $\times 10^{-8}$ m/s. This rate reflects the action of H_2O in the transformation process, reducing elastic strain energy and promoting rim growth (e.g., Du Frane *et al.*, 2013). The rim of a sample that reacted for 0.67 hr. (BB759Top; 41(11)-53(19) µm rim) has the same thickness (within error) as the rim of similar samples that reacted for only 0.25 hr. (BB583; 56(7) µm rim) and 0.17 hr. (BB527A; 52(8) µm rim). This is inferred to reflect the rapid buildup of elastic strain energy and subsequent decrease in reaction rate after the start of transformation (e.g., Du Frane *et al.*, 2013). Longer time steps between runs may be necessary to model subtle changes in rim growth for samples reacting for more than 10 min. at similar temperature and hydration conditions.

3.4.1.4. Rim Growth Rate for ~289 ppmw (900 °C) Samples

The transformation rate for samples with ~289 ppmw ^2H_2O at 900 °C is 1.6(0.6)$\times 10^{-9}$ m/s (Diedrich *et al.*, 2009). Despite higher starting ^2H_2O, this is only 40% the initial transformation rate for nominally anhydrous samples transformed at 1100 °C. Temperature is likely to be the primary factor for this difference in initial reaction rate. The samples with ~289 ppmw have a better sustained reaction rate over time. This is likely due to the availability of H_2O. The transformation rate calculated for ~289 ppmw ^2H_2O samples by Diedrich *et al.* (2009) is only ~70% the transformation rate calculated for samples with ~75 ppmw H_2O (900 °C) measured by Du Frane *et al.* (2013). Du Frane

et al. (2013) report that growth rates for the high pressure phases do not depend strongly on H_2O contents between 75-300 ppmw, if one assumes H_2O and ^2H_2O have similar effects.

3.4.1.5. Rim Growth Rate for ~289 ppmw (1100 °C) Samples

The rim-growth rate for samples with ~289 ppmw H_2O reacting at 1100 °C is ~1.5(0.3)×10^{-7} m/s (Diedrich *et al.*, 2009). This is the fastest initial growth rate among all the samples investigated here. Doubling the reaction time (0.17 hr. to 0.33 hr.) between BB350 and BB396 only created a ~51% increase in rim thickness (114(10) µm to 172(49) µm), which illustrates how the reaction rate decreases over time, despite having the highest abundance of ^2H_2O in this study. This is likely due to the onset of strain associated with transformation. The fact that the 100+ µm transformation rims on BB350 (0.17 hr.) and BB396 (0.33 hr.) are comparable to the thickness of the rim on a 298 ppmw ^2H_2O sample reacted for 25 hrs. at 900 °C (BB383) and comparable to the rim on a ~75 ppmw H_2O sample reacted for 26.13 hrs. at 900 °C (BB754Top) is evidence that the high temperature rather than the water content was the strongest factor controlling the reaction rate.

3.4.2. Rim Mineralogy

A number of studies (e.g., Liu *et al.*, 1998; Kerschhofer *et al.*, 1998; and Diedrich *et al.*, 2009) observed reaction rims of mixed ringwoodite and wadsleyite. However neither these studies, nor Du Frane *et al.*, (2013), conducted detailed investigation of the rim micromineralogy to determine the spatial and textural relations between these polymorphs to better understand how mixed rims develop.

In general, the results from the present study agree that wadsleyite nucleation follows ringwoodite nucleation, because a non-hydrostatic pressure drop caused by elastic strain occurs that shifts the system into the wadsleyite stability field (Fig. 3.1). Wadsleyite is likely a good indicator for elevated strain in transforming grains. For a given transformation temperature and time, samples with more ringwoodite in their rims than wadsleyite likely experienced less elastic strain. Co-nucleation of both wadsleyite and ringwoodite suggests that the free energy difference between ringwoodite and wadsleyite is small under the strained conditions.

Wadsleyite nucleation does not necessarily mark the point at which strain begins to build, nor the moment when the reaction rate begins to decline. For example, the rim growth rate of sample BB583 (Du Frane *et al.*, 2013) suggests that rim growth rate can slow without wadsleyite nucleation. Although samples bearing wadsleyite in their rims tend to show slower reaction rates than the initial rates (Du Frane *et al.*, 2013), the present data are insufficient to determine if there was any abrupt change in transformation rate associated with the start of wadsleyite nucleation. No abrupt change is expected, though, because strain is the primary control on transformation rate, not the stable high pressure polymorph.

For the nominally anhydrous samples in this study, very little ringwoodite formed before wadsleyite nucleation began. Sample BB395 reacted for only one hour, forming a reaction rim ~14(2) μm thick. In some places along this rim, the outer edge of ringwoodite is only ~5 μm or less. If the transformation rim grew more or less linearly and evenly within the first hour (Diedrich *et al.*, 2009), this would mean that the transformation reaction switched from nucleating ringwoodite exclusively, to nucleating

both ringwoodite and wadsleyite very early on in the transformation process, perhaps within the first ~20 min. These ringwoodite and wadsleyite polymorphs build on each other, forming jagged features along the core-rim boundaries of nominally anhydrous samples.

Like the nominally anhydrous samples, the rim mineralogies of the ~289 ppmw samples BB350 & BB396 (1100 °C) also show rapid onset of wadsleyite nucleation. These hydrous samples reacted for only 10-20 min., and wadsleyite had already begun to nucleate at the core-rim boundaries. As in the nominally anhydrous samples, ringwoodite and wadsleyite coexist in polyphase assemblages. Unlike the nominally anhydrous samples, these polymorphs do not necessarily produce jagged features along the core-rim boundaries of hydrous samples.

Ranking the transformation run products based on the decreasing prevalence of wadsleyite yields the following: (1) Nominally anhydrous (1100 °C), (2) ~289 ppmw (1100 °C), (3) ~289 ppmw (900 °C), (4) ~75 ppmw (1100 °C), and (5) ~75 ppmw (900 °C). The relative abundances of wadsleyite in the hydrated samples can not be ascribed to any one variable. The abundance does not exclusively follow relative hydration, rim thickness, or transformation temperature. Wadsleyite was found to occur more commonly in both the ~289 ppmw and nominally anhydrous samples, but was least abundant in samples with ~75 ppmw hydration. The ~75 ppmw samples were expected to be most like the nominally anhydrous samples, which is not the case here. The likelihood of accidental hydrous contamination, and the possible effects on transformation is discussed below in the section Hydrous Contamination.

Within a given hydration level, 1100 °C runs produced more wadsleyite than 900 °C runs. This is most easily explained by the positive Clapeyron slope marking the boundary between ringwoodite and wadsleyite stability fields (Helffrich and Wood, 2001; Fig. 3.1). The stability field of wadsleyite extends to higher pressures at higher temperatures. High temperature runs are closer to the wadsleyite stability field, such that less strain energy is necessary to trigger wadsleyite nucleation at 1100 °C than at 900 °C.

The change in rim mineralogy observed in hydrous samples BB350 and BB396 suggests H-partitioning into the ringwoodite rim provided temporary relief from strain by facilitating ringwoodite deformation until the H-reservoir (the core) was depleted, and the transformation strain built again as under anhydrous conditions. The basic structure of a grain that has undergone a transition from ringwoodite to wadsleyite nucleation is depicted in Figure 3.17. The fact that there were trace amounts of wadsleyite detected in the rims of BB527A and BB759Top suggests a very subtle transition away from nucleating ringwoodite exclusively.

If samples with ~289 ppmw and thick rims (114-172 μm) contain wadsleyite, then one should expect that drier samples with similar run temperature, reaction time, and similar rim thicknesses would also contain wadsleyite. Analysis of BB754Top (~75 ppmw; 900 °C, 26.13 hrs.; 109(54)-115(57) μm rim) suggests that the shape of the reaction rim is also a critical factor for wadsleyite nucleation. Compared with other samples in the present study (in particular, BB383 (~289 ppmw; 900 °C; 25 hrs.; 130(27) μm rim)), the nominal water content (~75 ppmw), run temperature (900 °C); run duration (26.13 hrs.), and average rim thickness (109(54)-115(57) μm) of sample BB754Top should have been sufficient to induce sufficient stress to nucleate wadsleyite. However,

the fact that the rim developed asymmetrically may have limited the strain experienced at the core-rim boundary.

3.4.3. Fractures in the Rim

At the end of transformation the samples undergo a temperature quench followed by a pressure quench. Quenching results in rapid differential volume changes between olivine and its high pressure polymorphs. Temperature quenching can cause differential thermal contraction, and pressure quenching can cause differential expansion. Of these two processes, pressure quenching is most likely to cause the greatest fracturing observed in the rims of the samples. The bulk modulus is much higher for olivine's high pressure phases, so they do not expand as much as olivine upon pressure release. As olivine expands under pressure quenching, it ruptures the comparatively rigid, shell-like ringwoodite/wadsleyite rim. Intracrystalline phases in the olivine interior are also ripped apart by this expansion process.

Although these fractures would not be expected in mantle olivine, they can provide clues to the transformation process. Fracturing patterns depend on the nature of the grain boundaries and the nature of the sample. Fractures preferentially propagate along grain boundaries rather than through grains. The polygonal network of fractures in the outer part of double rims suggests that the grains in these regions are coarse relative to those of the inner rim. Fractures that propagate through fine-grained matrices follow a more radial path to accommodate the circumferential tensile stress in the rim resulting from the expansion of the core.

3.4.4. Rim Grain Size

Ideally, electron backscatter detection (EBSD) would be used to assess crystal sizes. However, this option was not available at the time of this study. For monophase assemblages, grain sizes could not be directly observed with optical or BSE techniques either. For this reason fracture patterns were used to determine the relative grain sizes in monophase regions (see section discussing fractures, above). BSE allowed for better grain size estimation in polyphase regions. Co-existing olivine polymorphs have different backscatter intensities, and so grain boundaries for neighboring polymorphs can be distinguished by relative brightness in BSE images.

In general, the outer rims of double-rimed samples are coarse-grained, and the inner rims are fine-grained. Double rims are more commonly observed in hydrous samples, which suggests that H_2O facilitates the growth of fewer, but larger ringwoodite crystals. Fine inner rims suggest that as water becomes less abundant, nucleation sites increase, and crystal size decreases. Hydrous conditions and long reaction times may facilitate the growth of well-formed double rims, as in the case of sample BB383 (~289 ppmw; 25 hrs.; 900 °C). It is possible that if samples like BB344 (~289 ppmw; 10 hrs.; 900 °C) reacted for longer durations, their double rims would have been more complete.

3.4.5. Intracrystalline Phases

According to Kerschhofer *et al.* (1998), at 18 GPa, the process of intracrystalline nucleation involves (1) the formation of stacking faults (high energy sites) in the olivine, (2) coherent nucleation of ringwoodite-lamellae on these faults, and (3) nucleation of wadsleyite on the ringwoodite. The present study offered no evidence for nucleation on stacking faults, but it is possible that the orientation was not ideal for such analysis.

Lenses of high pressure phases (both ringwoodite and wadsleyite) are observed. Based on the observation that some of these lenses in BB755A have shared orientation, it is likely that these are following crystallographically-controlled directions. More commonly, lenses appear to be oriented randomly. Orientation is complicated by nucleation off of pre-existing inclusions. Additional TEM work may be required to determine what controls lens orientation in these cases.

It is likely that H_2O partitioned into high pressure intracrystalline phases as it did the rim phases. Hydrous olivine grains are more likely to have intracrystalline nucleation than anhydrous olivine grains. This suggests water facilitates the growth of intracrystalline phases. With sufficient intracrystalline transformation the rims may become starved of H_2O, resulting in narrower rims than otherwise expected (Kerschhofer *et al.*, 1998; Liu *et al.*, 1998). This may be what happened to BB759Top, which reacted longer than the other two samples in its category, and showed the greatest intracrystalline transformation, but had rims of comparable thickness to the other two samples in its category.

Indistinct boundaries between rim textures and intracrystalline textures (e.g., for BB759Top, BB755A, and BB754Top), may be places where intracrystalline phases intersected or nucleated off of rim phases. These boundaries are more common in anhydrous samples than in hydrous samples. This suggests that boundaries become less distinct as H_2O abundance decreases at the core-rim boundary.

3.4.6. Hydrous Contamination

As noted in the section discussing Methods, three of the samples investigated in the present study (BB621, BB527A, and BB583) were produced using Method 1 (Du

Frane *et al.*, 2013), which resulted in small amounts of water contamination during transformation. Here we discuss how this contamination affected transformation in these samples.

The reaction rate of nominally anhydrous sample BB621 (1100 °C) is inconsistently higher than the transformation rates of the other two nominally anhydrous samples (BB395 and BB392). As H_2O is known to increase reaction rates by promoting transformation kinetics (e.g., Hosoya *et al.*, 2005; Kubo *et al.*, 1998; Diedrich *et al.*, 2009; Du Frane *et al.*, 2013) the anomalously high reaction rate is the best explained by H_2O contamination associated with the use of Method 1 (Du Frane *et al.*, 2013). Sample BB621 is also the only nominally anhydrous sample to have intracrystalline phases. This suggests that the contaminating H_2O also facilitated intracrystalline nucleation of high pressure phases. The contamination was insufficient to prevent the nucleation of wadsleyite in the rim.

Discerning the effects of small amounts of hydrogen contamination on the transformation of samples BB527A and BB583 (both nominally ~75 ppmw; 1100 °C) is more difficult, as there is only one other sample in the category for comparison (BB759Top). BB759Top and BB527A both have trace wadsleyite in their rims, whereas BB583, which reacted for an intermediate length of time, did not. Small amounts of excess H_2O may have delayed the onset of wadsleyite nucleation in BB583. Both BB527A and BB583 have coarsely crystalline outer rims, and better-defined core-rim boundaries than sample BB759Top. Excess H_2O may have facilitated uniform rim growth in BB527A and BB583. Alternatively, the indistinct core-rim boundary of BB759 may be the result of a longer reaction time that lowered the H concentration in the rim. This

latter scenario is unlikely, though, because if sample BB759Top started with a similar H_2O concentration as the other two samples, all three samples should have developed a similar outer rim texture (e.g., all coarse-grained ringwoodite). Instead, BB759Top lacks any semblance of a coarse-grained outer rim. It does not appear that intracrystalline nucleation was enhanced in either BB527A or BB583, as might be expected from increased hydration, although the shorter reaction times (and consequently less transformation), make direct comparison with BB759Top tenuous.

3.4.7. Order of Hydrous Partitioning

The tendency for H to preferentially partition into ringwoodite (e.g., Diedrich *et al.*, 2009) and wadsleyite (e.g., Young *et al.*, 1993) led to redistribution of H within the olivine during transformation (Diedrich *et al.*, 2009). This was evidenced by the higher concentration of H_2O in the reaction rims than in the cores (Diedrich *et al.*, 2009; Du Frane *et al.*, 2013). Although no additional measurements of H_2O abundances were made in these samples as part of the present study, a close inspection of mineralogy and texture provides clues to H redistribution during olivine transformation. Hydrogen helps to reduce elastic strain energy, either by hydrolytic weakening of the rim, allowing for viscoelastic deformation (e.g., Kubo *et al.*, 1998; Diedrich *et al.*, 2009), or by aiding ion diffusion across the growth interface (Rubie, 1986). When it is in abundance, coarse grains of ringwoodite form a rim around the olivine grain. When hydrogen is almost entirely depleted, a polyphase assemblage of fine-grained ringwoodite and wadsleyite nucleate before the transformation effectively stops. Other observations fit between these endpoints and provide a kind of relativistic hygrometer. One possible progression of

events for a large (425-500 μm) hydrous grain (~75-289 ppmw; 18 GPa; 900-1100 °C) is provided below:

1) At the start of transformation a coarse outer ringwoodite rim begins to nucleate and grow. Initially, the rim growth rate is approximately constant (e.g., Diedrich *et al.*, 2009; Du Frane *et al.*, 2013). Hydrogen partitions into this rim as it forms, reducing the abundance of hydrogen in the core, but particularly at the core-rim boundary (e.g., Diedrich *et al.*, 2009; Du Frane *et al.*, 2013).

2) Intracrystalline nucleation begins shortly after the ringwoodite rim begins to grow. Misfit (elastic) strain does not increase around these intracrystalline phases, and so the intracrystalline reaction rate is not expected to decrease (Liu *et al.*, 1998). However, build-up of elastic strain could generate differential stress in the olivine that could enhance heterogeneous intracrystalline nucleation (Liu and Yund, 1995; Kerschhofer *et al.*, 1998; Diedrich *et al.*, 2009). Ringwoodite nucleates first, preferentially along pre-existing features in the olivine (Kerschhofer *et al.*, 1996; 1998; 2000). Hydrogen partitions into the intracrystalline ringwoodite from the core.

3) As the reaction proceeds, and the rim volume increases, the H_2O concentration in the rim decreases, and less H is available from the core. As the H_2O concentration in the rim decreases, strain energy builds. The H_2O concentration in the core must fall below 50 ppmw before the rim growth rate decreases significantly (Diedrich *et al.*, 2009; Du Frane *et al.*, 2013). This may have occurred in sample BB759Top. This sample has highly abundant intracrystalline phases, but its rim is not wider than others in its category, despite reacting longer. Alternatively, the growth of intracrystalline phases caused a volume decrease that may have resulted in an internal pressure drop in addition

to that caused by rim growth (Liu *et al.*, 1998). However, this is unlikely at 18 GPa, where the rate of intracrystalline transformation is relatively low (Liu *et al.*, 1998). Yet another possibility is that the intracrystalline phases physically inhibit rim growth through impingement (Liu *et al.*, 1998; Kerschhofer *et al.*, 1998). However, this also seems unlikely, because these features provide more surface area from which to nucleate new phases.

4) Efficient dehydration of the core olivine via H partitioning into the rim may reduce the rate of intracrystalline transformation. This would explain why there are well-developed rims but few inclusions in samples BB344 and BB383. It is likely that the driest olivine is the last to transform.

5) As H_2O abundance decreases and/or as elastic strain energy builds, a fine-grained inner ringwoodite rim begins to nucleate.

6) When the radial tensile elastic stress at the core-rim boundary reaches a critical threshold, it creates a non-hydrostatic pressure drop (Diedrich *et al.*, 2009) that facilitates wadsleyite nucleation along the inner edge of the fine-grained ringwoodite rim. The onset of wadsleyite nucleation follows the start of ringwoodite nucleation, but does not mark the end of ringwoodite nucleation. Wadsleyite does not exist as a well-defined layer between a ringwoodite outer rim and an olivine core. There are no such sharp boundaries. Fine-grained ringwoodite co-nucleates with fine-grained wadsleyite, creating polyphase assemblages. Even olivine spheres with as much as ~289±72 ppmw H_2O, that were transformed at 1100 °C for only 10-20 min. display these fine mixed phase regions.

7.) Intracrystalline wadsleyite nucleates on grain boundaries of existing intracrystalline ringwoodite (Kerschhofer *et al.*, 1996; 1998). Water partitions into both

intracrystalline phases, locally depleting the core olivine of H. Spatial variations in core H_2O abundance (Diedrich *et al.*, 2009) likely reflect variable sampling of H-rich intracrystalline phases. The fact that the intracrystalline phases identified in our study match one or more of the corresponding rim phases suggests that transformational conditions in the inner core are generally in sync with the conditions at the core-rim boundary. This suggests that H diffuses across the olivine efficiently. Whether there is a small delay between the onset of new phases in the rim and core could not be determined with the available data.

8) The core-rim boundary becomes rough and indistinct as 1) the elastic strain builds, and rim phases nucleate off of each other and extend into the core, and 2) intracrystalline phases intersect the rim as it grows. The abundance of water in samples BB344 and BB383 (~289 ppmw) and low reaction temperature likely allowed for the development of smooth, distinct core-rim interfaces.

9) The reaction slows significantly. Experimental samples are quenched.

The process of transformation for a nominally anhydrous olivine grain in the ringwoodite stability field may be recounted in the following steps:

1) A narrow, fine-grained ringwoodite rim begins to nucleate.

2) Elastic strain energy builds and reaches a critical threshold.

3) Wadsleyite begins to co-nucleate with ringwoodite on the inner edge of the rim. Very little ringwoodite growth occurs before elastic strain slows the transformation and causes wadsleyite nucleation in the rims.

4) The core-rim boundary becomes jagged as rim phases build on each other and extend into the core.

5) The reaction slows significantly. Experimental samples are quenched.

3.5. Conclusions

As olivine transforms to its high pressure polymorphs at 18 GPa and 900-1100 °C, there is a transition in the mineralogy of the transformation products. For samples with ~289 ppmw, the growth rim transitions from coarse-grained ringwoodite, to fine-grained ringwoodite, to fine-grained polyphase assemblages of ringwoodite and wadsleyite. Given drier starting compositions (e.g., ≤~75 ppmw), the initial stage (i.e., coarse grained ringwoodite) never forms, and the fine-grained ringwoodite rim is reduced in thickness. These changes are thought to be the system's response to decreasing H concentrations and increasing elastic strain at the core-rim boundary. As hydrogen concentration in the rim decreases, the transformation front (the core-rim boundary) becomes irregular and less-distinct. The development of intracrystalline phases offers additional complexity to the transformation process. These inclusions vary in shape, and generally form clusters, suggesting that nucleation of lenses along pre-existing features rapidly transitions to nucleation on grain boundaries of pre-existing intracrystalline phases. Hydration may help promote the nucleation and development of intracrystalline phases. Excess growth of these phases can potentially starve the rim of H.

The complex phase distributions and textures observed in the present study suggest that transformation models (e.g., Liu *et al.*, 1998; Kerschhofer *et al.*, 1998; Diedrich *et al.*, 2009; and Du Frane *et al.*, 2013) be updated to reflect how changing

water distributions lead to changes in strain and reaction pathways within different parts of a transforming olivine grain. These updated models should also relate specific H_2O abundances to the development of particular polyphase assemblages, and complex microstructures. Lastly, these different transformation processes and associated hydrogen abundances must be related to transformation rate. Olivine transformation is complex, and these details may have bearing on the accuracy of predictions for olivine metastability at depth.

Table 3.1. Analytical Conditions and Sample Descriptions.

Table 3.1. Analytical Conditions and Sample Descriptions.[1]

Sample	H_2O (ppmw)	T (°C)	Reaction t (hrs.)	Rim Thickness (μm)	Interface; Double Rim?	Wd Present?		Intracrystalline phase(s)[4]
						Rim	Core-Rim	
BB395	n.a.[2]	1100	1	14(2) [2]	r; n.o.	✓	✓	n.o.
BB621	n.a.[3]	1100	1.13	32(13) [3]	r; n.o.	✓	✓	wd + rw
BB392	n.a.[2]	1100	24	27(4) [2]	r; n.o.	✓	✓	n.o.
BB755A	75±15[3]	900	7	31(23) [3]	r;f; n.o.	n.o.	n.o.	unk.
BB754Top	75±15[3]	900	26.13	109(54)-115(57) [3]	r;f; n.o.	n.o.	n.o.	unk.
BB527A	75±15[3]	1100	0.17	52(8) [3]	m;f; part.	tr.	tr.	unk.
BB583	75±15[3]	1100	0.25	56(7) [3]	s; part.	n.o.	n.o.	unk.
BB759Top	75±15[3]	1100	0.67	41(11)-53(19) [3]	r; n.o.	tr.	tr.	rw + wd
BB344	289±72[2]	900	10	69(7) [2]	s;f; part.	tr.	tr.	unk.
BB383	289±72[2]	900	25	130(27) [2]	s;f; c.	tr.	tr.	unk.
BB350	289±72[2]	1100	0.17	114(10) [2]	r; n.c.	n.o.	✓	unk.
BB396	289±72[2]	1100	0.33	172(49) [2]	m;f; c.	n.o.	✓	wd (+other?)

[1]Abbreviations: s (smooth or distinct boundary between core and rim); r (rough, or indistinct boundary between core and rim); m (mixed or intermediate between smooth and rough boundary between core and rim); f (fractures paralleling core-rim boundary); n.a. (nominally anhydrous); n.o. (none observed); part. (partial double rim); c (complete double rim); n.c. (nearly complete double rim); tr. (trace abundance).
[2]From Diedrich *et al.* (2009); [2]H_2O
[3]From Du Frane *et al.* (2013); H_2O
[4]Only identified phases are named. The phrase "+other?" is used to indicate cases where the presence of additional phases cannot be ruled out. The abbreviation "unk." is used where intracrystalline transformation phases were observed, but have not been positively identified.

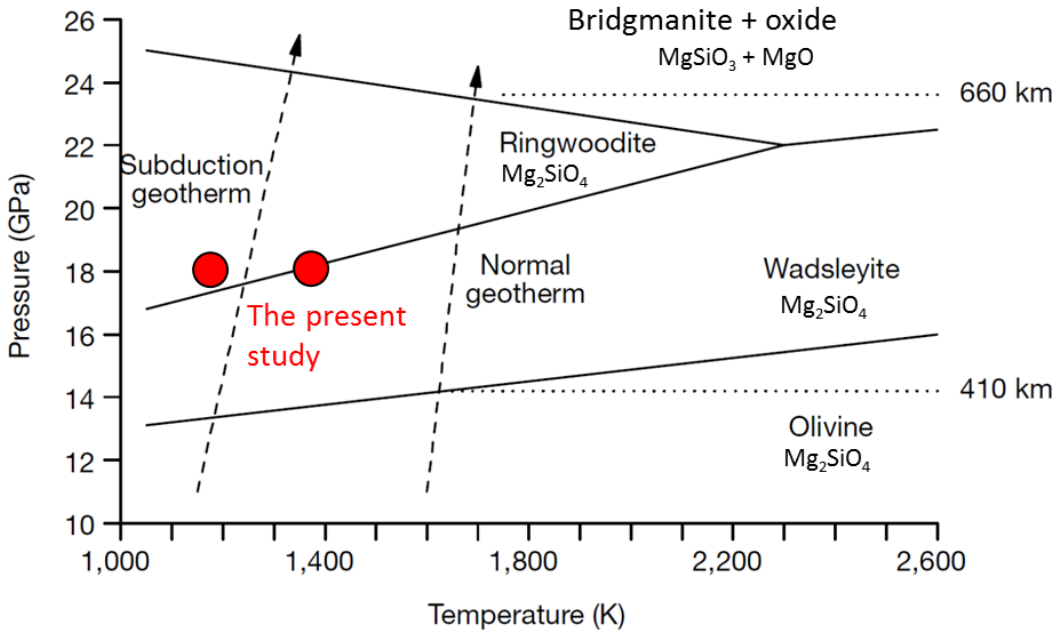

Fig. 3.1. Schematic Phase Diagram of Mg_2SiO_4 Olivine in Mantle Peridotite (From Helffrich and Wood, 2001).

Solid lines show the phase stability fields for olivine polymorphs, and perovskite + oxide. Dashed lines show approximate temperature increase with depth in the mantle (the "normal geotherm") and inside a subduction zone ("subduction geotherm"), as interpreted by Helffrich & Wood (2001). According to this model, cooler temperatures in subduction zones move the phase transitions either to shallower depths (olivine → wadsleyite) or deeper depths (ringwoodite → perovskite + oxide). Slab core temperatures (not shown) lag behind subduction geotherm temperatures. At 18 GPa slab cores are ~573 K – 1173 K (~300-900 °C; Kirby *et al.*, 1996). The red dots mark the conditions investigated in the present study: 18 GPa, and both 1173 K and 1373 K (900 °C and 1100 °C, respectively). Both these points lie within the ringwoodite stability field, but the point corresponding to 1373 K is very close to the wadsleyite stability field.

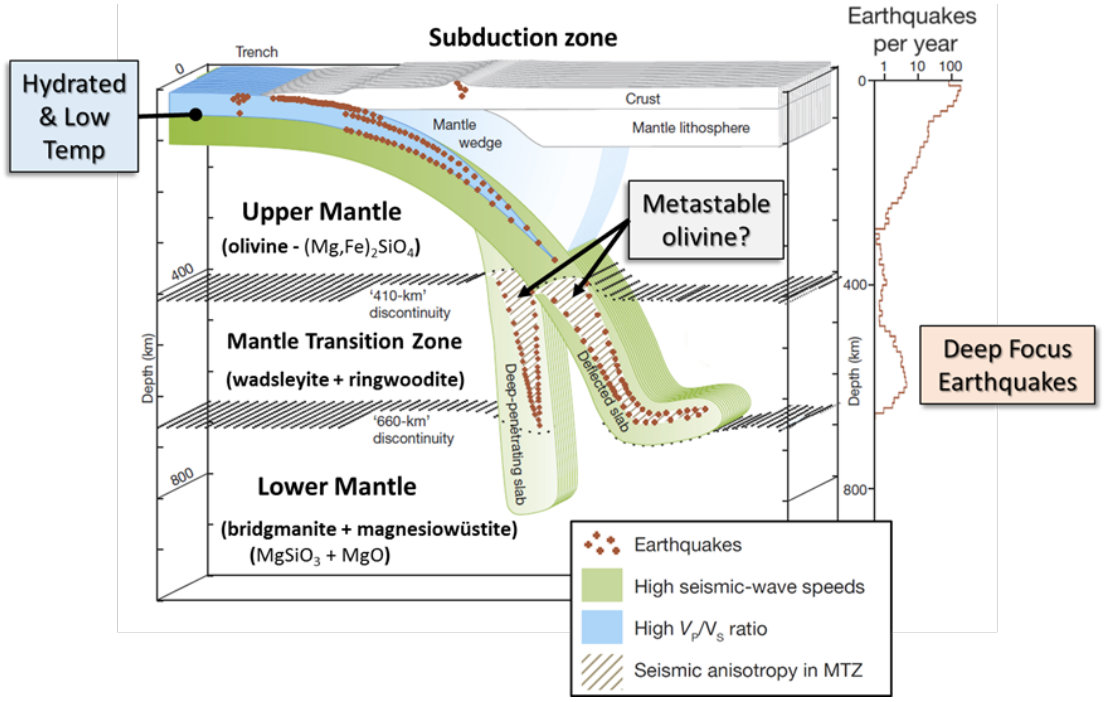

Fig. 3.2. Schematic Adapted from Green II *et al.* (2010) Illustrating Where Earthquakes and Mineral Stability Fields Occur in Subduction Zones.

In subduction zones, hydrated slabs of oceanic crust descend into the mantle. These slabs can descend to depths where only high pressure mineral phases are stable. The plot on the right represents the globally averaged number of earthquakes per year as a function of depth (see Green *et al.*, 2010 for details). Earthquakes (denoted by dots in the schematic diagram) occur within the cores of subducting oceanic slabs, but only at depths above the base of the mantle transition zone (MTZ). Below 680 km no earthquakes have been recorded. Transformational faulting is one of the leading hypotheses to explain the occurrence of earthquakes in the MTZ (e.g., Kirby *et al.*, 1996). In this model, low-pressure polymorphs persist metastably to depth in the cores of cold subducting slabs. In the MTZ, rapid transformation to stable high pressure polymorphs triggers earthquakes.

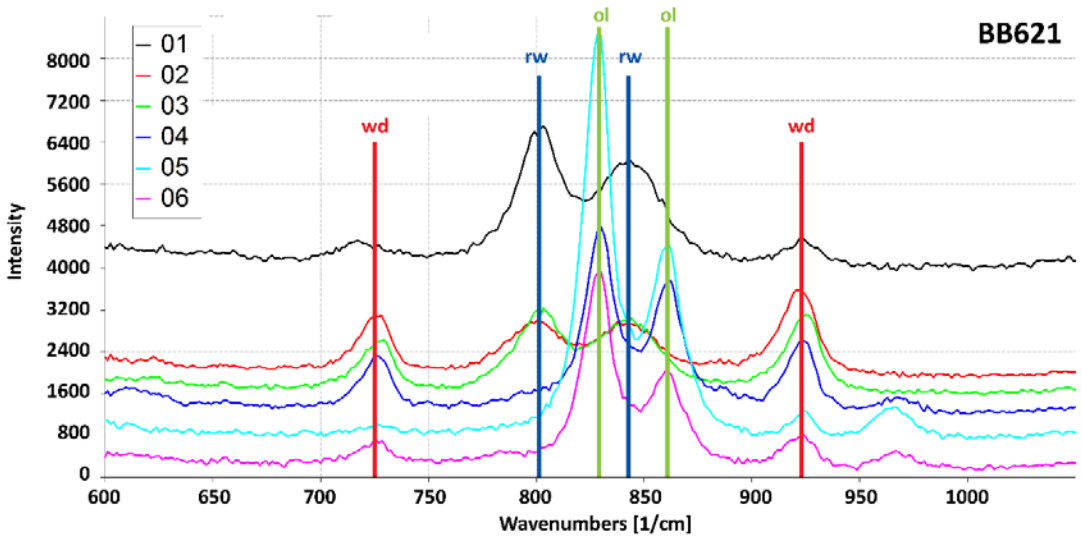

Fig. 3.3. Raman Spectra Collected on Nominally Anhydrous Sample BB621.

Spectra were offset from each other, and positioned in numerical order from top to bottom for clarity. The two most prominent peaks positions for olivine (ol; ~825 cm^{-1} and ~855 cm^{-1}), ringwoodite (rw; ~800 cm^{-1} and ~840 cm^{-1}) and wadsleyite (wd; ~725 cm^{-1} and ~920 cm^{-1}) are marked by pairs of vertical lines. Additional Raman data is provided in Fig. 3.7.

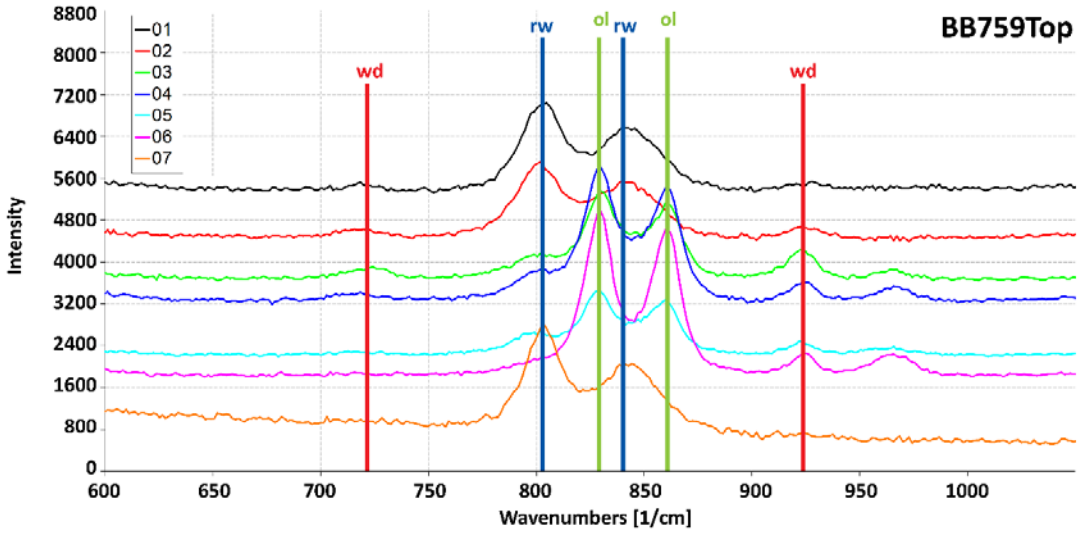

Fig. 3.4. Raman Spectra for Sample BB759 Top (~75 ppmw).

Each Raman spectrum corresponds to a location in sample BB759Top presented in Fig. 3.8. Spectra were offset from each other, and positioned in numerical order from top to bottom for clarity. The two most prominent peaks positions for olivine (ol; ~825 cm^{-1} and ~855 cm^{-1}), ringwoodite (rw; ~800 cm^{-1} and ~840 cm^{-1}) and wadsleyite (wd; ~725 cm^{-1} and ~920 cm^{-1}) are marked by pairs of vertical lines.

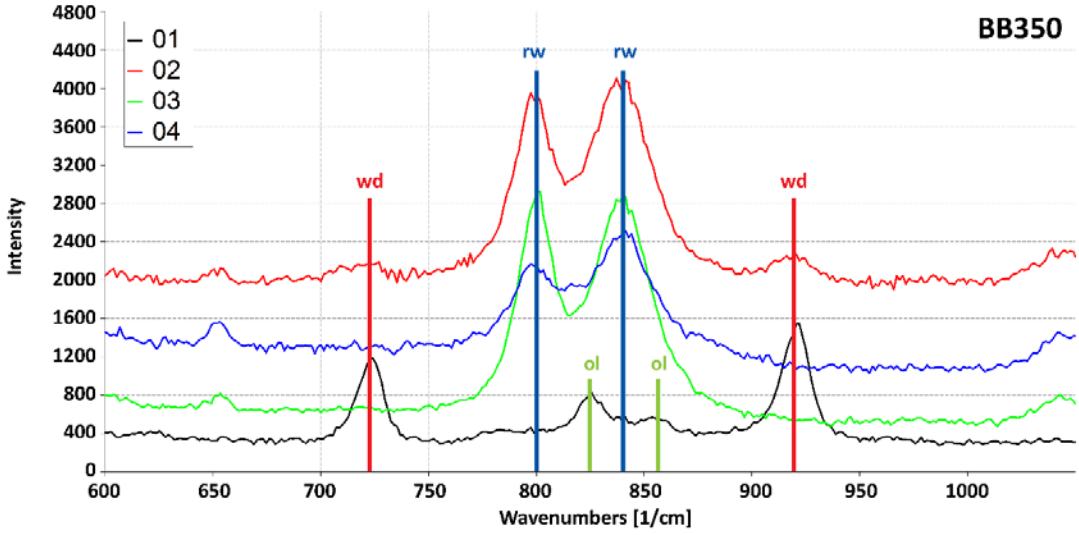

Fig. 3.5. Raman Spectra for Sample BB350 (~289 ppmw).

Each Raman spectrum corresponds to a location in sample BB350 presented in Fig. 3.9. Spectra were offset from each other, and positioned in numerical order from top to bottom for clarity. The two most prominent peaks positions for olivine (ol; ~825 cm^{-1} and ~855 cm^{-1}), ringwoodite (rw; ~800 cm^{-1} and ~840 cm^{-1}) and wadsleyite (wd; ~725 cm^{-1} and ~920 cm^{-1}) are marked by pairs of vertical lines.

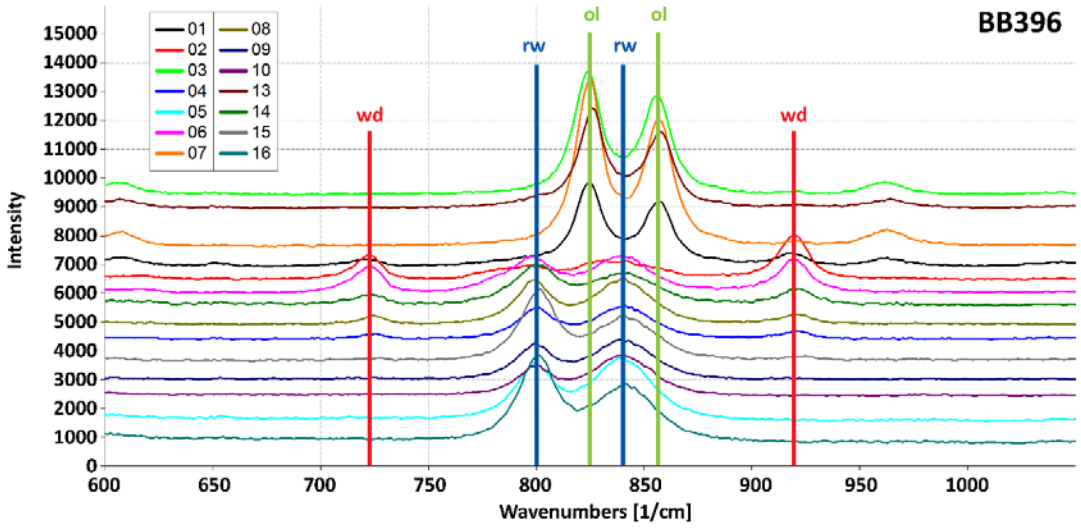

Fig. 3.6. Raman Spectra for Sample BB396 (~289 ppmw).

Each Raman spectrum corresponds to a location in sample BB396 presented in Fig. 3.10. Spectra were offset from each other, and positioned in numerical order from top to bottom for clarity. The two most prominent peaks positions for olivine (ol; ~825 cm^{-1} and ~855 cm^{-1}), ringwoodite (rw; ~800 cm^{-1} and ~840 cm^{-1}) and wadsleyite (wd; ~725 cm^{-1} and ~920 cm^{-1}) are marked by pairs of vertical lines.

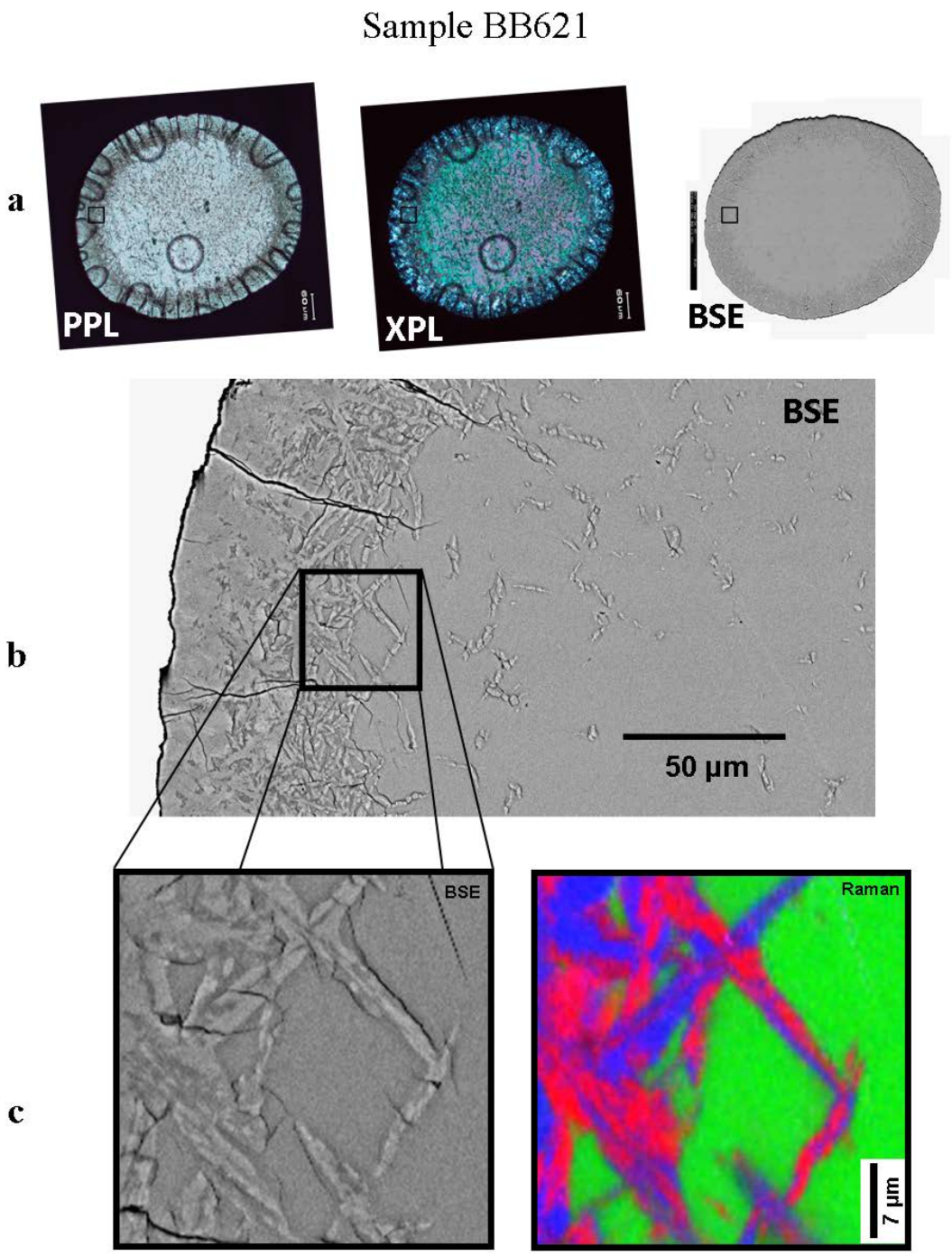

Fig. 3.7. Scanning Raman Analysis of Core-Rim Phase Variation in Partly Transformed Nominally Anhydrous Olivine Sample BB621, With Optical and Backscattered Electron (BSE) Images Provided for Context.

Black rectangles outline the region mapped with Raman. a) Plane Polarized Light (PPL), Cross-Polarized Light (XPL) and BSE images provided for spatial context. b) A

close-up BSE image of the core-rim boundary. c) A BSE image of the area mapped with Raman (left) with the corresponding Raman mineralogy map (right; green = olivine; red/pink = wadsleyite; blue = ringwoodite). Raman map for Sample BB621 was provided by Dr. Tom Sharp and WiTec.

Regions containing wadsleyite are anisotropic in XPL, have "wispy" microtextures in PPL, are marked by reduced backscatter intensity (compared with ringwoodite), and produce Raman peaks at ~723 cm^{-1} and ~919 cm^{-1}. Regions containing ringwoodite are isotropic in XPL, have a higher backscatter intensity (compared with wadsleyite), and produce Raman peaks at ~800 cm^{-1} and ~840 cm^{-1}. Olivine that did not transform is the dominant component of the sample cores. Olivine is anisotropic and produces Raman peaks at ~825 cm^{-1} and ~857 cm^{-1}. Additional, individual Raman spectra are provided in Fig. 3.3.

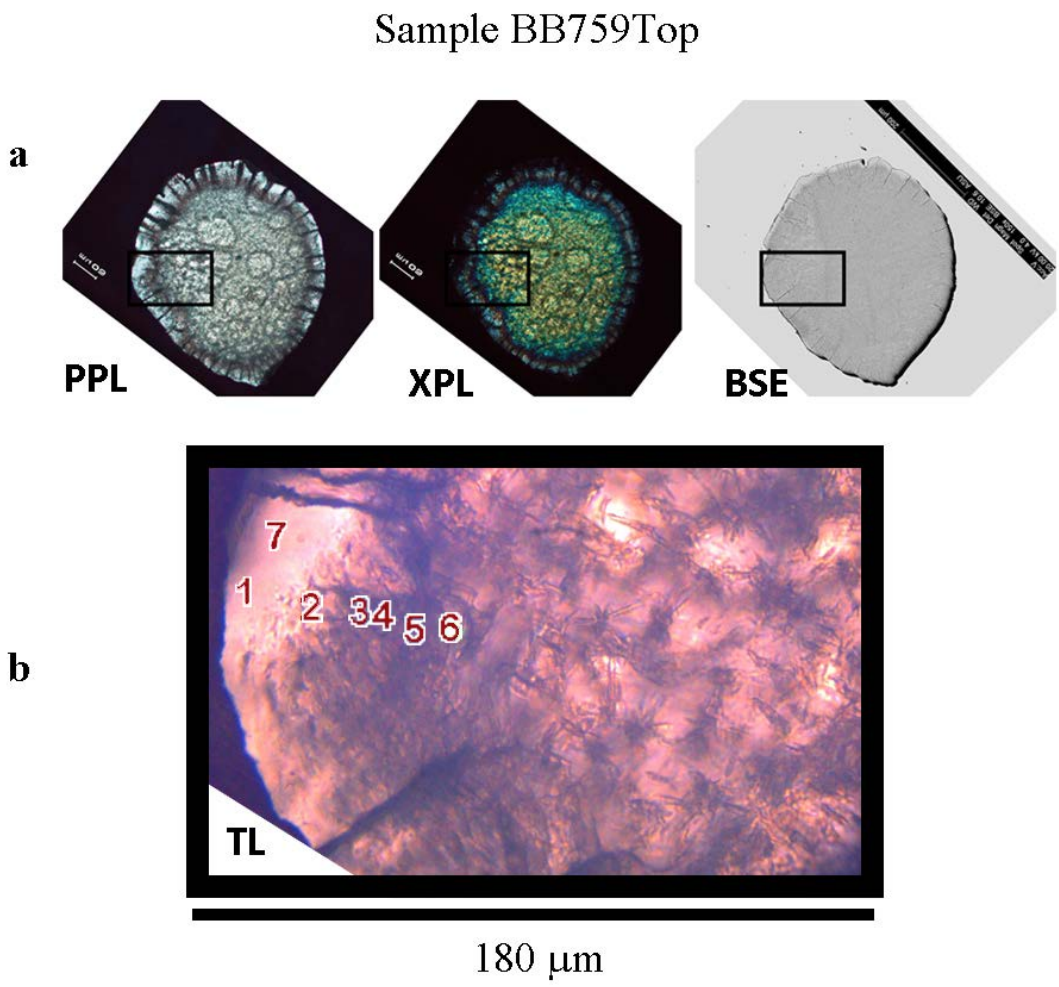

Fig. 3.8. Core-Rim Phase Variation in Partly Transformed Hydrous Olivine Sample BB759Top (~75 ppmw), Analyzed With Raman, and Optical and Backscattered Electron (BSE) Imaging.

Black rectangles outline the region mapped with Raman. a) Plane Polarized Light (PPL), Cross-Polarized Light (XPL) and BSE images provided for spatial context. b) A close-up Transmitted Light (TL) image of the core-rim boundary. The locations of individual Raman analyses are marked using their respective analysis numbers. Spectra for these individual analyses are provided in Fig. 3.4. A detailed BSE image of this region is presented in Fig. 3.11.

Regions containing wadsleyite are anisotropic in XPL, have "wispy" microtextures in PPL and TL, and are marked by reduced backscatter intensity (compared with ringwoodite). Regions containing ringwoodite are isotropic in XPL, and have a higher backscatter intensity (compared with wadsleyite). Olivine that did not transform is the dominant component of the sample cores. Olivine is anisotropic.

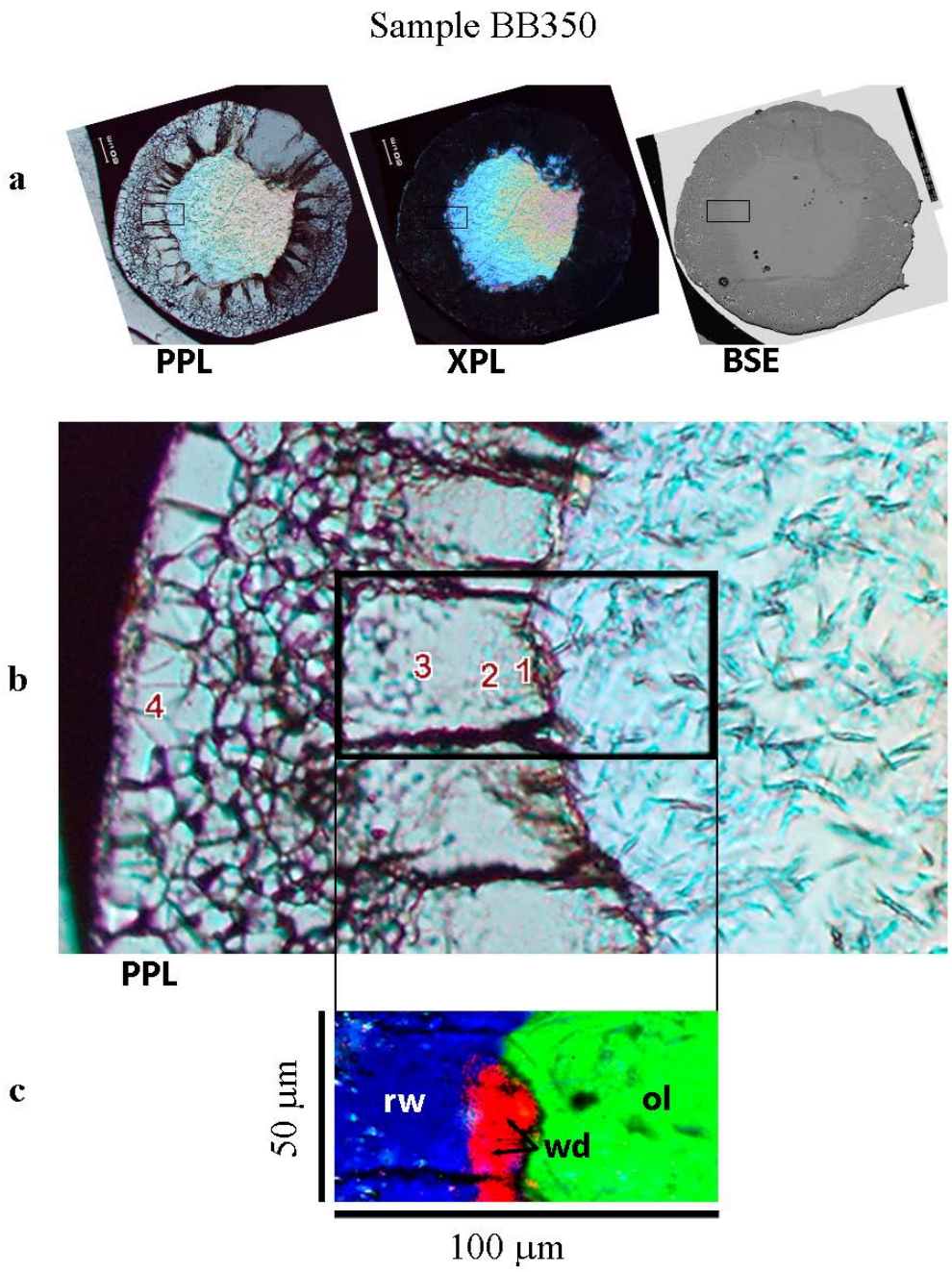

Fig. 3.9. Scanning Raman Analysis of Core-Rim Phase Variation in Partly Transformed Hydrous Olivine Sample BB350 (~289 ppmw), With Optical and Backscattered Electron (BSE) Images Provided for Context.

Black rectangles outline the region mapped with Raman. a) Plane Polarized Light (PPL), Cross-Polarized Light (XPL) and BSE images provided for spatial context. b) A close-up PPL image of the core-rim boundary. The locations of individual Raman analyses are marked using their respective analysis numbers. Spectra for these individual analyses are provided in Fig. 3.5. c) Raman mineralogy map (green = olivine; red/pink =

wadsleyite; blue = ringwoodite).). A detailed BSE image of this region is presented in Fig. 3.11.

Regions containing wadsleyite are anisotropic in XPL, have “wispy” microtextures in PPL, are marked by reduced backscatter intensity (compared with ringwoodite), and produce Raman peaks at ~723 cm^{-1} and ~919 cm^{-1}. Regions containing ringwoodite are isotropic in XPL, have a higher backscatter intensity (compared with wadsleyite), and produce Raman peaks at ~800 cm^{-1} and ~840 cm^{-1}. Olivine that did not transform is the dominant component of the sample cores. Olivine is anisotropic and produces Raman peaks at ~825 cm^{-1} and ~857 cm^{-1}.

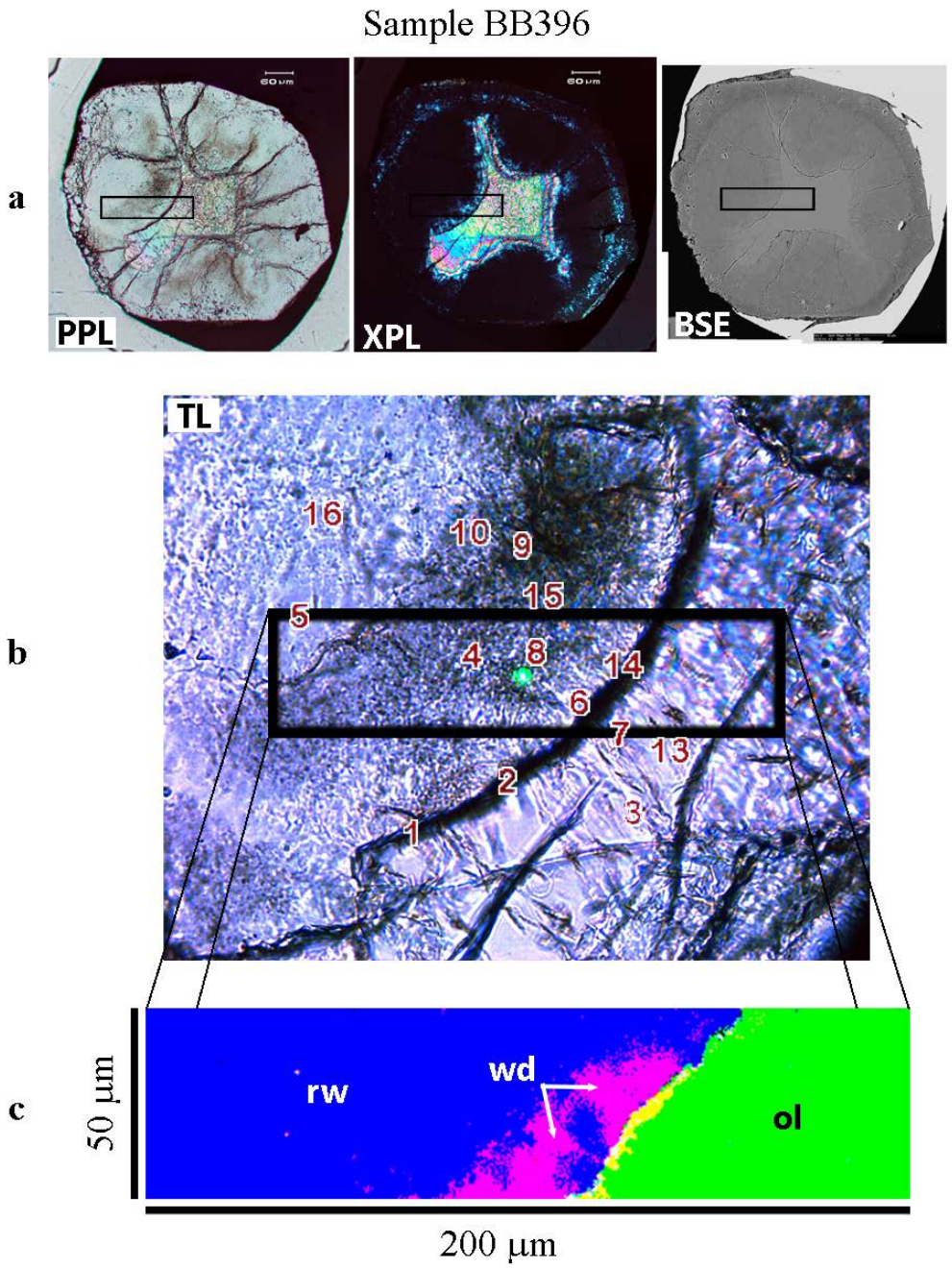

Fig. 3.10. Scanning Raman Analysis of Core-Rim Phase Variation in Partly Transformed Hydrous Olivine Sample BB396 (~289 ppmw), With Optical and Backscattered Electron (BSE) Images Provided for Context.

Black rectangles outline the region mapped with Raman. a) Plane Polarized Light (PPL), Cross-Polarized Light (XPL) and BSE images provided for spatial context. b) A close-up Transmitted Light (TL) image of the core-rim boundary. The locations of individual Raman analyses are marked using their respective analysis numbers. Spectra for these individual analyses are provided in Fig. 3.6. c) Raman mineralogy map (green =

olivine; red/pink = wadsleyite; blue = ringwoodite). A detailed BSE image of this region is presented in Fig. 3.11.

Regions containing wadsleyite are anisotropic in XPL, have "wispy" microtextures in PPL and TL, are marked by reduced backscatter intensity (compared with ringwoodite), and produce Raman peaks at ~723 cm^{-1} and ~919 cm^{-1}. Regions containing ringwoodite are isotropic in XPL, have a higher backscatter intensity (compared with wadsleyite), and produce Raman peaks at ~800 cm^{-1} and ~840 cm^{-1}. Olivine that did not transform is the dominant component of the sample cores. Olivine is anisotropic and produces Raman peaks at ~825 cm^{-1} and ~857 cm^{-1}.

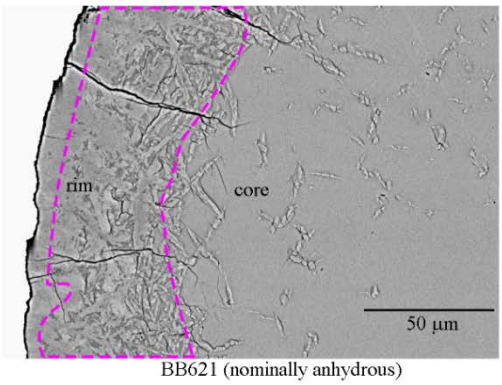

BB621 (nominally anhydrous)

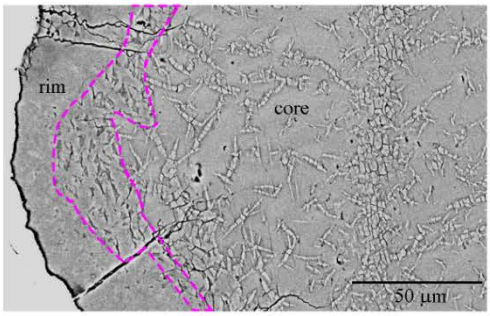

BB759Top (slightly hydrous)

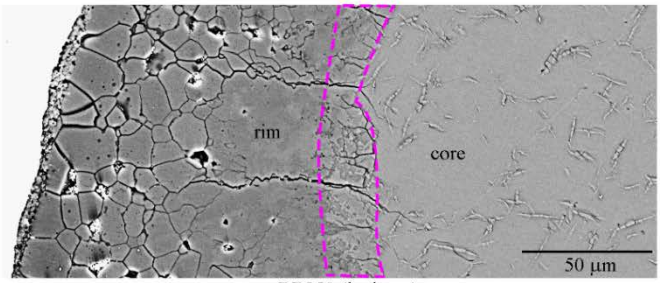

BB350 (hydrous)

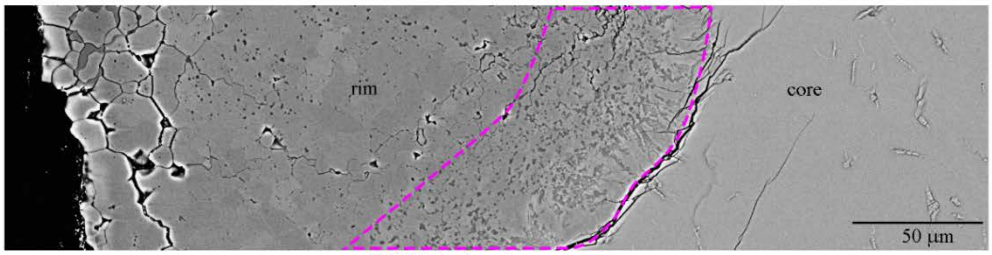

BB396 (hydrous)

Fig. 3.11. Backscatter Electron (BSE) Images of Representative Sections of Samples BB621 (Nominally Anhydrous), BB759Top (~75 ppmw), BB350 (~289 ppmw), and BB396 (~289 ppmw).

The regions depicted here for samples BB621, BB350 and BB396 include regions investigated by Raman (Figs. 3.7, 3.09, and 3.10). Dark lines are fractures resulting from

pressure-release. The three polymorphs of olivine produce different intensities of electron backscatter (seen here as brightness). Polyphase assemblages (the “mottled” regions) are outlined by the dashed lines.

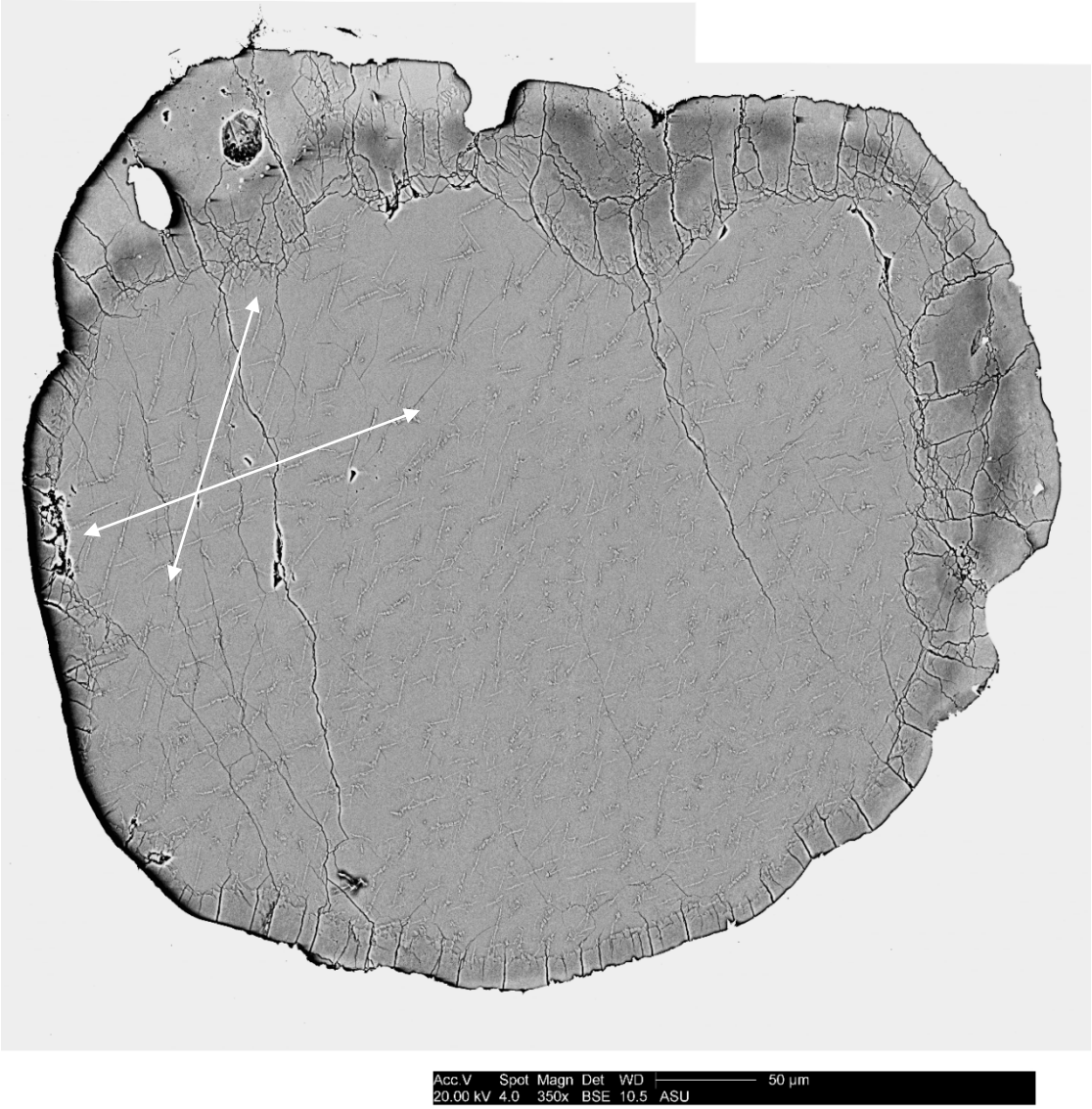

Fig. 3.12. BSE Image of Sample BB755A (~75 ppmw; 900 °C; 7 hrs.). Intracrystalline lenses of ringwoodite/wadsleyite tend to nucleate along preferred orientations (indicated by arrows).

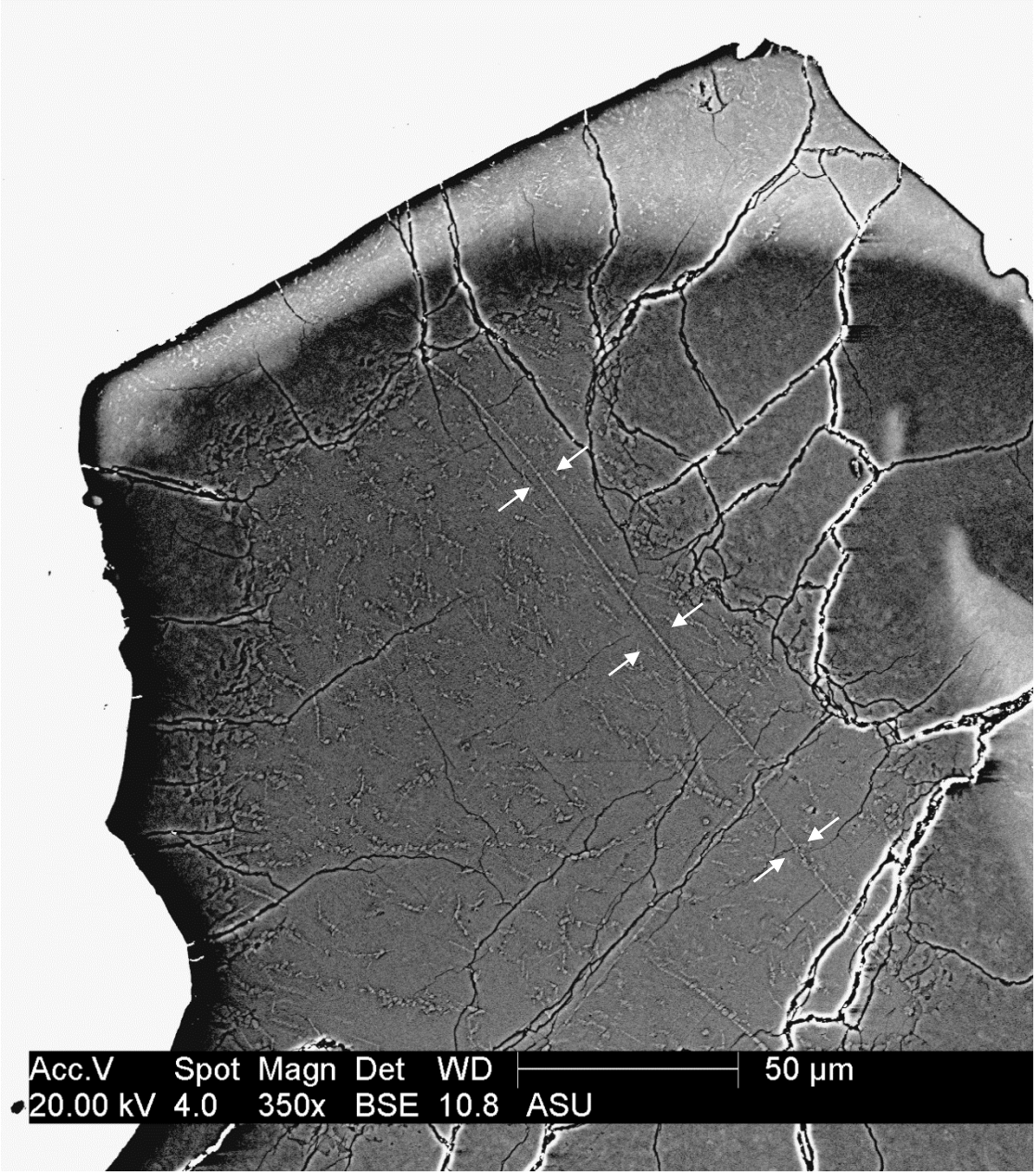

Fig. 3.13. BSE Image of Sample BB754Top (~75 ppmw; 900 °C; 26.13 hrs.).
Arrows indicate a linear intracrystalline phase (between arrows) extending from one part of the reaction rim, to another.

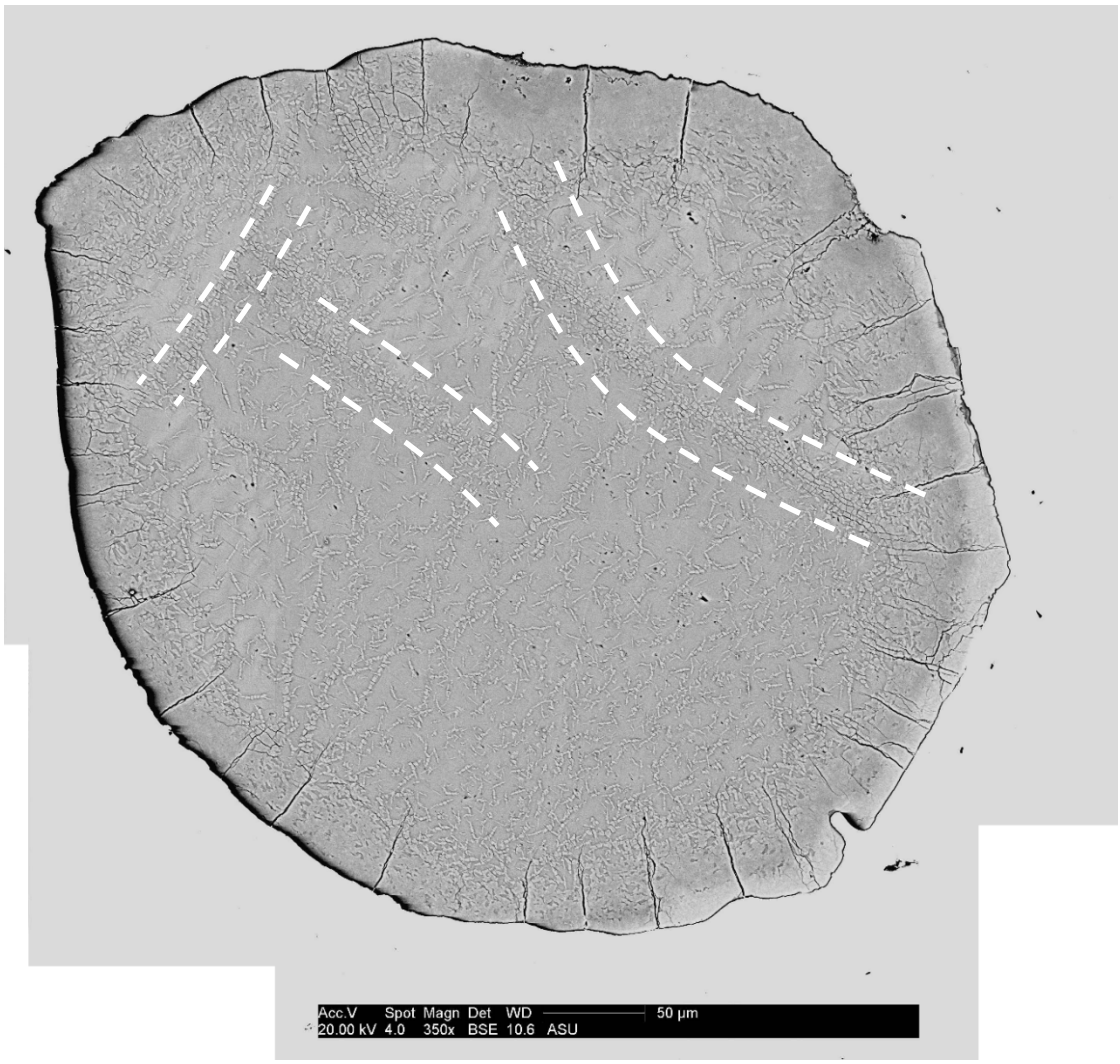

Fig. 3.14. BSE image of Sample BB759Top (~75 ppmw; 1100 °C; 0.67 hr.).
Dashed lines boarder linear features characterized by extensive intracrystalline nucleation of ringwoodite and wadsleyite.

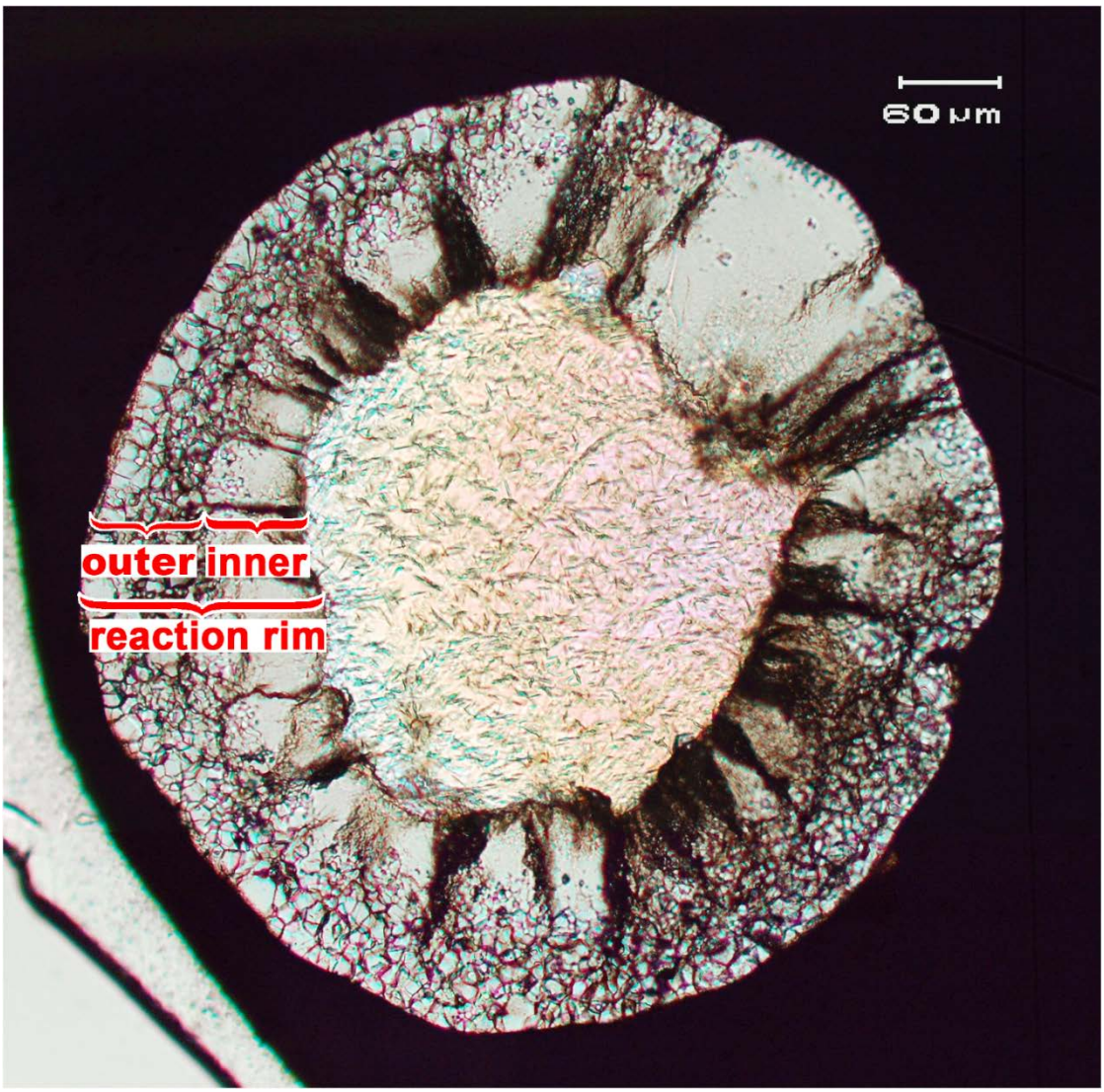

Fig. 3.15. Plane Polarized Image of an Abrupt Change in Rim Fracture Pattern Midway Between Inner and Outer Rim Edges of a Partly Transformed Hydrous Olivine Grain (BB350; ~289 ppmw).

This fracture pattern is suggestive of a change in texture (coarse to fine) from the outer edge inwards.

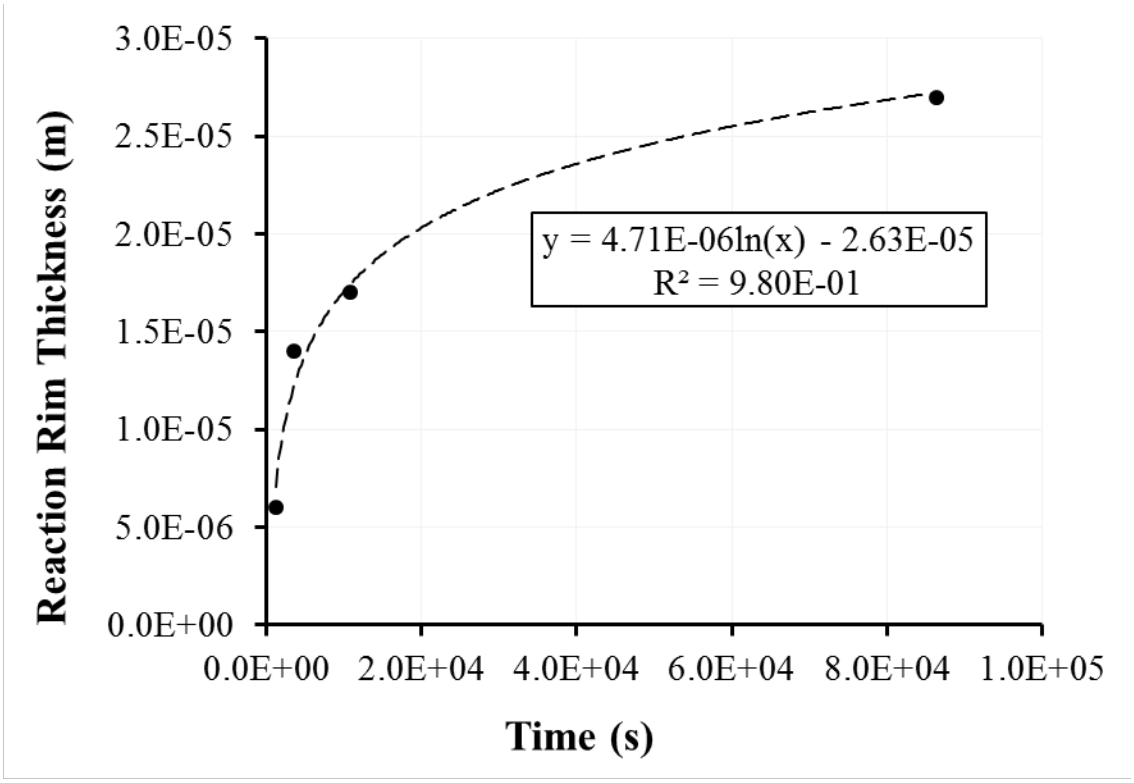

Fig. 3.16. Non-Linear Model of the Transformation Rim Growth Rate for Nominally Anhydrous Olivine at 1100 °C and 18 GPa (adapted from Diedrich *et al.*, 2009).

Data are from Diedrich *et al*., 2009. The dashed line represents the non-linear model calculated in the present study to describe the decreasing growth rate over time. The equation of this model and R^2 fit are given in the box.

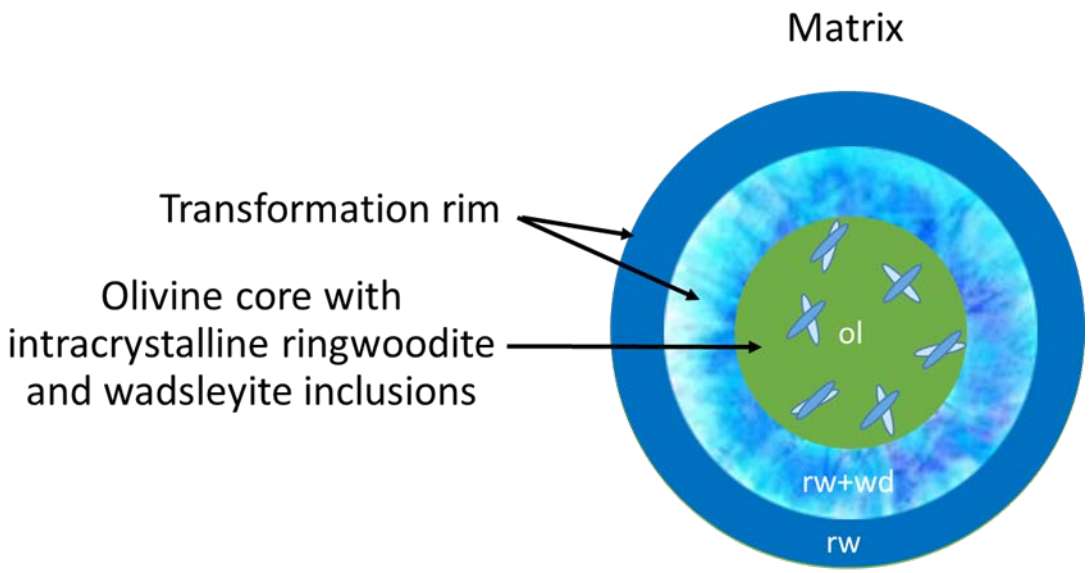

Fig. 3.17. Schematic Depicting a Partly Transformed Hydrous Olivine Grain in the Ringwoodite Stability Field That Surpassed the Critical Strain Necessary for Wadsleyite Nucleation in the Rim.

3.6. Acknowledgements

Samples were produced by T. Diedrich and W. Du Frane. We gratefully acknowledge the use of facilities within the LeRoy Eyring Center for Solid State Science at Arizona State University for analysis of these samples. We appreciate instrument assistance provided by E. Soignard, K. Mossman, Z. Liu, and S. Phrasavath, and others. We would also like to acknowledge student collaborator, J. Hu, for conducting complementary analyses that helped to elucidate our results. Funding for this research (Fall 2010-Summer 2011; Summer 2012) was provided by NSF grants (EAR208419 and EAR0739050) awarded to T. G. Sharp.

3.7. References for Chapter 3

Bai Q. and Kohlstedt D. L. 1992. Substantial hydrogen solubility in olivine and implications for water storage in the mantle. *Nature* 357:672-674.

Bell D. R. and Rossman G. R. 1992. Water in Earth's Mantle: The Role of Nominally Anhydrous Minerals. *Science* 255:1391-1397.

Burnley P. C. and Green II H. W. 1989. Stress dependence of the mechanism of the olivine-spinel transformation. *Nature* 338:753-756.

Chen J., Liu H., and Girard J. 2011. Comparative in situ X-ray diffraction study of San Carlos olivine: Influence of water on the 410 km seismic velocity jump in Earth's mantle. *American Mineralogist* 96:697-702.

Diedrich T., Sharp T. G. Leinenweber K., and Holloway J. R. 2009. The effect of small amounts of H2O on olivine to ringwoodite transformation growth rates and implications for subduction of metastable olivine. *Chemical Geology* 262:87-99.

Du Frane W. L., Sharp T. G., Mosenfelder J. L., and Leinenweber K. 2013. Ringwoodite growth rates from olivine with ~75 ppmw H2O: Metastable olivine must be nearly anhydrous to exist in the mantle transition zone. *Physics of the Earth and Planetary Interiors* 219:1-10.

Green II H. W., Chen W.-P., and Brudzinski M. R. 2010. Seismic evidence of negligible water carried below 400-km depth in subducting lithosphere. *Nature 467:828-831*.

Helffrich G. R. and Wood B. J. 2001. The Earth's Mantle. *Nature* 412:501-507.

Hosoya T., Kubo T., Ohtani E., Sano A., and Funakoshi K.-I. 2005. Water controls the fields of metastable olivine in cold subducting slabs. *Geophysical Research Letters* 32 (L17305):1-4.

Kerschhofer L., Sharp T. G., Rubie, D. C. 1996. Intracrystalline Transformation of Olivine to Wadsleyite and Ringwoodite Under Subduction Zone Conditions. *Science* 274: 79-81

Kerschhofer L., Dupas C., Liu M., Sharp T. G., Durham W. B., and Rubie D. C. 1998. Polymorphic transformations between olivine, wadsleyite and ringwoodite: mechanisms of intracrystalline nucleation and the role of elastic strain. *Mineralogical Magazine* 62:617-638.

Kerschhofer L., Rubie D. C., Sharp T. G., McConnell J. D. C., Dupas-Bruzek C. 2000. Kinetics of intracrystalline olivine–ringwoodite transformation. *Physics of the Earth and Planetary Interiors* 121:59–76.

Kirby S. H., Stein S., Okal E. A., and Rubie D. C. 1996. Metastable Mantle Phase Transformations and Deep Earthquakes in Subducting Oceanic Lithosphere. *Reviews of Geophysics* 34:261-306.

Kohlstedt D. L., Keppler H., Rubie D. C. 1996. Solubility of water in the α, β and γ phases of $(Mg,Fe)_2SiO_4$. *Contributions to Mineralogy and Petrology* 123:345-357.

Kubo T., Ohtani E. Kato T., Shinmei T., and Fujino K. 1998. Effects of water on the α-β transformation kinetics in San Carlos olivine. *Science* 281:85-87.

Leinenweber K. D., Mosenfelder J., Diedrich T., Soignard E., Sharp T. G., Tyburczy J. A., and Wang Y. 2006. High-pressure cells for in situ multi-anvil experiments. *High Pressure Research* 26:283-292.

Leinenweber K. D., Tyburczy J. A., Sharp T. G., Soignard E., Diedrich T., Petuskey W. B., Wang Y., and Mosenfelder J. L. 2012. Cell assemblies for reproducible multi-anvil experiments (the COMPRES assemblies). *American Mineralogist* 97:353-368.

Li Z.-X. A., Lee C.-T. A., Peslier A. H., Lenardic A., and Mackwell S. J. 2008. Water Water contents in mantle xenoliths from the Colorado Plateau and vicinity: Implications for the mantle rheology and hydration-induced thinning of continental lithosphere. B09210. *Journal of Geophysical Research* 113:1-22.

Liu M., Kerschhofer L., Mosenfelder J. L. Rubie D. C. 1998. The effect of strain energy on growth rates during the olivine-spinel transformation and implications for olivine metastability in subducting slabs. *Journal of Geophysical Research*. 103:23,897-23,909.

Liu M. and Yund R. A. 1995. The elastic strain energy associated with the olivine-spinel transformation and its implications. Physics of the Earth and Planetary Interiors 89:177-197.

Mosenfelder J. L., Marton F. C., Ross II C. R., Kerschhofer L., and Rubie D.C. 2001. Experimental constraints on the depth of olivine metastability in subducting lithosphere. *Physics of the Earth and Planetary Interiors* 127:165-180.

Mosenfelder J. L., Le Voyer M., Rossman G. R., Guan Y., Bell D. R., Asimow P. D., and Eiler J. M. 2011. Analysis of hydrogen in olivine by SIMS: Evaluation of standards and protocol. *American Mineralogist* 96 1725-1741.

Nitkiewicz A. and Sterner S. M. 1988. An improved Bond air mill for the preparation of spherical single crystals. *American Mineralogist* 73:662-666.

Pearson D. G., Brenker F. E., Nestola F., McNeill J., Nasdala L., Hutchison M. T., Matveev S., Mather K., Silversmit G., Schmitz S., Vekemans B., and Vincze L. 2014. Hydrous mantle transition zone indicated by ringwoodite included within diamond. Nature 507:221-224. doi:10.1038/nature13080.

Poirier J. P. 1981. On the kinetics of olivine-spinel transition. *Physics of the Earth and Planetary Interiors*. 26:179-187.

Rubie D. C. 1986. The catalysis of mineral reactions by water and restrictions on the presence of aqueous fluid during metamorphism. *Mineralogical Magazine* 50: 399-415.

Rubie D. C. and Ross II C. R. 1994. Kinetics of the olivine—spinel transformation in subducting lithosphere: experimental constraints and implications for deep slab processes. *Physics of the Earth and Planetary Interiors* 86:223—241.

Sung C.-M. and Burns R.G. 1976a. Kinetics of high-pressure phase transformations: Implications to the evolution of the olivine → spinel transition in the downgoing lithosphere and its consequences on the dynamics of the mantle. *Tectonophysics* 31:1-32.

Sung C.-M. and Burns R. G. 1976b. Kinetics of the olivine → spinel transition: Implications to deep-focus earthquake Genesis. *Earth and Planetary Science Letters* 32:165-170.

Vaughan P. J., Green II H. W., and Coe R. S. 1982. Is the olivine-spinel phase transformation martensitic? *Nature* 298:357-358.

Young T. E., Green II H. W., Hofmeister A. M., and Walker D. 1993. Infrared spectroscopic investigation of hydroxyl in β-$(Mg, Fe)_2SiO_4$ and coexisting olivine: Implications for mantle evolution and dynamics. *Physics and Chemistry of Minerals* 19:409-422.

4. REFERENCES

Aisenberg S. and Chabot R. 1971. Ion-Beam Deposition of Thin Films of Diamondlike Carbon. *Journal of Applied Physics* 42:2953-2958.

Alam T. M., Friedmann T. A., and Jurewicz A. J. G. 2002. Solid State ^{13}C MAS NMR Investigations of Amorphous Carbon Thin Films. In *Thin Films: Preparation, Characterization, Applications*, edited by Soriaga M. P., Stickney J., Bottomley L. A., and Kim Y.-G. New York: Springer, US. pp. 277-289.

Allton J. H., Kuhlman K. R., Allums K. K., Gonzalez C.P., Jurewicz A. J. G., Burnett D. S., and Woolum D. S. 2015. Genesis Solar Wind Sample 61422: Experiment in Variation of Sequence of Cleaning Solvent for Removing Carbon-Bearing Contamination (abstract 1896). 46th Lunar and Planetary Science Conference.

Allums K. K., Gonzalez C. P., Kuhlman K. R., and Allton J. H. 2015. Enhanced Cleaning of Genesis Solar Wind Sample 61348 for Film Residue Removal (abstract 2024). 46th Lunar and Planetary Science Conference.

Asplund M., Grevesse N., Sauval A. J., and Scott P. 2009. The Chemical Composition of the Sun. *Annual Review of Astronomy and Astrophysics* 47:481-522.

Bai Q. and Kohlstedt D. L. 1992. Substantial hydrogen solubility in olivine and implications for water storage in the mantle. *Nature* 357:672-674.

Barrat J. A., Zanda B., Moynier F., Bollinger C., Liorzou C., and Bayon G. 2012. Geochemistry of CI chondrites: Major and trace elements, and Cu and Zn Isotopes. *Geochimica et Cosmochimica Acta* 83:79–92.

Baumüller D., Butler, K., and Gehren T. 1998. Sodium in the Sun and in metal-poor stars. *Astronomy and Astrophysics* 338:637-650.

Bell D. R. and Rossman G. R. 1992. Water in Earth's Mantle: The Role of Nominally Anhydrous Minerals. *Science* 255:1391-1397.

Bochsler P. 2000. Abundances and Charge States of Particles in the Solar Wind. *Reviews of Geophysics* 38:247–266.

Bochsler P., Wimmer-Schweingruber R. F., and Wurz P. 2001. Sun, solar wind, meteorites and interstellar medium: What are the compositional relations? In *Solar and Galactic Composition*, edited by Wimmer-Schweingruber R. F. *Proceedings of the Joint SOHO/ACE Workshop in Bern, Switzerland 6–9 March 2001.* American Institute of Physics *Conference Proceedings* **598**:381-387.

Bochsler P. 2007. Minor ions in the solar wind. *The Astronomy and Astrophysics Review.* 14:1-40.

Brazzle J. D., Doheci M. R., and Mastrangelo C. H. 2004. Modeling and Characterization of Sacrificial Polysilicon Etching Using Vapor-Phase Xenon Difluoride. *Institute of Electrical and Electronics Engineers Micro Electro Mechanical Systems (Maastricht, The Netherlands, 2004).* pp. 737-740.

Breneman H. H. and Stone E. C. 1985. Solar Coronal and Photospheric Abundances from Solar Energetic Particle Measurements. *The Astrophysical Journal* 299:L57-L61.

Burger P. V. and Brearley A. J. 2005. Localized Chemical Redistribution During Aqueous Alteration in CR2 Carbonaceous Chondrites EET 87770 AND EET 92105 (abstract #2288). 36th Lunar and Planetary Science Conference.

Burnett D. S., Barraclough B. L., Bennett R., Neugebauer M., Oldham L. P., Sasaki C. N., Sevilla D., Smith N., Stansbery E., Sweetnam D., and Wiens R. C. 2003. The Genesis discovery mission: Return of solar matter to Earth. *Space Science Reviews* 105:509–534.

Burnett D. S., Woolum D. S., Jurewicz A. J. G., McKeegan K. D., and Guan Y. 2007. Solar Wind Elemental Abundances from Genesis Collectors (abstract #1843). 38th Lunar and Planetary Science Conference.

Burnett D. S., Jurewicz A. J. G., Woolum D. S., Wang J., Paque J. M., Nittler L. R., McKeegan K. D., Humayun M., Hervig R., Heber V. H., and Guan Y. 2015. Ion Implants as Matrix-Appropriate Measurement Standards for Geochemical Ion Probe Analyses. *Geostandards and Geoanalytical Research* 39:265-276.

Burnley P. C. and Green II H. W. 1989. Stress dependence of the mechanism of the olivine-spinel transformation. *Nature* 338:753-756.

Caffau E., Ludwig H.-G., Steffen M., Freytag B., and Bonifacio P. 2011. Solar Chemical Abundances Determined with a CO5BOLD 3D Model Atmosphere. *Solar Physics* 268: 255–269.

Chang F. I., Yeh R., Lin G., Chu P. B., Hoffman E., Kruglick E. J. J., and Kristofer S.J. Pister Gas-phase silicon micromachining with xenon difluoride. 1995. *SPIE* 2641:117-128.

Chen J., Liu H., and Girard J. 2011. Comparative in situ X-ray diffraction study of San Carlos olivine: Influence of water on the 410 km seismic velocity jump in Earth's mantle. *American Mineralogist* 96:697-702.

Cho S., Chasiotis I., Friedmann T. A., and Sullivan J. P. 2005. Young's modulus, Poisson's ratio and failure properties of tetrahedral amorphous diamond-like carbon for MEMS devices. *Journal of Micromechanics and Microengineering* 15:728–735.

Chu P., Chen J., Chu P., Lin G., Huang J., Warneke, B, and Pister, K. 1997. "Controlled Pulse-Etching with Xenon Difluoride," Int. Conf. Solid State Sensors and Actuators, (Transducers 97), pp. 665-668.

Cook W. R., Stone E. C., and Vogt R. E. 1984. Elemental Composition of Solar Energetic Particles. *The Astrophysical Journal*. 279:827-838.

Deng R.-C. and Williams P. 1989. Factors Affecting Precision and Accuracy in Quantitative Analysis by Secondary Ion Mass Spectrometry. *Analytical Chemistry* 67:1946-1948.

Diedrich T., Sharp T. G. Leinenweber K., and Holloway, J. R. 2009. The effect of small amounts of H2O on olivine to ringwoodite transformation growth rates and implications for subduction of metastable olivine. *Chemical Geology* 262:87-99.

Du Frane W. L., Sharp T. G., Mosenfelder J. L., and Leinenweber, K. 2013. Ringwoodite growth rates from olivine with ~75 ppmw H2O: Metastable olivine must be nearly anhydrous to exist in the mantle transition zone. *Physics of the Earth and Planetary Interiors* 219:1-10.

Feldman U. and Laming J. M. 2000. Element Abundances in the Upper Atmospheres of the Sun and Stars: Update of Observational Results. *Physica Scripta* 61:222-252.

Friedmann T. A., McCarty K. F., Barbour J. C., Siegal M. P., and Dibble D. C. 1996. Thermal stability of amorphous carbon films grown by pulsed laser deposition. *Applied Physics Letters* 68:1643-1645.

Friedmann T. A., Sullivan J. P., Knapp J. A., Tallant D. R., Follstaedt D. M., Medlin D. L., and Mirkarimi P. B. 1997. Thick stress-free amorphous-tetrahedral carbon films with hardness near that of diamond. *Applied Physics Letters* 71:3820-3822.

Fisk L. A., Schwadron N. A., and Zurbuchen T. H. 1998. On the Slow Solar Wind. *Space Science Reviews* 86:51-60.

Giammanco C., Wurz P., and Karrer R. 2008. Minor Ion Abundances in the Slow Solar Wind. *The Astrophysical Journal* 681:1703-1707.

Gloeckler G., Balsiger H., Bürgi A., Bochsler P., Fisk L. A., Galvin A. B., Geiss J., Gliem F., Hamilton D. C., Holzer T. E., Hovestadt D., Ipavich F. M., Kirsch E., Lundgren R. A., Ogilvie K. W., Sheldon R. B., and Wilken B. 1995. The solar WIND and suprathermal ion composition investigation on the WIND spacecraft. *Space Science Reviews* 71:79-124.

Goreva Y. G., Allums K. K., Gonzalez C. P., Jurewicz A. J., Burnett D. S., Allton J. H., Kuhlman K.R., Woolum D. 2015. Genesis Solar Wind Collector Cleaning Assessment: Update on 60336 Sample Case Study (abstract #2333). 46th Lunar and Planetary Science Conference.

Gottimukkala R. 2005. Growth and characterization of diamond and diamond like carbon films with interlayer. *M.S. thesis, Graduate School Theses and Dissertations, University of South Florida, Tampa, Florida, United States.* Paper 2904. http://scholarcommons.usf.edu/etd/2904.

Green II H. W., Chen W.-P., and Brudzinski M. R. 2010. Seismic evidence of negligible water carried below 400-km depth in subducting lithosphere. *Nature 467:828-831*.

Heber V. S., Wieler R., Baur H., Olinger C. T., and Burnett D. S. 2009. Noble gas composition of the solar wind as collected by the Genesis mission. *Geochimica et Cosmochimica Acta* 73:7414–7432.

Heber V. S., Guan Y., Jurewicz A. J. G., Kallio A. P., Olinger C., Woolum D. S., McKeegan K. D., Burnett D. S. 2010. Solar Wind Elemental Fractionation: Genesis C and O Fluences by Backside SIMS Profiling – Preliminary Data. (abstract #2234). 41st Lunar and Planetary Science Conference.

Heber V. S., Guan Y., Jurewicz A. J. G., Smith S., Olinger C., McKeegan K. D., and Burnett D. S. 2011. Abundances of Carbon, Nitrogen and Oxygen in the Solar Wind Measured by Backside SIMS Depth Profiling (abstract #2642). 42nd Lunar and Planetary Science Conference.

Heber V. S., Jurewicz A. J. G., Janney P., Wadhwa M., McKeegan K. D., and Burnett D. S. 2012. Magnesium Isotopic Composition of Solar Wind as Test for Isotopically Fractionated Solar Wind: A Progress Report (abstract # 2921). 43rd Lunar and Planetary Science Conference.

Heber V. S., McKeegan K. D., Smith S., Jurewicz A. J. G., Olinger C., Burnett D. S., and Guan Y. 2014a. Accurate Analysis of Shallow Solar Wind Ion Implants by SIMS Backside Depth Profiling (abstract #1203). 45th Lunar and Planetary Science Conference.

Heber V. S., McKeegan K. D., Bochsler P., Duprat J., Burnett D. S. 2014b. The Elemental Composition of Solar Wind with Implications for Fractionation Processes During Solar Wind Formation (abstract #2117). 45th Lunar and Planetary Science Conference.

Heber V. S., McKeegan K. D., Burnett D. S., Duprat J., Guan Y., Jurewicz A. J. G., Olinger C. T., Smith S. P. 2014c. Accurate analysis of shallowly implanted solar wind ions by SIMS backside depth profiling. *Chemical Geology* 390:61–73.

Helffrich G. R. and Wood B. J. 2001. The Earth's Mantle. *Nature* 412:501-507.

Hosoya T., Kubo T., Ohtani E., Sano A., and Funakoshi, K.-I. 2005. Water controls the fields of metastable olivine in cold subducting slabs. *Geophysical Research Letters* 32 (L17305):1-4.

Huss G. R., Ogliore R. C., Jurewicz A. J. G., Burnett D., S. and Nagashiima K. 2015. Estimate of Solar Wind Hydrogen Fluence from the Genesis Collectors (abstract #2577). 46th Lunar and Planetary Science Conference.

Ip W.-H. and Axford W. I. 1991. On the First Ionization Potential Effect of the Solar Corona. *Advances in Space Research* 11:(1)247-(1)250.

Ipavich F. M., *et al.* 1998. *Journal of Geophysical. Research* 103(A8):17215.

Ipavich F. M., Bochsler P., Lasley S. E., Paquette, J. A., and Wurz P. 1999. The Abundance of Sodium in the Solar Wind as Measured by SOHO/CELIAS/MTOF. *EOS* 80:256.

Ipavich F. M., Paquette J. A., Bochsler P., Lasley S. E., and Wurz P. 2001. Solar wind iron isotopic abundances: Results from SOHO/CELIAS/MTOF. In *American Institute of Physics Conference Proceedings.* Institute of Physics Publishing Ltd. 121-126.

Jones C. L., Brearley A. J. 2006. Experimental Aqueous Alteration of the Allende Meteorite under Oxidizing Conditions: Constraints on Asteroidal Alteration. *Geochimica et Cosmochimica Acta* 70:1040–1058.

Jurewicz A. J. G., Burnett D. S., Wiens R. C., Friedmann T. A., Hays C. C., Hohlfelder R. J., Nishiizumi K., Stone J. A., Woolum D. S., Becker R. H., Butterworth A. L., Campbell A., Ebihara M., Franchi I. A., Heber V. S., Hohenberg C. M., Humayun M., McKeegan K. D., McNamara K., Meshik A. P., Pepin R. O., Schlutter D. J., and Wieler R. 2003. The Genesis solar-wind collector materials. *Space Science Reviews* 105:535–560.

Jurewicz A. J. G., Burnett D. S., Woolum D. S., McKeegan K. D., Guan Y., and Hervig R. L. 2007. SIMS Results for Solar-Wind Elemental Abundances from Genesis Collectors (contribution # 5299). 70th Annual Meteoritical Society Meeting.

Jurewicz A. J. G., Burnett D. S., Woolum D. S., McKeegan K. D., Guan Y., and Hervig R. 2008. Solar Elemental Abundances from Genesis Collectors: Fe/Mg, Constraining Solar-Wind FIP Fractionation, and Comparisons with CI Chondrites (abstract # 2272). 39th Lunar and Planetary Science Conference.

Jurewicz A. J. G., Hervig R., Burnett D. S., Wiens R., Wadhwa M., and Rieck K. 2009. Fractionation of Mg Isotopes between the Sun's Photosphere and the Solar Wind (contribution # 5422). 72nd Annual Meteoritical Society Meeting.

Jurewicz A. J. G., Burnett D. S., Woolum D. S., McKeegan K. D., Heber V., Guan Y., Humayun M., and Hervig R. 2011. Solar-Wind Fe/Mg and a Comparison with CI Chondrites (abstract # 1917). 42nd Lunar and Planetary Science Conference.

Kerschhofer L., Sharp T. G., Rubie, D. C. 1996. Intracrystalline Transformation of Olivine to Wadsleyite and Ringwoodite Under Subduction Zone Conditions. *Science* 274: 79-81

Kerschhofer L., Dupas C., Liu M., Sharp T. G., Durham W. B., and Rubie D. C. 1998. Polymorphic transformations between olivine, wadsleyite and ringwoodite: mechanisms of intracrystalline nucleation and the role of elastic strain. *Mineralogical Magazine* 62:617-638.

Kerschhofer L., Rubie D. C., Sharp T. G., McConnell J. D. C., Dupas-Bruzek C. 2000. Kinetics of intracrystalline olivine–ringwoodite transformation. *Physics of the Earth and Planetary Interiors* 121:59–76.

Kirby S. H., Stein S., Okal E. A., and Rubie D. C. 1996. Metastable Mantle Phase Transformations and Deep Earthquakes in Subducting Oceanic Lithosphere. *Reviews of Geophysics* 34:261-306.

Krieger A. S., Timothy A. F., and Roelof E. C. 1973. A Coronal Hole and its Identification as the Source of a High Velocity Solar Wind Stream. *Solar Physics* 29:505-525.

Kohlstedt D. L., Keppler H., Rubie D. C. 1996. Solubility of water in the α, β and γ phases of $(Mg,Fe)_2SiO_4$. *Contributions to Mineralogy and Petrology* 123:345-357.

Krot A. N., Keil K., Scott E. R. D., Goodrich C. A., and Weisberg M. K. 2014. Classification of Meteorites and Their Genetic Relationships. In *Meteorites and Cosmochemical Processes,* edited by Davis A. M. Treatise on Geochemistry (Second Edition), vol. 1. Amsterdam: Elsevier. pp. 1-63.

Kubo T., Ohtani E., Kato T., Shinmei T., and Fujino K. 1998. Effects of water on the α-β transformation kinetics in San Carlos olivine. *Science* 281:85-87.

Laming J. M. 2015. The FIP and Inverse FIP Effects in Solar and Stellar Coronae. *Living Reviews in Solar Physics.* arXiv:1504.08325v1 [astro-ph.SR].

Leinenweber K. D., Mosenfelder J., Diedrich T., Soignard E., Sharp T. G., Tyburczy J. A., and Wang Y. 2006. High-pressure cells for in situ multi-anvil experiments. *High Pressure Research* 26:283-292.

Leinenweber K. D., Tyburczy J. A., Sharp T. G., Soignard E., Diedrich T., Petuskey W. B., Wang Y., and Mosenfelder J. L. 2012. Cell assemblies for reproducible multi-anvil experiments (the COMPRES assemblies). *American Mineralogist* 97:353-368.

Li Z.-X. A., Lee C.-T. A., Peslier A. H., Lenardic A., and Mackwell S. J. 2008. Water Water contents in mantle xenoliths from the Colorado Plateau and vicinity: Implications for the mantle rheology and hydration-induced thinning of continental lithosphere. B09210. *Journal of Geophysical Research* 113:1-22.

Liu M., Kerschhofer L., Mosenfelder J. L. Rubie D. C. 1998. The effect of strain energy on growth rates during the olivine-spinel transformation and implications for olivine metastability in subducting slabs. *Journal of Geophysical Research*. 103:23,897-23,909.

Liu M. and Yund R. A. 1995. The elastic strain energy associated with the olivine-spinel transformation and its implications. Physics of the Earth and Planetary Interiors 89:177-197.

Lodders K., Palme H., and Gail H. P. 2009. Abundances of the elements in the solar system. In *Landolt-Börnstein, New Series, Astronomy and Astrophysics, Vol. VI/4B, Chap. 4.4,* edited by Trümper J. E. Berlin, Heidelberg, New York:Springer-Verlag. pp. 560-630.

Luo J. K., Fu Y. Q., Le H. R., Williams J. A., Spearing S. M., and Milne W. I. 2007. Diamond and diamond-like carbon MEMS. *Journal of Micromechanics and Microengineering* 17:S147–S163.

McSween H. Y. 1993. Cosmic or Cosmuck? *Meteoritics* 28:3-4.

Morlok A., Bischoff A., Stephan T., Floss C., Zinner E., and Jessberger E. K. 2006. Brecciation and Chemical Heterogeneities of CI chondrites. *Geochimica et Cosmochimica Acta* 70:5371–5394.

Mosenfelder J. L., Marton F. C., Ross II C. R., Kerschhofer L., and Rubie D.C. 2001. Experimental constraints on the depth of olivine metastability in subducting lithosphere. *Physics of the Earth and Planetary Interiors* 127:165-180.

Mosenfelder J. L., Le Voyer M., Rossman G. R., Guan Y., Bell D. R., Asimow P. D., and Eiler J. M. 2011. Analysis of hydrogen in olivine by SIMS: Evaluation of standards and protocol. *American Mineralogist* 96 1725-1741.

Nitkiewicz A. and Sterner S. M. 1988. An improved Bond air mill for the preparation of spherical single crystals. *American Mineralogist* 73:662-666.

Outka D. A., Hsu W. L., Boehme D. R., Yang N. Y. C., Ottesen D. K., Johnsen H. A., Headley T. J., and Clift W. M. 1994. Compilation of Diamond-Like Carbon Properties for Barriers and Hard Coatings. *Sandia Report*, SAND94-8219, UC-404.

Palme H., Lodders K., and Jones A. 2014. Solar System Abundances of the Elements. In *Planets, Asteroids, Comets and the Solar System,* edited by Davis A. M. Treatise on Geochemistry (Second Edition), vol. 2. Amsterdam: Elsevier. pp.15-36.

Pearson D. G., Brenker F. E., Nestola F., McNeill J., Nasdala L., Hutchison M. T., Matveev S., Mather K., Silversmit G., Schmitz S., Vekemans B., and Vincze L. 2014. Hydrous mantle transition zone indicated by ringwoodite included within diamond. Nature 507:221-224. doi:10.1038/nature13080.

Pilleri P., Reisenfeld D. B., Zurbuchen T. H., Lepri S. T., Shearer P., Gilbert J. A., von Steiger R., and Wiens R. C. 2015. Variations in Solar Wind Fractionation as Seen by ACE/SWICS and the Implications for Genesis Mission Results. *The Astrophysical Journal* 812:1-10.

Poirier J. P. 1981. On the kinetics of olivine-spinel transition. *Physics of the Earth and Planetary Interiors*. 26:179-187.

Raymond J. C. 1999. Composition Variations in the Solar Corona and Solar Wind. *Space Science Reviews* 87:55–66

Reames D. V. 1994. Coronal Element Abundances Derived from Solar Energetic Particles. *Advances in Space Research* 14:(4)177-(4)180.

Reames D. V. 1995. Coronal Abundances Determined from Energetic Particles. *Advances in Space Research* 15:(7)41-(751).

Reames D. V. 1998. Solar Energetic Particles: Sampling Coronal Abundances. *Space Science Reviews* 85:327-340.

Reisenfeld D. B., Burnett D. S., Becker R. H., Grimberg A. G., Heber V. S., Hohenberg C. M., Jurewicz A. J. G., Meshik A., Pepin R. O., Raines J. M., Schlutter D. J., Wieler R., Wiens R. C., and Zurbuchen T. H. 2007. Elemental Abundances of the bulk solar wind: Analyses from Genesis and Ace. *Space Science Reviews* 130:79–86.

Reisenfeld D. B., Wiens R. C., Barraclough B. L., Steinberg J. T., Neugebauer M., Raines J., and Zurbuchen T. H. 2013. Solar Wind Conditions and Composition During the Genesis Mission as Measured by in situ Spacecraft. *Space Science Reviews* 175:125–164.

Rieck K. D., Jurewicz A. J. G., Wadhwa M., Burnett D. S., Hervig R., and Wiens R. 2010. SIMS Measurements of Mg Isotopes in the Solar Wind (abstract #2391). 41st Lunar and Planetary Science Conference.

Robertson J. 2002. Diamond-like amorphous carbon. *Materials Science and Engineering* R 37:129-281.

Rubie D. C. 1986. The catalysis of mineral reactions by water and restrictions on the presence of aqueous fluid during metamorphism. *Mineralogical Magazine* 50: 399-415.

Rubie D. C. and Ross II C. R. 1994. Kinetics of the olivine—spinel transformation in subducting lithosphere: experimental constraints and implications for deep slab processes. *Physics of the Earth and Planetary Interiors* 86:223—241.

Schmeltz J. T., Reames D. V., von Steiger R., and Basu S. 2012. Composition of the Solar Corona, Solar Wind, and Solar Energetic Particles. *The Astrophysical Journal* 755:33 doi:10.1088/0004-637X/755/1/33.

Schmitt A. K. and Zack T. 2012. High-sensitivity U–Pb rutile dating by secondary ion mass spectrometry (SIMS) with an O_2^+ primary beam. *Chemical Geology 332-333: 65-73.*

Scott E. R. D. and Krot A. N. 2007. Chondrites and their components. In *Meteorites, Comets and Planets, Chapter 1.07,* edited by Davis. A. M. Treatise on Geochemistry Update 1, Elsevier, online at http://www.sciencedirect.com/science/referenceworks/9780080437514

Scott P., Grevesse N., Asplund M., Sauval A. J., Lind K., Takeda Y., Collet R., Trampedach R., and Hayek W. 2015. The elemental composition of the Sun.: I. The intermediate mass elements Na to Ca.* *Astronomy & Astrophysics* 573, A25:1-19.

Sinha D. 2002. Correlating Chemical and Water Purity to the Surface Metal on Silicon Wafer During Wet Cleaning Process. *Chemical Engineering Communications.* 189:974-984.

Sung, C.-M. and Burns, R.G. 1976a. Kinetics of high-pressure phase transformations: Implications to the evolution of the olivine → spinel transition in the downgoing lithosphere and its consequences on the dynamics of the mantle. *Tectonophysics* 31:1-32.

Sung, C.-M. and Burns, R. G. 1976b. Kinetics of the olivine → spinel transition: Implications to deep-focus earthquake Genesis. *Earth and Planetary Science Letters* 32:165-170.

Vainonen E., Likonen J., Ahlgren T., Haussalo P., Keinonen J., and Wu C. H. 1997. Hydrogen migration in diamond-like carbon films. *Journal of Applied Physics* 82: 3791-3796.

Vaughan P. J., Green II H. W., and Coe R. S. 1982. Is the olivine-spinel phase transformation martensitic? *Nature* 298:357-358.

Veryovkin I. V., Zinovev A. V., Tripa C. E., and Burnett D. S. 2014. Depth Profiling of Genesis Diamond-on-Silicon Collectors: Direct Comparison Between Frontside and Backside Approaches (abstract # 2795). 45th Lunar and Planetary Science Conference.

Vogel N., Heber V. S., Baur H., Burnett D. S., and Wieler R. 2011. Argon, krypton, and xenon in the bulk solar wind as collected by the Genesis mission. *Geochimica et Cosmochimica Acta* 75:3057-3071.

von Steiger R., Schwadron N. A., Fisk L. A., Geiss J., Gloeckler G., Hefti S., Wilken B., Wimmer-Schweingruber R. F., and Zurbuchen T. H. 2000. Composition of quasistationary solar wind flows from Ulysses/Solar Wind Ion Composition Spectrometer. *Journal of Geophysical Research* 105:27217–27238.

von Steiger R., Zurbuchen T. H., and McComas D. J. 2010. Oxygen flux in the solar wind: Ulysses observations. *Geophysical Research Letters*, vol. 37, L22101, doi:10.1029/2010GL045389.

von Steiger R. and Zurbuchen T. H. 2011. Polar coronal holes during the past solar cycle: Ulysses observations. *Journal of Geophysical Research*, vol. 116, A01105, doi:10.1029/2010JA015835.

Waeselmann N., Humayun M., Goreva Y. S., Burnett D. S., and Jurewicz A. 2015. Impact of Acid-Cleaning on the Solar Wind Layer of Genesis Flight Wafers – Partial Dissolution and Recovery of the Lithium-6 Implant (abstract #1266). 46th Lunar and Planetary Science Conference.

Wang W. H., Bolse W., Illgner C., Lieb K. P., Keinonen J., and Ewert J. C. 1997. Recrystallization and diffusion in sodium-implanted silicon. *Thin Solid Films* 295:169-177.

Webb D. F. (2000) Coronal Mass Ejections: Origins, Evolution, and Role in Space Weather. *IEEE Transactions on Plasma Science* 28:1795-1806.

Williams P. 1979. The Sputtering Process and Sputtered Ion Emission. *Surface Science* 90:588-634.

Williams P. and Baker J. E. 1981. Implantation and Ion Beam Mixing in Thin Film Analysis. *Nuclear Instruments and Methods* 182-183:15-24.

Wilson R. G., Stevie F. A., and Magee C. W. 1989. Secondary ion mass spectrometry: A practical handbook for depth profiling and bulk impurity analysis. New York: John Wiley and Sons, Inc. 384 p.

Young T. E., Green II H. W., Hofmeister A. M., and Walker D. 1993. Infrared spectroscopic investigation of hydroxyl in β-$(Mg, Fe)_2SiO_4$ and coexisting olivine: Implications for mantle evolution and dynamics. *Physics and Chemistry of Minerals* 19:409-422.

APPENDIX A

CLEANING PROTOCOL

PART 1. Protocol for Pre-cleaning the Tools & Containers:

1. Clean Teflon beakers according to 1a-1b.

    a. Submerge beakers in sub-boiling 50% nitric acid for 16 hours.

    b. Submerge beakers in sub-boiling Milli-Q® water for 8 hours.

2. Clean the following according to 2a.-2e.:
    - Glass dishes, beakers, pipets
    - Fluoroware/plastic test tubes, vials, containers

    a. Put items in a ~2% Micro-90 solution (cold). Then heat both the beaker and the water bath it sits in to 50°C on a hot plate or in the sonicator (~15 minutes).

    b. Ultrasonicate* items for 15 minutes.

    c. Rinse items in ultra-high purity (UHP) water (1st rinse).

    d. Ultrasonicate* items in fresh UHP water for 15 minutes.

    e. Transfer items to a dust-free countertop in a cleanroom hood, and either a) blow off water droplets with clean air (a handheld pipette + squeeze bulb works), or b) use ethanol to remove H_2O. Keep items covered if air-drying! Once dry, immediately store cleaned sample containers in a clean sealable plastic bag.

*Note: Low power (≤35V) is recommended for ultrasonicating all samples and standards prior to thinning, and for glassware. Low power is strongly recommended for cleaning 1) Genesis wafers to reduce the risk of opening any microcracks that may be present, 2) Diamond-on-Silicon to reduce the risk of delamination, and 3) glassware. Ultrasonication is not recommended for cleaning thinned samples.

PART II. Pre-cleaning Protocol:

3. Place graphite planchets and silicon (separately) in UHP water at room temperature in clean glass beakers, and clean according to steps 4b.-4e. **Do not expose these samples to Micro-90.**

4. Clean the following flight samples / implant standards / substrates / blanks according to 4a.-4e.:

- DoS (Diamond-like Carbon (DlC) on Silicon)
- Glass standards
- GaAs

a. Place items in a ~2% Micro-90 solution (cold). Then heat both the beaker and the water bath it sits in to 50°C on a hot plate (~15 minutes).

b. Ultrasonicate* items on low power for 15 minutes.

c. Rinse items in UHP water (1st rinse).

d. Ultrasonicate* items on low power in fresh UHP water for 15 minutes.

e. Let the items soak in fresh UHP water until ready for Part III.

*Note: Low power (≤35V) is recommended for ultrasonicating all samples and standards prior to thinning, and for glassware. Low power is strongly recommended for cleaning 1) Genesis wafers to reduce the risk of opening any microcracks that may be present, 2) Diamond-on-Silicon to reduce the risk of delamination, and 3) glassware. Ultrasonication is not recommended for cleaning thinned samples.

PART III. Cleaning Protocol:

5. After performing pre-cleaning work, clean the following flight samples / implant standards / substrates / blanks according to 5a.-5e.:

- DoS
- Glass standards
- GaAs
- **Silicon**

a. Warm Xylenes (in a water bath) to 70°C (~ 15 minutes). (57-60°C is OK.) **Make sure to use enough Xylenes so that it won't all evaporate away (use 25+ mL per beaker).**

b. Ultrasonicate* items on low power in warm xylenes for 10-15 minutes.

c. Ultrasonicate* items on low power in acetone for 10-15 minutes. (48-57°C is OK.) **Make sure to use enough acetone so that it won't all evaporate away (use 30+ mL per beaker).**

d. Ultrasonicate* items on low in (m)ethanol for 10-15 minutes. (48-57°C is OK.) **Make sure to use enough (m)ethanol so that it won't all evaporate away (use 20+ mL per beaker).**

e. 10. Rinse all items in fresh UHP water at room temperature.

6. Place Silicon flight samples / implant standards / substrates / blanks in fresh UHP water at room temperature and clean according to steps 7b.-7e. **Do not expose Si samples to Micro-90.**

7. Clean the following flight samples / implant standards / substrates / blanks according to steps 7a.-7e.:

- DoS
- Glass standards
- GaAs

a. Place items in a ~2% Micro-90 solution (cold). Then heat the beakers and the water bath they sit in to 50°C on a hot plate (~15 minutes). **Micro-90 etches Si. Do not allow Micro-90 to contact the polished faces of any Si samples/standards.**

b. Ultrasonicate* items on low power for 10-15 minutes.

c. Rinse items in UHP water (1st rinse).

d. Ultrasonicate* items on low power in fresh UHP water for 10-15 minutes.

e. Rinse items in UHP water, and let them soak in fresh UHP water until the start of RCA cleaning, or use tweezers to transfer all items (face-up) to a dust-free countertop in a cleanroom hood, and blow off water droplets with clean air (a pipette + squeeze bulb works). **Avoid touching the front (polished) surfaces of the wafers. Keep items covered if air-drying!**

*Note: Low power (≤35V) is recommended for ultrasonicating all samples and standards prior to thinning, and for glassware. Low power is strongly recommended for cleaning 1) Genesis wafers to reduce the risk of opening any microcracks that may be present, 2) Diamond-on-Silicon to reduce the risk of delamination, and 3) glassware. Ultrasonication is not recommended for cleaning thinned samples.

PART IV. RCA Cleaning Protocol (slightly modified from the work of Sinha (2002)):

8. Check that there is enough SC1* and SC2** solution available, if not, make more.

*** SC1 (parts by volume) =**

Ammonium Hydroxide	**:**	**Hydrogen Peroxide**	**:**	**UHP Water**
NH_4OH	**:**	**H_2O_2**	**:**	**H_2O**
1	**:**	**2**	**:**	**20**

One batch:	1mL	:	2mL	: 20mL	=	23mL
Double batch:	2mL	:	4mL	: 40mL	=	46mL
2.5 batch:	2.5mL	:	**5mL**	: 50mL	=	57.5mL

**** SC2 (parts by volume) =**

Hydrochloric Acid	**:**	**Hydrofluoric Acid**	**:**	**UHP Water**
HCl	**:**	**HF**	**:**	**H_2O**
0.7	**:**	**1**	**:**	**100**

Half batch:	0.35mL:		0.5mL	: 50mL	=	50.85mL
One batch:	0.7mL	:	1mL	: 100mL	=	101.7mL

Only use ultra-high purity chemicals.
Keep the hydrogen peroxide chilled while it is in storage to retard dissociation.
Only add the hydrogen peroxide when you are ready to use the SC1 solution.

To make SC1:

Combine **Ammonium Hydroxide (NH_4OH)** and **ultra-high purity water (H_2O)** in a **1-to-20** ratio by volume. Make in bulk for future use. **Do not add peroxide until right before you are ready to use SC1, otherwise the peroxide may dissociate while in storage at room temperature.** When you are ready to use SC1, add **Hydrogen Peroxide (H_2O_2)** to the Ammonium Hydroxide-water solution in a **2:21** ratio by volume to make enough SC1 for use that day. An easy convention is to add 1mL H_2O_2 per every 10.5mL of NH_4OH+H_2O solution. Usually 15 mL of total solution is used for each tiny beaker of wafer fragments. Usually 60 mL of total solution is prepared at a time for use in 4 small Teflon beakers (the number I currently have available).

To make SC2:

Combine **Hydrochloric Acid (HCl)**, **Hydrofluoric Acid (HF)**, and **ultra-high purity water (H_2O)** in a **0.7-to-1-to-100** ratio by volume. Make in bulk for future use.

---

9. Clean the following flight samples / implant standards / substrates / blanks according to 9a.-9e.:

-DoS
-Si
-Glass Standards

a. Place items in Teflon beakers. Add SC1.
***SC1 = $NH_4OH:H_2O_2:H_2O$ (1:2:20)**

b. Heat both the beaker and the water bath it sits in to 60°C on a hot plate or in the sonicator. (53-56°C is OK.)

c. Ultrasonicate items on low power for 10-15 minutes.

d. Rinse items in UHP water at room temperature. Transfer waste solution to a waste container.

e. Let items soak in fresh UHP water until the next step.

---

10. Following SC1 cleaning, clean the following flight samples / implant standards / substrates / blanks according to 10a.-10g. **Wear two pairs of gloves!**

-DoS
- Si

a. Place items in Teflon beakers. Add SC2.
**** SC2 = $HCl:HF:H_2O$ (0.7:1:100)**

b. At room temperature, gently agitate the beaker of solution manually for 5 minutes. **Do not use sonicator.**

c. Rinse items in UHP water at room temperature

d. Allow items to soak in fresh UHP water until the space is cleared of solvents, chemical waste, and anything that could re-contaminate the samples if they accidently touched. Dispose of waste in separate containers according to lab protocol.

e. Remove items one at a time from the UHP water and blow off remaining water droplets with clean air (a handheld pipette + squeeze bulb works).

f. Use tweezers to transfer all dry items (face-up) to a dust free countertop in a cleanroom hood. Avoid touching the front (polished) surfaces of the wafers.

g. Photo-document the cleanliness of the items using a camera + microscope. Immediately afterwards, store items in clean containers.

PART V. Protocol for mounting and thinning:

11. Any clean Si flight samples / implant standards / blanks can be sent to Evans Analytical Group (EAG) for mounting and professional polishing. Clean DoS flight samples / implant standards / blanks can be mounted and thinned according to steps 11a.-11e.:

a. Use a pipet to apply epoxy to the intended substrate and mount the DoS DlC-side down into the epoxy (usually M-Bond 610).

b. Press together between aluminum foil the sample and the substrate using the metal piston designed for this purpose and cure the epoxy in an oven as per the epoxy's curing instructions.

c. Etch away the Si using XeF_2 as per the protocol of Argonne National Lab.

d. Use clean, compressed gas (e.g., air, Nitrogen) to remove trace residue. **Do not wet sample to remove residue! Residue is reactive and often forms a contaminant film during wet cleaning!**

e. Photo-document the samples.

APPENDIX B

WAFER THINNING EXPERIMENTS

Overview

Sample thinning is required for SIMS backside depth profiling analysis of Genesis solar wind collectors (Chapter 1). This appendix provides a brief overview of the basic approaches to sample thinning (both mechanical and chemical), the challenges inherent in each method, and the major results of various DoS thinning experiments. These results shaped how Genesis samples were prepared for SIMS backside depth profiling analysis. Also featured in this appendix are images of Genesis samples, both thinned and not-thinned.

Silicon

Silicon wafer thinning is a commercially available procedure, and has been used to prepare Genesis Si solar wind collectors for SIMS backside depth profiling analysis (e.g., Heber *et al.*, 2011). Most Genesis Si wafers designated for thinning as part of the present study were sent to Evans Analytical Group (EAG). Once there, each sample would be mounted face-down on a silicon substrate, and the backside of the Si wafer would be ground and polished until the sample was reduced to the desired thickness. In the course of polishing, it was common for sample edges to break and delaminate from the Si substrate, an effect exacerbated by the application of surface coatings (e.g., Si) to create a boundary layer between the sample and the mounting epoxy. Less often, and regardless of whether surface coatings were applied, entire samples would delaminate during the polishing process and be lost.

Once thinning was complete the remaining Si film would be as level as its substrate. Bubbles in the underlying mounting epoxy and contamination on the frontside surface would cause localized distortions in the Si film. Only the most level, uniform regions were targeted for SIMS analysis.

Heber V. S., Guan Y., Jurewicz A. J. G., Smith S., Olinger C., McKeegan K. D., and Burnett D. S. 2011. Abundances of Carbon, Nitrogen and Oxygen in the Solar Wind Measured by Backside SIMS Depth Profiling (abstract #2642). 42nd Lunar and Planetary Science Conference.

Genesis Si 60824

This sample was professionally mounted on Si and polished to the requested thickness (~1 μm) in preparation for SIMS backside depth profiling analysis. SIMS analyses were performed in the center of the Newton's Rings, where the film has more uniform thickness.

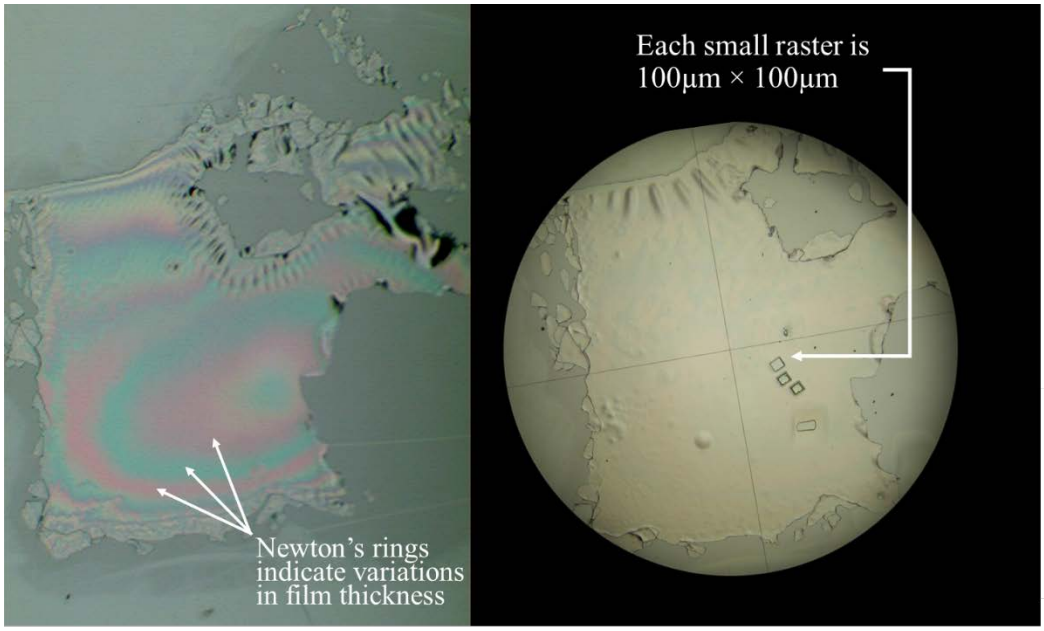

Genesis Si 61189

This sample was professionally mounted on Si and polished to the requested thickness (~2.5 μm) in preparation for SIMS analysis. Backside implantation of reference ions was performed on this sample. This is the first Genesis Si sample to be internally standardized using backside-implanted reference ions.

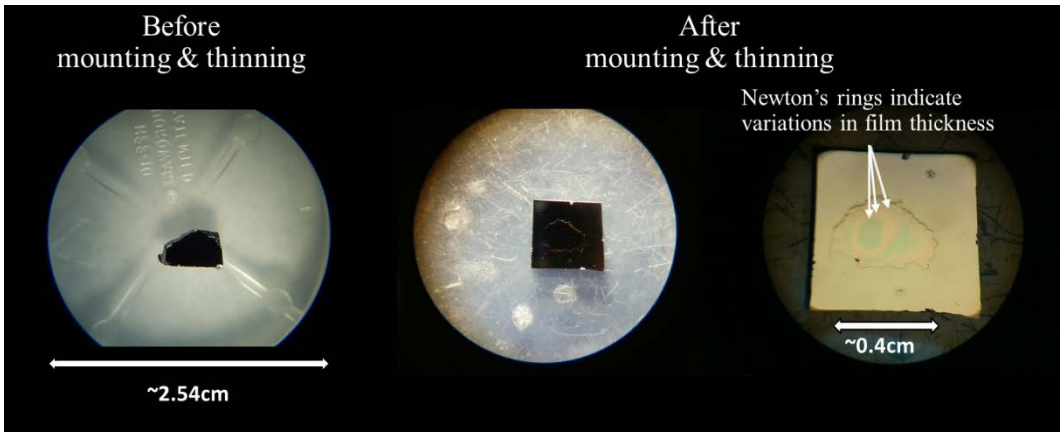

Genesis Si 61367.

This sample was accidently destroyed during professional mechanical polishing. It delaminated from its silicon substrate.

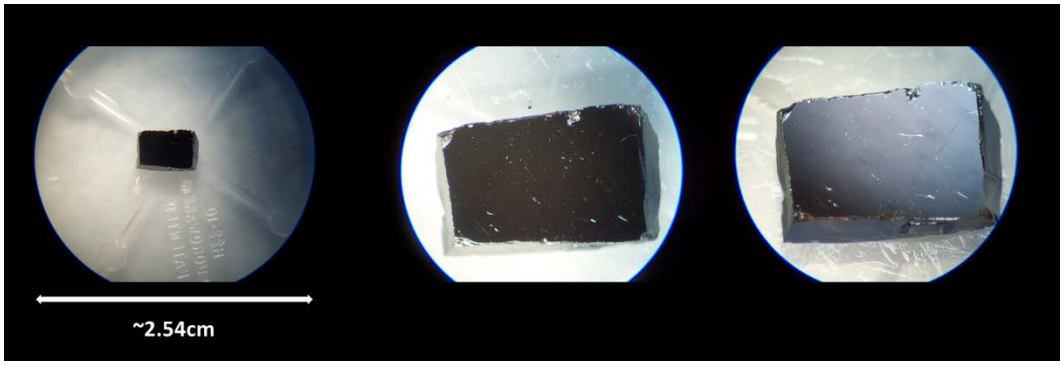

Diamond-like Carbon (DlC) on Silicon (DoS)

Unlike silicon wafers, the thinning of DoS wafers is not routinely performed for commercial purposes. As such, there was much experimentation to achieve the desired result. DlC film has internal stresses that cause it to be particularly fragile when the supporting Si backing is removed. As observed in the present study, Genesis era material and modern material differ in fragility, perhaps due to changes in the manufacturing and annealing processes implemented over time or to achieve different purposes (Chapter 1). Consequently, the thinning methods that work for modern DoS do not necessarily work for Genesis-era material.

Both chemical etching and mechanical polishing methods were tested as part of the present study. All approaches required the DoS wafer to be mounted face-down on a supportive substrate. All approaches ultimately resulted in some damage or distortion to the DlC film, however, the most successful (least destructive) approach was dry chemical etching with XeF_2. XeF_2 etching entails the removal of the Si backing through chemical reaction with XeF_2 gas in an etching chamber (Chapter 1). This reaction leaves the backside of the DoS exposed, except for a trace residue that can be removed with compressed gas. Coating the DlC with a protective metal film to create a boundary layer between the sample and the mounting epoxy decreased its structural integrity during thinning. All dry chemical etching was performed at ANL with assistance from I. V. Veryovkin and C. S. Miller, who helped develop this technique for Genesis DoS collectors. Details are provided in the main text of Chapter 1.

Following thinning, the Genesis DlC film was very fragile, and susceptible to delamination caused by its internal stresses. Etching alone resulted in minimal damage and distortion. However, damage could be induced or exacerbated by external factors. Particulates and bubbles in the underlying epoxy cause the Genesis DlC to bow outward around these localized features. Temperature changes (e.g., cooling caused by the evaporation of cleaning agents from the sample mount) can induce differential thermal expansion or contraction between the DlC and the supporting substrate, creating fractures and bulges. Such features do not necessarily remain local, but can propagate across a sample, especially if there are repeated thermal events. Only the most level, uniform regions were targeted for SIMS analysis. Fortunately, most of these external factors can be minimized or eliminated in future work.

Thinning Tests on Modern DoS

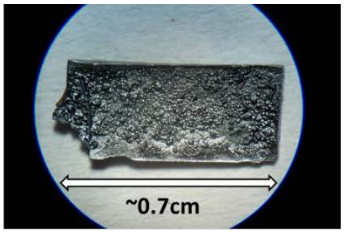

Liquid chemical etching – sample detached from substrate

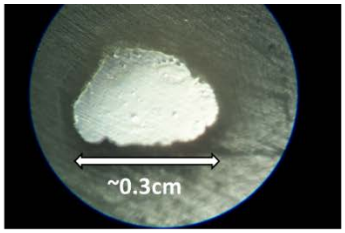

Polishing – sample conformed to uneven substrate

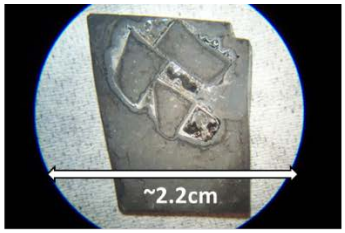

Polishing with leveling Si – still uneven polishing

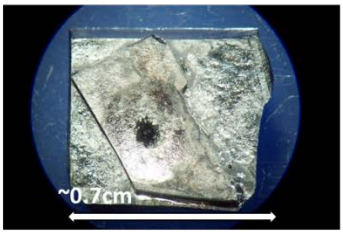

Dimpling and liquid chemical etching – sample bowed up in the crater

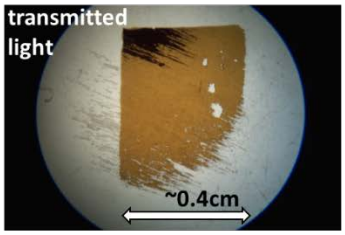

Polishing – too uneven, sample tearing

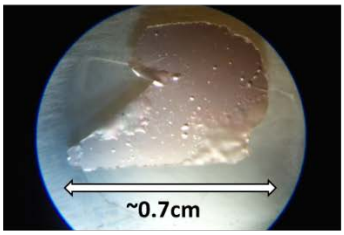

Polishing – topography, but mostly avoidable = success!

Thinning Tests on Flight-era DoS and on 1 Modern Piece of DoS for Comparison

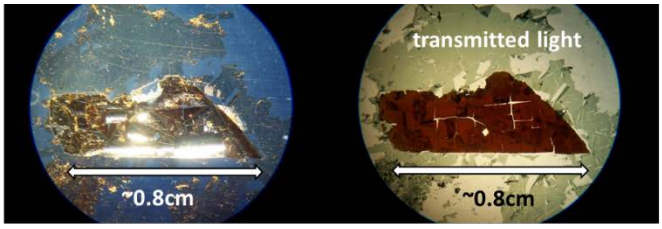

Polishing a ^{23}Na implant + SIMS – gold coat did not prevent eventual fracturing of the sample

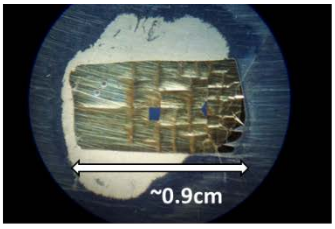

Polishing a ^{23}Na implant – sample fractured

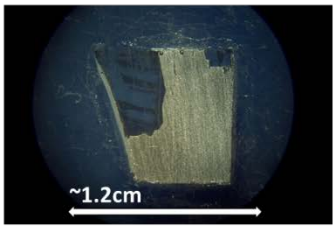

Polishing ^{25}Mg + ^{26}Mg implant – sample fractured and parts detached

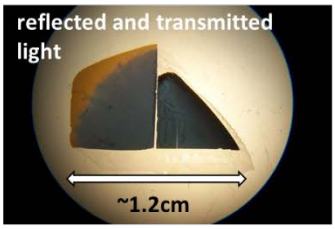

Polishing <u>modern blank (left)</u> – uneven *but intact!* Polishing ^{44}Ca implant (right) – fractures developed!

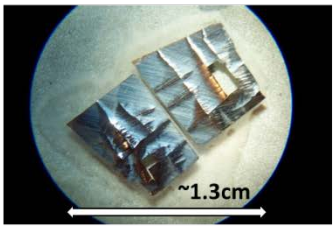

Polishing Mg implant and blank – fractures in both

6

Metal Coatings on Flight-Era DoS: Do They Help Preserve DoS During XeF_2 Etching? (No.)

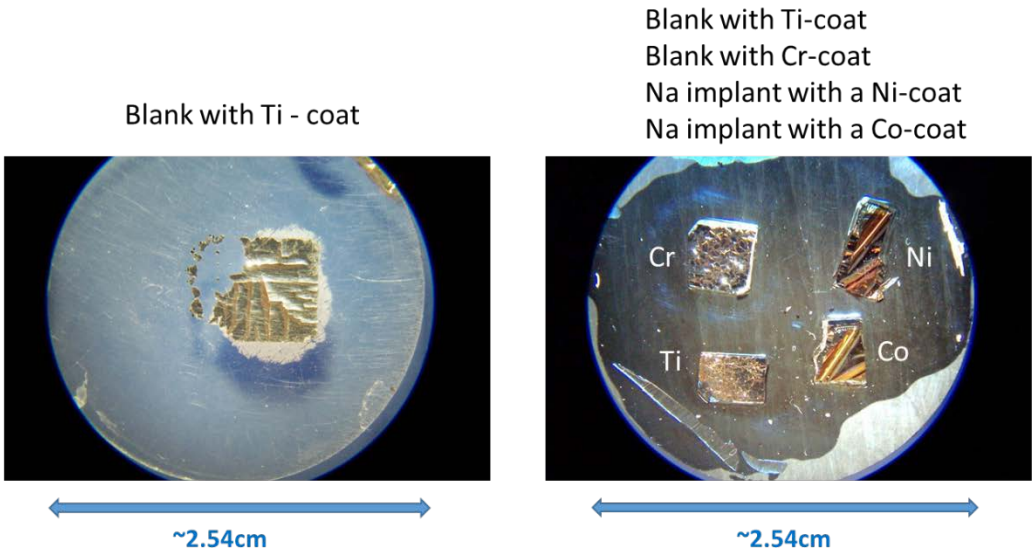

Metal coatings (Ti, Cr, Ni, Co) do not protect DlC film during XeF_2 etching. Samples fractured, delaminated from the substrate, and/or curled.

Etching Residue Removal Tests:

Part 1 – Etching. A DoS standard (Na and K) and a blank piece of modern DoS were thinned to DlC by XeF_2 etching for SIMS backside depth profiling analysis. Etching residue was formed.

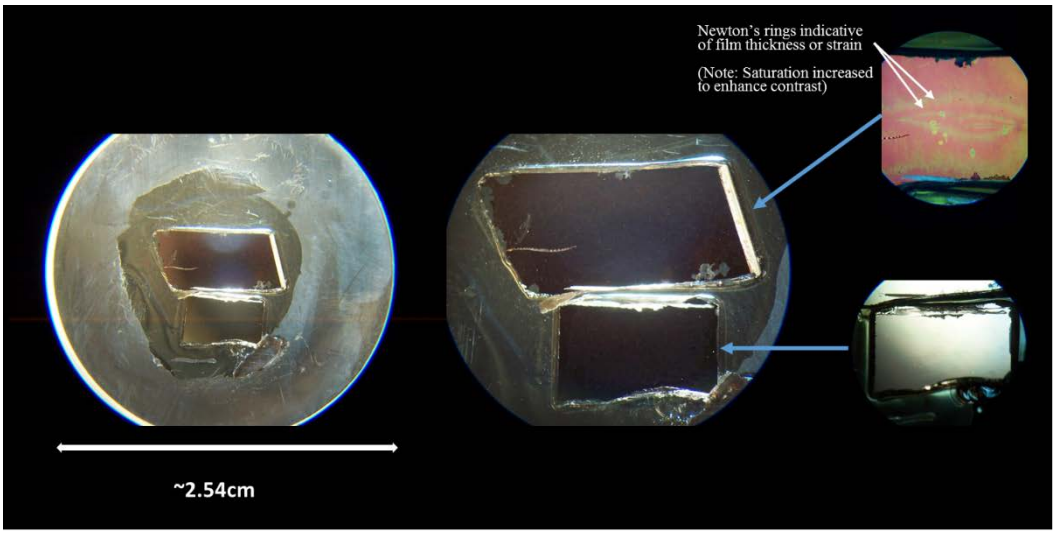

DlC standard begins to fracture, perhaps in part due to some pre-existing plane of weakness in the substrate, but the blank modern DoS remains intact.

Part 2 – Residue Removal Efforts. Air, ultra-high-purity water, and (later) acetone were used to remove surface contaminants. Compressed air removed residue from the etching process relatively effectively. Water was not effective. A whitish film produced when the sample was exposed to water was eventually removed with acetone (not shown).

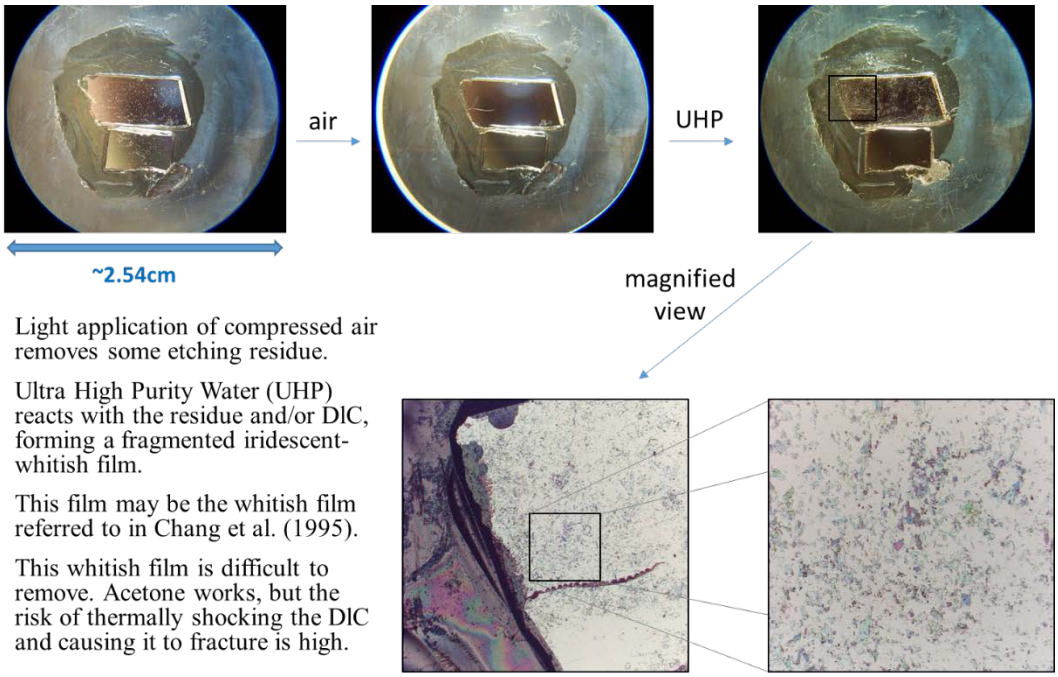

Thinning Tests on Genesis DoS

Genesis Dos 60630. This is the first Genesis DoS collector thinned to DlC for SIMS backside depth profiling analysis. This sample was mechanically polished part-way to the DlC film, and then XeF_2 etching was used to remove the remaining Si. This is also the first Genesis DoS collector to be etched using XeF_2.

Unfortunately, when the sample was being removed from the polishing mount, the surface was accidently contaminated with acetone and dissolved rubber cement solution. Acetone was used to remove the cement film. Unfortunately, fractures and localized delamination occurred in response to the differential thermal contraction between the sample and the substrate following acetone evaporation from the surface. SIMS was performed on the cleanest, most level portions of the sample. The accident increased surface contamination, but did not significantly affect the results of SIMS analysis (Chapter 1).

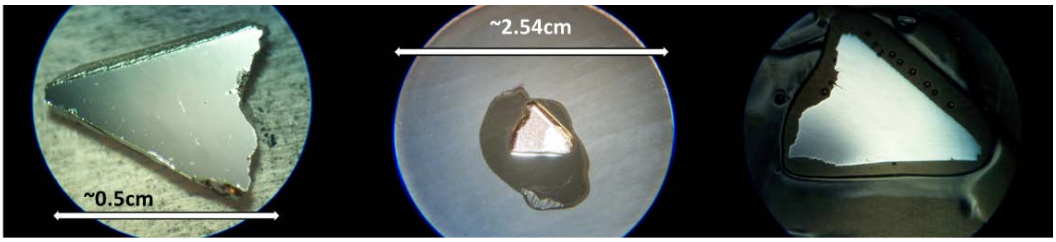

Not mounted

Mounted on graphite planchet

Mechanically polished partway

XeF_2 etch removes Si without detaching or seriously fracturing DlC = success!

...Oops...

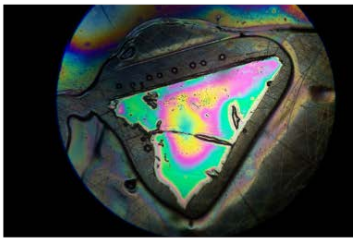

While removing planchet from polishing chuck with acetone, sample fell into acetone + rubber cement solution….

Genesis Dos 60630 (continued).

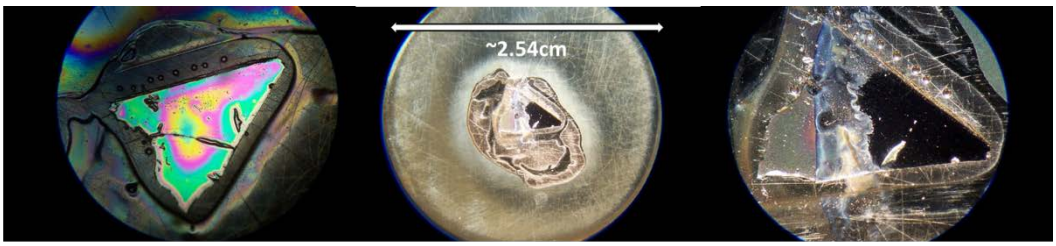

Rubber cement-coated sample

Acetone and lab wipes were used to delicately remove rubber cement film

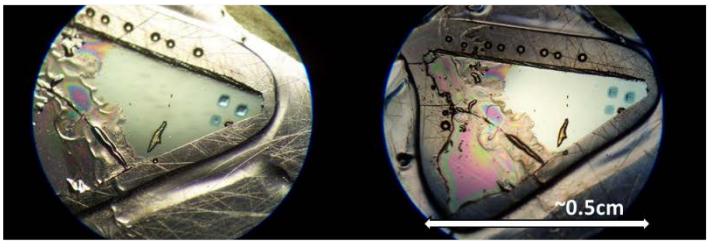

Enough rubber cement film was removed to permit SIMS analyses, although a gold-coat was required to ground the sample…

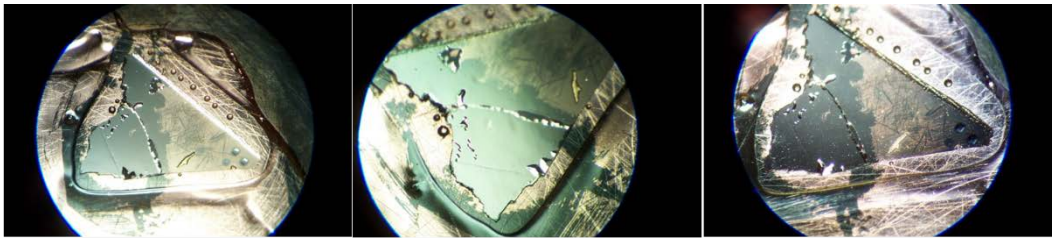

Acetone, alcohol and lab wipes were used to delicately remove more of the rubber cement film, until all the rubber cement film was removed. The gold coat partly rubs off.

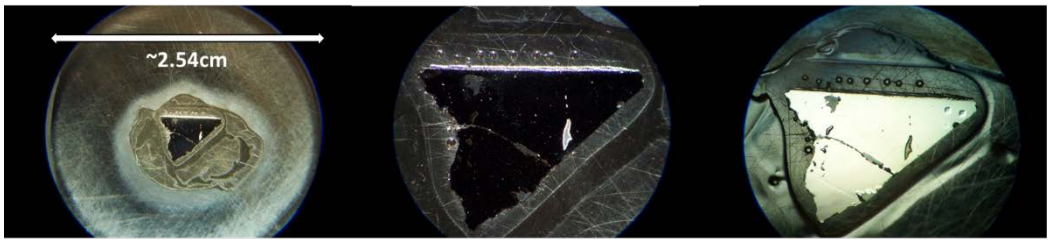

The gold coat was removed with KI solution.

Genesis Dos 60407. XeF_2 etching successfully removed the Si backing, leaving the DlC film intact.

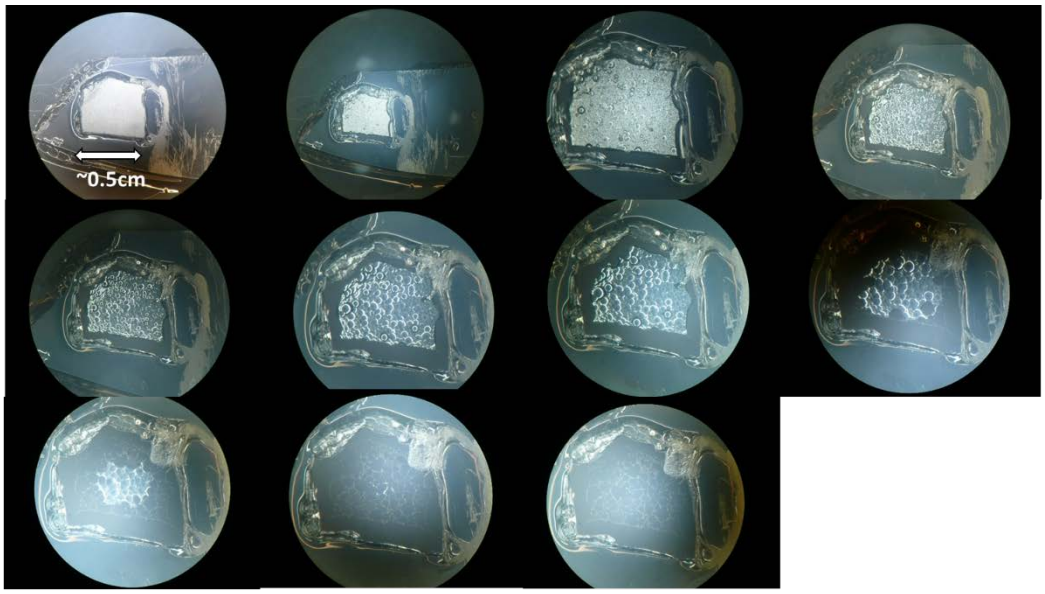

XeF_2 etching at ANL (7:57AM to 9:19AM) – Photos by I. V. Veryovkin

Following etching, part of the sample locally delaminated, producing topography. Later, delamination was exacerbated by surface cleaning methods involving acetone.

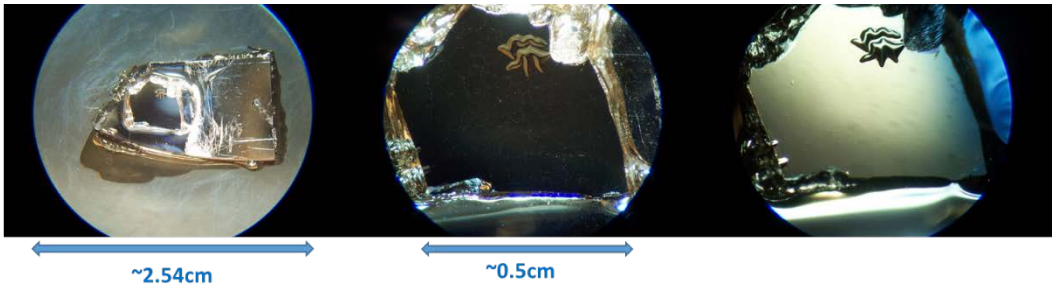

Sample underwent XeF_2 etching, removing the Si successfully, with only one bubble developing where the sample delaminated from the substrate. The sample remained stable until additional cleaning steps were performed.

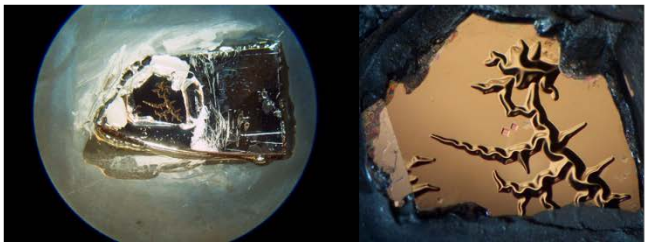

Genesis Dos 60867. XeF_2 etching successfully removed the Si backing, leaving the DlC film almost completely intact. Some fractures in the DlC were observed at the end of etching.

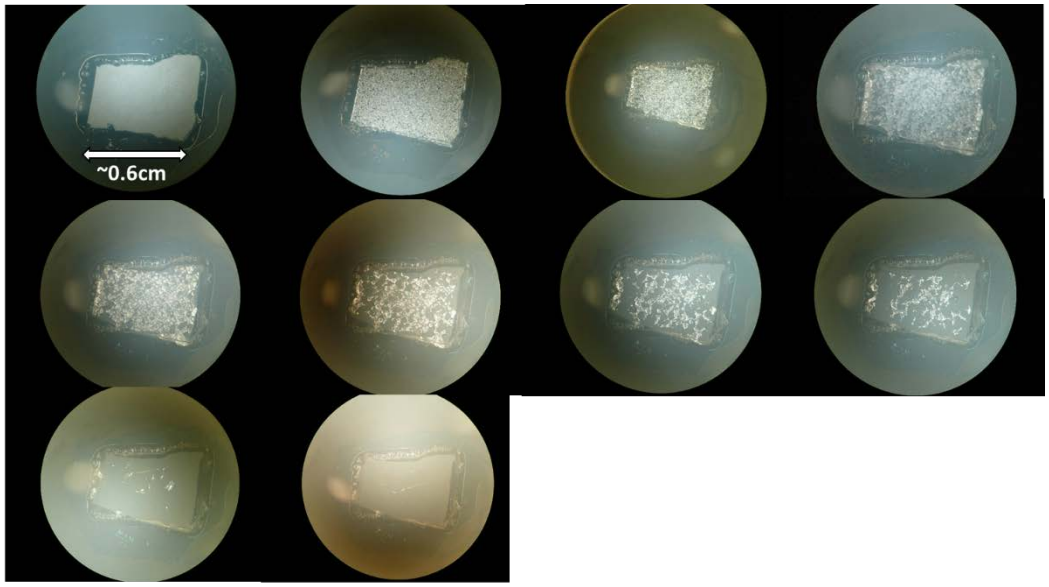

XeF_2 Etching at ANL (9:30AM to 1:08PM) – Photos by I. V. Veryovkin

Shortly after XeF_2 etching, additional fractures developed, but the sample remained generally stable from then on.

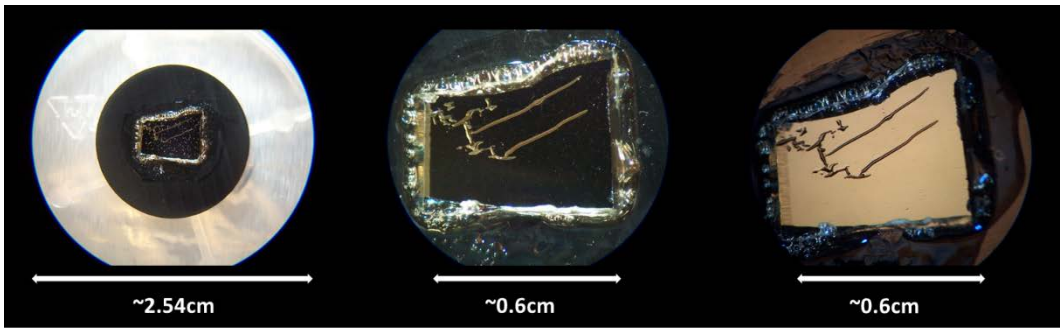

Genesis DoS That Were Not Thinned.

These samples were analyzed by traditional frontside depth profiling.

Genesis Dos 60878. Despite repeated cleaning efforts, surface contamination was too high to obtain a successful frontside depth profile by SIMS.

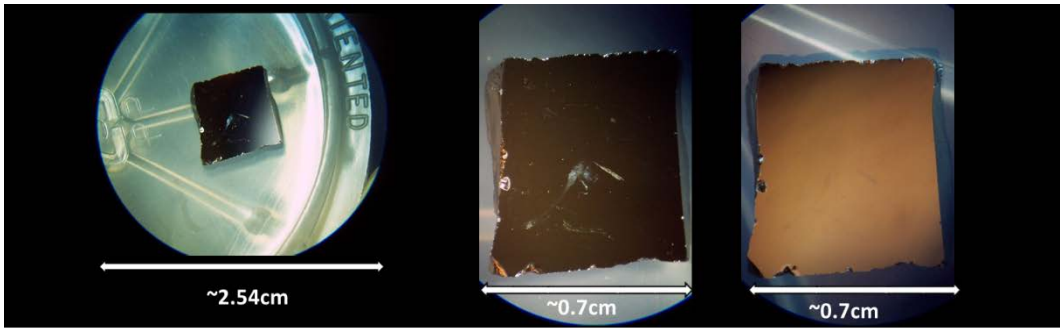

Genesis DoS 61090. Repeated cleaning efforts produced a surface sufficiently clean for frontside depth profiling by SIMS! This is the first Genesis DoS collector from which successful frontside depth profiles have been performed.

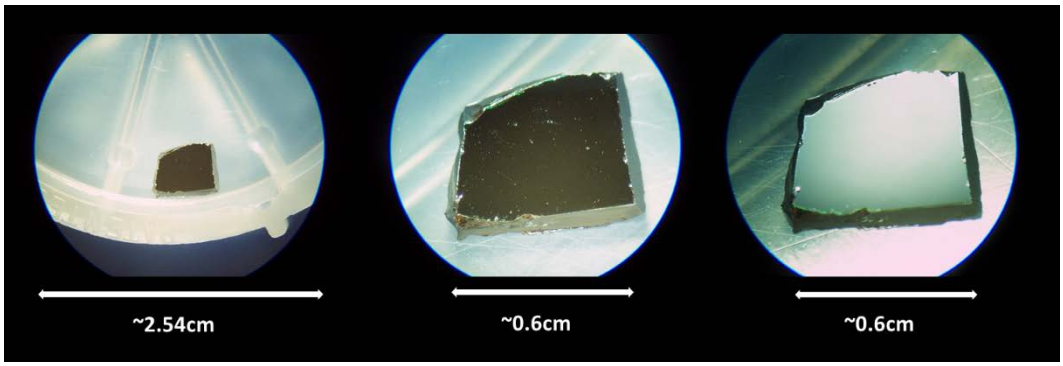

APPENDIX C

ION IMPLANT TARGET PLATES

Overview

The following images depict samples before ion implantation, or immediately after their return to ASU following ion implantation. Ion implantation was performed by Leonard Kroko, Inc. Samples were kept within a two inch radius to ensure even ion implantation. It was important to maintain proper conduction between samples and the target plate, so carbon paint and carbon tape were used to hold samples to the square metal target plate. Some samples were mounted as they were, others were already mounted on substrates, e.g., carbon planchets.

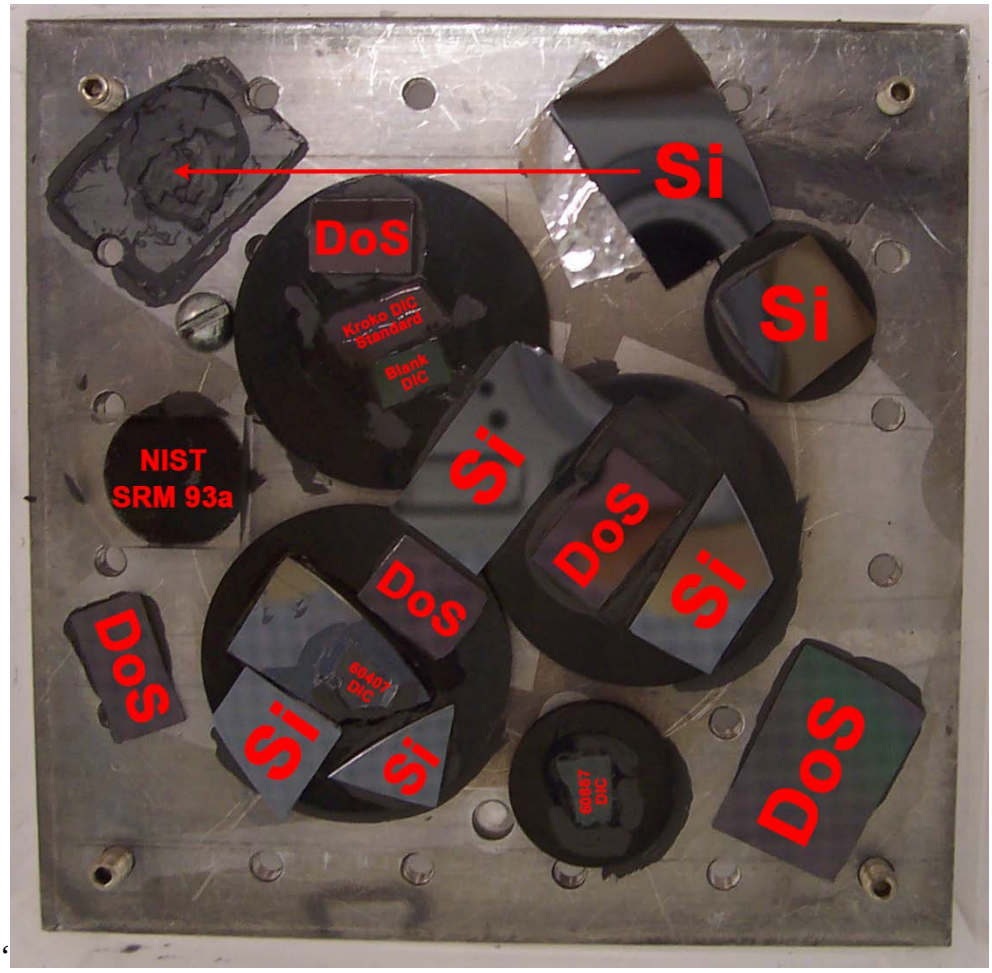

‘

Implant reference: “2e12 (1) R&J.” Ions: ^{23}Na & ^{41}K, 100keV each.
Note: One Si wafer loosened from the target plate after implantation during return shipping. Fortunately, the piece remained intact and there were no other problems.

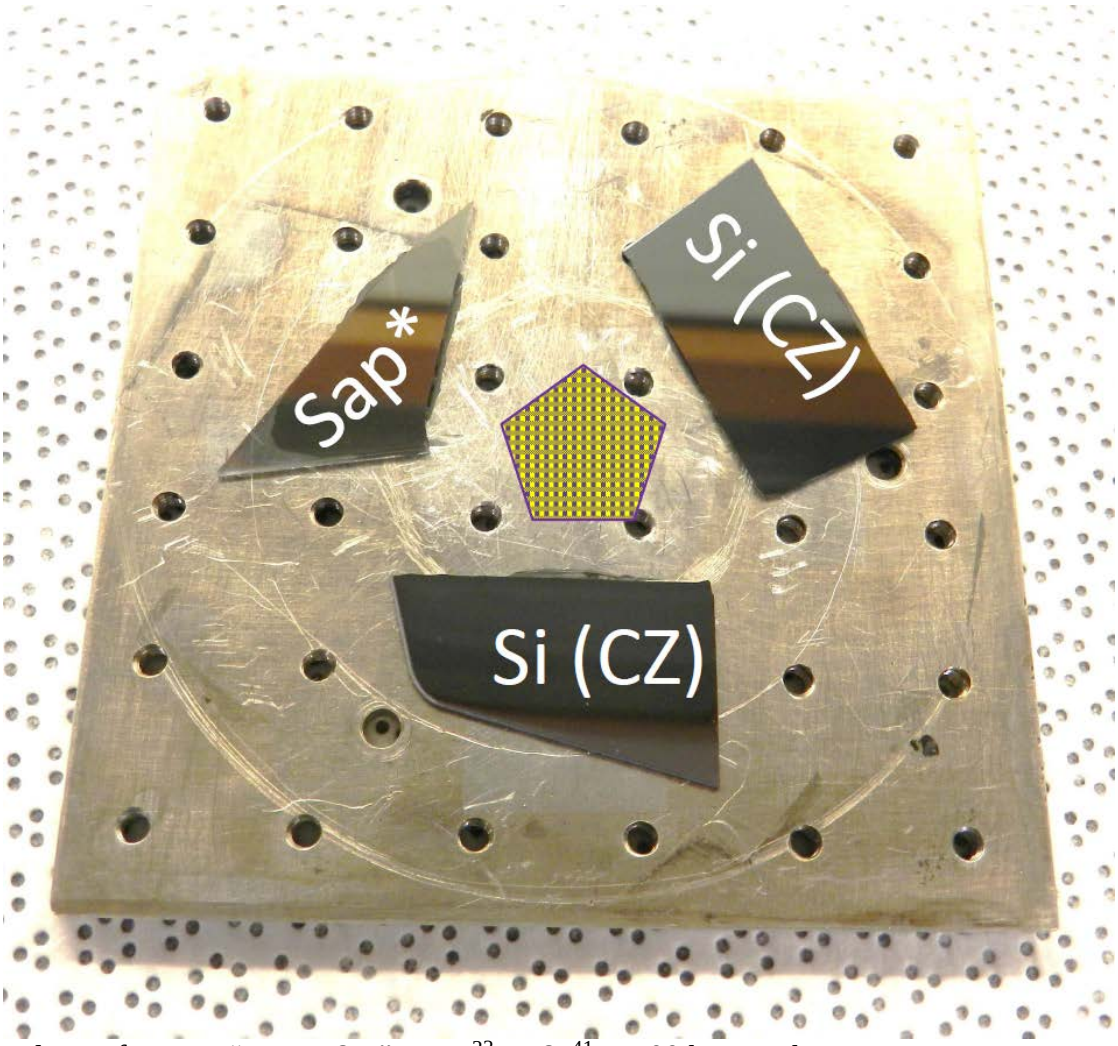

Implant reference: “1e14 R&J.” Ions: ^{23}Na & ^{41}K, 100 keV each.

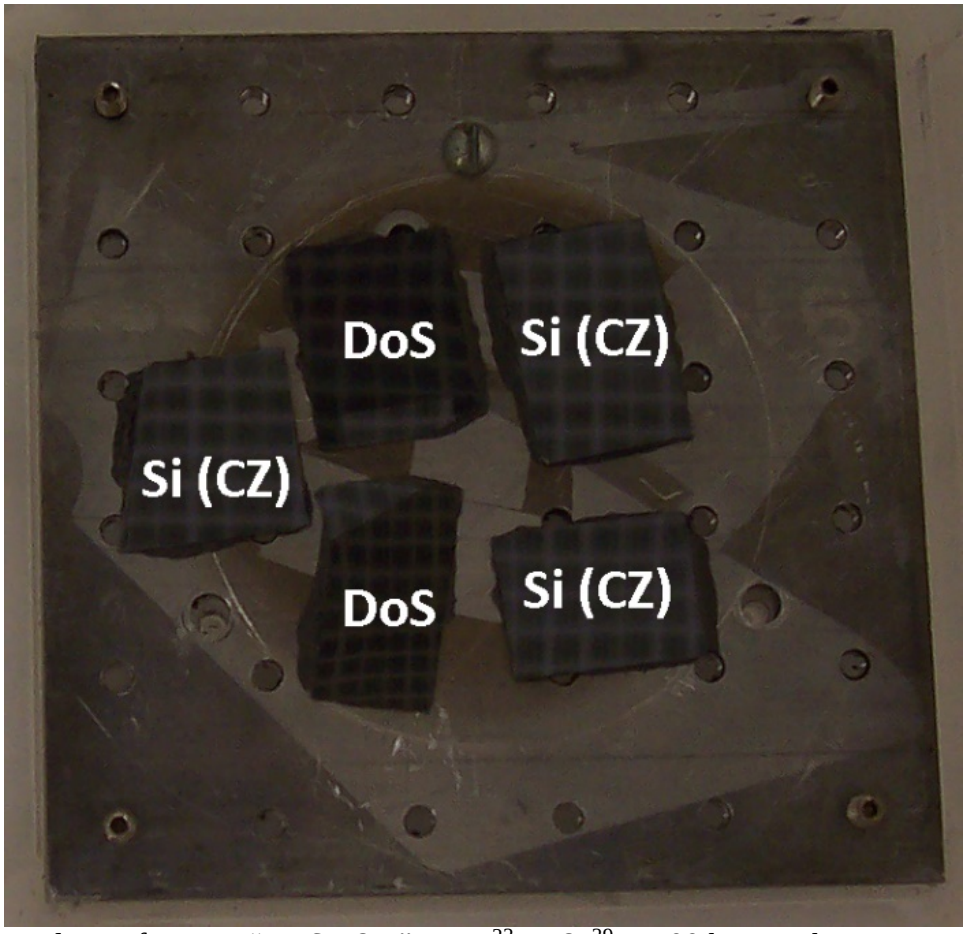

Implant reference: “1e16 R&J.” Ions: ^{23}Na & ^{39}K, 100 keV each.

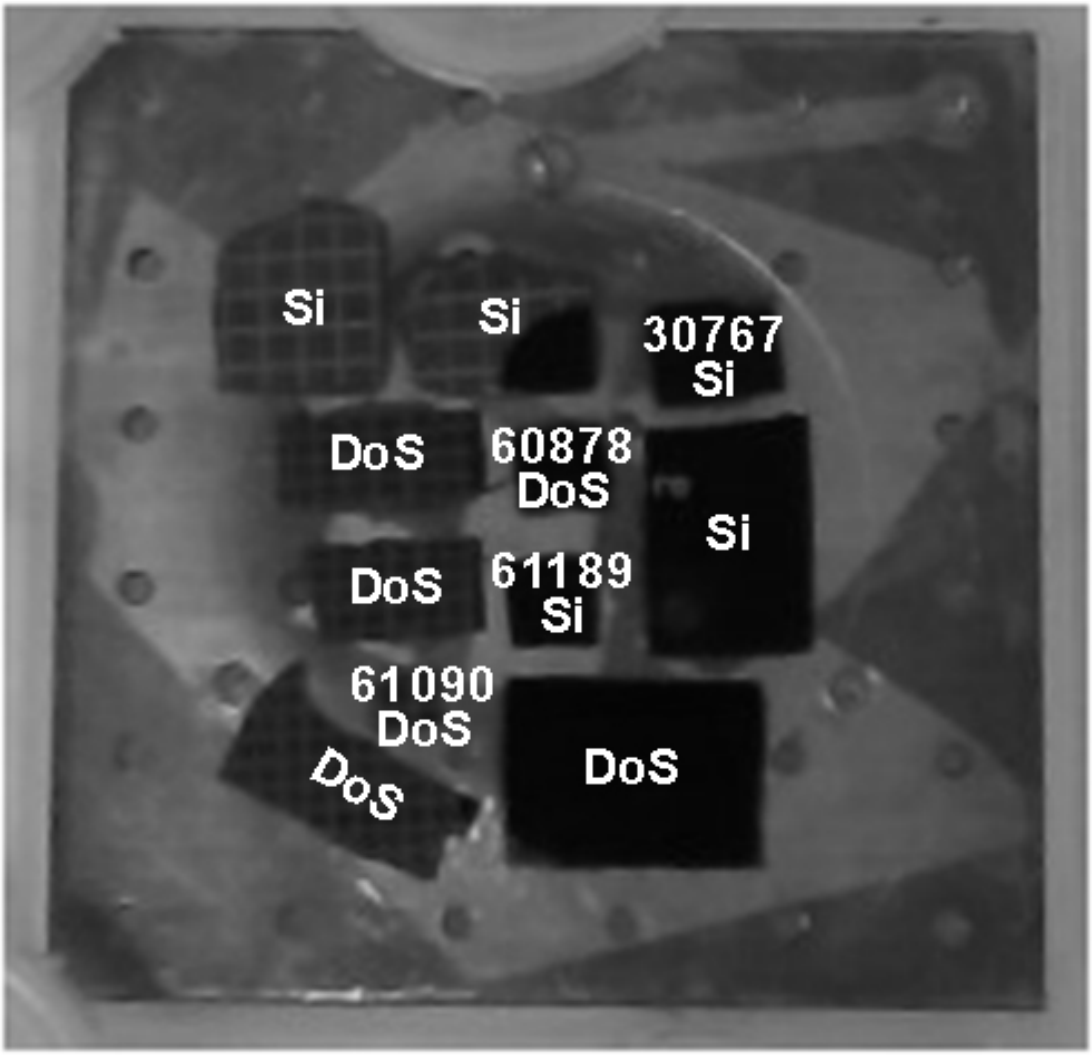

.

Implant reference: “2e12 (2) R&J.” Ions: ^{23}Na & ^{41}K, 100keV each.

APPENDIX D

ION IMPLANTATION AND DEPTH PROFILING

The following cartoons depict the major steps in the collection and analysis of Genesis samples in Diamond-on-Silicon (DoS) and Silicon (Si) solar wind (SW) collectors.

Genesis DoS Collectors: SW Collection and Sample Preparation

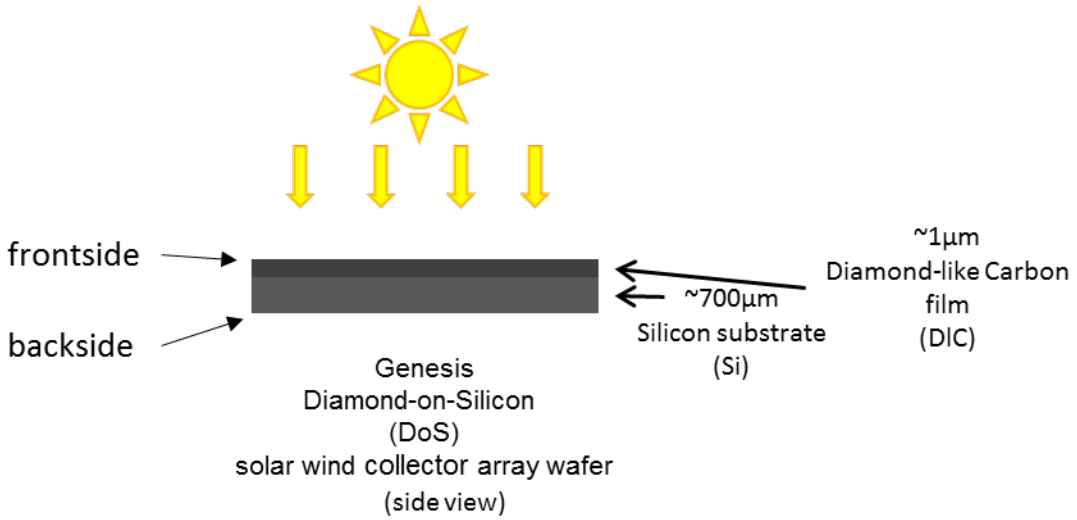

1) Solar wind ions implant into the front surfaces of Genesis DoS solar wind collector wafers.

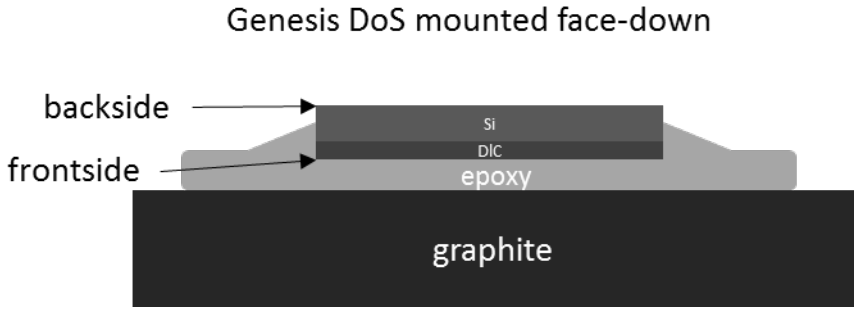

2) Genesis DoS wafers are cleaned and mounted face down in preparation for thinning

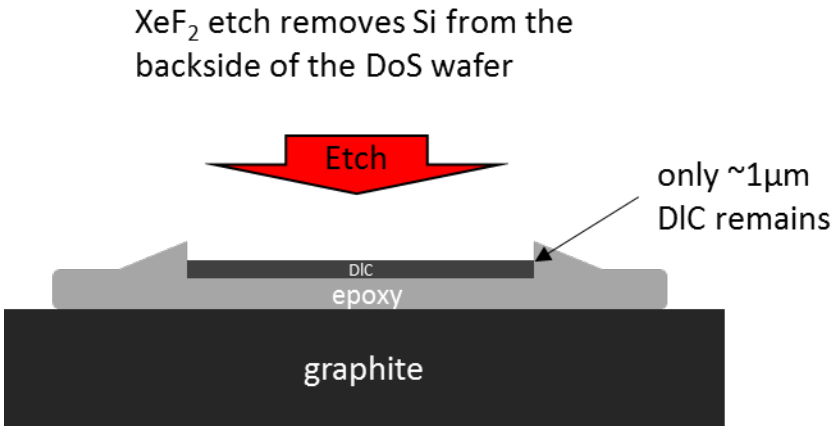

3) Diamond-on-silicon wafers are thinned with a chemical etchant, xenon difluoride, (XeF_2) prior to either (1) reference ion implantation from the back surface, or (2) backside depth profiling analysis.

Genesis Si Collectors: SW Collection and Sample Preparation

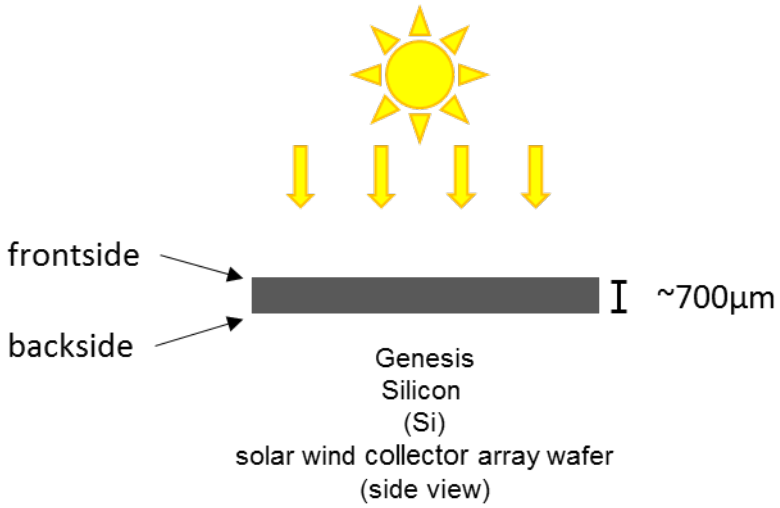

1) Solar wind ions implant into the front surfaces of Genesis Si solar wind collector wafers.

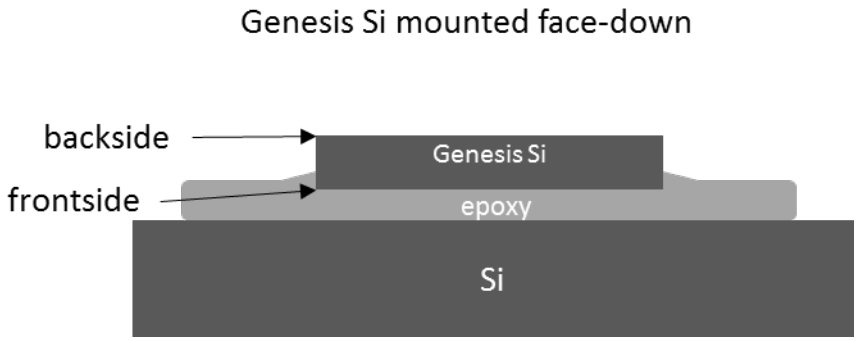

2) Genesis Si wafers are cleaned and mounted face down in preparation for thinning.

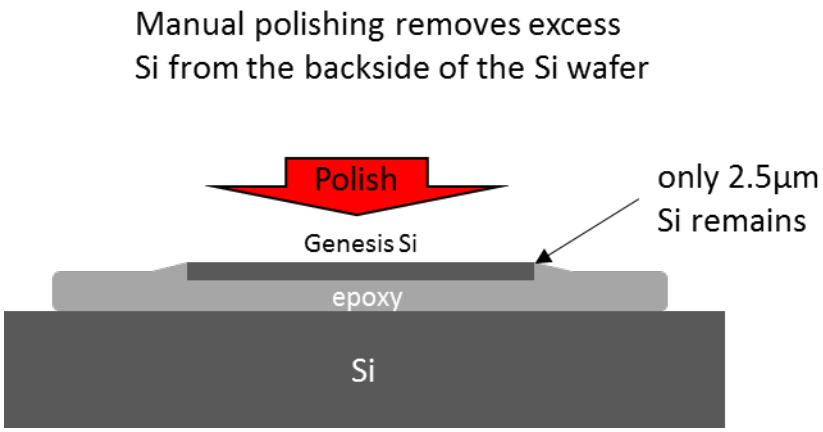

3) Silicon wafers are thinned with manual polishing prior to either 1) reference ion implantation from the back surface, or 2) backside depth profiling analysis. If no backside implantation will be performed, the Si can be thinned to ~1.2 µm.

Reference Ion Implantation into Genesis wafers and non-flight wafers.

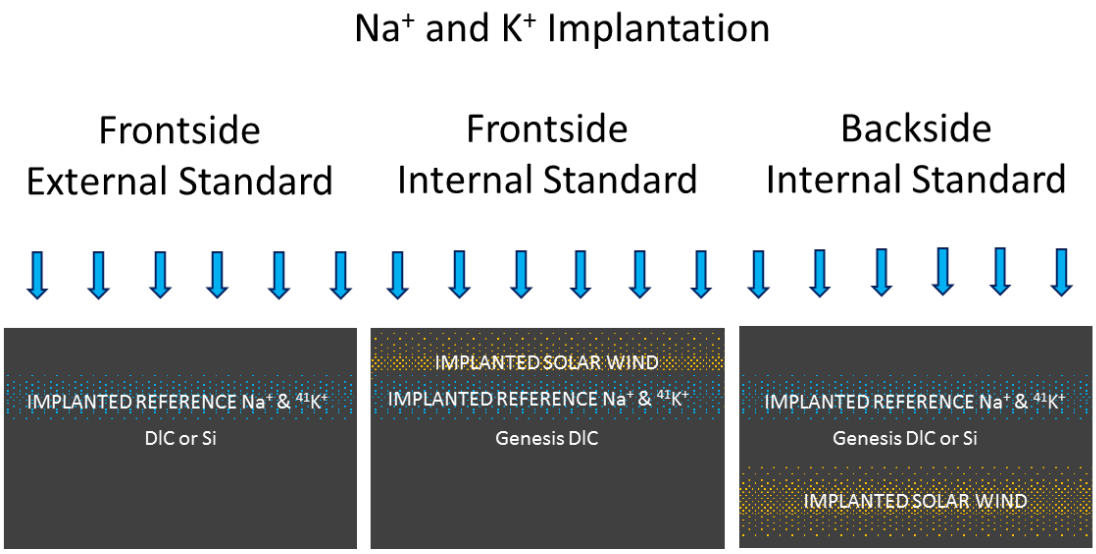

Reference ion species are implanted into either the front or back surfaces of DlC and Si wafers. This produces external standards and internal standards, which can be intercompared to look for measurement artifacts and matrix effects. Ion implantation was performed by Leonard Kroko, Inc.

SIMS Depth-Profiling Analyses in DlC

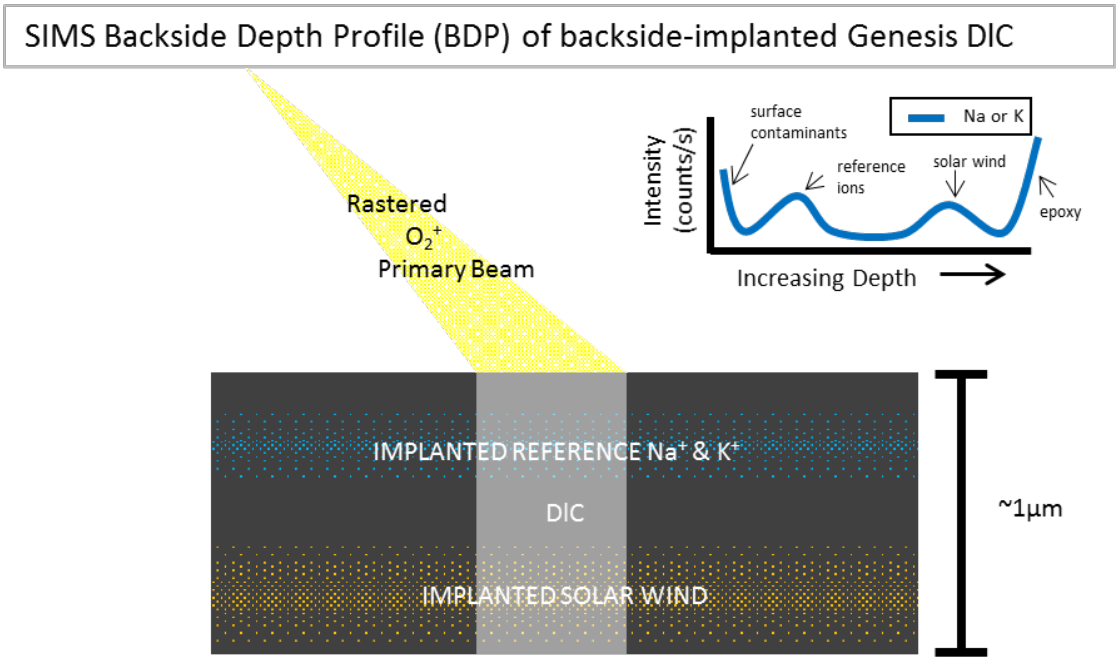

A model of a backside SIMS depth profile through DlC film. The depth profile begins in a backside-implanted reference ion layer, continues into a region free from ions, and then proceeds into a layer dominated by solar wind ions at the front surface of the film. Beneath the front surface of the film is a layer of terrestrial surface contaminants and mounting epoxy, which triggers a rise in ion abundance at the end of the profile.

SIMS Depth-Profiling Analyses in Si

Depth profiles though Si >1µm thick must be completed in three parts. Si samples ~1.2µm thick (without backside-implanted internal standards) require only a single depth profiling step with an O_2^+ primary beam.

Part I of the depth profile involves locally thinning the (thinned) sample with a Cs^+ beam. The profile begins in a backside-implanted reference ion layer, continues into a region free from ions, and stops short of the solar wind implanted region.

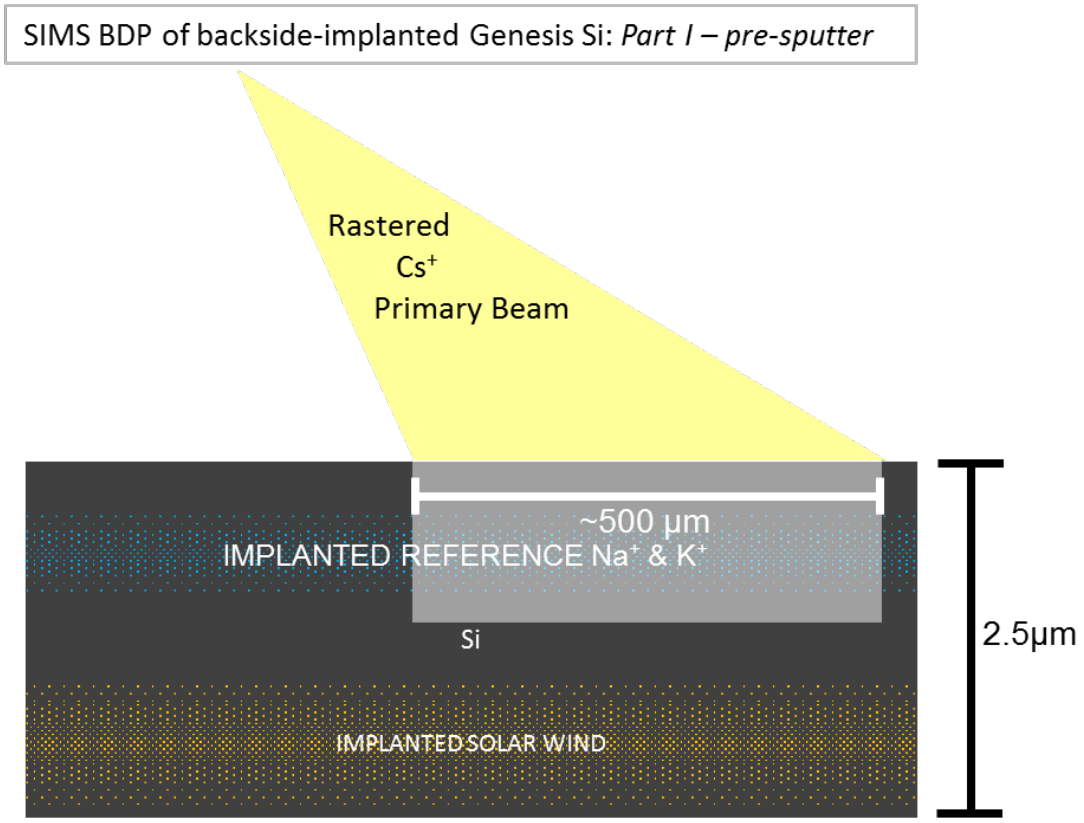

Part II involves measurement of a standard outside the SIMS-thinned region using an O_2^+ primary beam.

Part III involves measurement of the solar wind inside the SIMS-thinned region using an O_2^+ primary beam.

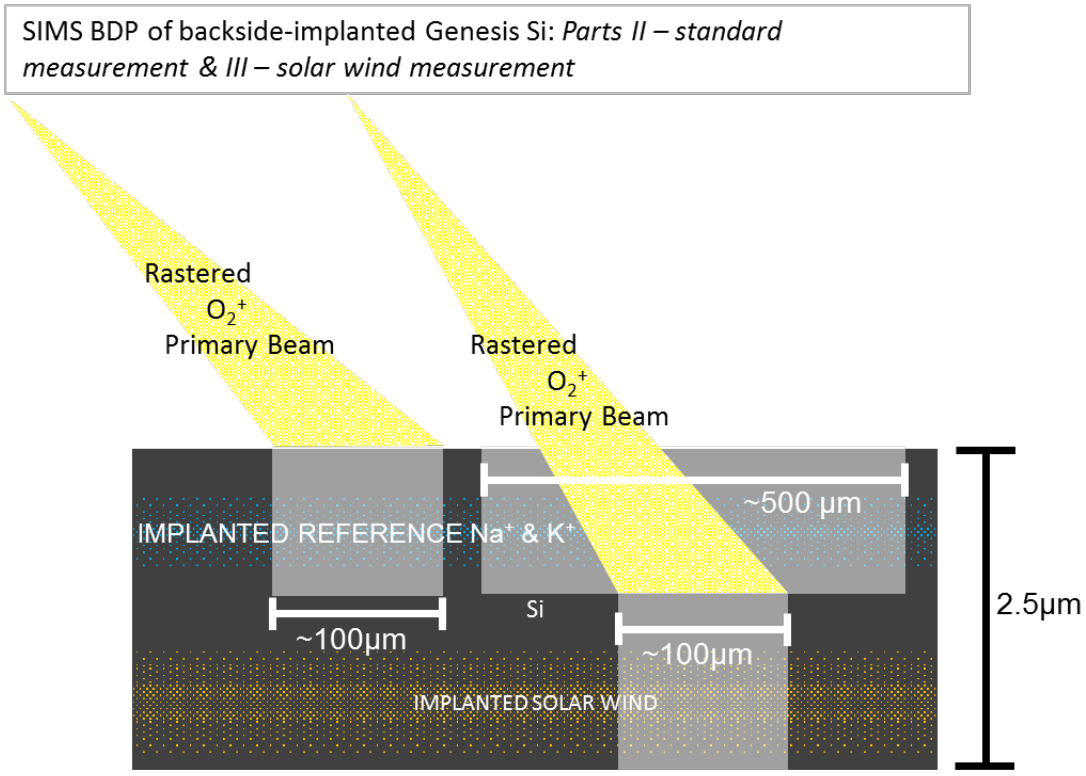

APPENDIX E

RAW RUTHERFORD BACKSCATTERING SPECTROMETRY (RBS) DATA

Overview

Rutherford Backscattering Spectrometry (RBS) was used to calibrate high dose (~1e16 atoms/cm^2) ^{23}Na and ^{39}K implants in two Diamond-like-Carbon on Silicon (DoS) wafers. The following plots are raw RBS profiles from this calibration. RBS measurements were calibrated with a Bismuth standard. Data processing was performed using RBS and RUMP software, with assistance from B. Wilkens (LeRoy Eyring Center for Solid State Science, Arizona State University) to convert the DoS profiles into meaningful abundances. The results of data processing are provided in Table 1.3.

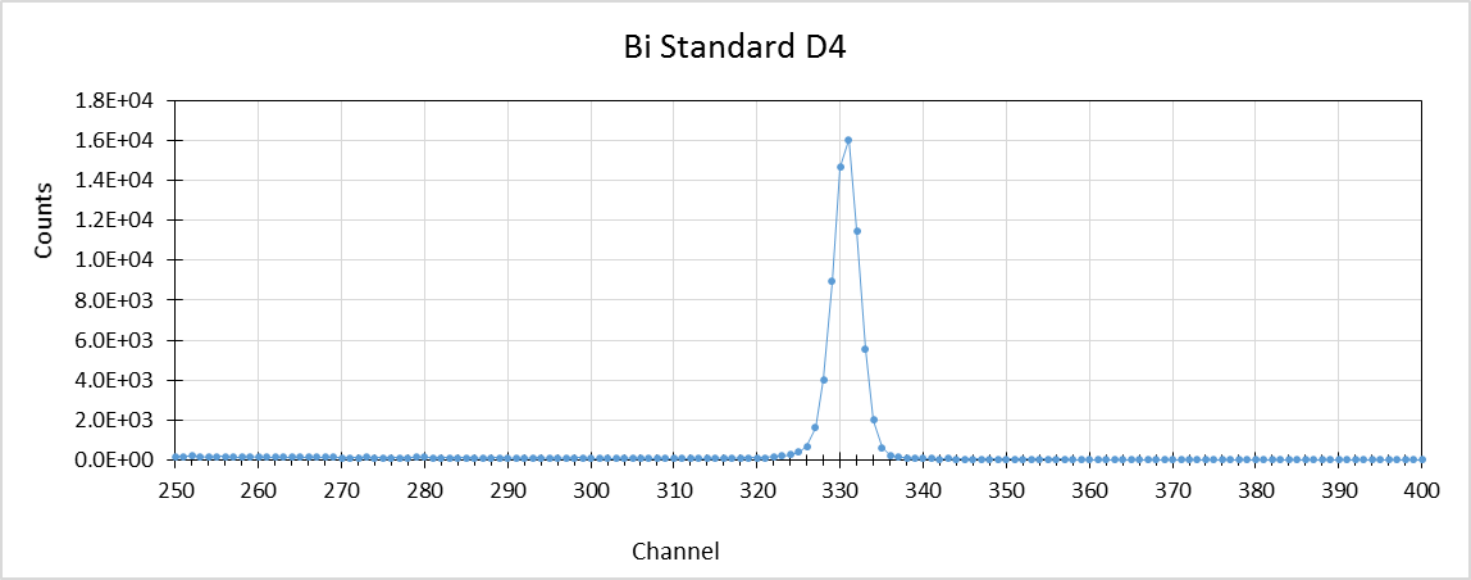

Bismuth intensity.

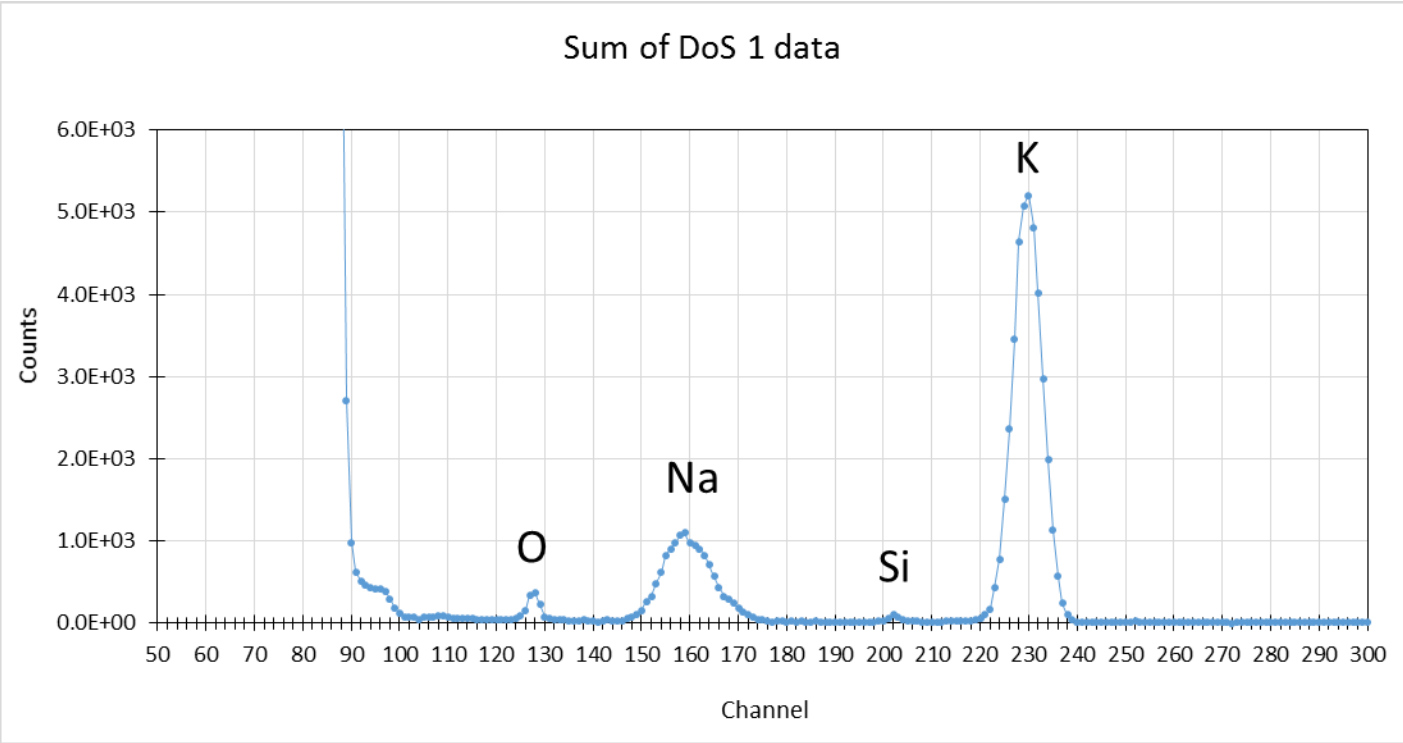

Intensities for O, Na, Si and K in the first DoS standard.

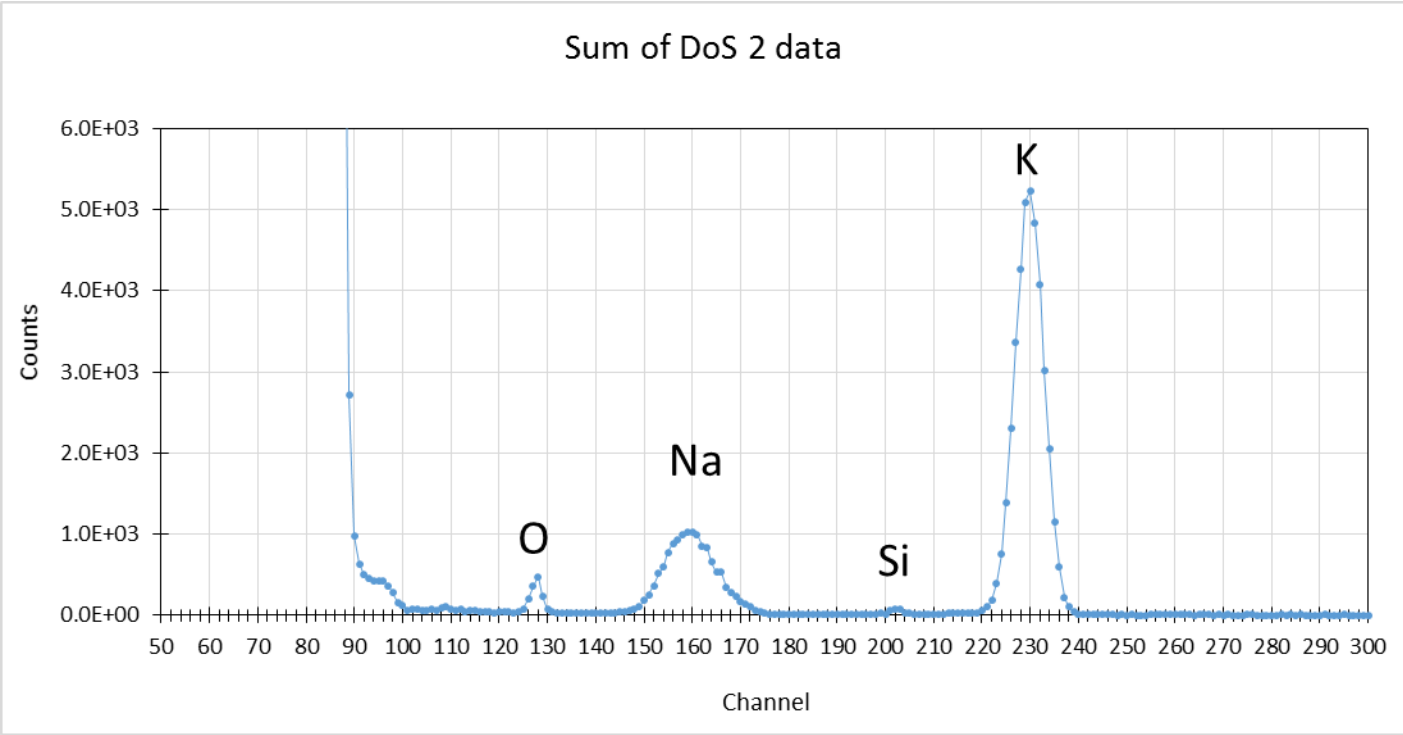

Intensities for O, Na, Si and K in the second DoS standard.

APPENDIX F

MATRIX EFFECTS FROM HIGH DOSE IMPLANTS

Overview

Standards were created for the present study using ion implantation. Ions were implanted into semiconductor materials: Si and DlC. Under ideal conditions, the implant dosages are sufficiently high for precise measurement and sufficiently low to prevent significant changes to the matrix composition. Significant changes to matrix composition can change the calibration between the standard and the sample.

High Dose Effects

High dose ion implants (1e16 $^{23}Na/cm^2$ and 1e16 $^{39}K/cm^2$; each 100keV) were required to precisely calibrate the standards by RBS. The following plots are SIMS frontside depth profiles in non-flight DoS and Si wafers, respectively. Localized decreases in matrix ion intensity (up to ~20%) were observed for both DlC (^{12}C) and Si (^{28}Si). These "dips" occur at depths corresponding to peak implant concentrations. This suggests that these decreases in matrix signal are likely the result of matrix effects.

DlC:

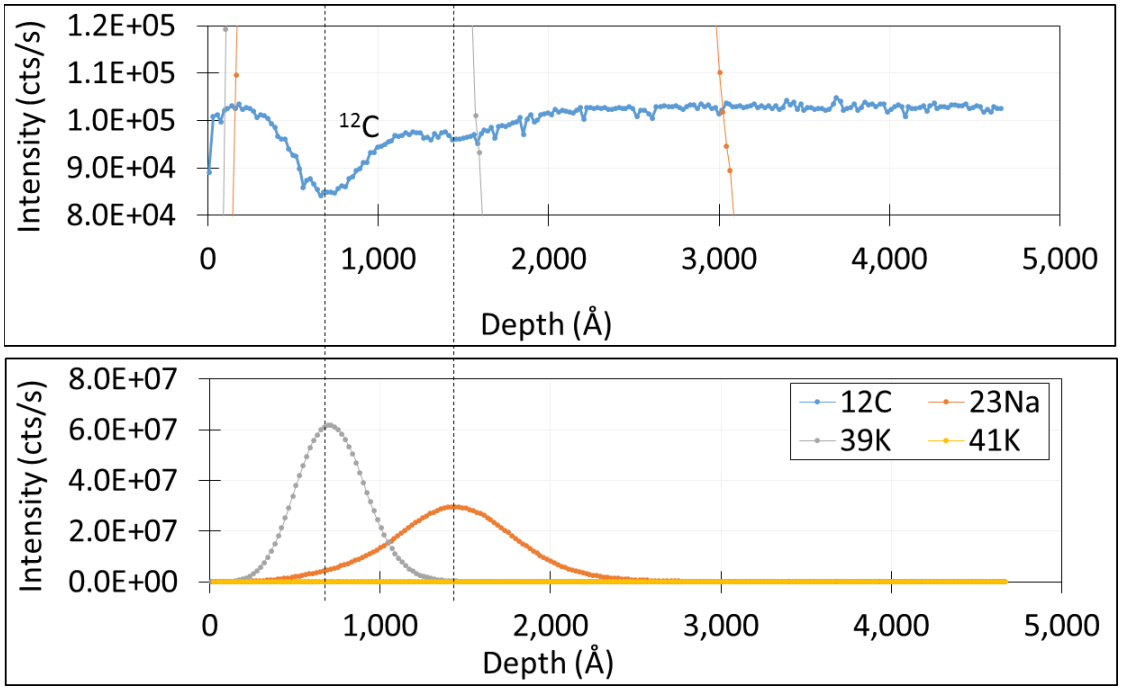

Si:

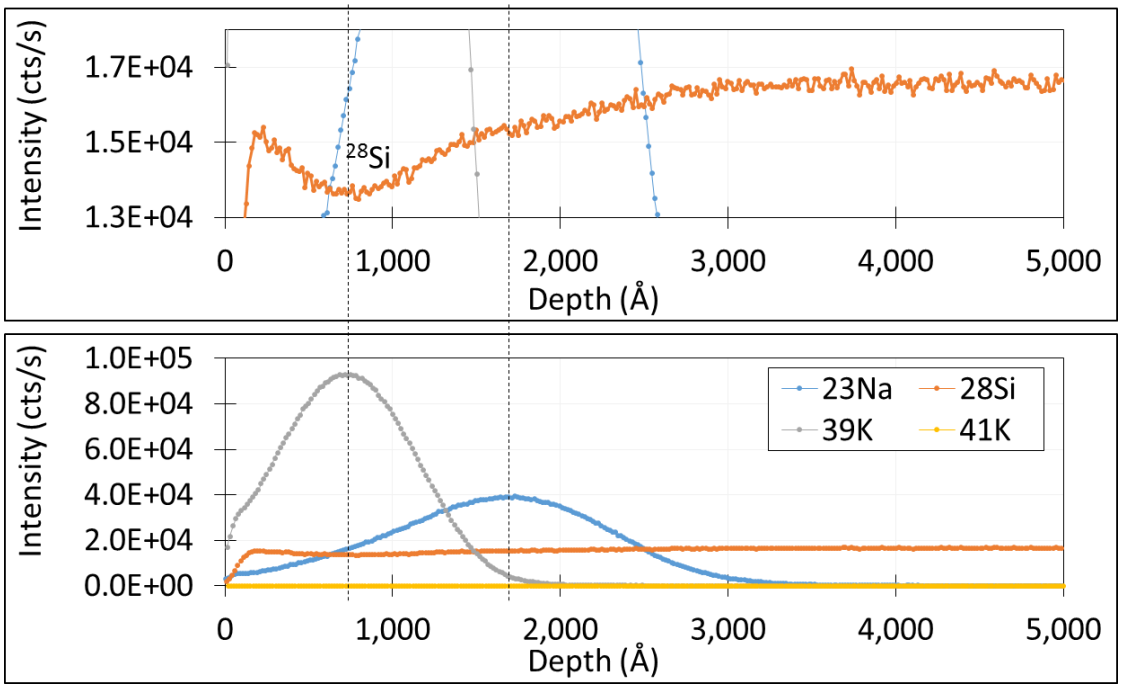
Intensity (cts/s)
1.7E+04
1.5E+04
1.3E+04
28Si
0
1,000
2,000
3,000
4,000
5,000
Depth (Å)
Intensity (cts/s)
1.0E+05
8.0E+04
6.0E+04
4.0E+04
2.0E+04
0.0E+00
23Na
28Si
39K
41K
0
1,000
2,000
3,000
4,000
5,000
Depth (Å)

Solar Wind Effects

The solar wind is primarily composed of hydrogen. The fluence of hydrogen in the Genesis samples is higher than the high dose implants discussed above. Specifically, the Genesis Ion Monitor detected 2.06e16 H/cm^2 in the bulk solar wind (Huss *et al.*, 2015), and Huss *et al.* (2015) measured 1.44e16 H/cm^2 in the Genesis DoS bulk solar wind collectors. Thus, it is important to investigate whether there are matrix effects associated with solar wind implantation.

Frontside analysis of Genesis DoS (61090) detected decreased C matrix signal (~2%) in the solar wind region below the transient sputtering region. This feature was not observed on other frontside depth profiles into (non-Genesis) DoS from the session. The trough of this feature correlates with the approximate depth of the peak concentration of implanted solar wind H. The peak implant depth of the solar wind hydrogen in DoS is approximately 160Å (TRIM; H implant energy = ~1 keV; matrix density = ~2.85 g/cm^3). Most of the solar wind hydrogen is concentrated in the upper ~750 Å) of the DoS (TRIM; Huss *et al.*, 2015).

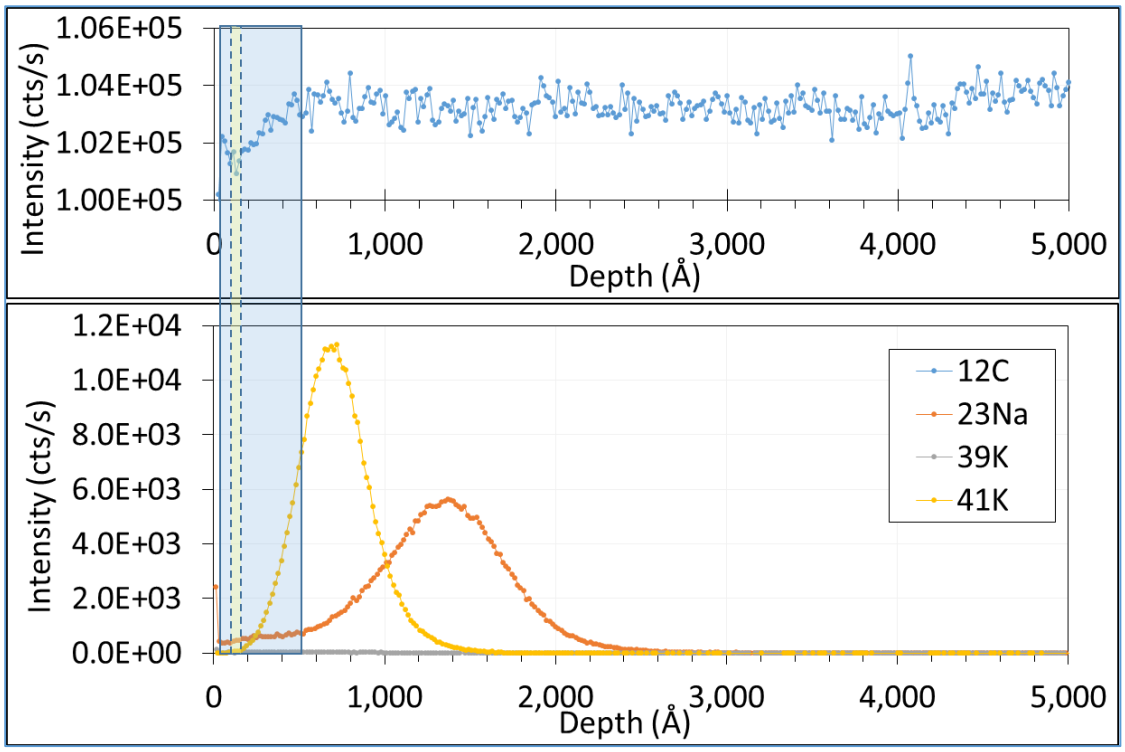

SIMS profiles from a single frontside depth-profile into frontside-standardized Genesis DoS (61090). The shaded blue region corresponds to the matrix count rate (^{12}C) anomaly. The SIMS transient region is not included in this box. The approximate position of the peak H implant depth is indicated by the yellow shaded box with dashed border.

The ^{12}C anomaly observed in Genesis DoS overlaps the approximate depth of the solar wind ^{23}Na and ^{39}K implants, and portions of the ^{23}Na and ^{41}K reference ion implants. Corrections were not made to solar wind measurements to adjust for this anomaly, because the change in C magnitude (≤~2%) was within the estimated curve fitting error (~10%).

The observations presented here suggest solar wind decreases C count rates during depth profiling measurements in Genesis DoS, but not so much as to alter the Na/C and K/C ratios more than a couple of percent.

Huss G. R., Ogliore R. C., Jurewicz A. J. G., Burnett D., S. and Nagashiima K. 2015. Estimate of Solar Wind Hydrogen Fluence from the Genesis Collectors (abstract #2577). 46th Lunar and Planetary Science Conference.

APPENDIX G

SIMS SOLAR WIND DEPTH PROFILES

This appendix provides plots of all the SIMS solar wind depth profiles measured in the present study.

These profiles have been minimally processed: 1) the measured ion intensities of implanted species were normalized to the measured intensity of a matrix species (^{12}C for DlC and ^{28}Si for Si), and 2) depth scales have been calculated from profilometry and interferometry of the craters, or were estimated using a Na^+ implant model (TRIM).

Generally, matrix species were measured for only the first half of each backside depth profile to dedicate more instrument time to the measurement of SW species in the SW-implanted region in the second half of the profile. In these cases, the matrix species count rate was extrapolated over the SW region, and the SW signal was normalized to the extrapolated matrix signal each analysis cycle. A single asterisk on the y-axis (*) denotes whether the matrix ion intensity used for normalization was extrapolated from shallower depths.

A double asterisk on the x-axis (**) denotes whether a TRIM model was used to estimate the depth scale. TRIM models were used for estimating the depth scales of profiles for which no profilometry or interferometry of SIMS craters was performed. (Profiles into internally standardized samples could be integrated by time rather than by depth, and so did not require crater depth information for fluence calculations.) A model of the internal standard was calculated with TRIM. The SIMS sputtering rate was calculated by dividing the depth corresponding to the peak concentration of implanted reference ions by the analysis time required to sputter to the peak implant depth. Multiplying the sputtering rate by the total duration of the depth profile provided an estimate of the crater depth, which was converted into a depth scale for the profile.

Plot titles contain the following information: 1) lowercase letters designating the individual profile, 2) wafer material (DoS or Si), 3) NASA code corresponding to the individual Genesis wafer fragment analyzed, 4) analysis session (year_month_day(s)), and 5) the analysis number(s) for that particular session and sample.

The lowercase letters corresponding the individual profile are provided to facilitate data comparison between these profiles and the corresponding fluences derived from them, which are provided in Tables 1.8 and 1.9, and presented graphically in Figure 1.14.

There is only one frontside depth profile (p. - DoS 61090 (2015_01_12-16; 1). The profiles of the internal standards are included for reference.

Most analyses were stopped once surface contaminants or epoxy were sampled, but some backside depth profiles were continued well into the underlying epoxy and substrate (e.g., profiles c. - DoS 60630 (2012_11_14-16; 1), q. - Si 60824 (2012_11_14-16; 1) and u. - Si 61189 (2015_01_12-16; 4)). This prolonged sputtering resulted in some unusual profile shapes at depth.

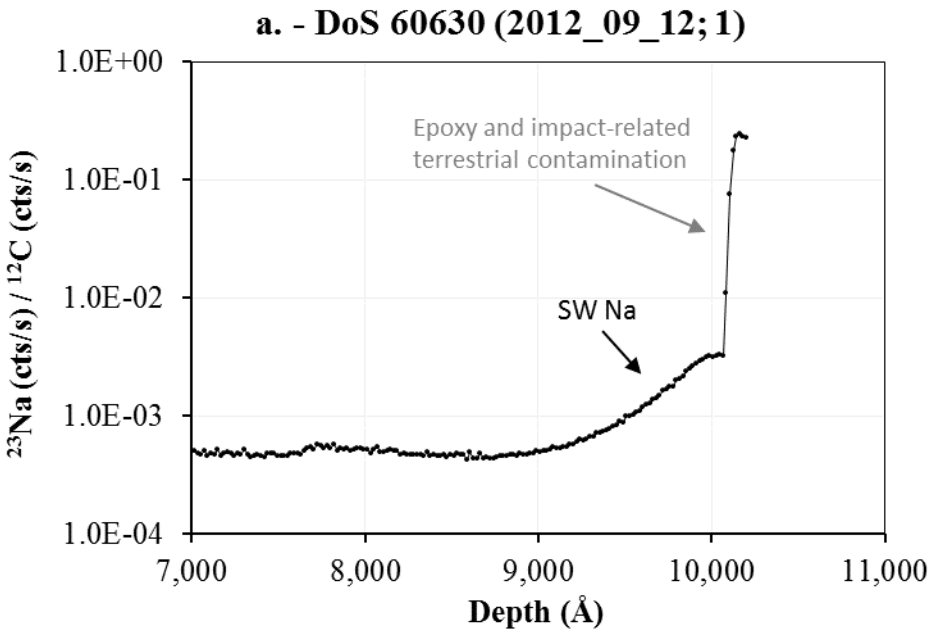
a. - DoS 60630 (2012_09_12; 1)
1.0E+00
1.0E-01
1.0E-02
1.0E-03
1.0E-04
^{23}Na (cts/s) / ^{12}C (cts/s)
Epoxy and impact-related terrestrial contamination
SW Na
7,000
8,000
9,000
10,000
11,000
Depth (Å)

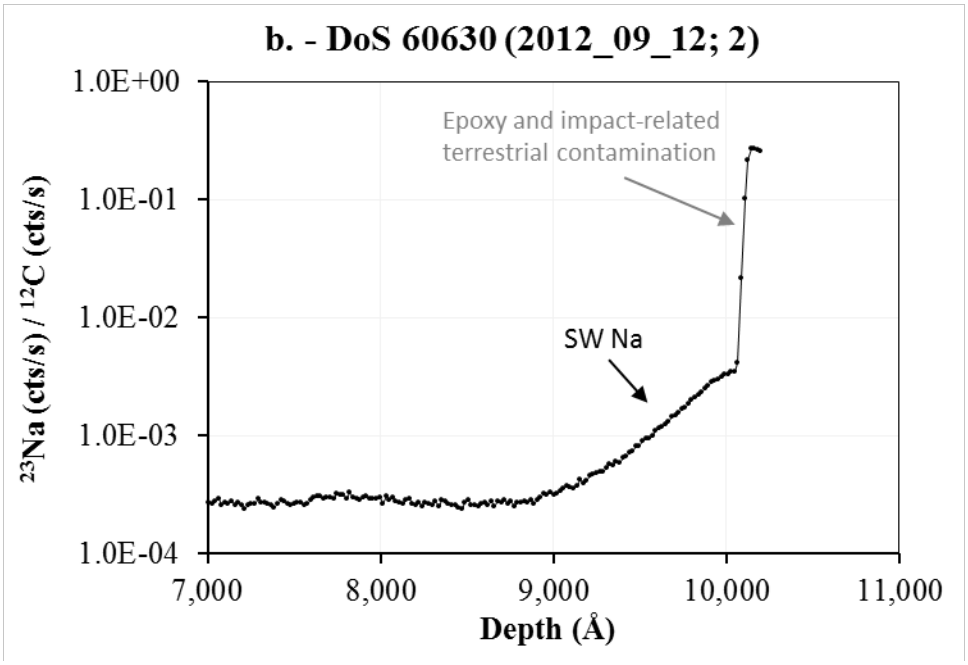
b. - DoS 60630 (2012_09_12; 2)
1.0E+00
1.0E-01
1.0E-02
1.0E-03
1.0E-04
^{23}Na (cts/s) / ^{12}C (cts/s)
Epoxy and impact-related terrestrial contamination
SW Na
7,000
8,000
9,000
10,000
11,000
Depth (Å)

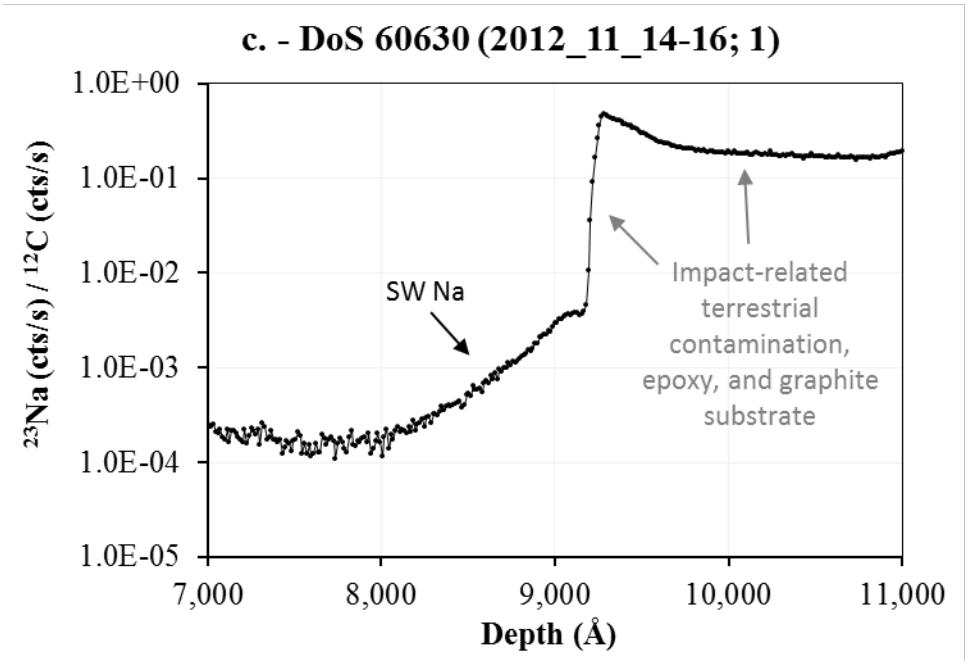
c. - DoS 60630 (2012_11_14-16; 1)
1.0E+00
1.0E-01
1.0E-02
1.0E-03
1.0E-04
1.0E-05
^{23}Na (cts/s) / ^{12}C (cts/s)
SW Na
Impact-related terrestrial contamination, epoxy, and graphite substrate
7,000
8,000
9,000
10,000
11,000
Depth (Å)

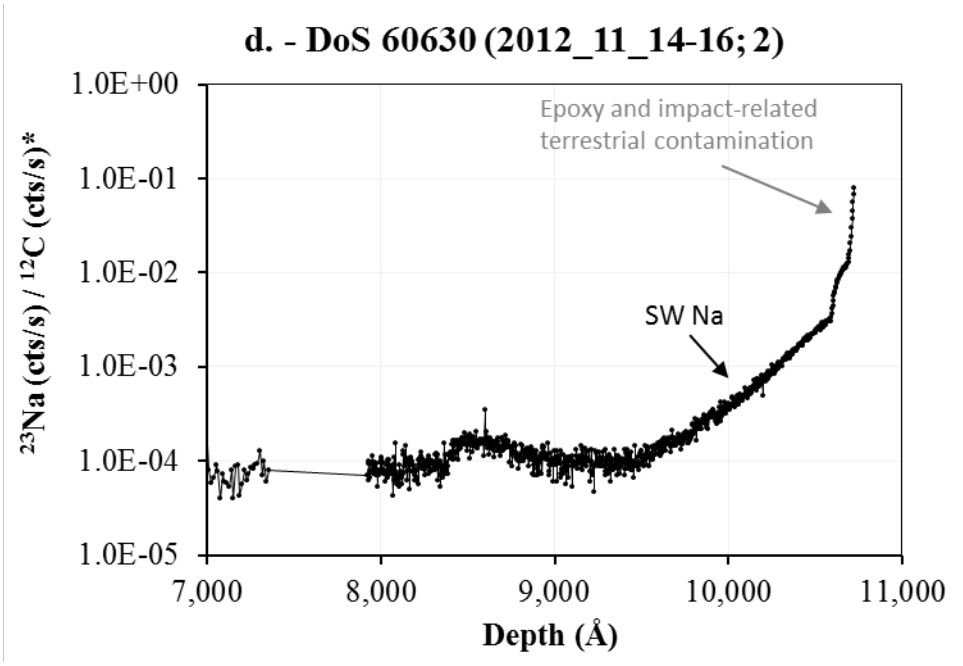
d. - DoS 60630 (2012_11_14-16; 2)
1.0E+00
1.0E-01
1.0E-02
1.0E-03
1.0E-04
1.0E-05
^{23}Na (cts/s) / ^{12}C (cts/s)*
Epoxy and impact-related terrestrial contamination
SW Na
7,000
8,000
9,000
10,000
11,000
Depth (Å)

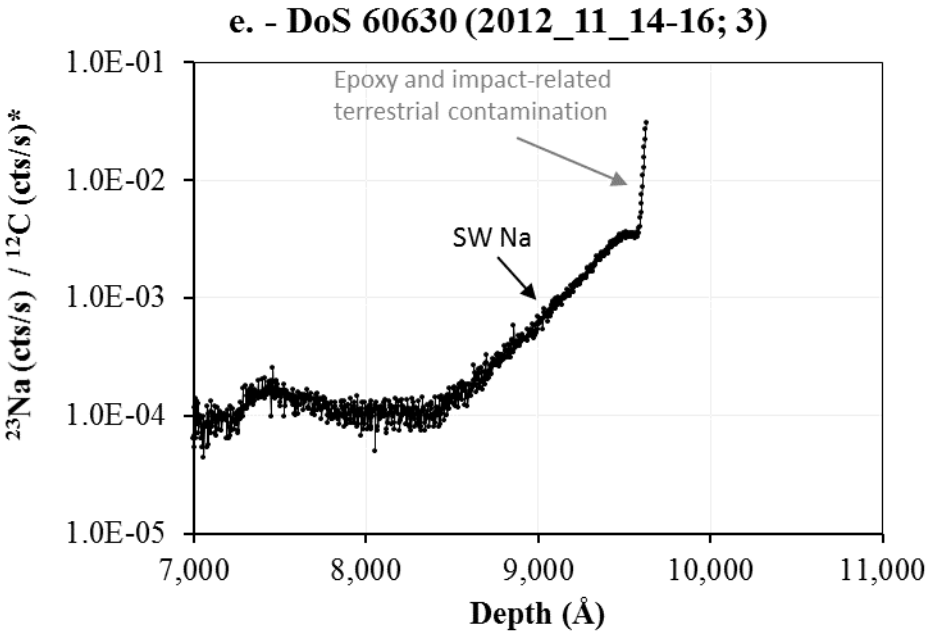
e. - DoS 60630 (2012_11_14-16; 3)
Epoxy and impact-related terrestrial contamination
SW Na
1.0E-01
1.0E-02
1.0E-03
1.0E-04
1.0E-05
7,000
8,000
9,000
10,000
11,000
Depth (Å)
23Na (cts/s) / 12C (cts/s)*

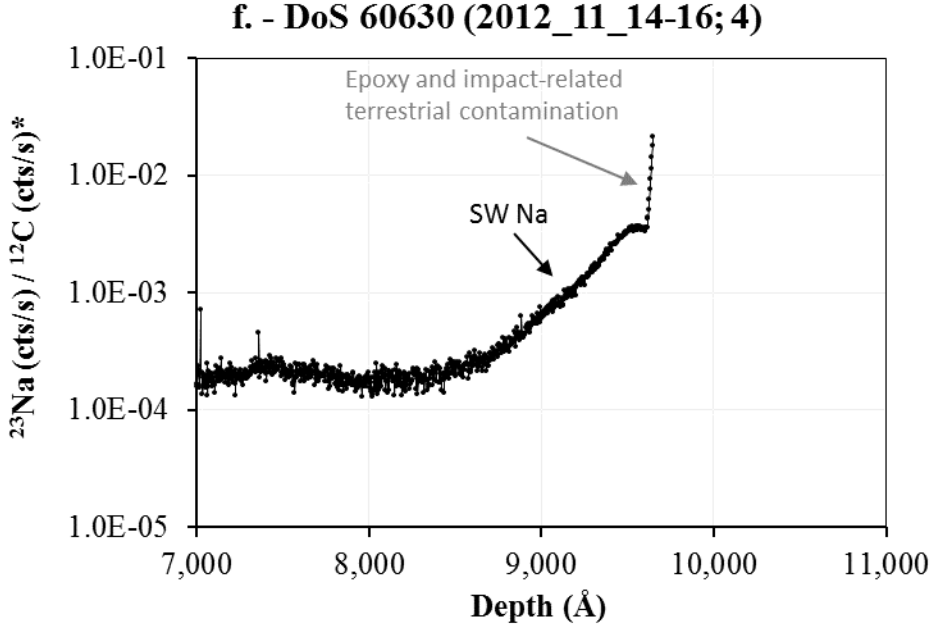
f. - DoS 60630 (2012_11_14-16; 4)
Epoxy and impact-related terrestrial contamination
SW Na
1.0E-01
1.0E-02
1.0E-03
1.0E-04
1.0E-05
7,000
8,000
9,000
10,000
11,000
Depth (Å)
23Na (cts/s) / 12C (cts/s)*

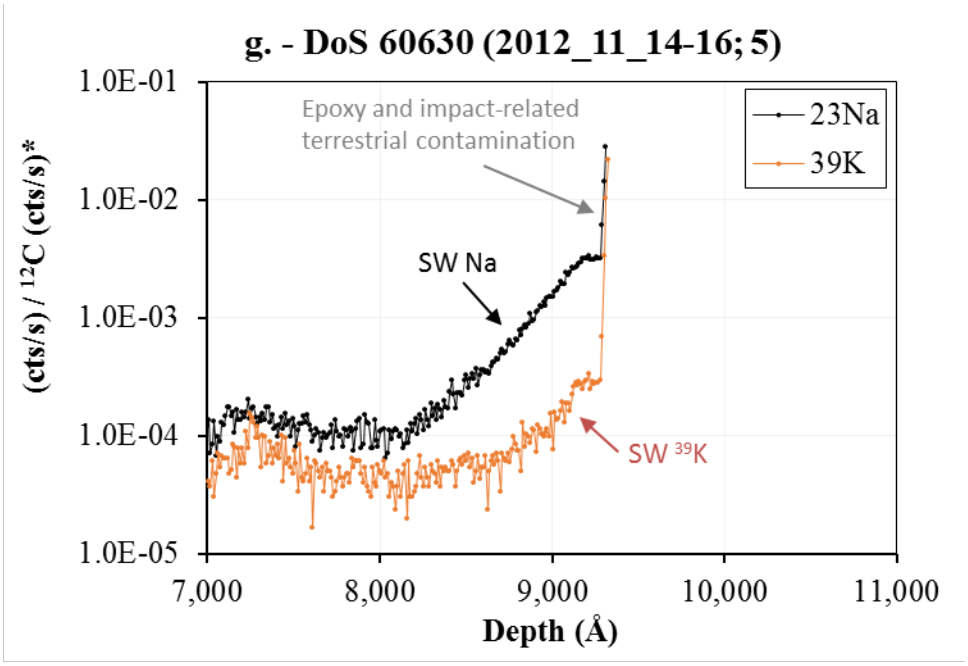
g. - DoS 60630 (2012_11_14-16; 5)
1.0E-01
1.0E-02
1.0E-03
1.0E-04
1.0E-05
(cts/s) / 12C (cts/s)*
Epoxy and impact-related terrestrial contamination
23Na
39K
SW Na
SW 39K
7,000
8,000
9,000
10,000
11,000
Depth (Å)

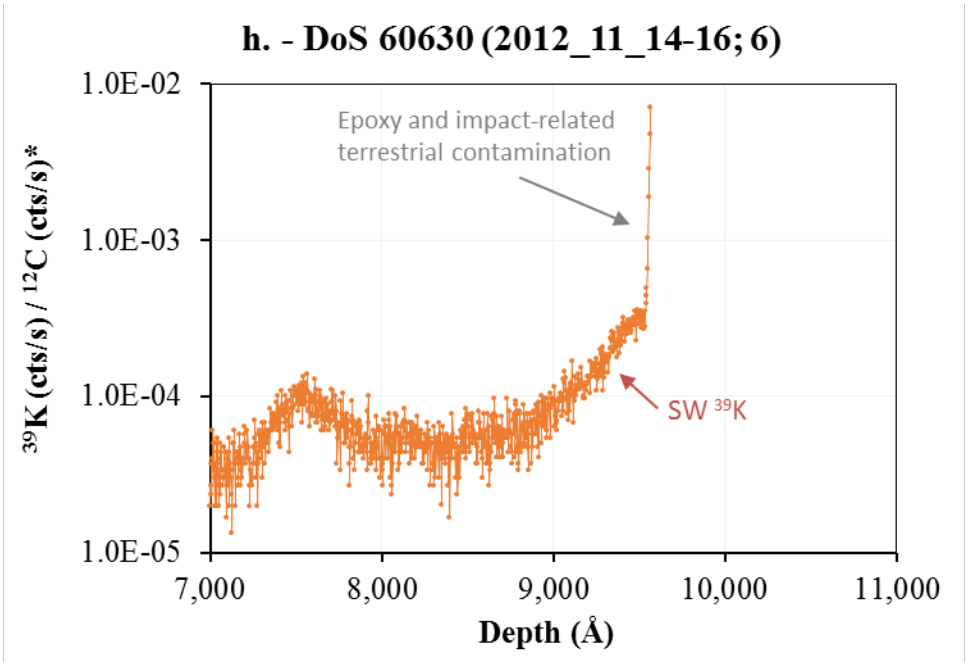
h. - DoS 60630 (2012_11_14-16; 6)
1.0E-02
1.0E-03
1.0E-04
1.0E-05
39K (cts/s) / 12C (cts/s)*
Epoxy and impact-related terrestrial contamination
SW 39K
7,000
8,000
9,000
10,000
11,000
Depth (Å)

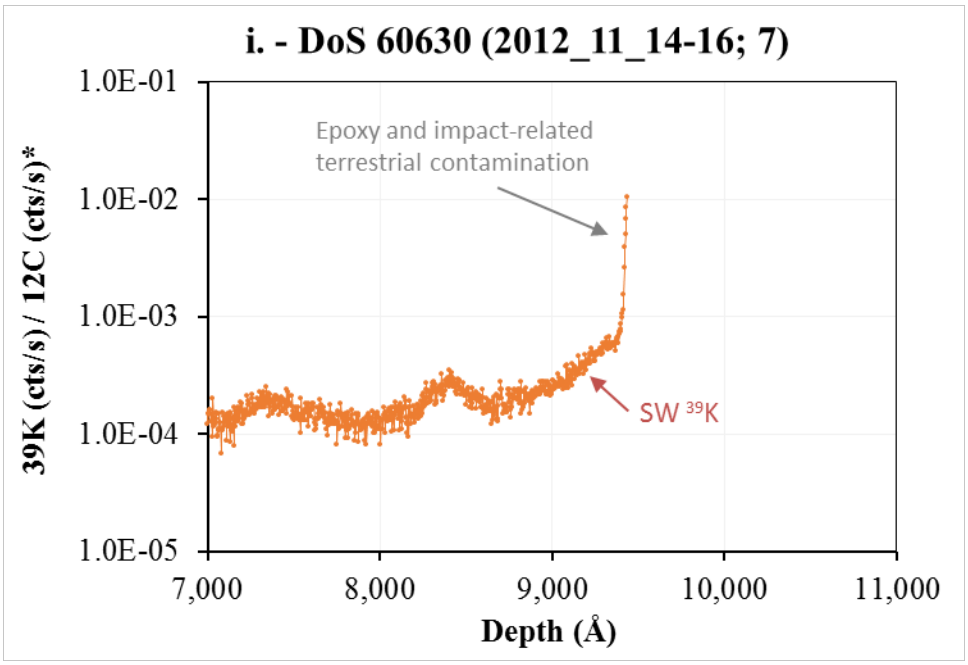
i. - DoS 60630 (2012_11_14-16; 7)
39K (cts/s) / 12C (cts/s)*
1.0E-01
1.0E-02
1.0E-03
1.0E-04
1.0E-05
Epoxy and impact-related terrestrial contamination
SW 39K
7,000
8,000
9,000
10,000
11,000
Depth (Å)

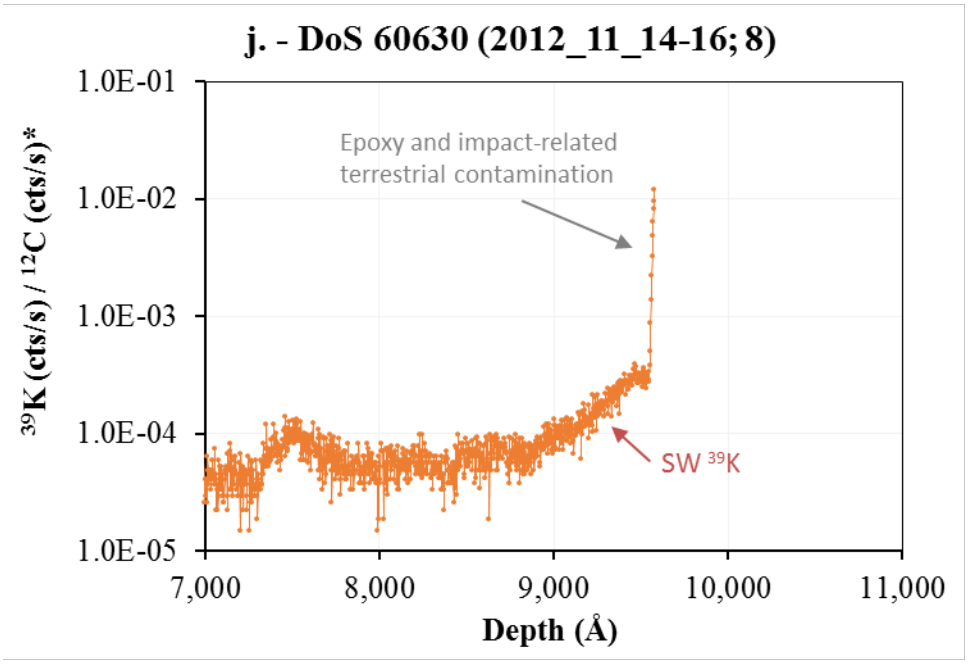
j. - DoS 60630 (2012_11_14-16; 8)
39K (cts/s) / 12C (cts/s)*
1.0E-01
1.0E-02
1.0E-03
1.0E-04
1.0E-05
Epoxy and impact-related terrestrial contamination
SW 39K
7,000
8,000
9,000
10,000
11,000
Depth (Å)

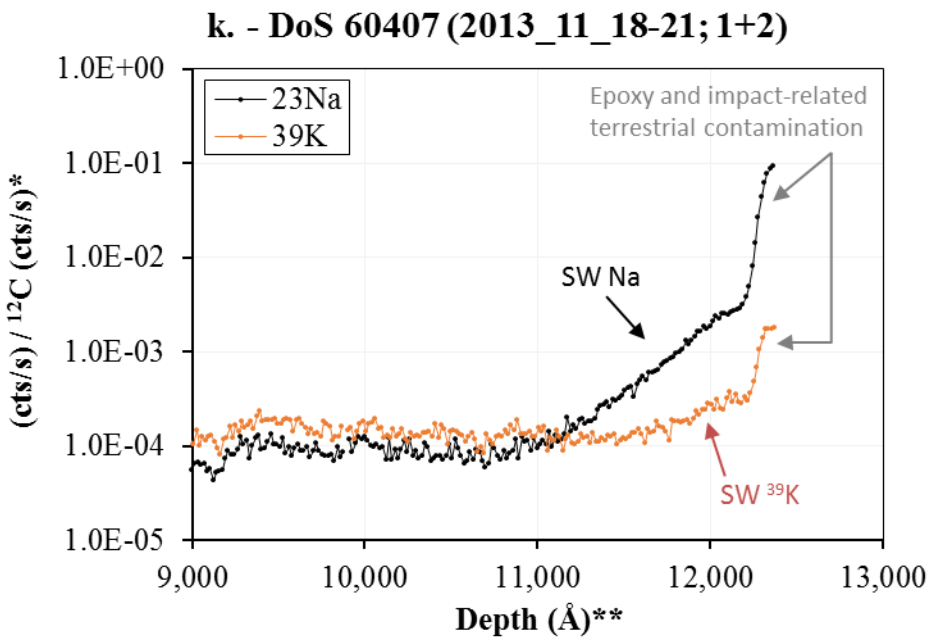
k. - DoS 60407 (2013_11_18-21; 1+2)
1.0E+00
1.0E-01
1.0E-02
1.0E-03
1.0E-04
1.0E-05
(cts/s) / 12C (cts/s)*
23Na
39K
Epoxy and impact-related terrestrial contamination
SW Na
SW 39K
9,000
10,000
11,000
12,000
13,000
Depth (Å)**

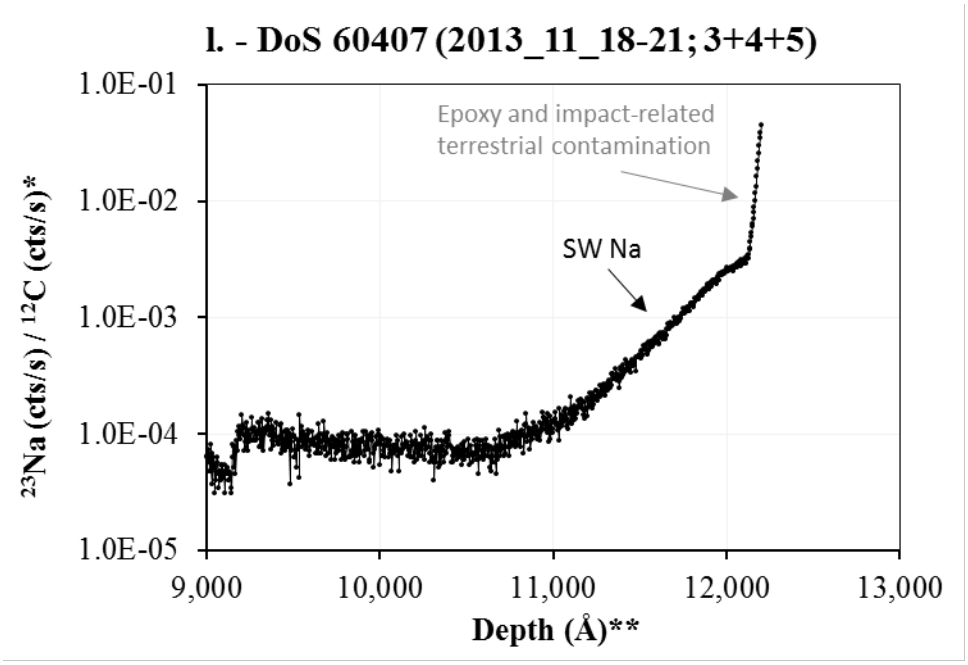
l. - DoS 60407 (2013_11_18-21; 3+4+5)
1.0E-01
1.0E-02
1.0E-03
1.0E-04
1.0E-05
23Na (cts/s) / 12C (cts/s)*
Epoxy and impact-related terrestrial contamination
SW Na
9,000
10,000
11,000
12,000
13,000
Depth (Å)**

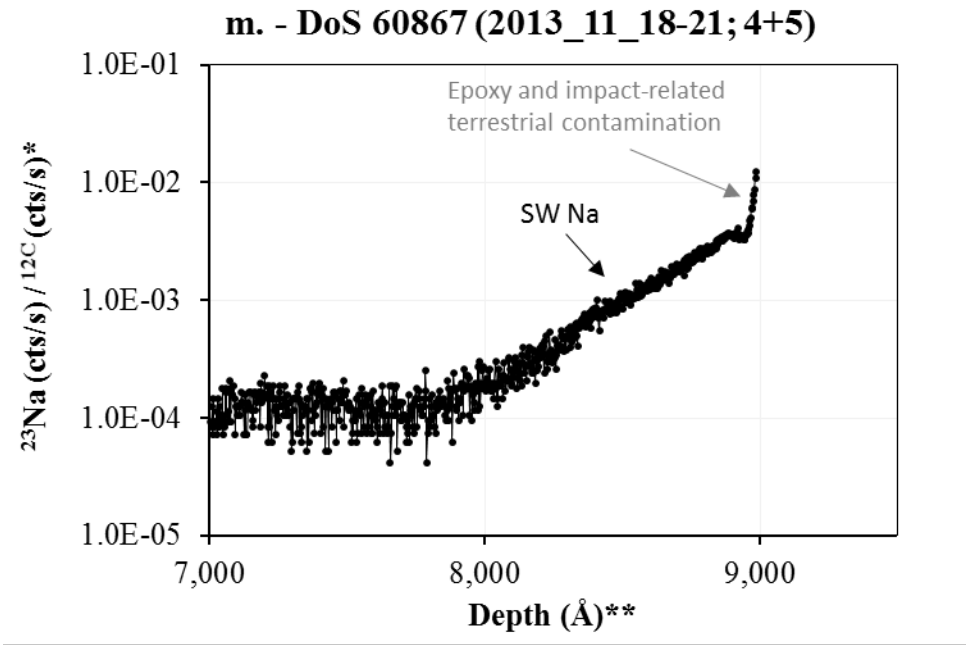
m. - DoS 60867 (2013_11_18-21; 4+5)
Epoxy and impact-related terrestrial contamination
SW Na
1.0E-01
1.0E-02
1.0E-03
1.0E-04
1.0E-05
7,000
8,000
9,000
Depth (Å)**
23Na (cts/s) / 12C (cts/s)*

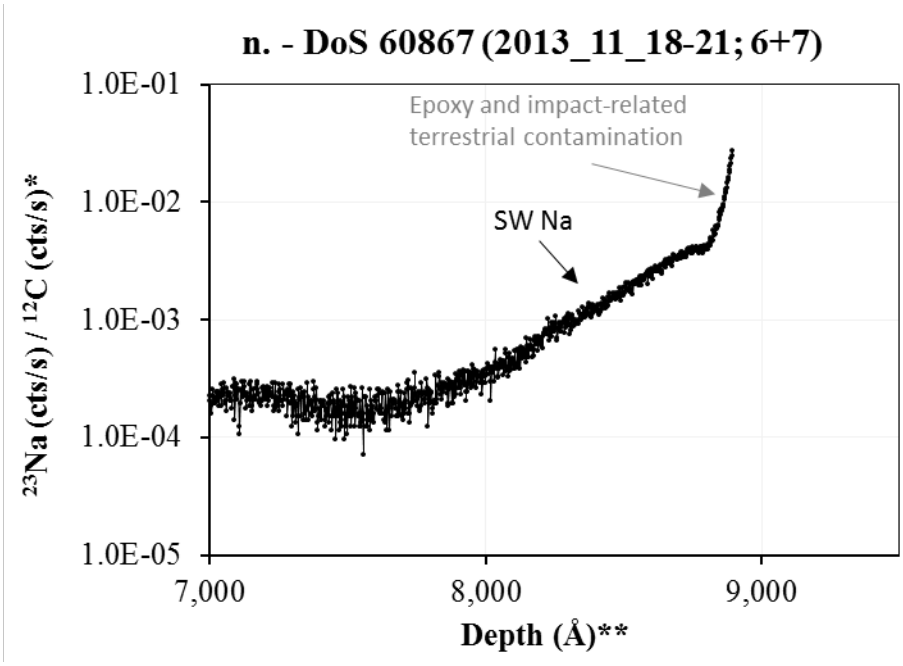
n. - DoS 60867 (2013_11_18-21; 6+7)
Epoxy and impact-related terrestrial contamination
SW Na
1.0E-01
1.0E-02
1.0E-03
1.0E-04
1.0E-05
7,000
8,000
9,000
Depth (Å)**
23Na (cts/s) / 12C (cts/s)*

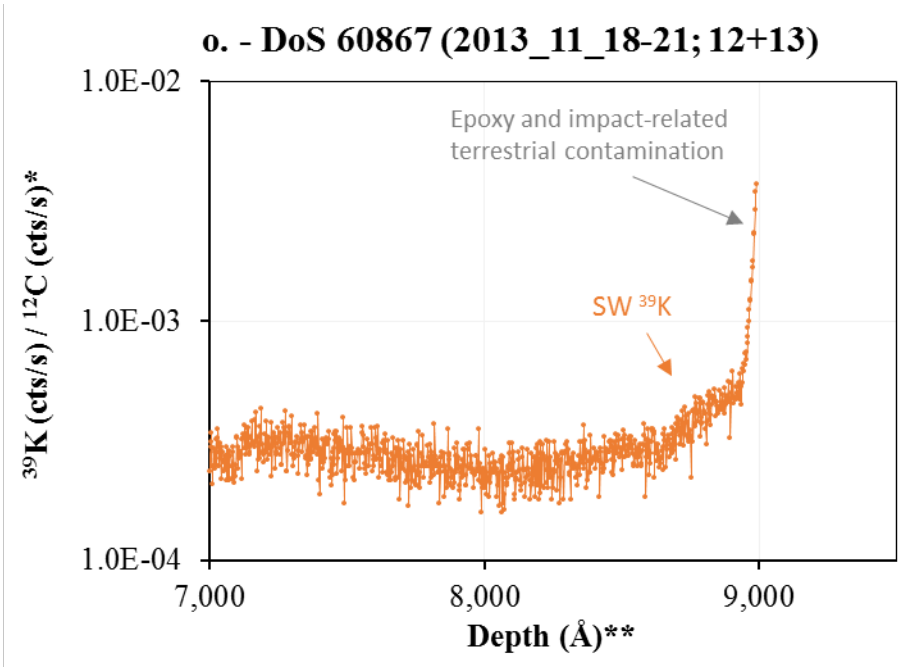
o. - DoS 60867 (2013_11_18-21; 12+13)
1.0E-02
1.0E-03
1.0E-04
7,000
8,000
9,000
Depth (Å)**
39K (cts/s) / 12C (cts/s)*
Epoxy and impact-related terrestrial contamination
SW 39K

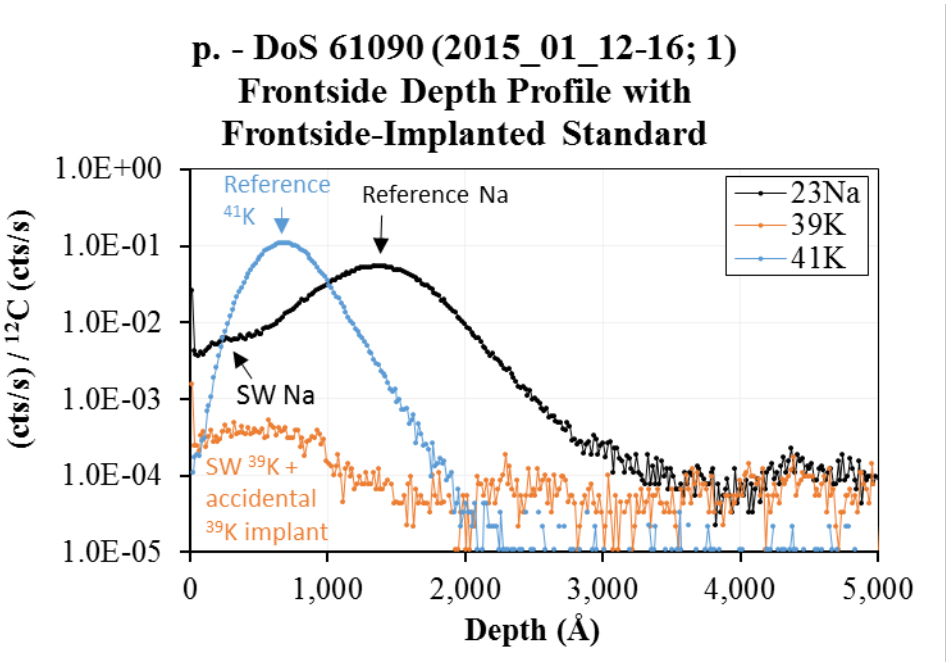
p. - DoS 61090 (2015_01_12-16; 1)
Frontside Depth Profile with
Frontside-Implanted Standard
1.0E+00
1.0E-01
1.0E-02
1.0E-03
1.0E-04
1.0E-05
0
1,000
2,000
3,000
4,000
5,000
Depth (Å)
(cts/s) / 12C (cts/s)
Reference 41K
Reference Na
23Na
39K
41K
SW Na
SW 39K + accidental 39K implant

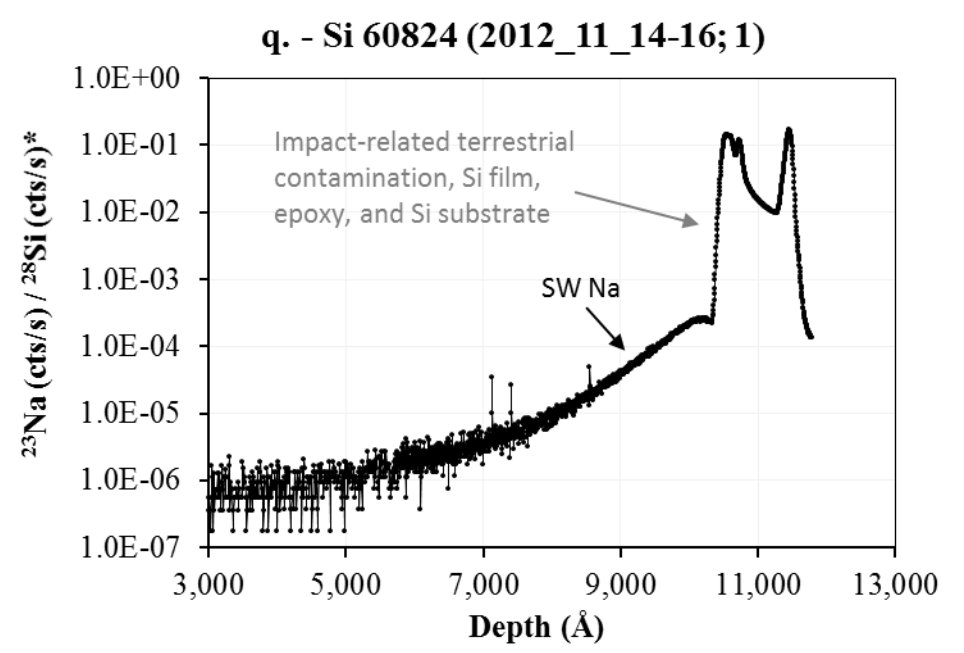
q. - Si 60824 (2012_11_14-16; 1)
1.0E+00
1.0E-01
1.0E-02
1.0E-03
1.0E-04
1.0E-05
1.0E-06
1.0E-07
^{23}Na (cts/s) / ^{28}Si (cts/s)*
Impact-related terrestrial contamination, Si film, epoxy, and Si substrate
SW Na
3,000
5,000
7,000
9,000
11,000
13,000
Depth (Å)

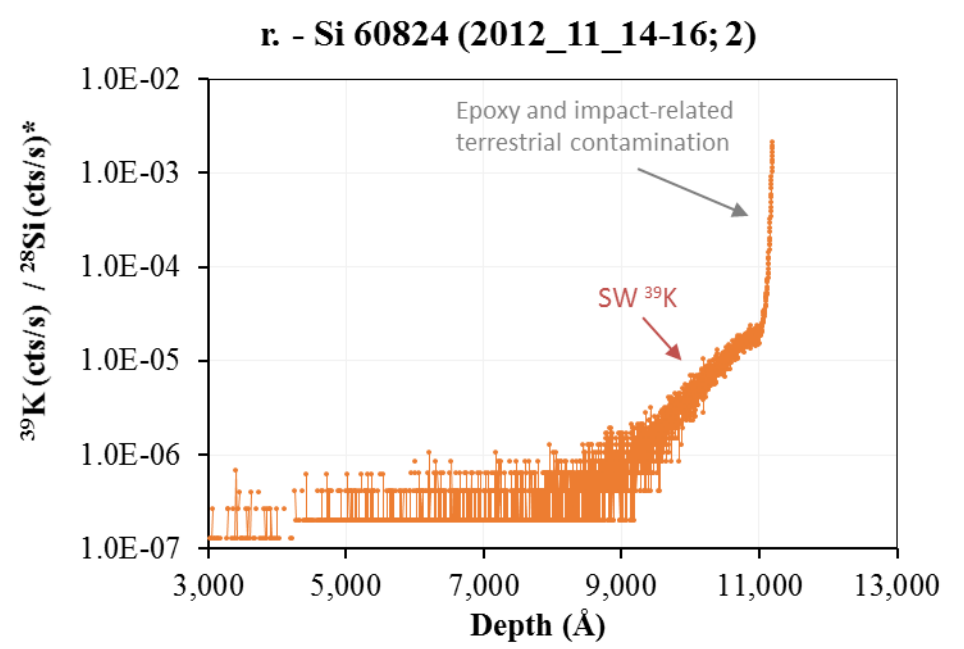
r. - Si 60824 (2012_11_14-16; 2)
1.0E-02
1.0E-03
1.0E-04
1.0E-05
1.0E-06
1.0E-07
^{39}K (cts/s) / ^{28}Si (cts/s)*
Epoxy and impact-related terrestrial contamination
SW ^{39}K
3,000
5,000
7,000
9,000
11,000
13,000
Depth (Å)

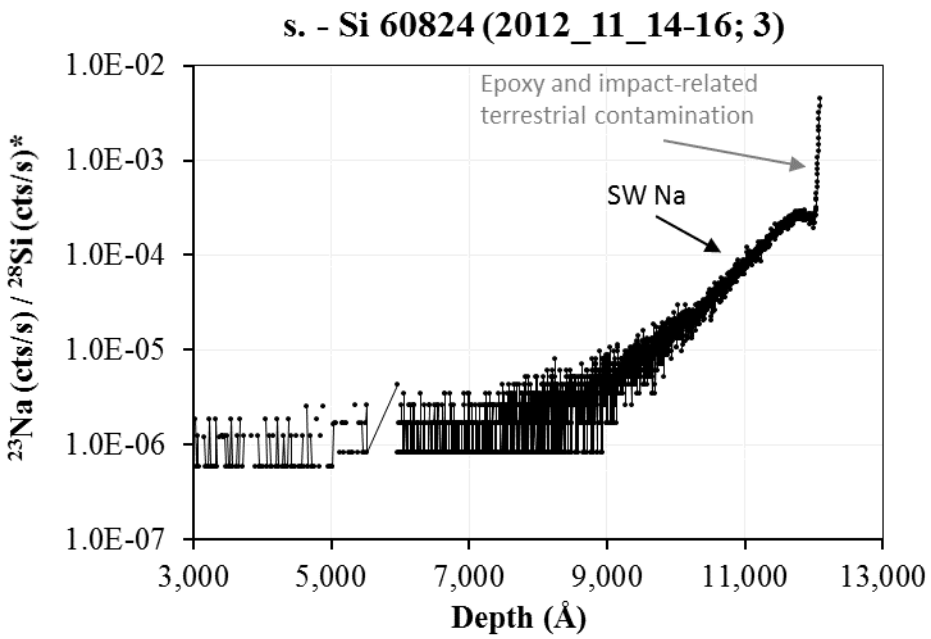
s. - Si 60824 (2012_11_14-16; 3)
1.0E-02
1.0E-03
1.0E-04
1.0E-05
1.0E-06
1.0E-07
^{23}Na (cts/s) / ^{28}Si (cts/s)*
Epoxy and impact-related
terrestrial contamination
SW Na
3,000
5,000
7,000
9,000
11,000
13,000
Depth (Å)

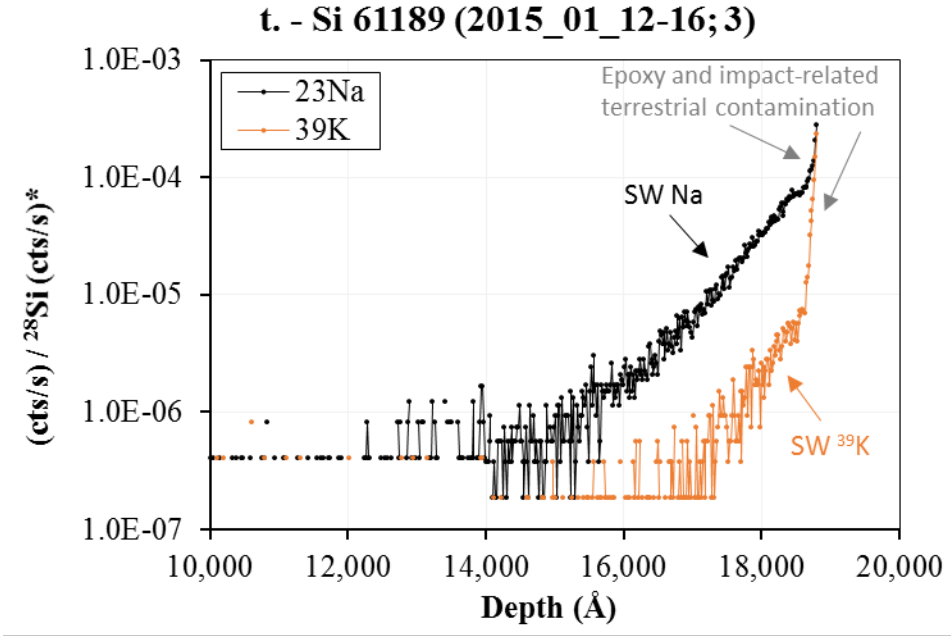
t. - Si 61189 (2015_01_12-16; 3)
1.0E-03
1.0E-04
1.0E-05
1.0E-06
1.0E-07
(cts/s) / ^{28}Si (cts/s)*
23Na
39K
Epoxy and impact-related
terrestrial contamination
SW Na
SW ^{39}K
10,000
12,000
14,000
16,000
18,000
20,000
Depth (Å)

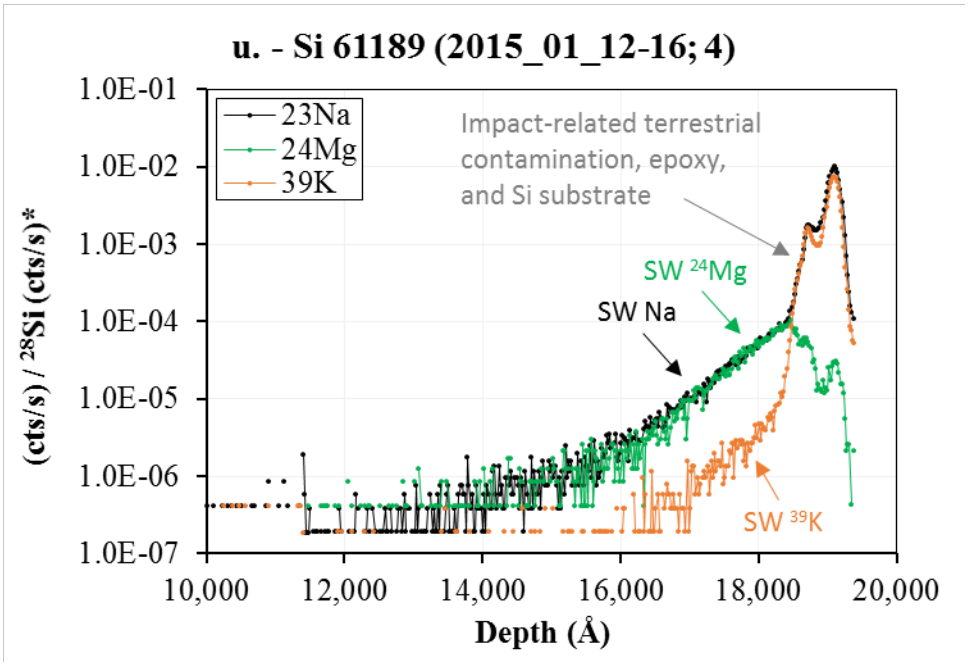
u. - Si 61189 (2015_01_12-16; 4)
1.0E-01
1.0E-02
1.0E-03
1.0E-04
1.0E-05
1.0E-06
1.0E-07
(cts/s) / 28Si (cts/s)*
23Na
24Mg
39K
Impact-related terrestrial contamination, epoxy, and Si substrate
SW 24Mg
SW Na
SW 39K
10,000
12,000
14,000
16,000
18,000
20,000
Depth (Å)

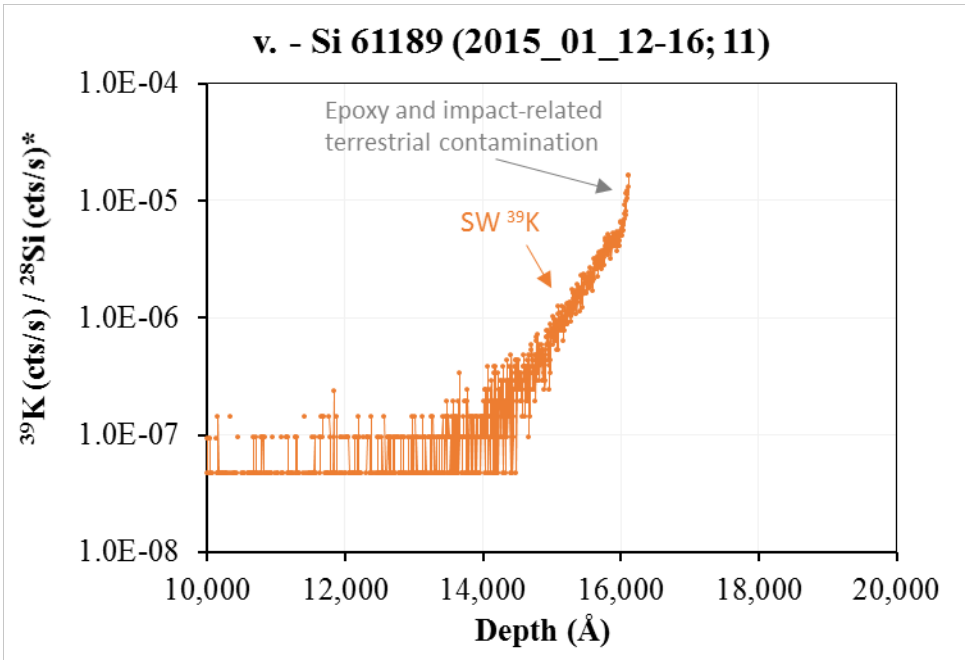
v. - Si 61189 (2015_01_12-16; 11)
1.0E-04
1.0E-05
1.0E-06
1.0E-07
1.0E-08
39K (cts/s) / 28Si (cts/s)*
Epoxy and impact-related terrestrial contamination
SW 39K
10,000
12,000
14,000
16,000
18,000
20,000
Depth (Å)

APPENDIX H

SIMS CRATER FLOOR TOPOGRAPHY

Overview

During SIMS depth profiling analysis, the primary ion beam sputters material from the sample, forming a crater. Uniform sputtering of the sample is critical for 1) achieving high depth resolution analyses, 2) accurately calibrating relative ion yields (Wilson *et al.*, 1989), and 3) facilitating crater depth measurements required for signal integration. Uneven sputtering can be caused by (or accentuated by) the sample matrix, the depth of the crater, how well the primary ion beam is tuned, and the ion species selected for the primary ion beam (e.g., O_2^+ or Cs^+). The following graphics represent a sampling of interferometry data collected as part of the present study. The craters were all produced with well-tuned primary ion beams on the Caltech 7f SIMS. The samples are all Genesis DlC and Si solar wind collectors. Some craters floors are smoother than others. The roughest crater floors were produced by sputtering into sample mounting epoxy with an O_2^+ primary ion beam.

Wilson R. G., Stevie F. A., and Magee C. W. 1989. Secondary ion mass spectrometry: A Practical Handbook for Depth Profiling and Bulk Impurity Analysis. New York: John Wiley and Sons, Inc. 384 p.

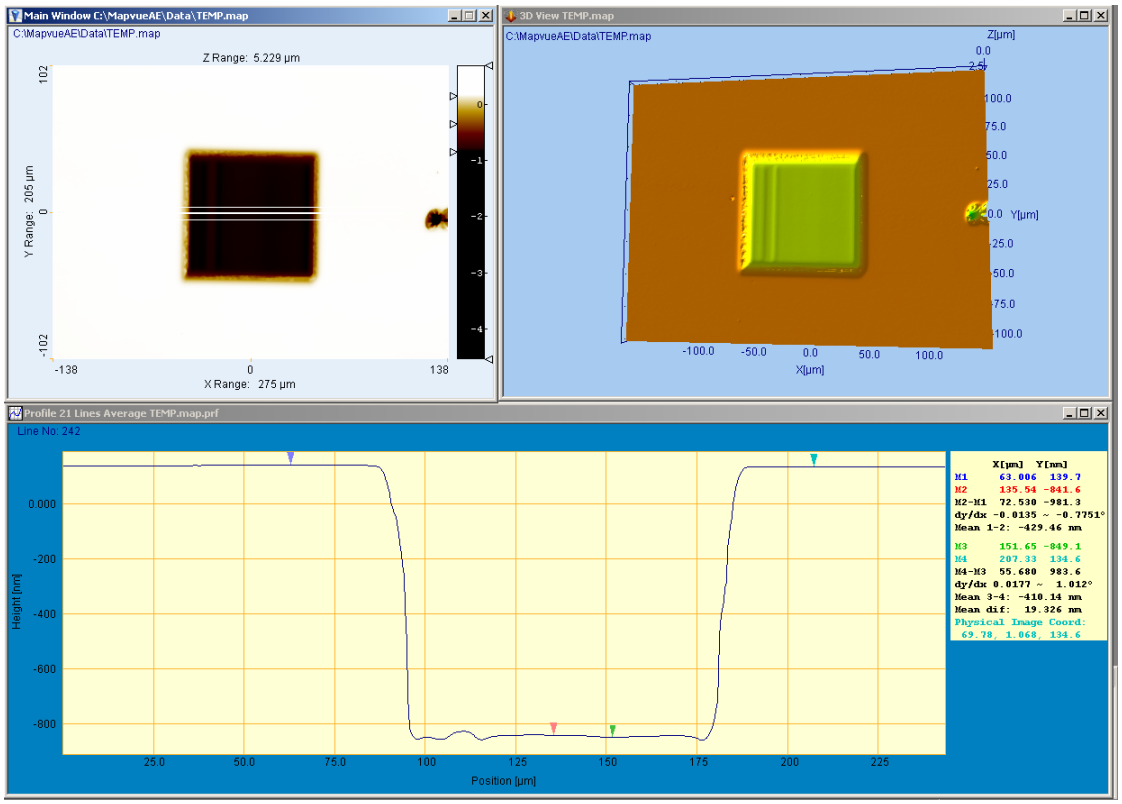

Interferometry measurements for the single frontside depth profile into Genesis DoS 61090 using an O_2^+ primary beam. The depth profile analysis (~10kÅ) was ended shortly after sputtering into the Si substrate. The crater floor is relatively even, except for a ridge-like feature down the left side, which is a sputtering artifact that appeared in every analysis from this session. Signal from this feature was blocked by the field aperture.

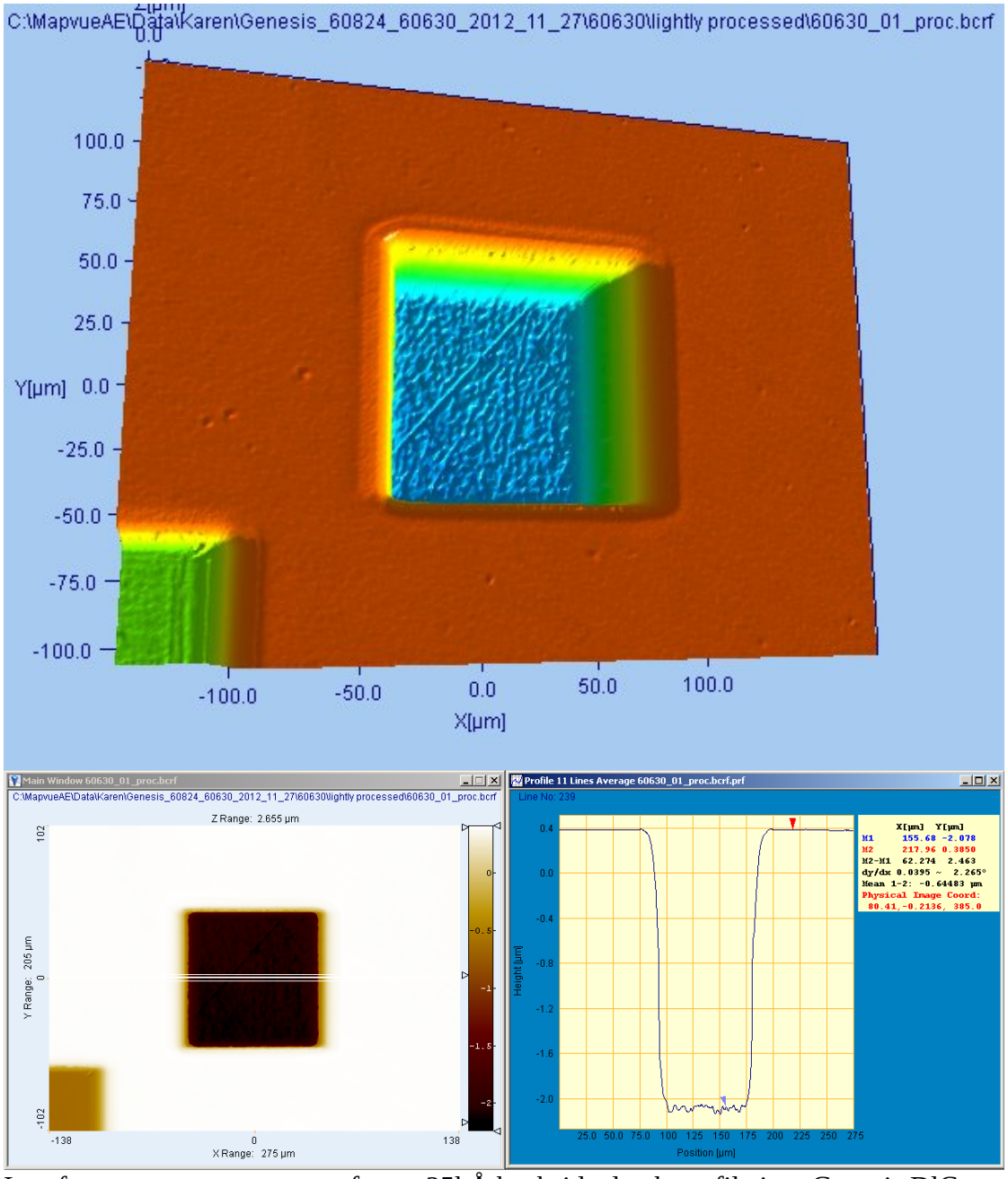

Interferometry measurements for a ~25kÅ backside depth profile into Genesis DlC (60630) using an O_2^+ primary beam. The profile extends through the DlC film (~10-12kÅ), the underlying mounting epoxy, and into the graphite planchet. The crater floor is relatively rough. The sputter rate through the DlC portion was calculated using the sputter rate on an external standard, and scaling for changes in current.

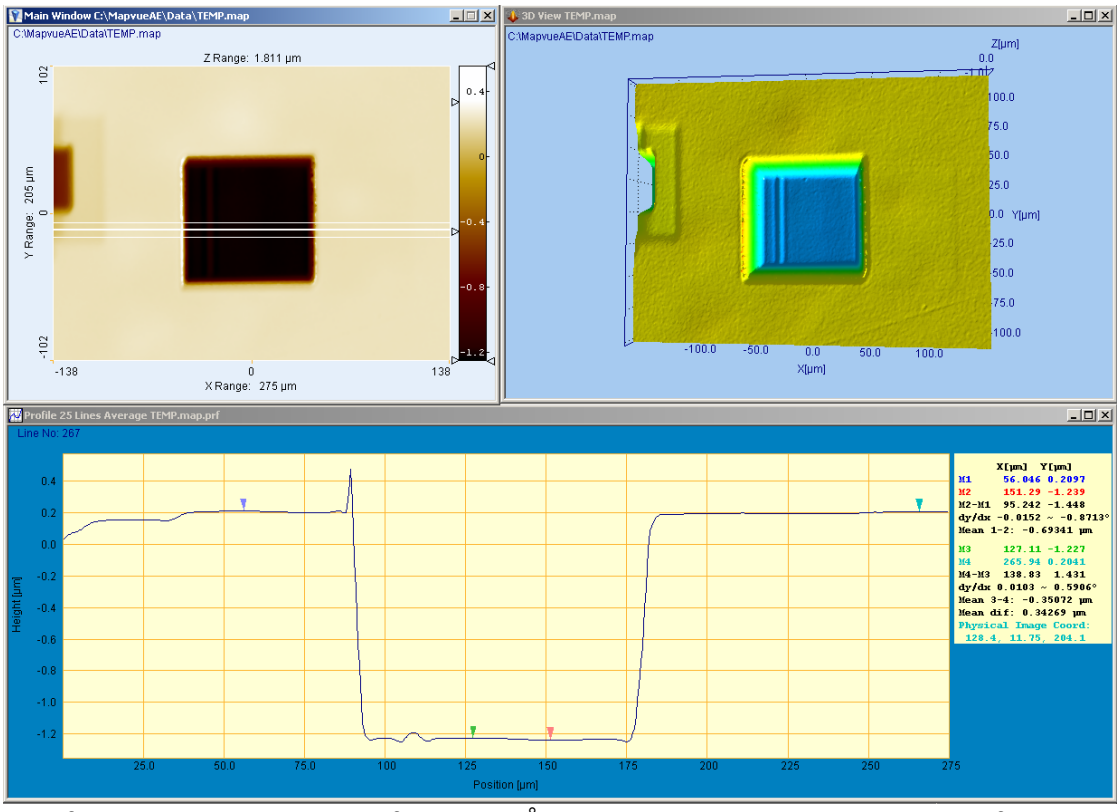

Interferometry measurements for a ~14kÅ crater made by backside depth profiling into thinned Genesis Si 61189 using an O_2^+ primary beam. The thinned Si is ~25kÅ thick, so the profile has not reached the depth of the underlying epoxy. The crater floor is relatively even, except for a ridge that runs along the left hand side, which is a sputtering artifact that appeared in every analysis from this session. Signal from this linear feature was blocked by the field aperture, which was positioned over the center of the raster. Data from this profile were used for instrument set-up and tuning purposes only.

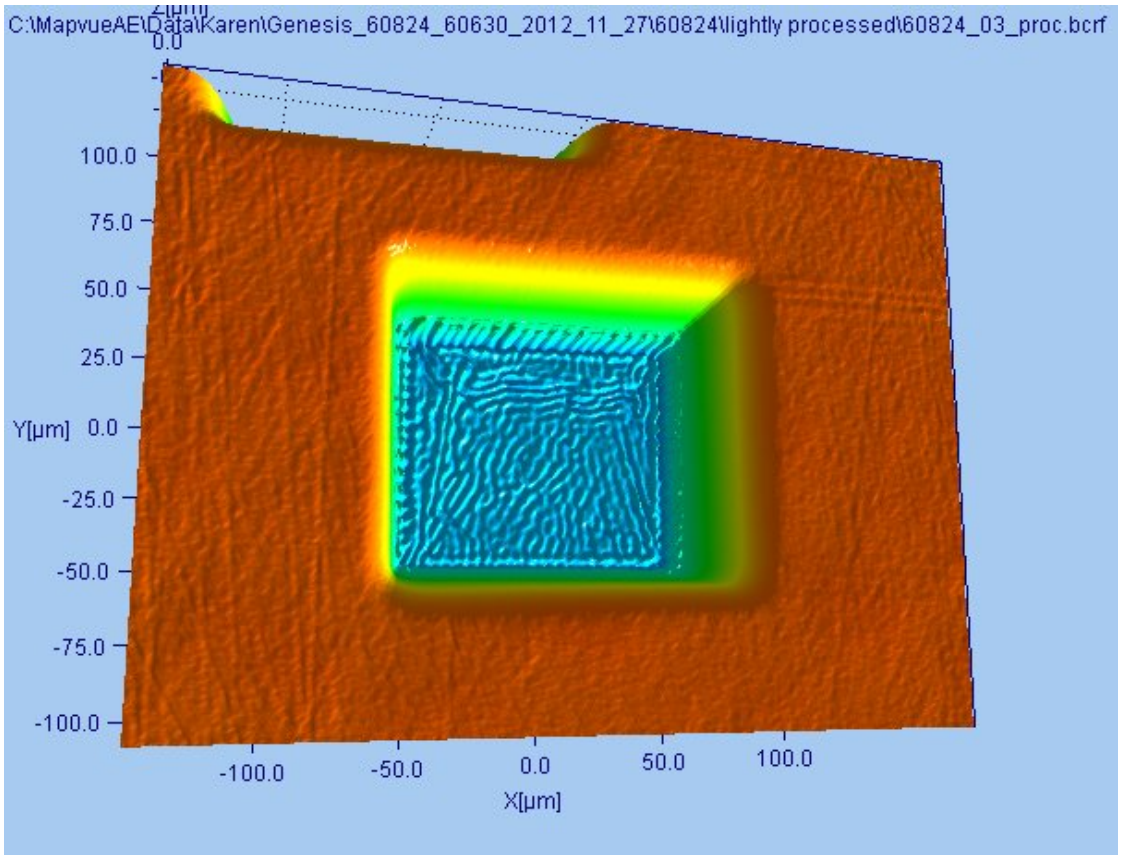

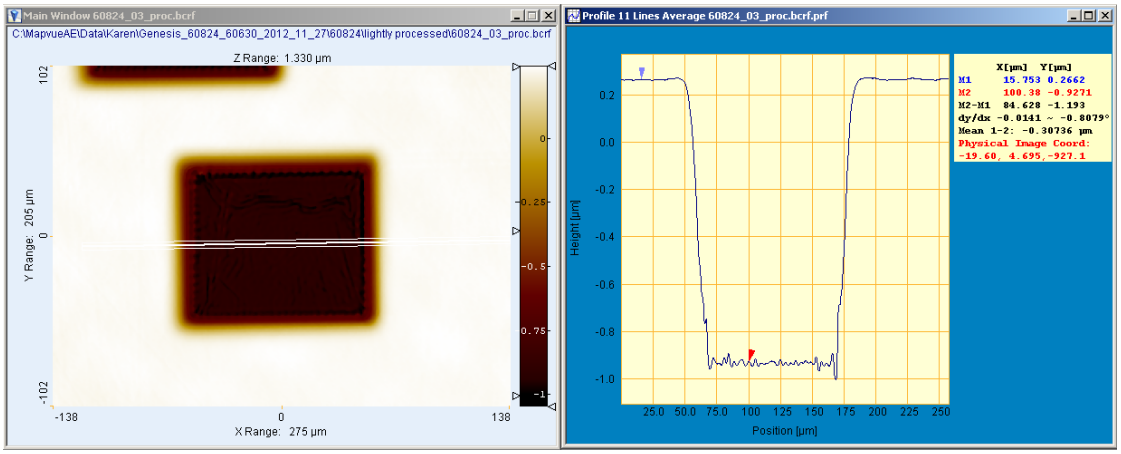

Interferometry measurements for a backside depth profile into Genesis Si (60824) using an O_2^+ primary beam. The depth profile (~12kÅ) extended through the thinned Si into the mounting epoxy, and possibly into the Si substrate. The crater floor is relatively rough. The sputter rate through the Si portion was calculated using the sputter rate on an external standard, and scaling for changes in current.

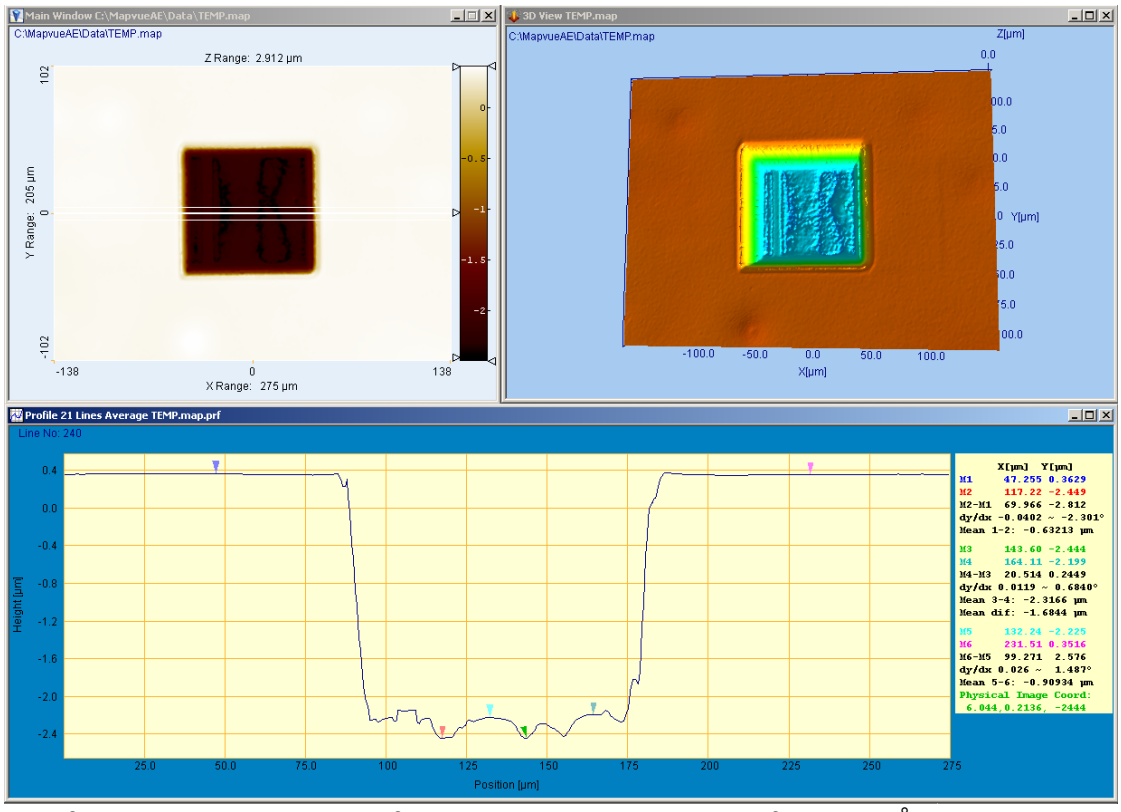

Interferometry measurements for a deep backside depth profile (~27kÅ) into thinned Genesis Si 61189 using an O_2^+ primary beam. The profile extends through the thinned Si (~25kÅ) into the mounting epoxy, and possibly into the Si underneath. The crater floor is relatively rough. This analysis was not used.

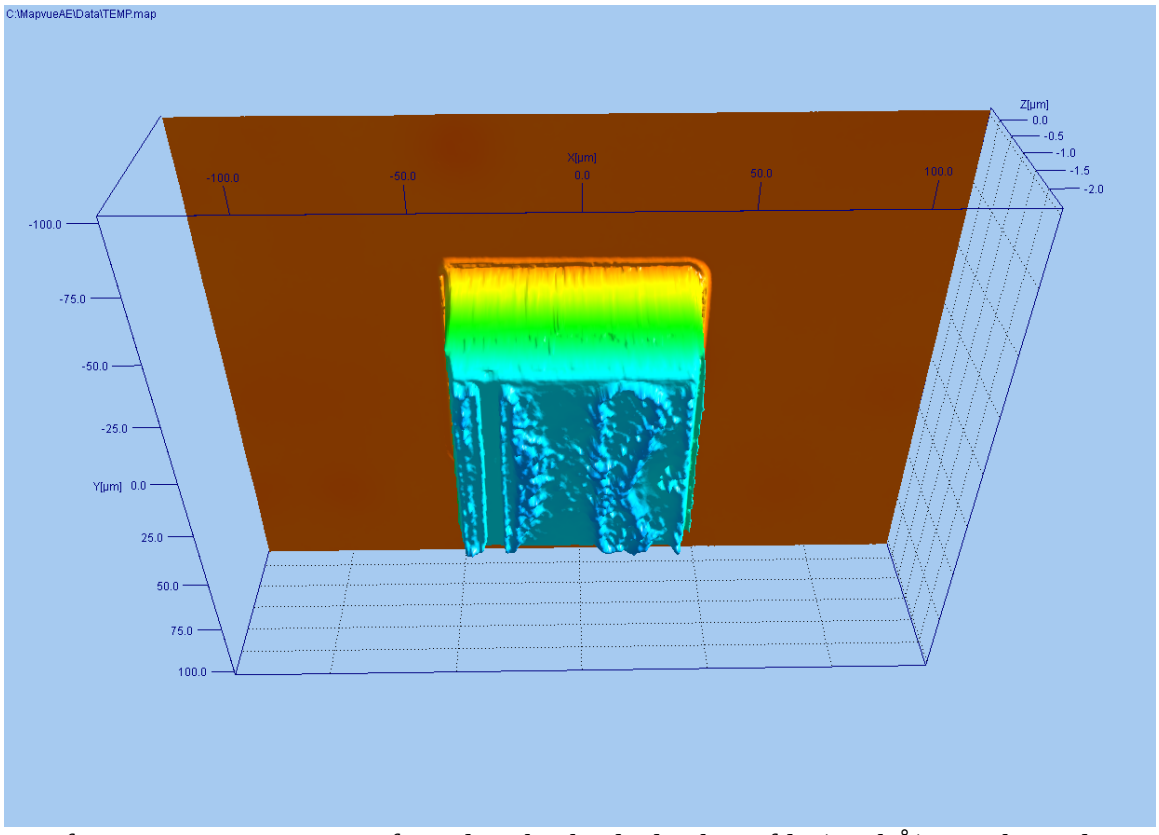

Interferometry measurements for a deep backside depth profile (~27kÅ) into thinned Genesis Si 61189 using an O_2^+ primary beam. This is the same crater as depicted in the preceding figure, but the view is from the base of the crater and the relief is inverted to highlight the uneven crater floor. The analysis has penetrated complexly through the thinned Si, into the epoxy, and possibly into the Si substrate.

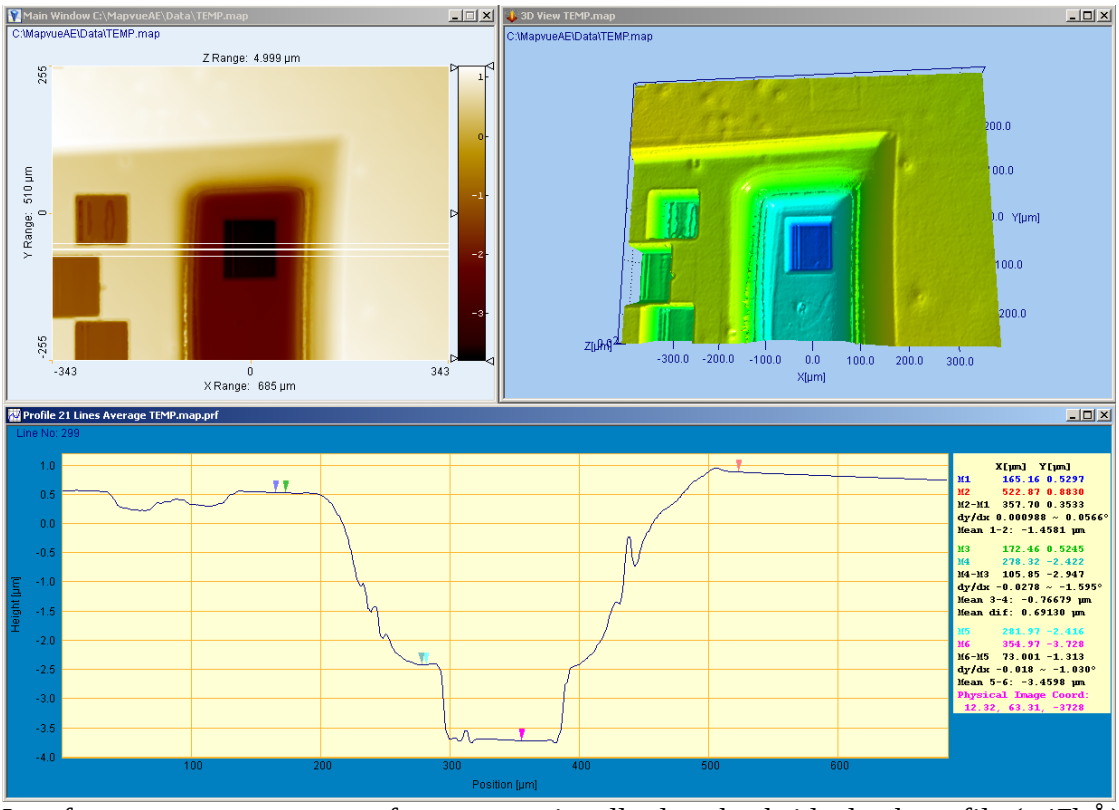

Interferometry measurements for an exceptionally deep backside depth profile (~47kÅ) into thinned Genesis Si 61189 using a combination of Cs^+ and O_2^+ primary beams. Cs^+ prevents the formation of crater floor topography, but O_2^+ allows for better depth resolution. Cs^+ was to be used for presputtering only. O_2^+ was to be used for solar wind analysis. The profile extends through the thinned Si (2.5kÅ) and mounting epoxy into the Si substrate. The depths sputtered by the Cs^+ and O_2^+ primary beams were ~34kÅ and ~13kÅ respectively. This analysis was not used because the second stage of Cs^+ profiling accidently removed all the solar wind before the primary beam was switched to O_2^+ for solar wind measurement. The crater floor is relatively even, except for a ridge-like feature down the left side, which is a sputtering artifact that appeared in every analysis from this session.

APPENDIX I

CONCISE SUMMARY OF OPTICAL, SEM (BSE) AND RAMAN DATA FOR ALL OLIVINE SAMPLES

Overview:

This appendix provides brief one page summaries of data collected by optical microscopy, scanning electron microscopy (SEM), and Raman for the olivine samples discussed in Chapter 3. Optical data was collected in reflected light (RFL), plane-polarized light (PPL), and cross-polarized light (XPL). Backscattered electron (BSE) images were collected with SEM. Additional details are provided in Chapter 3 (Characterization).

“Nominally anhydrous” – 18 GPa – 1100°C
(TD/?) (1.00 hr.)
BB395: rwd + wad reaction rim surrounding ol core

Optical Analysis (RFL, PPL, XPL)

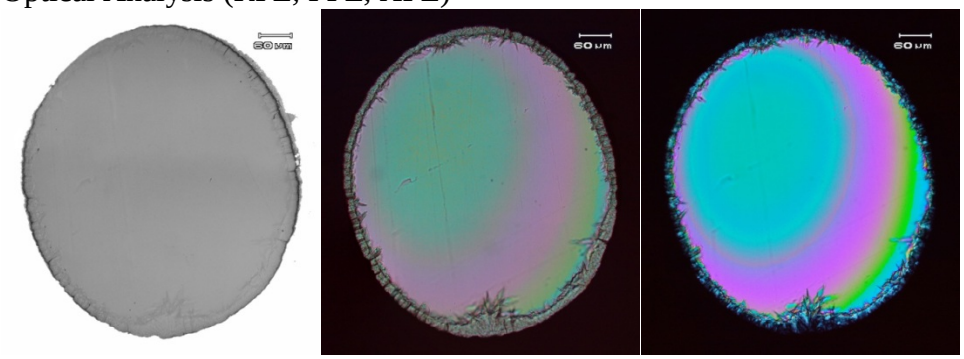

SEM:

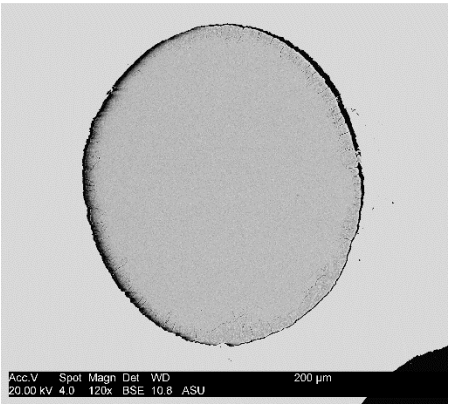

Raman:

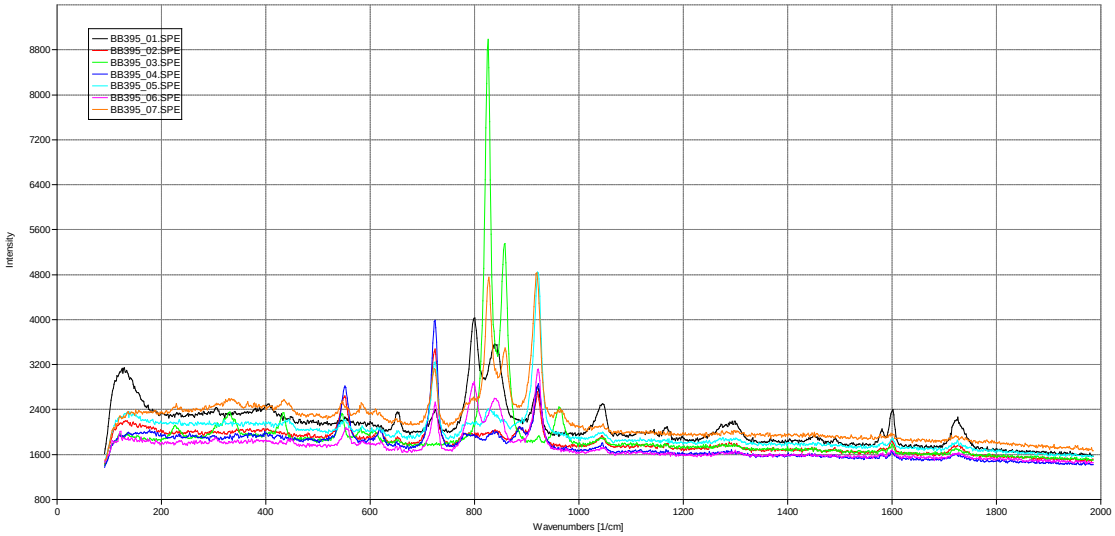

“Nominally anhydrous” – 18 GPa – 1100°C
(WD/ESPI) (1.00 hr.)
BB618B: rwd + wad reaction rim surrounding ol core containing intracrystalline wad (+ rwd?)

Optical Analysis (RFL, PPL, XPL)

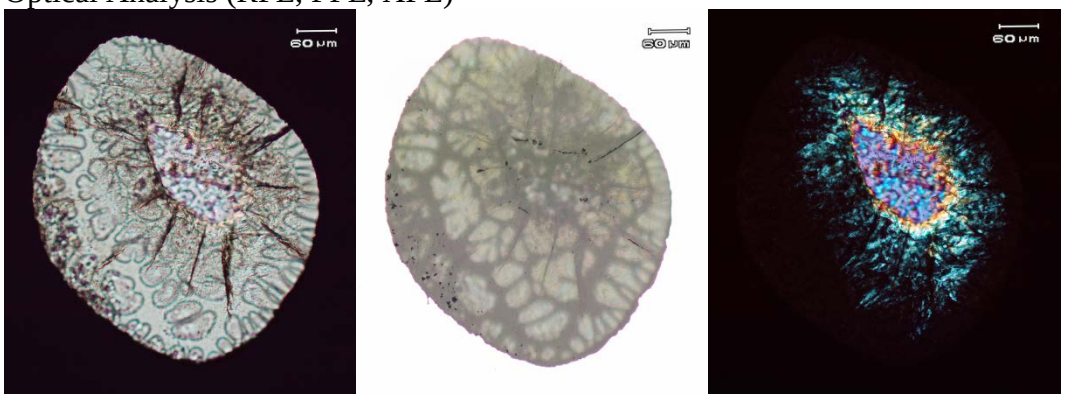

SEM: no data

Raman:

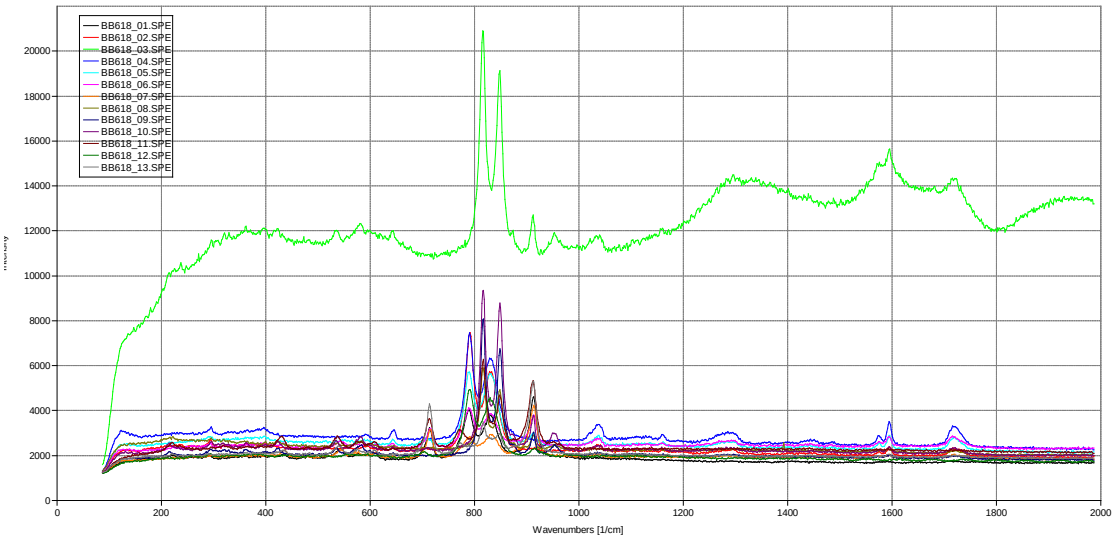

“Nominally anhydrous” – 18 GPa – 1100°C
(WD/ESPI) (1.13 hrs.)
BB621: rwd + wad reaction rim surrounding ol core containing intracrystalline wad (+ rwd?)

Optical Analysis (RFL, PPL, XPL)

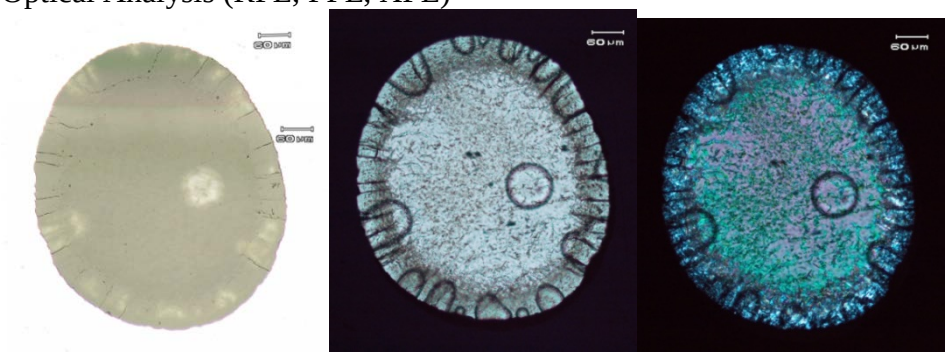

SEM (BSE):

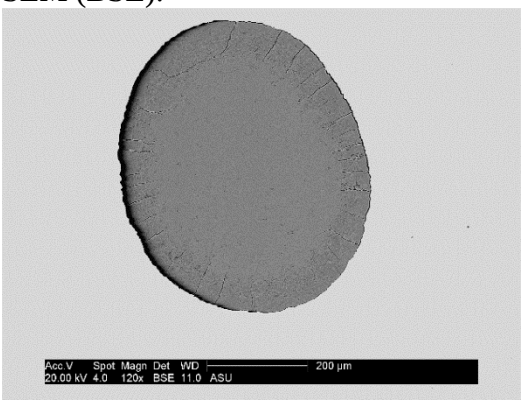

Raman:

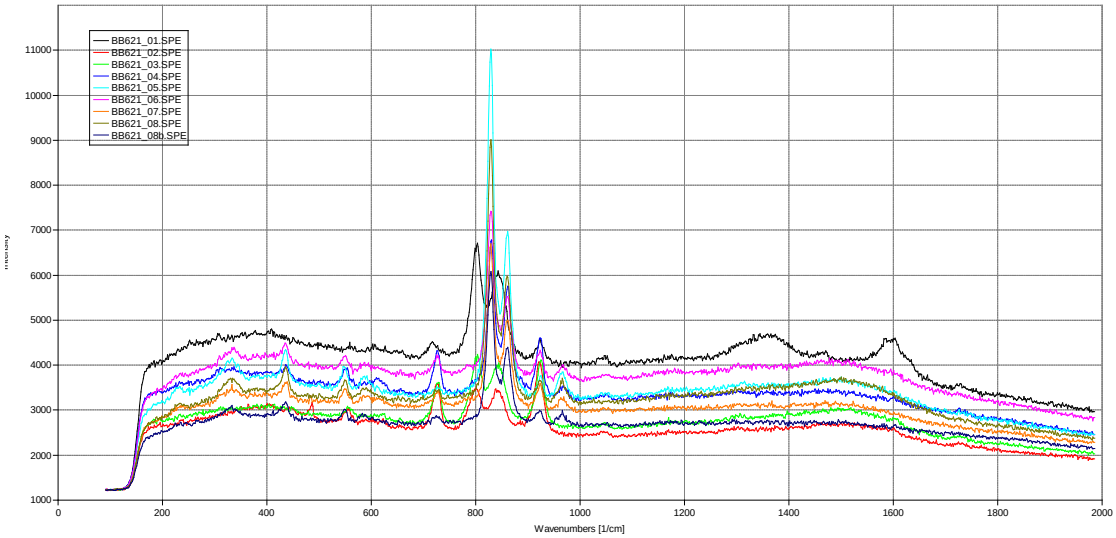

“Nominally anhydrous” – 18 GPa – 1100°C
(TD/?) (24 hrs.)
BB392: rwd + wad reaction rim surrounding ol core

Optical Analysis (RFL, PPL, XPL)

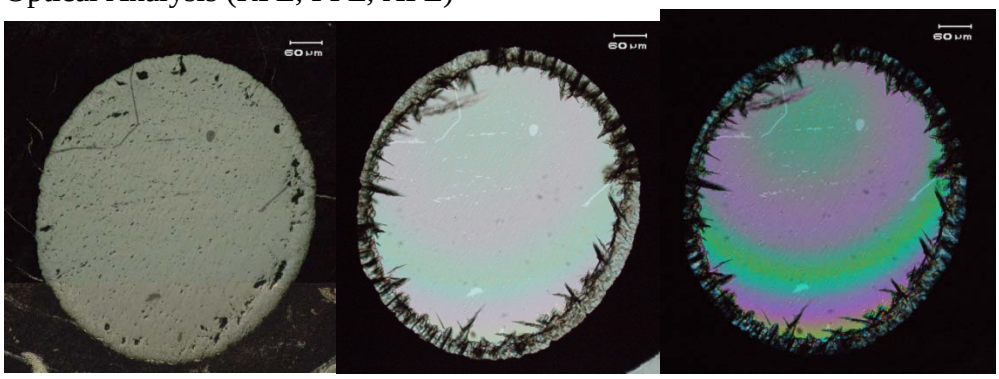

SEM (BSE):

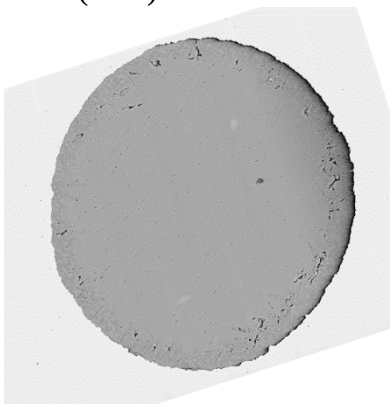

Raman:

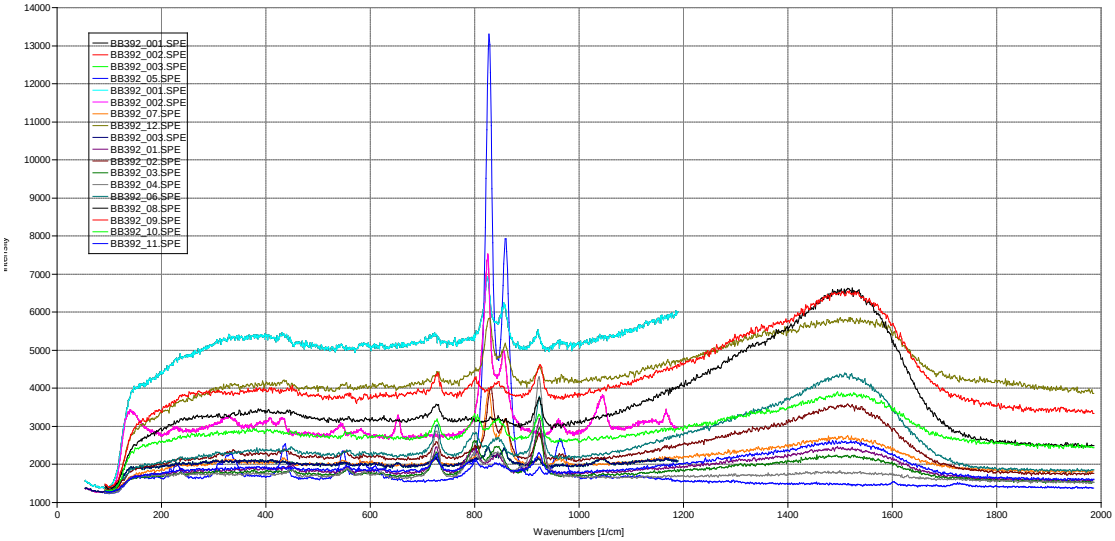

“Moist” (75±15 ppmw $^{2}H_2O$) – 18 GPa – 900°C
(WD/Goodfellow) (7.00 hrs.)
BB755A: primarily rwd reaction rim surrounding ol core containing intracrystalline rwd

Optical Analysis (RFL, PPL, XPL)

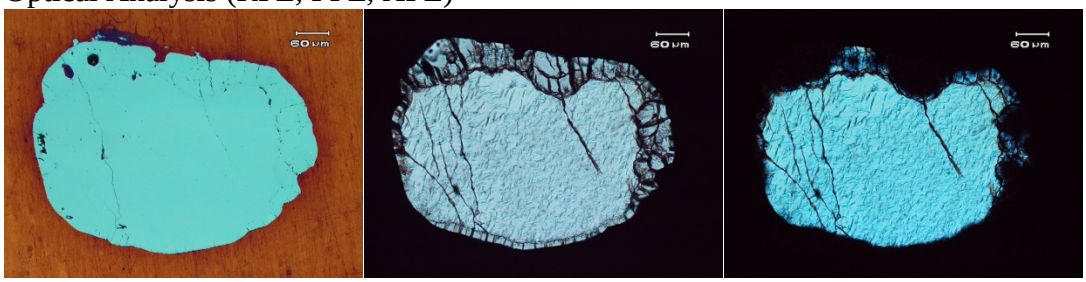

SEM (BSE):

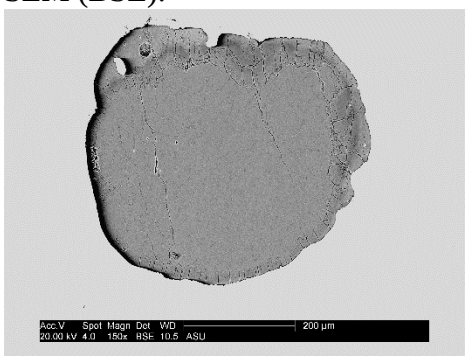

Raman:

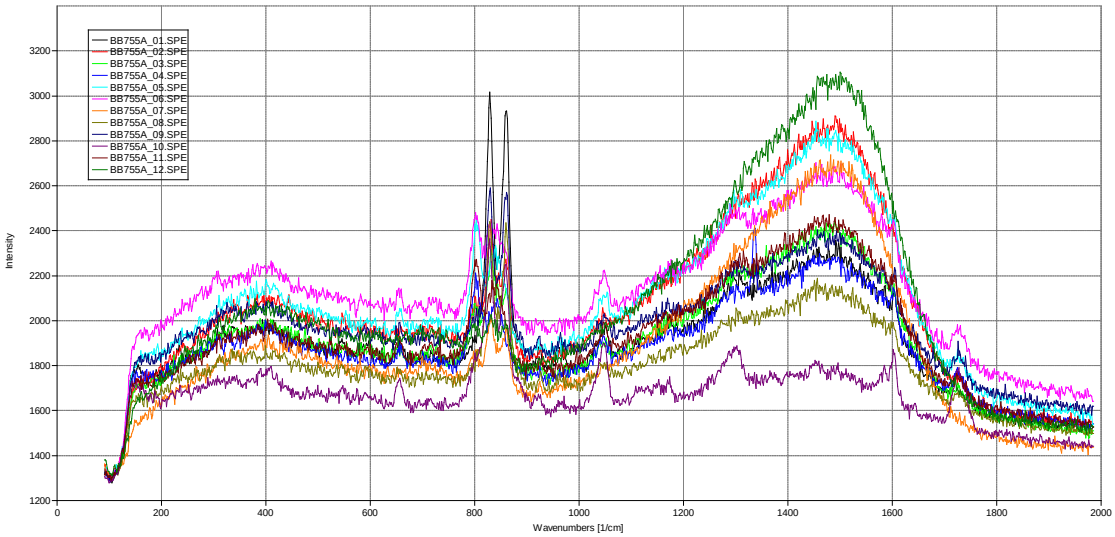

"Moist" (75±15 ppmw $^{2}H_2O$) – 18 GPa – 900°C
(WD/Goodfellow) (26.13 hrs.)
BB754Top: rwd reaction rim surrounding ol core containing intracrystalline rwd(?)

Optical Analysis (RFL, PPL, XPL)

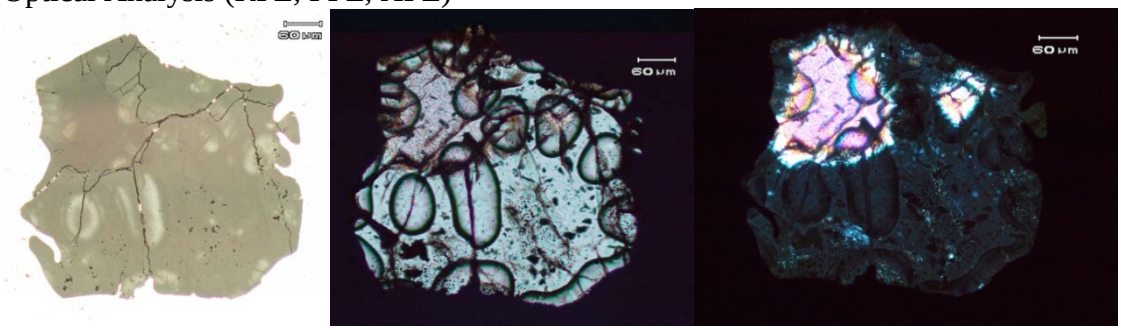

SEM (BSE):

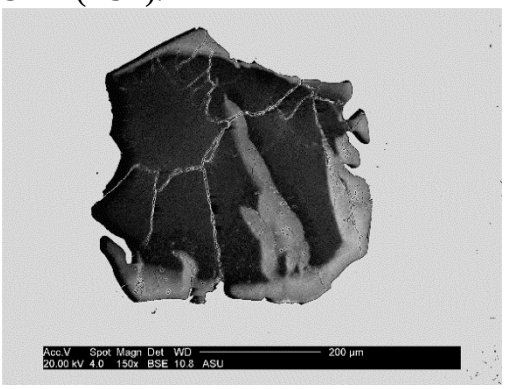

Raman:

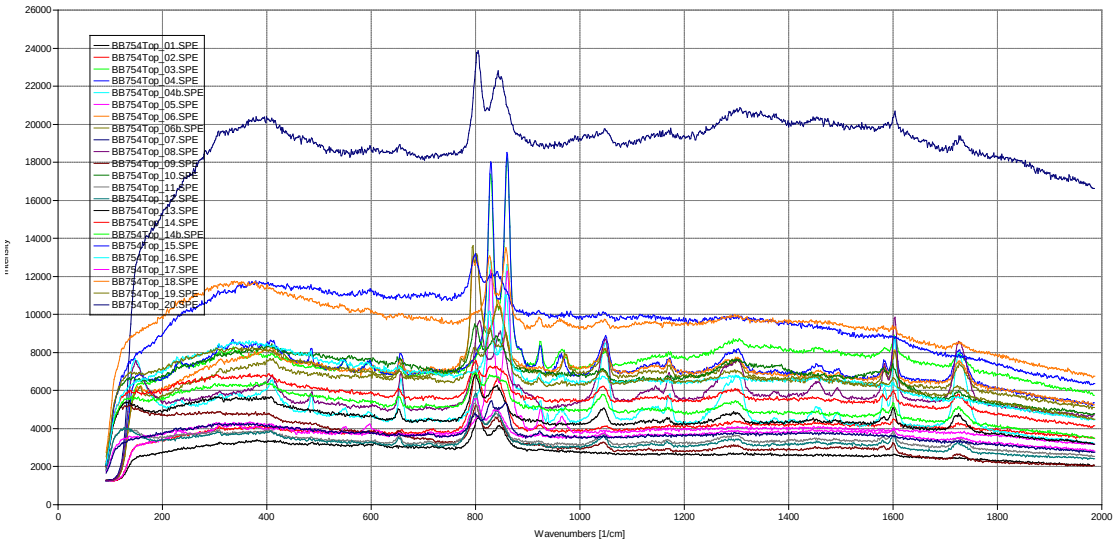

“Moist” (75±15 ppmw $^{2}H_2O$) – 18 GPa – 1100°C
(WD/Goodfellow) (0.67 hours)
BB759Top: rwd + minor wad reaction rim surrounding ol core containing intracrystalline rwd

Optical Analysis (RFL, PPL, XPL)

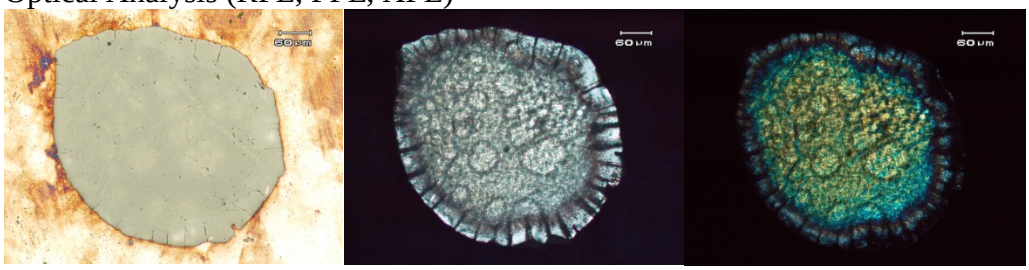

SEM (BSE):

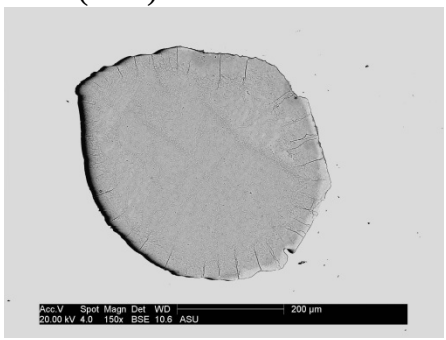

Raman:

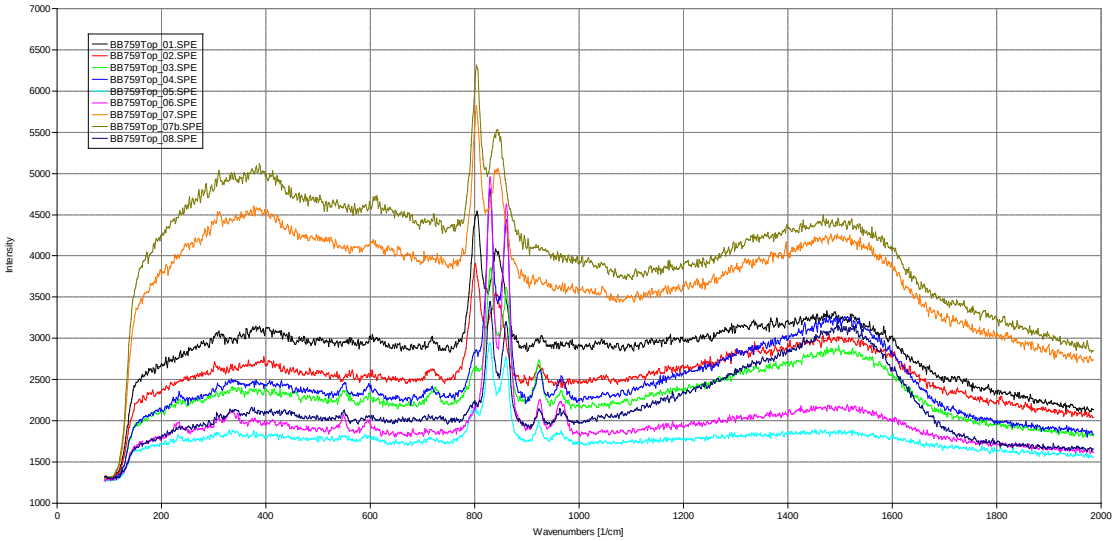

“Moist” (75±15 ppmw $^{2}H_2O$) – 18 GPa – 1100°C
(WD/ESPI) (0.17 hours)
BB527A: rwd + (some) wad reaction rim surrounding ol core containing intracrystalline rwd (?)

Optical Analysis (RFL, PPL, XPL)

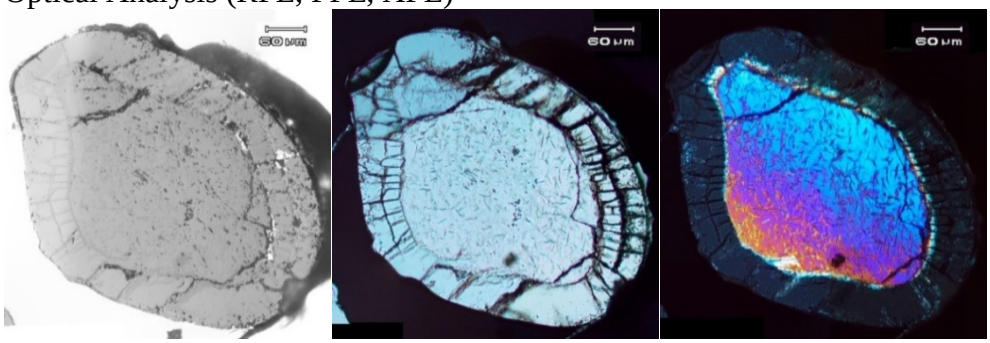

SEM (BSE):

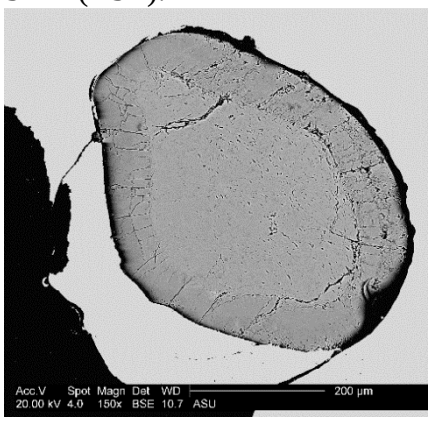

Raman:

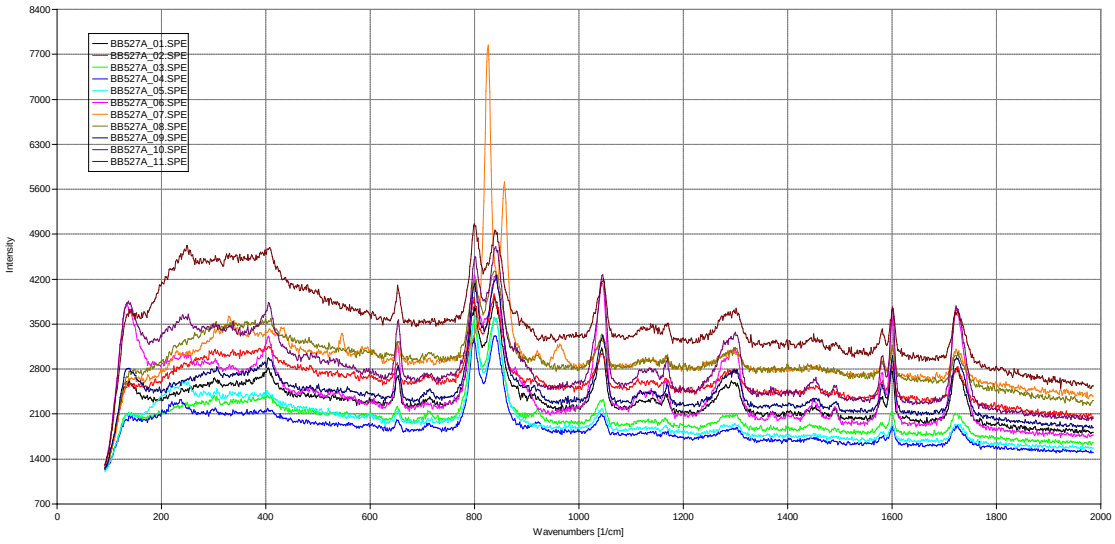

“Moist” (75±15 ppmw $^{2}H_2O$) – 18 GPa – 1100°C
(WD/ESPI) (0.25 hrs.)
BB583: rwd reaction rim surrounding ol core containing intracrystalline rwd(?)

Optical Analysis (RFL, PPL, XPL)

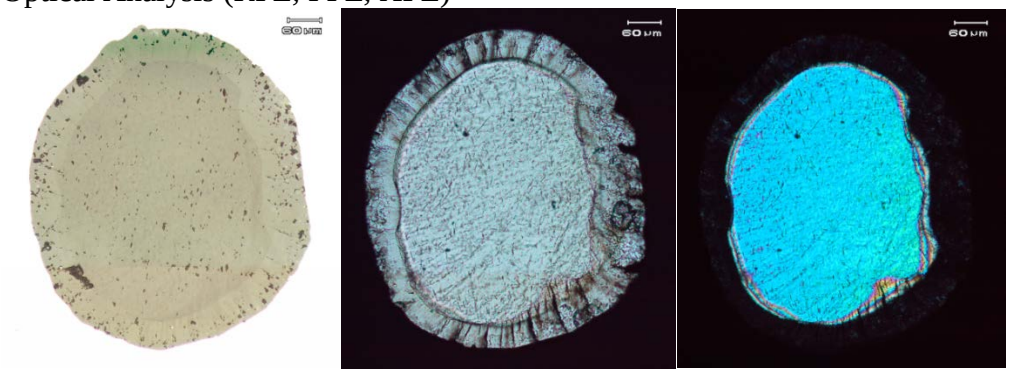

SEM (BSE):

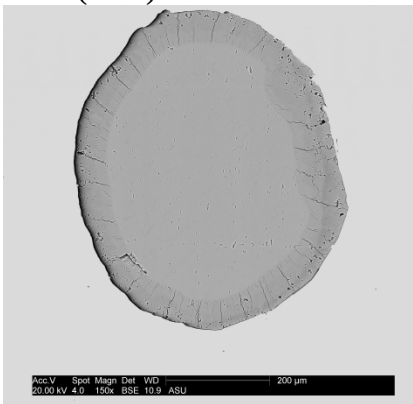

Raman:

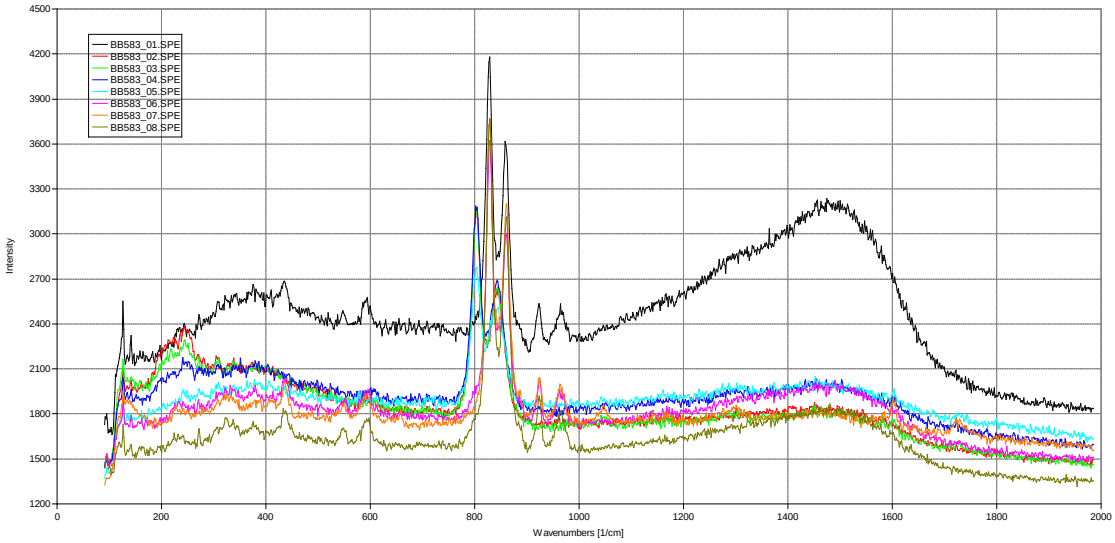

"Wet" (289±72 ppmw $^{2}H_2O$) – 18 GPa – 900°C
(TD/?) (10 hrs.)
BB344: rwd (+ hint of wad) reaction rim surrounding ol core containing intracrystalline rwd (?)

Optical Analysis (RFL, PPL, XPL)

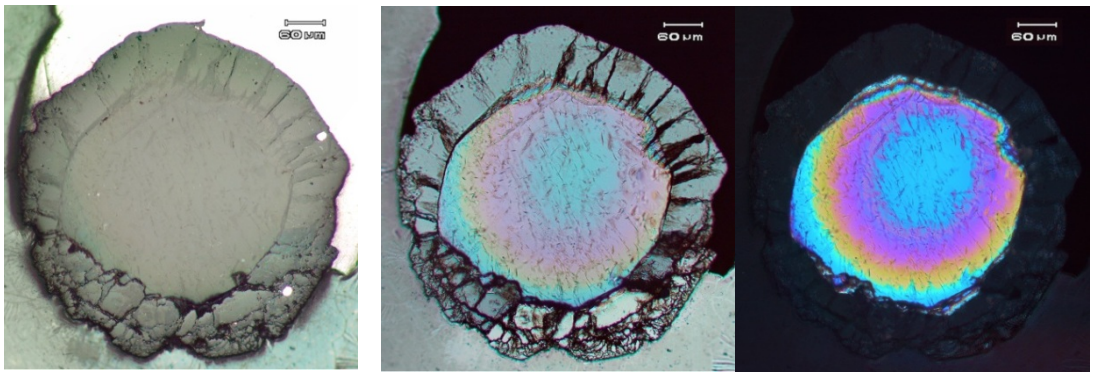

SEM (BSE):

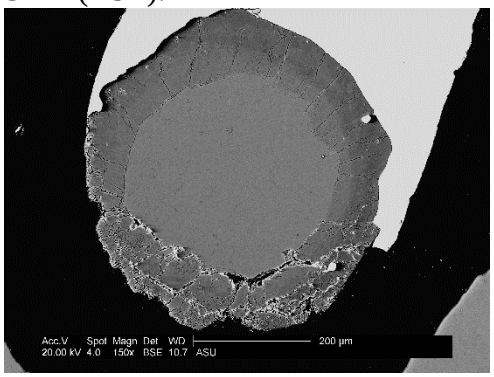

Raman:

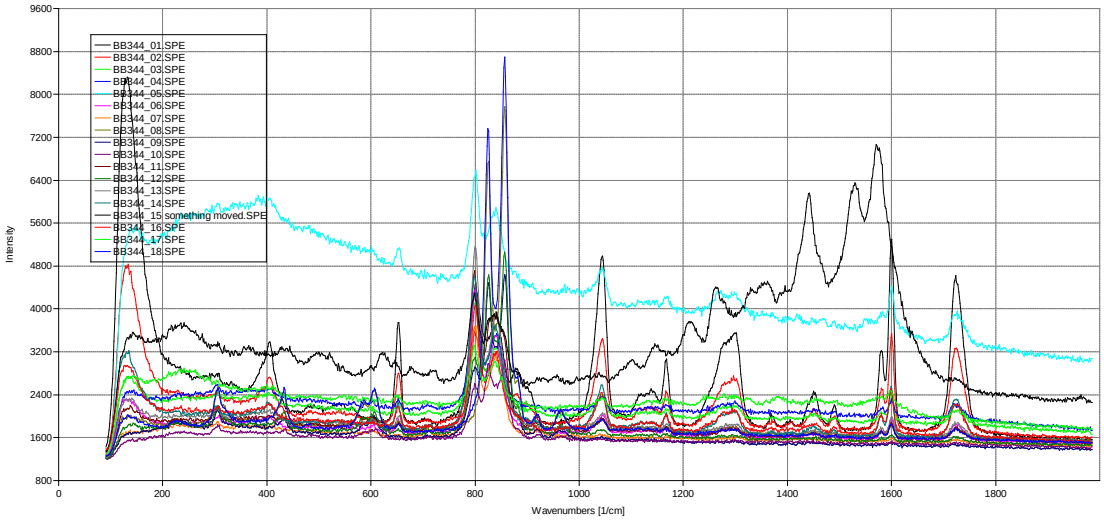

"Wet" (289±72 ppmw $^{2}H_2O$) – 18 GPa – 900°C
(TD/?) (25 hrs.)
BB383: Thick rwd (+ hint of wad) reaction rim surrounding ol core, with wad interface

Optical Analysis (RFL, PPL, XPL)

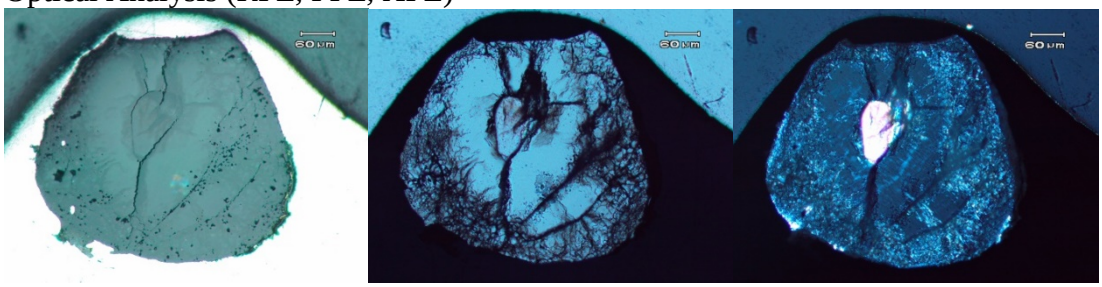

SEM (BSE):

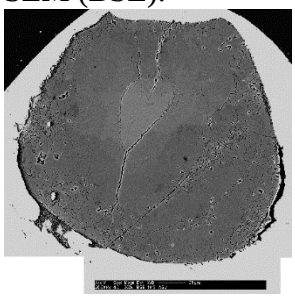

Raman:

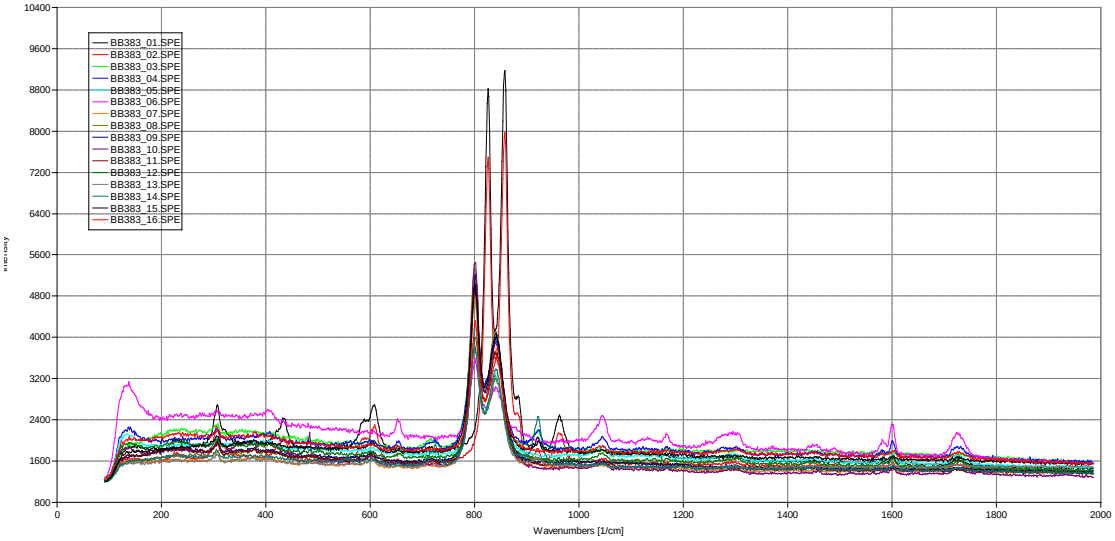

"Wet" (289±72 ppmw $^{2}H_2O$) – 18 GPa – 1100°C
(TD/?) (0.167 hrs.)
BB350: primarily rwd reaction rim surrounding ol core containing intracrystalline rwd(?), with wad at the core-rim interface

Optical Analysis (RFL, PPL, XPL)

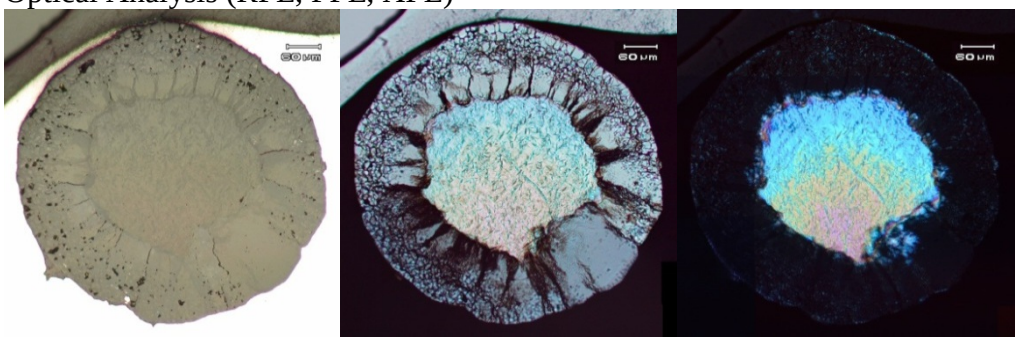

SEM (BSE):

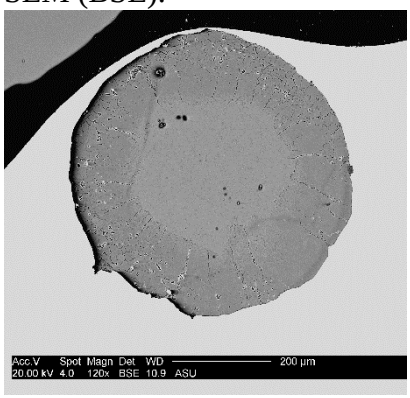

Raman:

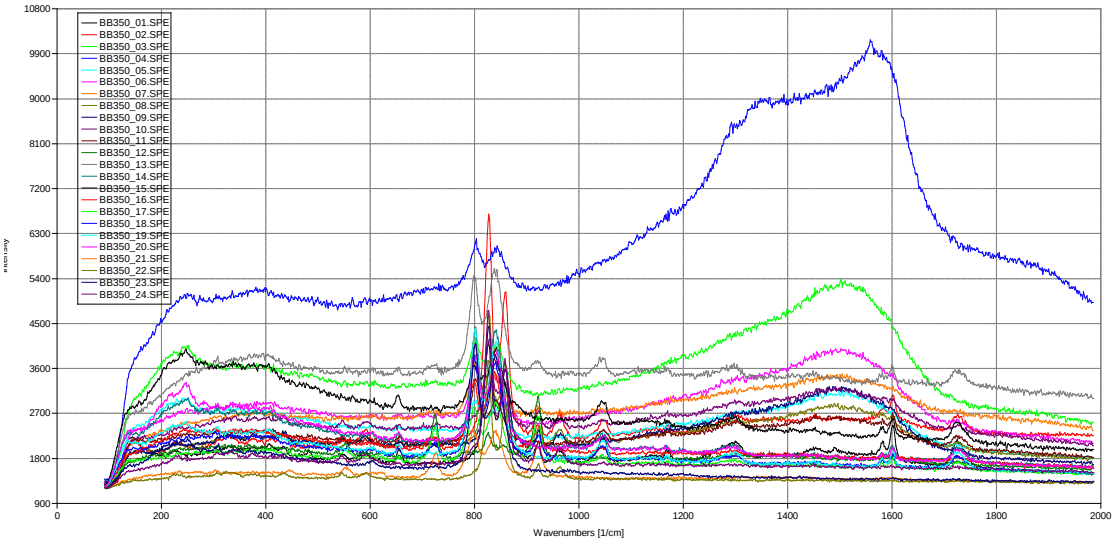

"Wet" (289±72 ppmw $^{2}H_2O$) – 18 GPa – 1100°C
(TD/?) (0.333 hr.)
BB396: primarily rwd rim, surrounding ol core containing intracrystalline wad & rwd(?), with wad at the core-rim interface

Optical Analysis (RFL, PPL, XPL)

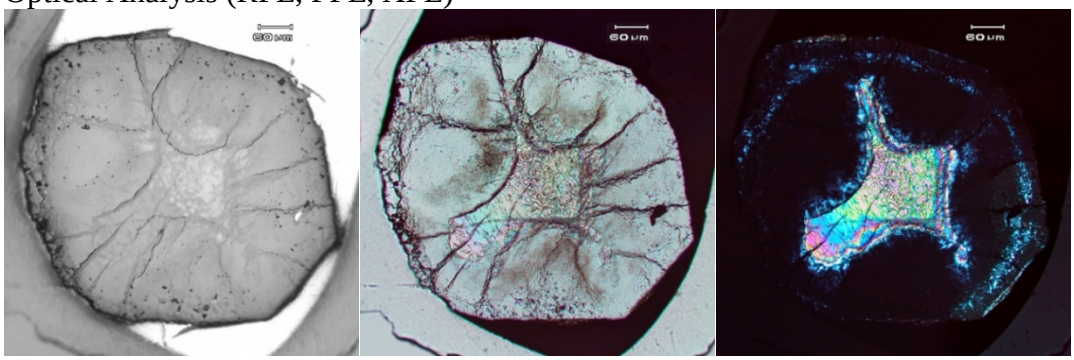

SEM (BSE):

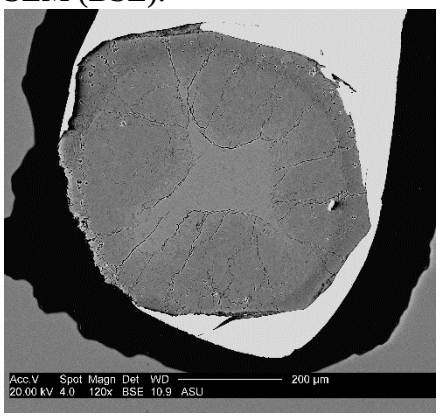

Raman: